

# Wave packet dynamics in atomic systems and Bose-Einstein condensates

Von der Fakultät für Mathematik und Physik der Universität Stuttgart  
zur Erlangung der Würde eines Doktors der  
Naturwissenschaften (Dr. rer. nat.) genehmigte Abhandlung

Vorgelegt von

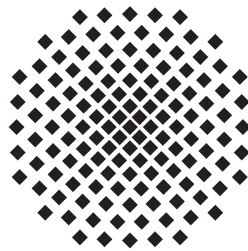
**Tomaž Fabčić**

aus Stuttgart

Hauptberichter: Prof. Dr. J. Main

Mitberichter: Prof. Dr. H. P. Büchler

Tag der mündlichen Prüfung: 14. Juli 2008



1. Institut für Theoretische Physik der Universität Stuttgart

2008



# Contents

<b>1. Introduction</b>	<b>5</b>
<b>2. Time-dependent variational principle</b>	<b>9</b>
2.1. Least action principle . . . . .	10
2.2. McLachlan variational principle . . . . .	12
2.3. Conservation laws . . . . .	17
2.3.1. Conservation of norm and energy . . . . .	17
2.4. Error estimation . . . . .	18
<b>3. Application of the TDVP to GWP</b>	<b>19</b>
<b>4. Inequality constrained TDVP</b>	<b>27</b>
4.1. Inequality constrained TDVP on arbitrary trial functions . . . . .	28
4.2. Inequality constrained TDVP applied to GWP . . . . .	31
4.3. 2D diamagnetic hydrogen atom . . . . .	33
4.3.1. Error introduced by the constraints . . . . .	39
4.3.2. Comparison with exact computations . . . . .	40
<b>5. Wave packet dynamics in the hydrogen atom</b>	<b>47</b>
5.1. Regularization of the hydrogen atom . . . . .	48
5.1.1. Eigenstates of the regularized hydrogen atom . . . . .	49
5.2. Restricted Gaussian wave packets in Kustaanheimo-Stiefel coordinates . . . . .	51
5.3. Analytical wave packet dynamics in the hydrogen atom . . . . .	54
5.3.1. Propagation of wave packets without well defined angular momentum . . . . .	55
5.3.2. Propagation of wave packets with conserved angular momentum component $l_z$ . . . . .	59
5.3.3. Wave packet propagation with conserved angular momentum $l^2, l_z$ . . . . .	66
<b>6. Wave packet dynamics in the hydrogen atom in external fields</b>	<b>71</b>
6.1. Regularized hydrogen atom in external fields . . . . .	71
6.2. Variational GWP dynamics in the diamagnetic hydrogen atom . . . . .	73
6.3. Variational GWP dynamics in the hydrogen atom in crossed fields . . . . .	81

<b>7. Wave packet dynamics of Bose-Einstein condensates with attractive <math>1/r</math> interaction</b>	<b>85</b>
7.1. TDVP for BECs with attractive $1/r$ interaction . . . . .	87
7.2. Linear stability of the bifurcating states . . . . .	88
7.3. Dynamics of the condensate . . . . .	90
7.3.1. Variational approach . . . . .	90
7.3.2. Exact time-dependent calculations with the split-operator method	95
<b>8. Dynamics of Bose-Einstein condensates with dipolar interaction</b>	<b>105</b>
8.1. TDVP for the dipolar BEC . . . . .	107
8.2. Poincaré surfaces of section . . . . .	109
<b>9. Conclusion</b>	<b>117</b>
<b>Zusammenfassung</b>	<b>119</b>
<b>A. Gaussian type integrals</b>	<b>131</b>
A.1. Gaussian type moments in two dimensions . . . . .	131
A.2. Integrals for the diamagnetic hydrogen atom . . . . .	132
A.3. Integrals for the hydrogen atom in crossed electric and magnetic fields . .	134
A.4. Integrals for Bose-Einstein condensates with $1/r$ interaction . . . . .	135
A.5. Integrals for Bose-Einstein condensates with dipolar interaction . . . . .	136
<b>B. Reduction of the number of parameters in the matrices <math>B, C</math></b>	<b>139</b>
<b>C. Split-operator method</b>	<b>141</b>
<b>Bibliography</b>	<b>143</b>
<b>Danksagung</b>	<b>151</b>
<b>Lebenslauf</b>	<b>153</b>

# 1. Introduction

The effort of a numerically exact solution of the time-dependent Schrödinger equation increases exponentially with the dimension of the investigated system and approximate methods are needed. Different approaches to this problem are subject of investigation ranging from semiclassical methods as the initial value representation [1, 2] to methods based on the time-dependent variational principle (TDVP), as e.g. the multi configurational time-dependent Hartree method [3] or the method of Gaussian wave packet propagation [4–9].

The method of Gaussian wave packet propagation introduced by Heller [10] allows for a wide range of different levels of approximation. In its simplest versions [11] it presents the starting point for the initial value representations, whereas the more sophisticated versions [5–9, 12, 13] based on the TDVP allow for accurate computations of quantum dynamics. The idea of the Gaussian wave packet method is to approximate the time evolution of a quantum mechanical wave function by the evolution of Gaussian wave packets. Within this approximation it is assumed that an initially Gaussian wave packet (GWP) stays Gaussian for all times, i.e. the GWP is moving in an effective harmonic, possibly time-dependent potential, which fits the original potential of the underlying system. The time evolution of the wave packet is given by the time evolution of its parameters, which describe the shape and position of the GWP, like width, phase, center, and momentum [10]. This procedure allows for the reduction of the time-dependent Schrödinger equation to a set of ordinary first-order differential equations for the parameters of the GWPs.

For a single GWP, the GWP method is generally only valid for short time propagation. The approximation can significantly be improved if a superposition of GWPs is used and these GWPs are propagated in concert by the TDVP, since the number of adjustable parameters is increased and the overall wave function is no longer restricted to a Gaussian shape [6–9]. The time-dependent variational principle is presented in general in chapter 2 and is applied to a superposition of GWPs in chapter 3.

Although being rather accurate, the equations of motion for the Gaussian parameters as obtained from the time-dependent variational principle, have the drawback, that they become ill-conditioned from time to time during the integration, depending on how many GWP are used. The reasons for the ill-conditioned behavior of the differential equations are near singularities of a matrix [6, 7, 9, 14, 15] that has to be inverted after each time step of integration to determine the coefficients of the effective potential. Using step size control the time steps of the integration algorithm can become extremely small making the method impracticably slow. In the worst case even a failure of the numerical matrix inversion or the further integration may occur.

Different solutions to this numerical problem have been proposed [6, 7, 9, 14–17], however, none of the suggested methods is fully satisfactory, each of them having some drawbacks or being inapplicable in some situations. These numerical problems reduce the general applicability of the method to quantum systems.

It is one of the aims of this thesis to find a method to ameliorate the numerical behavior of the equations of motion to make the method of GWP propagation numerically efficient and universally applicable [13]. A solution to this problem based on the introduction of adequate constraints is presented in chapter 4.

The GWP method has been applied mainly in molecular [4, 5, 10, 15, 18, 19] and in nuclear physics [20, 21]. Another goal of this work is to extend the application of the GWP method to atomic systems. In particular we are interested in the hydrogen atom with and without external fields. At first sight the choice of Gaussian wave packet trial functions appears to be not especially convenient, since the Coulomb potential is far from being harmonic. Nevertheless, in the one-dimensional Coulomb model potential Gaussian wave packet propagation has already been performed [22–24] with good but not exact results. Therefore, a procedure for exact wave packet dynamics in the hydrogen atom is desired. There exists a regularization procedure [25, 26] that transforms the three-dimensional hydrogenic Schrödinger equation to a four-dimensional harmonic oscillator problem. The extension from three to four dimensions introduced by the regularized Kustaanheimo-Stiefel coordinates, implies an additional constant of motion which manifests itself as a restriction on physically allowed wave functions. The Gaussian wave packets present exact solutions to the regularized hydrogen atom if they are able to satisfy the restriction, i.e. the impact of the restriction on Gaussian wave packets must be investigated first. The question arises whether four-dimensional GWPs in Kustaanheimo-Stiefel coordinates can fulfill the restriction, such that the set of restricted GWPs is still a complete basis. In chapter 5 it is shown that the answer is yes.

The analytical solvability of the hydrogen atom is lost when an external magnetic and crossed electric and magnetic fields are applied. Both systems show a transition from regular to chaotic behavior of the underlying classical dynamics and allow for the investigation of “quantum chaos”, i.e. the influence of classical chaos on quantum spectra [27–30]. External electromagnetic fields applied to the hydrogen atom allow for the regularization using Kustaanheimo-Stiefel coordinates in the same manner as for the field-free hydrogen atom. The external fields introduce anharmonic perturbations to the harmonic potential resulting from the Coulomb potential, and the restricted GWPs are no longer exact solutions of the system and their evolution is determined variationally. In this thesis, in particular the diamagnetic hydrogen atom which presents a system with two non separable degrees of freedom and the hydrogen atom in crossed electric and magnetic fields with three non separable degrees of freedom are investigated by means of the GWP propagation in chapter 6.

A further class of systems where the application of variational methods using Gaussian wave packet trial functions are common are Bose-Einstein condensates [31–33] in the

---

mean-field limit, where the system is described by the Gross-Pitaevskii equation. The Gross-Pitaevskii equation is a nonlinear equation, and qualitatively different modes of dynamics, viz. oscillations and collapse of the condensate, appear. The GWP trial functions are mainly used in the time-independent version [31, 32] to reduce the mean-field energy functional to a function of the Gaussian parameters and the stationary points of the mean-field energy present the variational stationary states of the Gross-Pitaevskii equation. But also time-dependent computations have been performed [33]. The isotropic short-range contact interaction between the particles results from the s-wave scattering and the strength can be varied by changing the scattering length via a Feshbach resonance [34, 35].

In this thesis the dynamics of Bose-Einstein condensates with additional long-range particle interactions are investigated. Two different kinds of long-range particle interactions are discussed. An isotropic electromagnetically induced long range attractive  $1/r$  particle interaction [31, 32] is considered. The system is especially appealing since it allows for a self-trapping of the condensate without external trap. The second long-range particle interaction, which is of special importance in view of the experimental realization [36], is the anisotropic dipole-dipole interaction. This occurs for atoms with a large magnetic dipole, e.g.  $^{52}\text{Cr}$  [35]. This system allows for a tuning of the relative strengths of the dipolar interaction and the contact interaction by tuning the scattering length using a Feshbach resonance.

A special attention is turned to the regular or chaotic dynamics of the Bose-Einstein condensates. The equations of motion resulting from the time-dependent variational principle have a generalized Poissonian structure [37, 38] and the common tools known from Hamiltonian mechanics, e.g. investigation of the generalized phase space by a Poincaré surface of section, can be employed.

The thesis is organized as follows. In chapter 2 the time-dependent variational principle is introduced. Two different formulations are discussed and the variational conservation of expectation values is investigated. An upper error bound for the variational approximation is presented. Chapter 3 treats the application of the TDVP to Gaussian wave packet trial functions, and the numerical problems associated with the method are discussed. In Chapter 4 a solution to the numerical problems arising from the variational propagation of the GWPs is introduced. A general formulation for arbitrary parametrized trial functions is followed by the specialization to GWP trial functions. The solution is based on introducing constraints into the variation. Suitable constraints are formulated and a numerical example is presented. In chapter 5 the GWP method is applied to the three-dimensional hydrogen atom. The regularization based on Kustaanheimo-Stiefel coordinates is presented. The effect of the restriction on the four-dimensional GWP is discussed. The exact analytic evolution of the restricted GWP is presented, and the expansion in the restricted Gaussian basis states and the exact propagation of a localized initial wave function in the fictitious time are shown. Symmetry subspaces with conserved magnetic quantum number  $m$  and with conserved angular momentum quantum numbers  $l, m$  are treated separately. In chapter 6.1 the H atom

## 1. Introduction

---

in in a homogeneous magnetic field and in perpendicular external electric and magnetic fields is treated. The TDVP is applied to the wave packets developed in chapter 5 for the field-free H atom. In chapter 7 the stability analysis of the stationary states of the Bose-Einstein condensate with attractive  $1/r$  interaction is presented. The dynamics of the condensate is investigated variationally and numerically exact and the results are compared. In chapter 8 regularity of the dynamics of a Bose-Einstein condensate with dipolar interaction is investigated variationally.



## 2. Time-dependent variational principle

The propagation of GWPs investigated in this thesis is based on the application of the time-dependent variational principle (TDVP). In contrast to the local harmonic approximation introduced by Heller, the TDVP allows for a more accurate approximation. The basic equations of the TDVP as well as some corollaries are discussed in this chapter.

The evolution of a quantum mechanical wave function of a quantum system with the Hamiltonian  $H$  is determined by the Schrödinger equation (in atomic units)

$$i\dot{\psi}(t) = H\psi(t) \tag{2.1}$$

where the wave function  $\psi(t)$  is an element of the Hilbert space. The numerical effort for the numerical exact solution of the Schrödinger equation grows exponentially with the dimension of the system. Therefore for high dimensional systems approximate solutions of the Schrödinger equation are needed. The idea of the time-dependent variational principle is to reduce the dimensionality of the problem by searching an approximate solution of the Schrödinger equation not in the whole Hilbert space but on a manifold in Hilbert space. The trial function of the approximation manifold is denoted by  $\chi(t)$ . The time evolution of the exact wave function  $\psi(t)$  is then approximated by the time evolution of the trial wave function  $\chi(t)$  with  $\chi(0) = \psi(0)$ . The trial function is assumed to be parametrized by a set of time-dependent parameters  $\mathbf{z}(t) = (z_1(t), \dots, z_{n_p}(t))$ , i.e.  $\chi(t) = \chi(\mathbf{z}(t))$ . Of course the TDVP is also applicable to non parametrized trial functions, these are however not the subject of investigation in this work. The results of this chapter can easily be rewritten for non parametrized wave functions. There is much freedom in approximating the exact wave function  $\psi(t)$  by the trial function  $\chi(\mathbf{z}(t))$  as “good” as possible by adjusting the time evolution of the parameters  $\mathbf{z}(t)$ . Variationally “optimal” evolution of the trial function is obtained by the time-dependent variational principle (TDVP) [39–42]. Instead of computationally expensively solving a partial differential equation the problem is reduced to an initial value problem with ordinary first order differential equations for the set of parameters. Different formulations of the TDVP exist, which, depending on the trial function, do or do not lead to different equations of motion for the parameters. It turns out that the different formulations of the TDVP lead to the same equations of motion provided the space of admissible variations is a complex vector space. It is the object of this work to use Gaussian wave packets as trial functions where the resulting equations of motion for the parameters are

known to be the same for the different formulations of the variational principle. Since the different approaches can make various aspects more clear, two variational principles, viz. the least action principle and the McLachlan variational principle are presented in the following.

## 2.1. Least action principle

In the least action principle, in analogy to classical mechanics a quantum Lagrangian

$$L(t) = \langle \chi | i\partial_t - H | \chi \rangle \quad (2.2)$$

is defined. The variation of the functional  $S$  with respect to  $\chi$  is supposed to vanish [41]

$$S = \int_{t_1}^{t_2} dt L(t), \quad (2.3)$$

where the variation at the endpoints vanishes as in classical mechanics. In order to make differences between the various TDVP clear we assume now that the parameters  $\mathbf{z}(t)$  of the trial function are real. Actually this means no restriction on the parametrization since any complex variational parameter can be split into its real and imaginary part leading to two real parameters. With these variational parameters  $\mathbf{z}(t) = (z_1(t), \dots, z_{n_p}(t))$  the Lagrangian reads

$$L(\mathbf{z}, \dot{\mathbf{z}}) = \left\langle \chi(\mathbf{z}) \left| i \frac{\partial \chi(\mathbf{z})}{\partial \mathbf{z}} \cdot \dot{\mathbf{z}} - H \chi(\mathbf{z}) \right. \right\rangle, \quad (2.4)$$

where the time derivative of  $\chi$  has been performed assuming that the wave function  $\chi(\mathbf{z}(t))$  is time dependent exclusively through the time-dependence of the variational parameters. With the parametrization, the variation of  $\chi$  leads to variations of the parameters  $\mathbf{z}(t)$ , whose variations are restricted to vanish at the endpoints  $\delta \mathbf{z}(t_1) = \delta \mathbf{z}(t_2) = 0$ , as in classical mechanics. The equations of motion for the parameters are then the Euler-Lagrange equations

$$\frac{d}{dt} \frac{\partial L(\mathbf{z}, \dot{\mathbf{z}})}{\partial \dot{z}_k} - \frac{\partial L(\mathbf{z}, \dot{\mathbf{z}})}{\partial z_k} = 0, \quad k = 1, \dots, n_p. \quad (2.5)$$

The first term in (2.5) reads

$$\begin{aligned} \frac{d}{dt} \frac{\partial L(\mathbf{z}, \dot{\mathbf{z}})}{\partial \dot{z}_k} &= \frac{d}{dt} \left\langle \chi(\mathbf{z}) \left| i \frac{\partial \chi(\mathbf{z})}{\partial z_k} \right. \right\rangle \\ &= \left\langle \frac{\partial \chi(\mathbf{z})}{\partial z_l} \dot{z}_l \left| i \frac{\partial \chi(\mathbf{z})}{\partial z_k} \right. \right\rangle + \left\langle \chi(\mathbf{z}) \left| i \frac{\partial^2 \chi(\mathbf{z})}{\partial z_k \partial z_l} \dot{z}_l \right. \right\rangle, \quad k = 1, \dots, n_p, \end{aligned} \quad (2.6)$$

where Einstein's sum convention is used. The second term in (2.5) yields

$$\begin{aligned} \frac{\partial L(\mathbf{z}, \dot{\mathbf{z}})}{\partial z_k} &= \left\langle \frac{\partial \chi(\mathbf{z})}{\partial z_k} \left| i \frac{\partial \chi(\mathbf{z})}{\partial z_l} \dot{z}_l \right. \right\rangle + \left\langle \chi(\mathbf{z}) \left| i \frac{\partial^2 \chi(\mathbf{z})}{\partial z_k \partial z_l} \dot{z}_l \right. \right\rangle \\ &\quad - \left\langle \frac{\partial \chi(\mathbf{z})}{\partial z_k} \left| H \right| \chi(\mathbf{z}) \right\rangle - \left\langle \chi(\mathbf{z}) \left| H \right| \frac{\partial \chi(\mathbf{z})}{\partial z_k} \right\rangle, \quad k = 1, \dots, n_p. \end{aligned} \quad (2.7)$$

Taking the difference between (2.6) and (2.7) according to the Euler-Lagrange equation (2.5), the second term in the second line of (2.6) and the second term in the first line of (2.7) cancel out. The Euler-Lagrange equations now read

$$\begin{aligned} &i \left( \left\langle \frac{\partial \chi(\mathbf{z})}{\partial z_l} \left| \frac{\partial \chi(\mathbf{z})}{\partial z_k} \right. \right\rangle - \left\langle \frac{\partial \chi(\mathbf{z})}{\partial z_k} \left| \frac{\partial \chi(\mathbf{z})}{\partial z_l} \right. \right\rangle \right) \dot{z}_l \\ &+ \left\langle \frac{\partial \chi(\mathbf{z})}{\partial z_k} \left| H \right| \chi(\mathbf{z}) \right\rangle + \left\langle \chi(\mathbf{z}) \left| H \right| \frac{\partial \chi(\mathbf{z})}{\partial z_k} \right\rangle = 0. \end{aligned} \quad (2.8)$$

Introducing the complex Hermitean matrix

$$K \equiv K_{kl} \equiv \left\langle \frac{\partial \chi(\mathbf{z})}{\partial z_k} \left| \frac{\partial \chi(\mathbf{z})}{\partial z_l} \right. \right\rangle, \quad (2.9)$$

equation (2.8) can be written in compact notation

$$2 \operatorname{Im} K_{kl} \dot{z}_l = -\frac{\partial}{\partial z_k} \langle H \rangle, \quad k = 1, \dots, n_p \quad \text{or} \quad 2 \operatorname{Im} K \dot{\mathbf{z}} = -\frac{\partial}{\partial \mathbf{z}} \langle H \rangle. \quad (2.10)$$

The Hermitean matrix  $K$  introduced in (2.9) is positive semi-definite since

$$\mathbf{c}^\dagger \left\langle \frac{\partial \chi}{\partial \mathbf{z}} \left| \frac{\partial \chi}{\partial \mathbf{z}} \right. \right\rangle \mathbf{c} = \left\langle \frac{\partial \chi}{\partial \mathbf{z}} \cdot \mathbf{c} \left| \frac{\partial \chi}{\partial \mathbf{z}} \cdot \mathbf{c} \right. \right\rangle = \left\| \frac{\partial \chi}{\partial \mathbf{z}} \cdot \mathbf{c} \right\|^2 \geq 0, \quad \forall \mathbf{c} \in \mathbb{C}^{n_p}, \quad (2.11)$$

which leads to the fact that its imaginary part is a skew symmetric real valued  $n_p \times n_p$  matrix  $S = 2 \operatorname{Im} K$ . Skew symmetric real matrices have pairwise complex conjugate purely imaginary eigenvalues, i.e. for the skew symmetric  $n_p \times n_p$  matrix  $S$  to be invertible it is necessary that its dimension  $n_p$  is even.

The favor of the least action VP is the resemblance to the classical Hamilton's principle and as we will see the structural similarity of the resulting quantum and classical equations of motion. Suppose that the wave function is parametrized by an even number  $n_p$  of real parameters  $\mathbf{z}$ . The equations of motion turn to the canonical ones if a suitable parametrization is found where the skew symmetric matrix  $S$  takes the canonical symplectic form

$$S = \begin{pmatrix} 0 & -1 \\ 1 & 0 \end{pmatrix}. \quad (2.12)$$

## 2. Time-dependent variational principle

---

Such a convenient parametrization for GWPs is investigated in [37] and is used in chapter 7. Otherwise, the equations of motion (2.10) have some generalized Poissonian structure [37, 38].

To investigate the relation of the resulting equations of motion obtained from the least action variational principle to other variational principles it is convenient to rewrite equation (2.8) in a slightly different form,

$$\begin{aligned}
 & \left( - \left\langle i \frac{\partial \chi(\mathbf{z})}{\partial z_l} \middle| \frac{\partial \chi(\mathbf{z})}{\partial z_k} \right\rangle - \left\langle \frac{\partial \chi(\mathbf{z})}{\partial z_k} \middle| i \frac{\partial \chi(\mathbf{z})}{\partial z_l} \right\rangle \right) \dot{z}_l \\
 & + \left\langle \frac{\partial \chi(\mathbf{z})}{\partial z_k} \middle| H \middle| \chi(\mathbf{z}) \right\rangle + \left\langle \chi(\mathbf{z}) \middle| H \middle| \frac{\partial \chi(\mathbf{z})}{\partial z_k} \right\rangle \\
 = & - \left\langle \frac{\partial \chi(\mathbf{z})}{\partial z_k} \middle| i \dot{\chi}(\mathbf{z}) - H \chi(\mathbf{z}) \right\rangle - \left\langle i \dot{\chi}(\mathbf{z}) - H \chi(\mathbf{z}) \middle| \frac{\partial \chi(\mathbf{z})}{\partial z_k} \right\rangle = 0, \quad k = 1, \dots, n_p.
 \end{aligned} \tag{2.13}$$

Altogether the least action principle for trial functions with real parameters leads to the compact equations

$$\text{Re} \left\langle \frac{\partial \chi(\mathbf{z})}{\partial \mathbf{z}} \middle| i \dot{\chi}(\mathbf{z}) - H \chi(\mathbf{z}) \right\rangle = 0. \tag{2.14}$$

It is however not intuitively obvious in which sense this variational principle leads to “optimal” approximations.

## 2.2. McLachlan variational principle

A more descriptive approach is the formulation of McLachlan [42], or equivalently the minimum error method [9], where the norm of the deviation between the right and the left hand side of the Schrödinger equation (2.1) with respect to the trial function is to be minimized. The quantity

$$I = \|i\dot{\phi}(t) - H\chi(t)\|^2 \stackrel{!}{=} \min \tag{2.15}$$

is to be varied with respect to  $\phi$  only, and then  $\dot{\chi} \equiv \dot{\phi}$  is chosen, i.e. for any time  $t$  the fixed wave function  $\chi(t)$  is supposed to be given and its time derivative  $\dot{\chi}(t)$  is determined by the requirement to minimize  $I$ . Again it is supposed that the wave function  $\chi(t)$  is parametrized by a set of parameters  $\mathbf{z}(t) = (z_1(t), \dots, z_{n_p}(t))$ ,  $\chi(t) = \chi(\mathbf{z}(t))$ . For brevity the arguments of the wave function are dropped in the following. Expressed in terms of the parameters  $\mathbf{z}(t)$  the quantity  $I$  reads

$$I = \left\langle \frac{\partial \chi}{\partial \mathbf{z}} \cdot \dot{\mathbf{z}} \middle| \frac{\partial \chi}{\partial \mathbf{z}} \cdot \dot{\mathbf{z}} \right\rangle - i \left\langle H \chi \middle| \frac{\partial \chi}{\partial \mathbf{z}} \cdot \dot{\mathbf{z}} \right\rangle + i \left\langle \frac{\partial \chi}{\partial \mathbf{z}} \cdot \dot{\mathbf{z}} \middle| H \chi \right\rangle + \left\langle H \chi \middle| H \chi \right\rangle \tag{2.16}$$

which is a quadratic function of  $\dot{\mathbf{z}}$  for fixed values of  $\mathbf{z}$ . The variation  $\delta\phi$  carries over to variations  $\delta\dot{\mathbf{z}}$

$$\delta |\dot{\chi}(\mathbf{z}, \dot{\mathbf{z}})\rangle = \left| \frac{\partial \dot{\chi}}{\partial \mathbf{z}} \cdot \delta \mathbf{z} \right\rangle + \left| \frac{\partial \dot{\chi}}{\partial \dot{\mathbf{z}}} \cdot \delta \dot{\mathbf{z}} \right\rangle = \left| \frac{\partial}{\partial \dot{\mathbf{z}}} \left( \frac{\partial \chi}{\partial \mathbf{z}} \cdot \dot{\mathbf{z}} \right) \cdot \delta \dot{\mathbf{z}} \right\rangle = \left| \frac{\partial \chi}{\partial \mathbf{z}} \cdot \delta \dot{\mathbf{z}} \right\rangle. \quad (2.17)$$

For fixed  $\chi(\mathbf{z})$  variations  $\delta\mathbf{z}$  of the parameters themselves are not allowed, since then the wave function  $\chi(\mathbf{z})$  would not be fixed. Thus the term  $\left| \frac{\partial \dot{\chi}}{\partial \dot{\mathbf{z}}} \cdot \delta \dot{\mathbf{z}} \right\rangle$  in equation (2.17) vanishes. Consider now variations of  $I$  in equation (2.15),

$$\begin{aligned} \delta I &= \langle \delta \dot{\chi} | \dot{\chi} \rangle + \langle \dot{\chi} | \delta \dot{\chi} \rangle - \langle i \delta \dot{\chi} | H \chi \rangle - \langle H \chi | i \delta \dot{\chi} \rangle \\ &= \langle \delta \dot{\chi} | \dot{\chi} + i H \chi \rangle + \langle \dot{\chi} + i H \chi | \delta \dot{\chi} \rangle \\ &= \left\langle \frac{\partial \chi}{\partial \mathbf{z}} \cdot \delta \dot{\mathbf{z}} \middle| \dot{\chi} + i H \chi \right\rangle + \left\langle \dot{\chi} + i H \chi \middle| \frac{\partial \chi}{\partial \mathbf{z}} \cdot \delta \dot{\mathbf{z}} \right\rangle = 0 \end{aligned} \quad (2.18)$$

It must now be distinguished between real and complex parameters  $\mathbf{z}$ . For real parameters it is  $\delta \dot{z}_k^* = \delta \dot{z}_k$ ,  $k = 1, \dots, n_p$ . The variations  $\delta \dot{\mathbf{z}}$  in the bra-vector and in the ket-vector in (2.18) are then not independent and the equations turn to

$$\text{Re} \left\langle \frac{\partial \chi}{\partial \mathbf{z}} \middle| \dot{\chi} + i H \chi \right\rangle \cdot \delta \dot{\mathbf{z}} = 0. \quad (2.19)$$

The variations  $\delta \dot{\mathbf{z}}$  are arbitrary and therefore it leads to

$$\begin{aligned} \text{Re} \left\langle \frac{\partial \chi}{\partial \mathbf{z}} \middle| \dot{\chi} + i H \chi \right\rangle &= 0 \\ \Leftrightarrow \text{Re} \left\langle i \frac{\partial \chi}{\partial \mathbf{z}} \middle| i \dot{\chi} - H \chi \right\rangle &= 0 \\ \Leftrightarrow \text{Im} \left\langle \frac{\partial \chi}{\partial \mathbf{z}} \middle| i \dot{\chi} - H \chi \right\rangle &= 0. \end{aligned} \quad (2.20)$$

In case of complex parameters  $\mathbf{z}$  it must be considered that the variations  $\delta \dot{z}_k^*$  and  $\delta \dot{z}_k$ ,  $k = 1, \dots, n_p$  are independent and each bracket in (2.18) must vanish itself

$$\delta \dot{\mathbf{z}}^\dagger \cdot \left\langle \frac{\partial \chi}{\partial \mathbf{z}} \middle| \dot{\chi} + i H \chi \right\rangle = 0 \quad (2.21)$$

and therefore

$$\left\langle \frac{\partial \chi}{\partial \mathbf{z}} \middle| i \dot{\chi} - H \chi \right\rangle = 0. \quad (2.22)$$

From considering the variations  $\delta \dot{\mathbf{z}}$  instead of  $\delta \dot{\mathbf{z}}^\dagger$  the adjoint equations of (2.22) are obtained from equations (2.18). Altogether, for real parameters, the McLachlan variational principle requires the imaginary parts of the brackets in (2.22) to vanish, while the least action variational principle demands their real parts to be zero. For complex

## 2. Time-dependent variational principle

---

parameters both variational principles lead to the same equations (2.22) known as the *Dirac-Frenkel* variational principle. To show this the wave function is supposed to be an analytic function of the parameters with respect to complex differentiation. Then  $\chi$  fulfills the Cauchy-Riemann differential equations

$$\frac{\partial \chi_r}{\partial \mathbf{z}_r} = \frac{\partial \chi_i}{\partial \mathbf{z}_i}, \quad (2.23)$$

$$\frac{\partial \chi_r}{\partial \mathbf{z}_i} = -\frac{\partial \chi_i}{\partial \mathbf{z}_r}, \quad (2.24)$$

where the splitting  $\chi = \chi_r + i\chi_i$  and  $\mathbf{z} = \mathbf{z}_r + i\mathbf{z}_i$  of complex quantities into their real and imaginary parts has been used. Multiplying (2.24) with the imaginary unit and subtracting it from (2.23) yields

$$\frac{\partial(\chi_r + i\chi_i)}{\partial \mathbf{z}_r} = \frac{\partial(\chi_i - i\chi_r)}{\partial \mathbf{z}_i} = -i \frac{\partial(\chi_r + i\chi_i)}{\partial \mathbf{z}_i}, \quad (2.25)$$

or by putting together again the real and the imaginary part of the wave function

$$\frac{\partial \chi}{\partial \mathbf{z}_r} = -i \frac{\partial \chi}{\partial \mathbf{z}_i}. \quad (2.26)$$

Now it is clear that if the trial function is a complex differentiable function of the complex parameters  $\mathbf{z}$ , then both, the least action as well as the McLachlan VP lead to the same results since inserting (2.26) in (2.14) gives

$$\operatorname{Re} \left\langle \frac{\partial \chi}{\partial \mathbf{z}_r} \middle| i\dot{\chi} - H\chi \right\rangle = \operatorname{Re} \left\langle -i \frac{\partial \chi}{\partial \mathbf{z}_i} \middle| i\dot{\chi} - H\chi \right\rangle = \operatorname{Im} \left\langle \frac{\partial \chi}{\partial \mathbf{z}_i} \middle| i\dot{\chi} - H\chi \right\rangle = 0, \quad (2.27)$$

and also

$$\operatorname{Re} \left\langle \frac{\partial \chi}{\partial \mathbf{z}_i} \middle| i\dot{\chi} - H\chi \right\rangle = \operatorname{Re} \left\langle i \frac{\partial \chi}{\partial \mathbf{z}_r} \middle| i\dot{\chi} - H\chi \right\rangle = -\operatorname{Im} \left\langle \frac{\partial \chi}{\partial \mathbf{z}_r} \middle| i\dot{\chi} - H\chi \right\rangle = 0. \quad (2.28)$$

If the real part of (2.22) is zero then also the imaginary part is zero and vice versa, if the trial function is analytic or more generally if it satisfies (2.26), which is called “complementary principle” by some authors [37]. An illustration of equation (2.22) is presented in fig. 2.1. Here the manifold of approximation  $M$ , consisting of all possible configurations  $\chi(\mathbf{z})$ , is plotted schematically as a 2D-surface in the Hilbert space. The tangent space of the manifold in the point  $\chi$  is a linear vector space and is spanned by the derivatives  $\frac{\partial \chi}{\partial z_k}$ ,  $k = 1, \dots, n_p$ . The tangent space is denoted by  $T_\chi M$  in fig. 2.1. According to the Schrödinger equation the exact time derivative  $\dot{\chi}$  is given by  $-iH\chi$ , denoted by the arrow with the black head. In general the exact time derivative does not lie in the tangent space, otherwise the trial function would be an exact solution of the Schrödinger equation. The variational approximation to the exact time derivative is

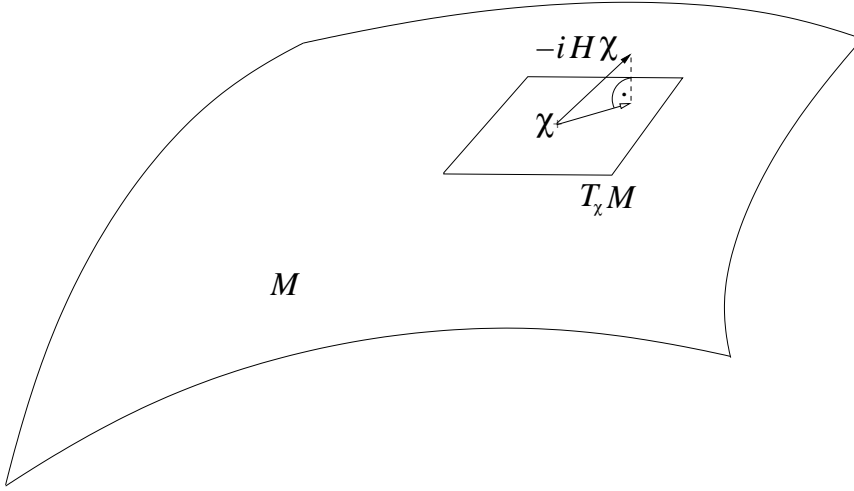


Figure 2.1.: Sketch of the manifold  $M$  of approximation of the trial wave function  $\chi(\mathbf{z})$ . The variational evolution of the trial function, denoted by the arrow with the white head is obtained as the projection of the exact time evolution  $-iH\chi$ , denoted by the arrow with the black head onto the tangent space  $T_\chi M$  of the manifold  $M$  in the point  $\chi$ .

given by that vector of the tangent space which has minimal deviation from the exact one. This is the orthogonal projection of the exact time derivative onto the tangent space, denoted by the arrow with the white head in fig. 2.1.

For parametrized wave functions the variational principle (2.15) simply reduces to a quadratic minimization problem where the gradient of  $I$  with respect to the time derivatives of the parameters must be zero

$$\frac{\partial I}{\partial \dot{z}_k} = 0, \quad k = 1, \dots, n_p. \quad (2.29)$$

For complex parameters  $z_k = z_{kr} + iz_{ki}$  one has the freedom to take either  $\partial I / \partial \dot{z}_{kr} = 0$  together with  $\partial I / \partial \dot{z}_{ki} = 0$  or to treat  $\dot{z}_k^*$  and  $\dot{z}_k$  formally as independent parameters and to take either  $\partial I / \partial \dot{z}_k = 0$  or  $\partial I / \partial \dot{z}_k^* = 0$ . The resulting equations of motion are (2.20) in the first case and (2.22) in the second case. Analogous to (2.10) for the least action VP explicit equations of motion for the McLachlan VP are directly obtained from (2.20), i.e.

$$\text{Re } K \dot{\mathbf{z}} = \text{Im } \mathbf{h}, \quad (2.30)$$

with

$$\mathbf{h} = \left\langle \frac{\partial \chi}{\partial \mathbf{z}} \middle| H \middle| \chi \right\rangle. \quad (2.31)$$

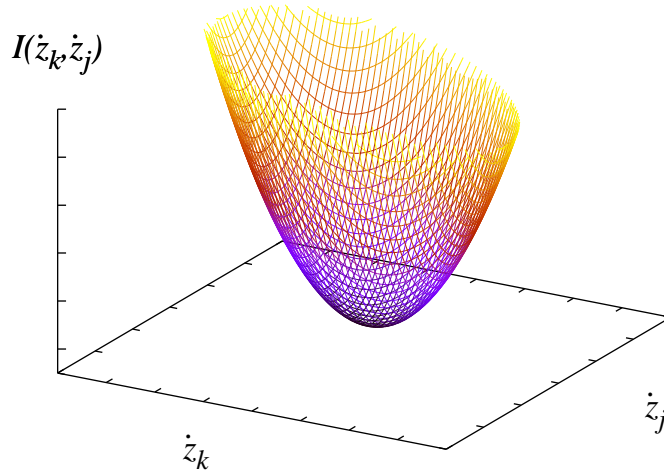


Figure 2.2.: Schematic illustration of the parabolic function  $I(\dot{\mathbf{z}}^\dagger, \dot{\mathbf{z}})$  of the derivatives of the parameters. The parameters themselves are fixed in the plot. They determine the shape and position of the parabola. The position of the minimum determines the further evolution of the parameters and is located where the gradient is zero and is determined by solving a matrix equation.

For complex parameters the TDVPs lead to the same equations and read

$$K\dot{\mathbf{z}} = -i\mathbf{h}. \quad (2.32)$$

As already shown, the Hermitean matrix  $K$  is positive definite ensuring that the extremum of the quadratic quantity  $I$  in the  $\dot{\mathbf{z}}$  space for fixed  $\mathbf{z}$  is a minimum. This is sketched in fig. 2.2 for two parameters  $\dot{z}_k$  and  $\dot{z}_j$ . The minimum is located where the gradient of  $I$  vanishes with respect to the time derivatives of the parameters. The shape and the position of the parabola depend on the fixed parameters  $\mathbf{z}$  as well as the minimal value  $I_{\min} \geq 0$ , which is a measure of the accuracy of the variational approximation.

In this work mainly GWPs are used as trial functions, which may be parametrized by a set of complex parameters. For the time evolution of the GWP it is therefore unimportant which TDVP is applied. However we use the McLachlan TDVP when inequality constraints are accounted for within the variational process in chapter 4 due to the descriptive approach via the quadratic minimization problem.

For parametrized wave functions the TDVP leads to a reduction of the Schrödinger equation to a system of ordinary first order differential equations of motion for the parameters  $\mathbf{z}(t)$ . The matrix equation (2.32) must be solved numerically after every time step of integration for the time derivatives  $\dot{\mathbf{z}}$  if a numerical algorithm for ordinary differential equations, e.g. Runge-Kutta or Adams, is used.



## 2.3. Conservation laws

An interesting question is whether the expectation value of a conserved observable  $A$ , i.e. an observable that commutes with the Hamiltonian  $[A, H] = 0$ , is also conserved within the variational approximation [37, 38]. Assume the simple sufficient condition that  $A\chi$  lies in the space spanned by the vectors  $|\partial\chi/\partial\mathbf{z}\rangle$ , i.e. in the space of feasible variations of the trial function  $\chi(\mathbf{x}, \mathbf{z}(t))$ . In terms of fig. 2.1 this is the tangent space  $T_\chi M$  of the manifold of approximation in the point  $\chi$ . We then have [38]

$$\frac{d}{dt} \langle \chi | A | \chi \rangle = 2\text{Re} \langle A\chi | \dot{\chi} \rangle = 2\text{Re} \langle A\chi | (-iH) | \chi \rangle = \langle \chi | -i[H, A] | \chi \rangle = 0 \quad (2.33)$$

where equation (2.20) is used and the above assumption that  $A\chi$  can be written as a linear combination of the vectors  $|\partial\chi/\partial\mathbf{z}\rangle$ , i.e.,  $A\chi \in T_\chi M$ . Since (2.20) is used, it gives a criterion for expectation value conservation within the McLachlan VP, and of course also for the Dirac-Frenkel formulation of the VP (2.22), but not for the least action VP, unless the parameters satisfy equation (2.26).

### 2.3.1. Conservation of norm and energy

The two especially important cases of norm and energy conservation are investigated explicitly. It has been just shown (2.33) that  $\langle \chi | A | \chi \rangle$  is conserved within the McLachlan VP if  $A\chi \in T_\chi M$  and  $[H, A] = 0$ . For the investigation of the norm conservation consider now the special case  $A = 1$ . The identity operator commutes with the Hamiltonian, and therefore according to (2.33) the norm of the trial wave function is conserved within the McLachlan TDVP if  $\chi \in T_\chi M$ , but not within the least action TDVP unless the parameters satisfy equation (2.26). For parametrized wave functions the condition  $\chi \in T_\chi M$  is equivalent to the requirement that there is one parameter  $z_0$  such that  $\frac{\partial\chi}{\partial z_0}$  is a multiple of  $\chi$ .

In general, the trial function will not provide an exact solution to the Schrödinger equation, i.e.  $H\chi \notin T_\chi M$ . Otherwise the variational solution would be exact. Therefore the mean-field energy is not conserved within the McLachlan VP according to section 2.3 as long as the parameters do not satisfy equation (2.26). The mean-field energy is however conserved within the least action VP since

$$\begin{aligned} \frac{d}{dt} \langle \chi | H | \chi \rangle &= 2\text{Re} \langle \dot{\chi} | H | \chi \rangle \\ &= 2\text{Re} (\langle \dot{\chi} | H | \chi \rangle - \langle \dot{\chi} | i\dot{\chi} \rangle) \\ &= 2\text{Re} \langle \dot{\chi} | H - i\dot{\chi} \rangle = 0. \end{aligned} \quad (2.34)$$

It has been used that  $\text{Re} i \langle \dot{\chi} | \chi \rangle = 0$ , equation (2.14) and that  $\dot{\chi} \in T_\chi M$  is always fulfilled. The mean-field energy is in general not conserved for the McLachlan TDVP, unless the parameters obey (2.26). The GWP trial functions used in this work have a

normalization parameter, say  $z_0$ , such that  $\frac{\partial \chi}{\partial z_0}$  is a multiple of  $\chi$ . Additionally they may be parametrized by complex parameters leading to (2.26), i.e. the equations of motion resulting from the least action and the McLachlan TDVP are equivalent. Therefore the norm as well as the expectation value of the Hamiltonian are conserved for variational GWP propagation.

## 2.4. Error estimation

The error made by the variational approximation is defined as the norm of the difference between the exact solution of the Schrödinger equation  $\psi(t)$  and its variational approximation  $\chi(t)$ , i.e.  $\|\psi(t) - \chi(t)\|$ . To obtain an estimation of the error [43, 44] consider

$$|\dot{\chi} - \dot{\psi}\rangle = |\dot{\chi}\rangle - \frac{1}{i}H|\chi\rangle + \frac{1}{i}H|\chi\rangle - \frac{1}{i}H|\psi\rangle. \quad (2.35)$$

An error bound follows from multiplying the above equation (2.35) with  $\langle \chi(t) - \psi(t) |$  and taking the real part, i.e.

$$\begin{aligned} \operatorname{Re} \langle \chi - \psi | \dot{\chi} - \dot{\psi} \rangle &= \operatorname{Re} \left\langle \chi - \psi \left| \dot{\chi} - \frac{1}{i}H\chi \right. \right\rangle + \operatorname{Re} \left\langle \chi - \psi \left| \frac{1}{i}H\chi - \dot{\psi} \right. \right\rangle \\ &\leq \|\chi - \psi\| \cdot \|i\partial_t \chi - H\chi\|, \end{aligned} \quad (2.36)$$

where the Hermiticity of the Hamiltonian has been used, which makes the second term in (2.36) zero, since the bracket is imaginary. On the other hand it is

$$\|\chi - \psi\| \frac{d}{dt} \|\chi - \psi\| = \frac{1}{2} \frac{d}{dt} \|\chi - \psi\|^2 = \operatorname{Re} \langle \chi - \psi | \dot{\chi} - \dot{\psi} \rangle, \quad (2.37)$$

such that the local error bound is

$$\frac{d}{dt} \|\chi - \psi\| \leq \|i\partial_t \chi - H\chi\|, \quad (2.38)$$

or in the integral version

$$\|\chi(t) - \psi(t)\| \leq \int_0^t \|i\partial_{t'} \chi(t') - H\chi(t')\| dt', \quad (2.39)$$

when  $\chi(0) = \psi(0)$  is assumed.

### 3. Application of the TDVP to GWPs

The TDVP described in chapter 2 is applied to Gaussian wave packets as trial functions. The accuracy of approximation is considerably increased if the wave function is not approximated by a single GWP but is expanded as a superposition of GWPs. First the propagation of a single GWP based on a local harmonic expansion of the potential introduced by Heller [10] is sketched. Then the equations of motion for the Gaussian parameters of a superposition of GWPs are derived from the TDVP.

A single GWP in  $D$  dimensional coordinate space ( $\mathbf{x} \in \mathbb{R}^D$  and  $\hbar = 1$ ) can be written as

$$g(\mathbf{y}, \mathbf{x}) = e^{i((\mathbf{x}-\mathbf{q})A(\mathbf{x}-\mathbf{q})+\mathbf{p}\cdot(\mathbf{x}-\mathbf{q})+\gamma)}, \quad (3.1)$$

where  $A$  is a complex symmetric  $D \times D$  matrix, the momentum  $\mathbf{p}$  and center  $\mathbf{q}$  are real,  $D$ -dimensional vectors (the expectation values of the momentum and the position operator, respectively, i.e.  $\mathbf{p} = \langle g | \frac{1}{i} \frac{\partial}{\partial \mathbf{x}} | g \rangle$  and  $\mathbf{q} = \langle g | \mathbf{x} | g \rangle$ ), and the phase and normalization is given by the complex scalar  $\gamma$ . The Gaussian parameters, summarized by  $\mathbf{y} = (A, \mathbf{p}, \mathbf{q}, \gamma)$  are time-dependent, their time argument is omitted for brevity. The time evolution of the GWP is given by the time evolution of the parameters  $\mathbf{y}$ . By construction, the GWP stays Gaussian during the propagation. Therefore the GWP does not evolve in the original potential of the system but rather in an effective time-dependent harmonic potential

$$V_h(\mathbf{x}) = v_0 + \mathbf{v}_1 \cdot \mathbf{x} + \frac{1}{2} \mathbf{x} V_2 \mathbf{x}, \quad (3.2)$$

which can be computed by different methods. In the simple local harmonic approximation [10] the potential  $V(\mathbf{x})$  of the Schrödinger equation is expanded in a Taylor series of second order around the center of the GWP, i.e.

$$V_h(\mathbf{q}) = V(\mathbf{q}), \quad \left. \frac{\partial V_h(\mathbf{x})}{\partial \mathbf{x}} \right|_{\mathbf{q}} = \left. \frac{\partial V(\mathbf{x})}{\partial \mathbf{x}} \right|_{\mathbf{q}}, \quad \left. \frac{\partial^2 V_h(\mathbf{x})}{\partial \mathbf{x} \partial \mathbf{x}} \right|_{\mathbf{q}} = \left. \frac{\partial^2 V(\mathbf{x})}{\partial \mathbf{x} \partial \mathbf{x}} \right|_{\mathbf{q}}. \quad (3.3)$$

A typical situation of a GWP in a Morse potential, together with the associated local harmonic potential is plotted in fig. 3.1. The potentials  $V(\mathbf{x})$  (red line) and  $V_h(\mathbf{x})$  (green line) as well as their first two derivatives coincide at the center of the GWP (blue line). The effective potential travels together with the GWP, and is in general time-dependent except for (time-independent) harmonic underlying potentials, where the expansion becomes exact.

The equations of motion for the Gaussian parameters are then obtained by inserting the GWP trial function into the Schrödinger equation with the potential  $V(\mathbf{x})$  replaced

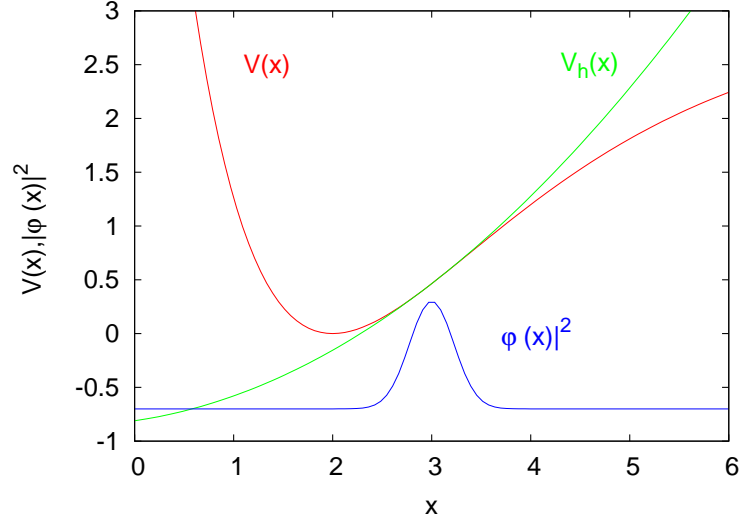


Figure 3.1.: Probability density of a GWP (blue line) running in a Morse potential (red line). The local harmonic potential (green line), as suggested by Heller coincides with the underlying potential at the center of the GWP in the zeroth, first and second derivative. The traveling GWP is accompanied by the effective potential  $V_h(\mathbf{x})$  along its trajectory.

by  $V_h(\mathbf{x})$ , i.e.  $i\dot{g}(\mathbf{y}, \mathbf{x}) = (T + V_h(\mathbf{x}))g(\mathbf{y}, \mathbf{x})$  where the splitting of the Hamiltonian  $H = T + V$  is assumed. The equations of motion follow from comparison of the coefficients. This simple method works as long as the GWP is sufficiently narrow. In practice this is valid only for short times.

A more accurate method is to determine the evolution of the GWP by the TDVP, which fits the effective time-dependent harmonic potential coefficients  $v_0, \mathbf{v}_1, V_2$  variationally to the underlying potential. For numerical reasons it is advantageous not to build up a matrix equation of the form (2.32) for the time derivatives of the parameters directly, but to determine the coefficients  $v_0, \mathbf{v}_1, V_2$  of the effective potential first and then to set up the differential equations for the parameters in a second step. The reason for this procedure is revealed at the end of this chapter. The starting point for the derivation of the equations of motion are eqs. (2.22) and (2.20) for the complex parameters  $A, \gamma$  and for the real parameters  $\mathbf{p}, \mathbf{q}$ , respectively.

Now we turn to a trial function consisting of a superposition of  $N$  GWPs. A superscript  $k$  with  $k = 1, \dots, N$  to distinguish between the different GWPs is introduced. The Gaussian parameters of the  $k$ -th GWP are denoted by  $\mathbf{y}^k = (A^k, \mathbf{p}^k, \mathbf{q}^k, \gamma^k)$ . Their time argument is omitted for brevity. The trial function  $\chi$  is a superposition of  $N$  GWPs

$$\chi(\mathbf{z}, \mathbf{x}) = \sum_{k=1}^N g(\mathbf{y}^k, \mathbf{x}), \quad \mathbf{z} = (\mathbf{y}^1, \dots, \mathbf{y}^N). \quad (3.4)$$

In order to evaluate eqs. (2.22) and (2.20) for a GWP the action of the kinetic operator on a GWP as well as the time derivative of a GWP are investigated. Using a splitting of the Hamiltonian  $H = T + V$  in atomic units and assuming Cartesian coordinates, the Laplace operator applied to a GWP yields

$$\begin{aligned} T g(\mathbf{y}^k, \mathbf{x}) &= -\frac{1}{2} \Delta g(\mathbf{y}^k, \mathbf{x}) \\ &= \left[ -i \operatorname{tr} A^k + (\mathbf{x} - \mathbf{q}^k) 2(A^k)^2 (\mathbf{x} - \mathbf{q}^k) + 2\mathbf{p}^k A^k (\mathbf{x} - \mathbf{q}^k) + \frac{(\mathbf{p}^k)^2}{2} \right] g(\mathbf{y}^k, \mathbf{x}), \end{aligned} \quad (3.5)$$

and the time derivative of the GWP reads

$$\begin{aligned} \frac{\partial g(\mathbf{y}^k, \mathbf{x})}{\partial t} &= \frac{\partial g(\mathbf{y}^k, \mathbf{x})}{\partial A^k} \dot{A}^k + \frac{\partial g(\mathbf{y}^k, \mathbf{x})}{\partial \mathbf{p}^k} \cdot \dot{\mathbf{p}}^k + \frac{\partial g(\mathbf{y}^k, \mathbf{x})}{\partial \mathbf{q}^k} \cdot \dot{\mathbf{q}}^k + \frac{\partial g(\mathbf{y}^k, \mathbf{x})}{\partial \gamma^k} \dot{\gamma}^k \\ &= i \left[ (\mathbf{x} - \mathbf{q}^k) \dot{A}^k (\mathbf{x} - \mathbf{q}^k) + (\mathbf{x} - \mathbf{q}^k) \cdot \dot{\mathbf{p}}^k \right. \\ &\quad \left. + (-2A^k (\mathbf{x} - \mathbf{q}^k) - \mathbf{p}^k) \cdot \dot{\mathbf{q}}^k + \dot{\gamma} \right] g(\mathbf{y}^k, \mathbf{x}). \end{aligned} \quad (3.6)$$

Both expressions have the same form with respect to the coordinates  $\mathbf{x}$ , consisting of a quadratic polynomial in  $\mathbf{x}$  times the GWP itself, and thus it can be summarized as

$$\begin{aligned} i\dot{\chi} - T\chi &= \sum_{k=1}^N \left( \left[ -\dot{\gamma}^k + i \operatorname{tr} A^k + \mathbf{p}^k \cdot (\dot{\mathbf{q}}^k - \frac{1}{2} \mathbf{p}^k) \right] \right. \\ &\quad \left. + [-\dot{\mathbf{p}}^k + 2A^k (\dot{\mathbf{q}}^k - \mathbf{p}^k)] \cdot (\mathbf{x} - \mathbf{q}^k) \right. \\ &\quad \left. + (\mathbf{x} - \mathbf{q}^k) [-\dot{A}^k - 2(A^k)^2] (\mathbf{x} - \mathbf{q}^k) \right) g(\mathbf{y}^k, \mathbf{x}) \\ &= \sum_{k=1}^N \left( \mathbf{x} (-\dot{A}^k - 2(A^k)^2) \mathbf{x} \right. \\ &\quad \left. + (-\dot{\mathbf{p}}^k + 2A^k (\dot{\mathbf{q}}^k - \mathbf{p}^k) - 2(-\dot{A}^k - 2(A^k)^2) \mathbf{q}^k) \mathbf{x} \right. \\ &\quad \left. + \mathbf{q}^k (-\dot{A}^k - 2(A^k)^2) \mathbf{q}^k - (-\dot{\mathbf{p}}^k + 2A^k (\dot{\mathbf{q}}^k - \mathbf{p}^k)) \mathbf{q}^k \right. \\ &\quad \left. + (-\dot{\gamma}^k + \mathbf{p}^k \cdot \dot{\mathbf{q}}^k + i \operatorname{tr} A^k - \frac{(\mathbf{p}^k)^2}{2}) \right) g(\mathbf{y}^k, \mathbf{x}) \\ &\equiv \sum_{k=1}^N \left( v_0^k + \mathbf{v}_1^k \cdot \mathbf{x} + \frac{1}{2} \mathbf{x} V_2^k \mathbf{x} \right) g(\mathbf{y}^k, \mathbf{x}). \end{aligned} \quad (3.7)$$

Eq. (3.7) defines, after sorting by powers of  $\mathbf{x}$ , the complex symmetric  $D \times D$  matrices  $V_2^k$

$$\frac{1}{2} V_2^k = -\dot{A}^k - 2(A^k)^2, \quad (3.8)$$

the complex vectors  $\mathbf{v}_1^k \in \mathbb{C}^D$

$$\begin{aligned} \mathbf{v}_1 &= -\dot{\mathbf{p}}^k + 2A^k (\dot{\mathbf{q}}^k - \mathbf{p}^k) - 2(-\dot{A}^k - 2(A^k)^2) \mathbf{q}^k \\ &= -\dot{\mathbf{p}}^k + 2A^k (\dot{\mathbf{q}}^k - \mathbf{p}^k) - V_2^k \mathbf{q}^k \end{aligned} \quad (3.9)$$

### 3. Application of the TDVP to GWPs

---

and the complex scalars  $v_0^k$

$$\begin{aligned} v_0^k &= \mathbf{q}^k(-\dot{A}^k - 2(A^k)^2)\mathbf{q}^k - (-\dot{\mathbf{p}}^k + 2A^k(\dot{\mathbf{q}}^k - \mathbf{p}^k))\mathbf{q}^k - \dot{\gamma}^k + \mathbf{p}^k \cdot \dot{\mathbf{q}}^k + i \operatorname{tr} A^k - \frac{(\mathbf{p}^k)^2}{2} \\ &= \mathbf{q}^k V_2^k \mathbf{q}^k - (-\dot{\mathbf{p}}^k + 2A^k(\dot{\mathbf{q}}^k - \mathbf{p}^k))\mathbf{q}^k - \dot{\gamma}^k + \mathbf{p}^k \cdot \dot{\mathbf{q}}^k + i \operatorname{tr} A^k - \frac{(\mathbf{p}^k)^2}{2} \end{aligned} \quad (3.10)$$

as the coefficients of a second order polynomial in  $\mathbf{x}$ , i.e. the coefficients of the effective harmonic potential. The equations of motion are obtained by solving eqs. (3.8)-(3.10) for the time derivatives, however the coefficients must first be determined. To set up the equations for determining the coefficients (2.20) and (2.22), the derivatives of the GWPs with respect to the real Gaussian parameters  $\mathbf{p}^k, \mathbf{q}^k$  and the complex parameters  $A^k, \gamma^k$  are needed. Switching the superscript from  $k$  to  $l$ , for each set  $\mathbf{y}^l$ ,  $l = 1, \dots, N$  these derivatives are

$$\begin{aligned} \frac{\partial g(\mathbf{y}^l, \mathbf{x})}{\partial \gamma^l} &= ig(\mathbf{y}^l, \mathbf{x}), \\ \frac{\partial g(\mathbf{y}^l, \mathbf{x})}{\partial \mathbf{p}^l} &= i(\mathbf{x} - \mathbf{q}^l)g(\mathbf{y}^l, \mathbf{x}), \\ \frac{\partial g(\mathbf{y}^l, \mathbf{x})}{\partial \mathbf{q}^l} &= -i(2A(\mathbf{x} - \mathbf{q}^l) + \mathbf{p}^l)g(\mathbf{y}^l, \mathbf{x}), \\ \frac{\partial g(\mathbf{y}^l, \mathbf{x})}{\partial A_{\alpha\beta}^l} &= i(x_\alpha - q_\alpha^l)(x_\beta - q_\beta^l)g(\mathbf{y}^l, \mathbf{x}), \quad \alpha, \beta = 1, \dots, D. \end{aligned} \quad (3.11)$$

Using (3.11) equation (2.20) concerning the derivatives with respect to the real parameters  $\mathbf{p}^l$  and  $\mathbf{q}^l$  read

$$\operatorname{Im} \left\langle i(x_\alpha - q_\alpha^l)g(\mathbf{y}^l, \mathbf{x}) \middle| (i\partial_t - H)\chi \right\rangle = 0, \quad (3.12)$$

$$\operatorname{Im} \left\langle i(2A_{\alpha\beta}^l(x_\beta - q_\beta^l) + p_\alpha^l)g(\mathbf{y}^l, \mathbf{x}) \middle| (i\partial_t - H)\chi \right\rangle = 0, \quad (3.13)$$

with  $l = 1, \dots, N$  and  $\alpha, \beta = 1, \dots, D$ . For the complex parameters  $A^l$  and  $\gamma^l$  the variational equations (2.22) are

$$\left\langle i(x_\alpha - q_\alpha^l)(x_\beta - q_\beta^l)g(\mathbf{y}^l, \mathbf{x}) \middle| (i\partial_t - H)\chi \right\rangle = 0, \quad (3.14)$$

$$\left\langle ig(\mathbf{y}^l, \mathbf{x}) \middle| (i\partial_t - H)\chi \right\rangle = 0. \quad (3.15)$$

The resulting set of linear equations is not very favorable since then it must be distinguished between the real and complex parameters. This is especially disadvantageous if a usual numerical algorithm for solving matrix equations like factorizing the matrix by  $LU$ -decomposition or Cholesky factorization for positive Hermitean matrices is used which does not distinguish between real and complex equations. However a superposition

of eqs. (3.12)-(3.15) is possible where a distinction between real and complex parameters is not necessary and additionally the integrals become even simpler. Since (3.15) holds, equations (3.12) and (3.13) may be replaced by

$$\text{Im} \left\langle ix_\alpha g(\mathbf{y}^l, \mathbf{x}) \middle| (i\partial_t - H)\chi \right\rangle = 0, \quad (3.16)$$

$$\text{Im} \left\langle i2A_{\alpha\beta}^l x_\beta g(\mathbf{y}^l, \mathbf{x}) \middle| (i\partial_t - H)\chi \right\rangle = 0. \quad (3.17)$$

The complex matrices  $A^l$  are split into their real and imaginary parts  $A^l = A_r^l + iA_i^l$ . Inserting these splittings into (3.17) yields

$$\begin{aligned} & \text{Im} \left\langle i2(A_r^l)_{\alpha\beta} x_\beta g(\mathbf{y}^l, \mathbf{x}) - 2(A_i^l)_{\alpha\beta} x_\beta g(\mathbf{y}^l, \mathbf{x}) \middle| (i\partial_t - H)\chi \right\rangle \\ \stackrel{(3.16)}{=} & \text{Im} \left\langle -2(A_i^l)_{\alpha\beta} x_\beta g(\mathbf{y}^l, \mathbf{x}) \middle| (i\partial_t - H)\chi \right\rangle \\ = & \text{Re} \left\langle 2i(A_i^l)_{\alpha\beta} x_\beta g(\mathbf{y}^l, \mathbf{x}) \middle| (i\partial_t - H)\chi \right\rangle \\ = & 2(A_i^l)_{\alpha\beta} \text{Re} \left\langle ix_\beta g(\mathbf{y}^l, \mathbf{x}) \middle| (i\partial_t - H)\chi \right\rangle = 0. \end{aligned} \quad (3.18)$$

In order for the GWP to be normalizable, the imaginary part of the width matrices  $A_i^l$  must not be singular but positive definite. Therefore the only solution of the set of linear equations (3.18) is the trivial solution

$$\text{Re} \left\langle ix_\beta g(\mathbf{y}^l, \mathbf{x}) \middle| (i\partial_t - H)\chi \right\rangle = 0. \quad (3.19)$$

From (3.16) and (3.19) follows that both the real and the imaginary part of the complex bracket must vanish, i.e.

$$\left\langle x_\beta g(\mathbf{y}^l, \mathbf{x}) \middle| (i\partial_t - H)\chi \right\rangle = 0, \quad \beta = 1, \dots, D, \quad l = 1, \dots, N. \quad (3.20)$$

The bra-vector of equation (3.14) is expanded as

$$\begin{aligned} & \left\langle i(x_\alpha - q_\alpha^l)(x_\beta - q_\beta^l)g(\mathbf{y}^l, \mathbf{x}) \middle| (i\partial_t - H)\chi \right\rangle \\ = & \left\langle i(x_\alpha x_\beta - q_\alpha^l x_\beta - q_\beta^l x_\alpha + q_\alpha^l q_\beta^l)g(\mathbf{y}^l, \mathbf{x}) \middle| (i\partial_t - H)\chi \right\rangle \\ \stackrel{(3.15)}{=} & \left\langle i(x_\alpha x_\beta - q_\alpha^l x_\beta - q_\beta^l x_\alpha)g(\mathbf{y}^l, \mathbf{x}) \middle| (i\partial_t - H)\chi \right\rangle \\ \stackrel{(3.20)}{=} & \left\langle ix_\alpha x_\beta g(\mathbf{y}^l, \mathbf{x}) \middle| (i\partial_t - H)\chi \right\rangle = 0. \end{aligned} \quad (3.21)$$

Altogether the equations (3.12)-(3.15) may be replaced by the equivalent equations

$$\left\langle g(\mathbf{y}^l, \mathbf{x}) \middle| (i\partial_t - H)\chi \right\rangle = 0, \quad (3.22)$$

$$\left\langle x_\alpha g(\mathbf{y}^l, \mathbf{x}) \middle| (i\partial_t - H)\chi \right\rangle = 0, \quad (3.23)$$

$$\left\langle x_\alpha x_\beta g(\mathbf{y}^l, \mathbf{x}) \middle| (i\partial_t - H)\chi \right\rangle = 0, \quad \alpha, \beta = 1, \dots, D, \quad l = 1, \dots, N, \quad (3.24)$$

### 3. Application of the TDVP to GWPs

---

where it need not be distinguished between real and complex equations, and additionally the integrals that must be computed to set up the set of linear equations are simpler.

Note that this set of linear equations is directly obtained if instead of the parametrization of the GWP in equation (3.1) the equivalent parametrization of the GWP

$$g(\tilde{\mathbf{y}}, \mathbf{x}) = e^{i(\mathbf{x}A\mathbf{x} + \mathbf{b}\cdot\mathbf{x} + c)}, \quad \tilde{\mathbf{y}} = (A, \mathbf{b}, c) \quad (3.25)$$

with the same complex symmetric  $D \times D$  matrix  $A$  as in (3.1), a complex vector  $\mathbf{b} \in \mathbb{C}^D$  and the complex phase  $c$  would have been chosen. The two parametrizations (3.1) and (3.25) are equivalent and the derivatives of the GWP with respect to the parameters  $A, \mathbf{b}, c$  gives directly the bra-vectors of the equations (3.22)-(3.24), except for a common prefactor  $i$  which cancels out. This parametrization is however not used because the integration of the trajectories  $A(t), \mathbf{b}(t), c(t)$  is numerically difficult.

Inserting (3.7) in the ket-vectors of equations (3.22)-(3.24), the compact form

$$\left\langle x_\alpha^m x_\beta^n g(\mathbf{y}^l, \mathbf{x}) \left| \sum_{k=1}^N \left( v_0^k + \mathbf{v}_1^k \cdot \mathbf{x} + \frac{1}{2} \mathbf{x} V_2^k \mathbf{x} - V(\mathbf{x}) \right) g(\mathbf{y}^k, \mathbf{x}) \right. \right\rangle = 0 \quad (3.26)$$

is obtained with

$$l = 1, \dots, N; \quad m + n = 0, 1, 2; \quad \alpha, \beta = 1, \dots, D. \quad (3.27)$$

Sorting terms in (3.26) and abbreviating  $g(\mathbf{y}^k, \mathbf{x}) \equiv g^k$  yields

$$\begin{aligned} & \sum_{k=1}^N v_0^k \langle g^l | x_\alpha^m x_\beta^n | g^k \rangle + \sum_{k=1}^N \langle g^l | x_\alpha^m x_\beta^n \mathbf{x} \cdot \mathbf{v}_1^k | g^k \rangle \\ & + \frac{1}{2} \sum_{k=1}^N \langle g^l | x_\alpha^m x_\beta^n \mathbf{x} V_2^k \mathbf{x} | g^k \rangle = \sum_{k=1}^N \langle g^l | x_\alpha^m x_\beta^n V(\mathbf{x}) | g^k \rangle; \end{aligned} \quad (3.28)$$

$$l = 1, \dots, N; \quad m + n = 0, 1, 2; \quad \alpha, \beta = 1, \dots, D.$$

Equation (3.28) can be written in the compact form of a matrix equation

$$K\mathbf{v} = \mathbf{r} \quad (3.29)$$

when all coefficients  $(v_0^k, \mathbf{v}_1^k, V_2^k)$ ,  $k = 1, \dots, N$  are put together into the complex vector  $\mathbf{v}$ . The dimension of the complex matrix equation is  $N(D(D+1)/2 + D + 1)$  for  $N$  GWPs, because there are  $ND(D+1)/2$  equations due to the complex symmetric  $D \times D$  matrices  $A^k$ ,  $ND$  complex equations result from the  $2ND$  real parameters  $p_\alpha^k$  and  $q_\alpha^k$  and  $N$  equations due to the  $N$  complex parameters  $\gamma^k$ . For a convenient arrangement of the elements in  $K$ , the matrix  $K$  is Hermitean positive definite. All inner products in the Hilbert space denoted by  $\langle \cdot | \cdot \rangle$  are calculated in position space representation in this work. The integrals that build up the components of the matrix  $K$  on the left hand side



of equation (3.28) can be solved analytically, as well as the integrals on the right hand side, provided the potential is of special form, e.g. polynomial, Gaussian or exponential.

The matrix equation (3.28) is derived for fully occupied width matrices  $A^l$  which have no restrictions except for the requirement  $A^l = (A^l)^T$ . Further symmetries or restrictions of the matrices  $A^l$  can enter eq. (3.11) such that the dimension of the resulting matrix equation (3.28) is reduced. Such symmetries or restrictions are e.g. choosing the matrices  $A^l$  to be diagonal, which would lead to the restriction  $\beta = \alpha$  in eq. (3.28). The width matrices can also be kept fixed, called “frozen Gaussians” [11]. Other restrictions on the width matrices will be encountered in chapter 5. Similarly, the GWPs can also be restricted to be located at the origin by the restrictions  $\mathbf{p}^l = 0$  and  $\mathbf{q}^l = 0$ , which leads to  $\mathbf{v}_1 = 0$  and  $m + n = 0, 2$  in eq. (3.28).

It is straightforward to calculate the time derivatives of the Gaussian parameters once the linear equations (3.28) are solved. The differential equations for the Gaussian parameters are expressed by  $(v_0^k, \mathbf{v}_1^k, V_2^k)$ ,  $k = 1, \dots, N$  according to their definition in equations (3.8), (3.9), (3.10) and read

$$\dot{A}^k = -2(A^k)^2 - \frac{1}{2}V_2^k, \quad (3.30a)$$

$$\dot{\mathbf{q}}^k = \mathbf{p}^k + \mathbf{s}^k, \quad (3.30b)$$

$$\dot{\mathbf{p}}^k = 2\text{Re } A^k \mathbf{s}^k - \text{Re } \mathbf{v}_1^k - \text{Re } V_2^k \mathbf{q}^k, \quad (3.30c)$$

$$\dot{\gamma}^k = -v_0^k + i\text{tr } A^k + \frac{1}{2}(\mathbf{p}^k)^2 - \mathbf{v}_1^k \cdot \mathbf{q}^k - \frac{1}{2}\mathbf{q}^k V_2^k \mathbf{q}^k + \mathbf{p}^k \cdot \mathbf{s}^k, \quad (3.30d)$$

where  $\mathbf{s}^k = \frac{1}{2}(\text{Im } A^k)^{-1}(\text{Im } \mathbf{v}_1^k + \text{Im } V_2^k \mathbf{q}^k)$ . Numerically it is more appropriate to introduce two additional  $D \times D$  complex matrices  $B^k, C^k$  according to

$$A^k = \frac{1}{2}B^k(C^k)^{-1}, \quad (3.31)$$

and to integrate the equations of motion

$$\begin{aligned} \dot{C}^k &= B^k, \\ \dot{B}^k &= -V_2^k C^k \end{aligned} \quad (3.32)$$

instead of integrating  $A^k(t)$  directly, because the oscillating  $(A^k(t))^2$  term causes numerical difficulties [45]. There is some freedom for the initial choice of  $B$  and  $C$ . Most simple is to set  $C^k(0) = \mathbf{1}$ ,  $B^k(0) = 2A^k(0)$ . For numerical accuracy, it is appropriate to symmetrize the matrix  $A^k(t)$  after each time step. Note that the symmetry  $A^k = (A^k)^T$  of the matrices  $A^k$  is not maintained in these two auxiliary matrices  $B^k, C^k$ , such that the number of parameters related to the width matrix grows from  $D \times (D+1)/2$  to  $2D^2$ . The increase of the number of parameters only affects the number of coupled differential equations, but not the dimension of the matrix equation (3.28). In case of further symmetries of the width matrix, e.g. if it is diagonal, the dramatic increase of the number

of parameters can however be reduced. For the special form of the matrices  $A^k$  for the GWPs in the regularized hydrogen atom, this topic is discussed in detail in chapter 6.

In the general case, the motion of the GWPs within the superposition is coupled, i.e. the GWPs affect each others motion. If however the underlying potential  $V(\mathbf{x})$  is harmonic they decouple. This can be best visualized by eq. (3.26). For a harmonic potential the expression in the round bracket vanishes and the coefficients  $v_0^k, \mathbf{v}_1^k, V_2^k$  are equal for all  $k = 1, \dots, N$ , such that the effective potential exactly matches the original potential.

Given some initial wave function, i.e. the initial parameters  $\mathbf{z}(t = 0)$ , the wave function is propagated by integrating the trajectories of the parameters. At every time step equation (3.28) must be solved for the coefficients  $\mathbf{v}$  which are inserted in (3.30a)-(3.30d) to obtain  $\dot{\mathbf{z}}$ . In the course of integration, depending on how many GWP are propagated in common, it will sooner or later happen that the matrix  $K$  associated with the set of linear equations (3.28) becomes ill-conditioned, or even numerically singular. As a result the time step of the integration routine becomes extremely small, rendering the method of GWP propagation impracticably slow [13]. In the worst case, further integration or matrix inversion respectively, can even fail. A detailed discussion and a solution to this outstanding problem is one of the goals of this thesis and is presented in chapter 4.

## 4. Inequality constrained TDVP

The equations of motion resulting from the TDVP especially for a large number of coupled GWP become badly behaved from time to time during the integration, making it hardly possible if ever to integrate them. These numerical problems are based on the singularity of the matrix  $K$  in eq. (3.29). A solution to circumvent the problem is now presented.

Matrix singularity problems arise from overcrowding the basis set, i.e. from situations where fewer GWP would be sufficient to represent the wave function. On the other hand for an accurate approximation of the wave function it is desirable to have a large number of adjustable parameters. However, there is a discrepancy between the number of GWPs necessary to give accurate results and the maximum number of GWPs that can be propagated using the TDVP without numerical difficulties [6]. There exist different proposals to overcome this numerical problem, such as a singular value decomposition of the matrix  $K$  [14] or reducing the number of GWPs when overcrowding takes place [7, 9, 16]. Also reducing the variational freedom by freezing the widths [6, 7, 9, 11] and choosing classical trajectories for the centers of the GWPs [8, 15, 17] has been discussed. However, the different methods have some drawbacks. The singular value decomposition indeed prevents the method to break down due to the singularity of the matrix, but does not heal the problem with the tiny step sizes caused by badly behaved differential equations [12]. The idea to reduce the number of GWPs during propagation when necessary requires a fit of the new, reduced basis set to the original wave function. Problems occur to find a reduced basis that reproduces the original wave function accurately and simultaneously is well behaved. Despite the large variety of different proposals an adequate solution for the matrix singularity problem is still lacking.

In this chapter, the approach of regularizing the equations of motion for the parameters is based on minimizing the quantity  $I$  in (2.16) while certain inequality constraints are applied. The constraints must be chosen in such a way that they prevent the matrix  $K$  in (3.28) to become ill-conditioned. This means all Gaussian parameters evolve freely according to the TDVP, and the constraints only become active from time to time whenever the unconstrained evolution would drive the parameters in domains where the matrix would be singular, and are switched off as soon as these “forbidden” domains are left again. Formally spoken we reduce the space of admissible configurations to regions where the associated matrix  $K$  is regular.

To demonstrate the generality of our method we first apply constraints to the general case of an arbitrary trial function  $\chi(\mathbf{z}(t))$  whose parameters  $\mathbf{z}(t)$  evolve according to

equation (2.32). We derive their modified equations of motion which are obtained if the parameters  $\mathbf{z}(t)$  are subject to some arbitrary inequality constraints. Then we return to GWP trial functions (3.4) and derive the modification of equation (3.28) obtained when the GWPs are subject to inequality constraints. Adequate constraints which prevent the matrix from singularity are presented for a model Hamiltonian, viz. the two-dimensional diamagnetic Kepler problem. The method will also be applied in chapter 6 for the wave packet propagation in the 3D hydrogen atom in external fields.

Due to real inequality constraints it is convenient to use a real formulation of the equations. Complex quantities are split into their real and imaginary parts, which are denoted by the subscripts  $r$  and  $i$ , respectively.

## 4.1. Inequality constrained TDVP on arbitrary trial functions

Consider an arbitrary trial function  $\chi(\mathbf{z}(t))$  and assume a real inequality constraint on the parameters  $\mathbf{z}(t) \in \mathbb{C}^{n_p}$  which can be written in the form

$$f(\mathbf{z}, \mathbf{z}^*) \equiv f(\mathbf{z}_r, \mathbf{z}_i) \equiv f(\bar{\mathbf{z}}) \geq f_{\min} \quad (4.1)$$

where the function  $f$  is explicitly known. For brevity, the notation  $\bar{\mathbf{z}} \equiv (\mathbf{z}_r, \mathbf{z}_i) \in \mathbb{R}^{2n_p}$  will be used.

As long as  $f(\mathbf{z}_r, \mathbf{z}_i) > f_{\min}$ , all parameters evolve according to equation (2.32) without being affected by the restriction. When  $f(\mathbf{z}_r, \mathbf{z}_i) = f_{\min}$  is reached at some point in time  $t$ , the constraint becomes active, and we have to demand  $\dot{f}(t) \geq 0$ , otherwise  $f(t + \Delta t)$  with some small positive  $\Delta t$  would violate the constraint (4.1). Therefore the quantity  $I$  of equation (2.16) at fixed  $\mathbf{z}$  must be minimized with respect to  $\dot{\mathbf{z}}$ , where  $(\dot{\mathbf{z}}_r, \dot{\mathbf{z}}_i)$  are now subject to the constraint

$$\dot{f} = \frac{\partial f}{\partial \mathbf{z}_r} \cdot \dot{\mathbf{z}}_r + \frac{\partial f}{\partial \mathbf{z}_i} \cdot \dot{\mathbf{z}}_i \equiv \frac{\partial f}{\partial \bar{\mathbf{z}}} \cdot \dot{\bar{\mathbf{z}}} \geq 0. \quad (4.2)$$

In other words the possibly nonlinear constraint (4.1) on  $\mathbf{z}$  has been reduced to the linear constraint (4.2) on  $\dot{\mathbf{z}}$  when  $f = f_{\min}$ . Then the allowed domain of  $(\dot{\mathbf{z}}_r, \dot{\mathbf{z}}_i)$  for searching the minimum of  $I$  is no more the whole space  $\mathbb{R}^{2n_p}$ , but the half-space  $f \geq 0$  linearly restricted by equation (4.2). In general, minimization of a function on a given domain requires two steps, firstly to find the local internal minima and secondly, to find the local minima on the boundaries. The global minimum in the given domain is obtained by comparison. Here it is sufficient to search for the minimum of  $I$  solely on the boundary of the domain defined by equation (4.2) where the equality sign is fulfilled. That means the inequality (4.2) may be replaced by the computationally much more feasible constraint

$$\frac{\partial f}{\partial \mathbf{z}_r} \cdot \dot{\mathbf{z}}_r + \frac{\partial f}{\partial \mathbf{z}_i} \cdot \dot{\mathbf{z}}_i \equiv \frac{\partial f}{\partial \bar{\mathbf{z}}} \cdot \dot{\bar{\mathbf{z}}} = 0. \quad (4.3)$$

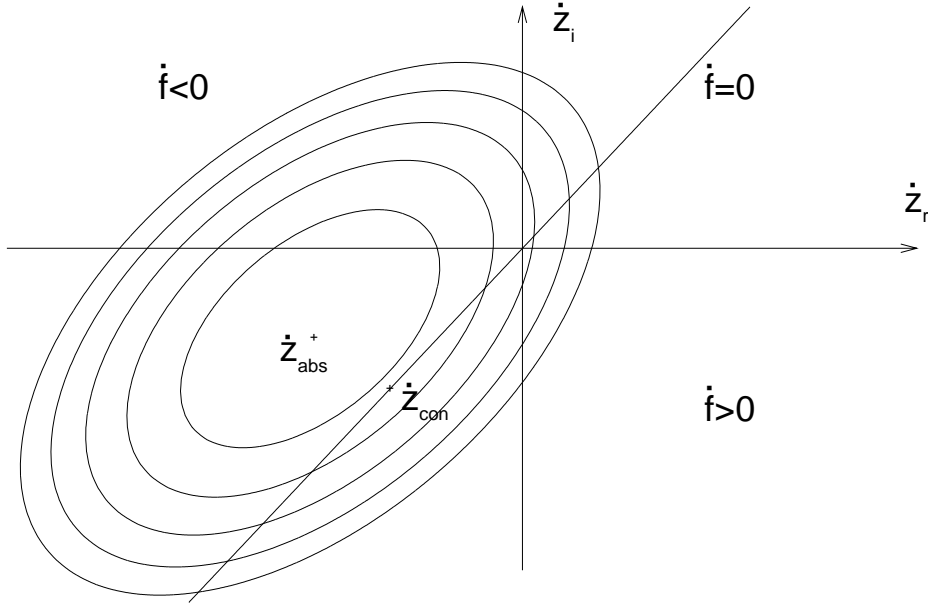


Figure 4.1.: The ellipses schematically represent isolines of  $I$  in equation (2.16) for fixed parameters  $\mathbf{z}$ . The domain of allowed  $\dot{\mathbf{z}}$  for the minimum of  $I$  is the full space, when  $f > f_{\min}$  and is reduced to the half space  $\dot{f} \geq 0$ , when  $f = f_{\min}$  is reached.

The reason is that  $I$  is a positive definite parabolic function of  $\dot{\mathbf{z}}$  whose absolute minimum lies outside the allowed domain by assumption. Since there are no internal minima,  $I$  obviously takes its allowed minimum on the boundary of the allowed domain. The constraint is switched off again as soon as the trajectory  $\dot{\mathbf{z}}(t)$  of the absolute minimum of  $I$  crosses the plane given by equation (4.3) in the  $(\dot{\mathbf{z}}_r, \dot{\mathbf{z}}_i)$ -space at fixed values of  $(\mathbf{z}_r, \mathbf{z}_i)$ . Note that arbitrary nonlinear constraints (4.1) on  $\mathbf{z}$  always lead to linear constraints (4.2) on  $\dot{\mathbf{z}}$  leading to a linearly equality constrained quadratic minimization problem, which can directly be solved by a matrix equation as in the unconstrained case (2.32). The strategy is illustrated in figure 4.1, which shows schematically the elliptical isolines of  $I$  for fixed  $\mathbf{z}$  as a function of  $(\dot{\mathbf{z}}_r, \dot{\mathbf{z}}_i)$ . The values of the parameters  $\mathbf{z}$  determine the shape and the position of the parabola as well as the slope of the plane  $\dot{f} = 0$ . In figure 4.1,  $\dot{\mathbf{z}}_{\text{abs}}$  denotes the absolute minimum of  $I$ , obtained from equation (2.32). The plane  $\dot{f} = 0$  (equation (4.3)) divides the  $2n_p$ -dimensional  $(\dot{\mathbf{z}}_r, \dot{\mathbf{z}}_i)$ -space into the two half-spaces  $\dot{f} < 0$  and  $\dot{f} \geq 0$ . The point  $\dot{\mathbf{z}}_{\text{con}}$  is the constrained minimum of  $I$  in the half-space  $\dot{f} \geq 0$ , which lies on its boundary, i.e. on the plane  $\dot{f} = 0$  as explained above.

As long as  $f > f_{\min}$ ,  $\dot{\mathbf{z}}_{\text{abs}}$  determines the evolution of the parameters. However when  $f = f_{\min}$  is reached, then  $\dot{\mathbf{z}}_{\text{con}}$  is taken for the further integration of the trajectories  $\mathbf{z}(t)$  until  $\dot{\mathbf{z}}_{\text{abs}}$ , driven by the constrained evolution of the parameters, eventually crosses the

plane  $\dot{f} = 0$  from  $\dot{f} < 0$  to  $\dot{f} > 0$ . At this point,  $\dot{\mathbf{z}}_{\text{abs}}$  and  $\dot{\mathbf{z}}_{\text{con}}$  coincide and  $\dot{\mathbf{z}}_{\text{abs}}$  is taken again for further integration, since  $\dot{f} > 0$  leads to an increase of  $f(t)$  with time, according to the constraint.

For the extension to multiple, say  $m$ , active constraints the real scalar valued function  $f(\mathbf{z}_r, \mathbf{z}_i)$  is simply replaced by the real vector valued function  $\mathbf{f}(\mathbf{z}_r, \mathbf{z}_i) \equiv \mathbf{f}(\bar{\mathbf{z}}) = (f_1, \dots, f_m) \in \mathbb{R}^m$ .

Now that the nonholonomic nonlinear inequality constraints (4.1) on  $\mathbf{z}$  are reduced to the holonomic linear equality constraints (4.3) on  $\dot{\mathbf{z}}$  by the constrained TDVP, we can determine the constrained minimum  $\dot{\mathbf{z}}_{\text{con}}$  by a standard method like Lagrangian multipliers. Alternatively, the constrained minimum can also be obtained by elimination of the dependent variational parameters. We prefer the method of Lagrange multipliers due to its generality. The method of Lagrange multipliers yields a compact form of the equations of motion for arbitrary constraints and the conditions for switching off the constraints are obtained with only little additional numerical effort as will be shown below. Both methods, however, require a minimization problem with equality constraints. When inequality constraints are applied, the elimination of dependent variational parameters is not possible.

We construct the function

$$L = I + \boldsymbol{\lambda} \bar{M} \dot{\mathbf{z}} \quad (4.4)$$

with the Lagrangian multipliers  $\boldsymbol{\lambda} \in \mathbb{R}^m$  and the real valued  $m \times 2n_p$  matrix  $\bar{M} = \frac{\partial \mathbf{f}}{\partial \dot{\mathbf{z}}}$ . The minimum of  $I$  under the constraint (4.2) is found by  $\partial L / \partial \boldsymbol{\omega} = 0$  where

$$\boldsymbol{\omega} \equiv \begin{pmatrix} \dot{\mathbf{z}}_r \\ \dot{\mathbf{z}}_i \\ \boldsymbol{\lambda} \end{pmatrix} \equiv \begin{pmatrix} \dot{\mathbf{z}} \\ \boldsymbol{\lambda} \end{pmatrix} \in \mathbb{R}^{2n_p+m}.$$

We obtain a set of linear equations

$$\left( \begin{array}{c|c} \bar{K} & \bar{M}^T \\ \hline \bar{M} & 0 \end{array} \right) \begin{pmatrix} \dot{\mathbf{z}} \\ \boldsymbol{\lambda} \end{pmatrix} = \begin{pmatrix} \bar{\mathbf{h}} \\ 0 \end{pmatrix}, \text{ with } \bar{K} = \begin{pmatrix} K_r & -K_i \\ K_i & K_r \end{pmatrix}, \bar{\mathbf{h}} = \begin{pmatrix} \mathbf{h}_i \\ -\mathbf{h}_r \end{pmatrix}, \quad (4.5)$$

where the matrix  $K$  and the vector  $\mathbf{h}$  are the complex quantities of equation (2.32). If no constraint is active, i.e.  $m = 0$ , then equation (4.5) obviously reduces to the real formulation of equation (2.32). We use a real formulation, i.e. complex quantities are split into their real and imaginary parts, because real constraints like  $f > f_{\text{min}}$  naturally lead to real Lagrangian multipliers.

The constraint (4.3) is switched off again when  $\dot{\mathbf{z}}_{\text{abs}}$  crosses the plane  $\dot{f} = 0$  from  $\dot{f} < 0$  to  $\dot{f} > 0$ . Finding this event can be accomplished in two ways. The trivial but computationally expensive way is to calculate not only  $\dot{\mathbf{z}}_{\text{con}}$  from (4.5), which is needed for integration, but additionally  $\dot{\mathbf{z}}_{\text{abs}}$  (from equation (2.32)) after every time step of integration and to check when  $\dot{f}|_{\dot{\mathbf{z}}_{\text{abs}}}$  changes its sign. This inefficient procedure would require the solution of a complex  $n_p \times n_p$  matrix equation for  $\dot{\mathbf{z}}_{\text{abs}}$  and additionally the solution of the real  $(2n_p + m) \times (2n_p + m)$  matrix equation for  $\dot{\mathbf{z}}_{\text{con}}$ . However it is much

more efficient to check when  $\lambda$  changes its sign for the special case  $m = 1$ . If more than one constraint is active,  $m > 1$ , it is recommended to solve the matrix equation (4.5) by decomposition into two blocks, as indicated by the horizontal line in equation (4.5), namely into

$$\bar{K}\dot{\mathbf{z}} + \bar{M}^T \boldsymbol{\lambda} = \bar{\mathbf{h}} \quad (4.6)$$

obtained by the upper part of equation (4.5), and the lower part

$$\bar{M}\dot{\mathbf{z}} = 0, \quad (4.7)$$

which represents the active constraints. The solution for the unknowns  $\dot{\mathbf{z}}, \boldsymbol{\lambda}$  is obtained by first solving equation (4.6) for  $\dot{\mathbf{z}}$

$$\dot{\mathbf{z}} = \bar{K}^{-1}\bar{\mathbf{h}} - \bar{K}^{-1}\bar{M}^T \boldsymbol{\lambda} \quad (4.8)$$

and inserting it in equation (4.7) in order to eliminate  $\dot{\mathbf{z}}$ . The result is a small  $m \times m$  matrix equation for determining  $\boldsymbol{\lambda}$

$$\underbrace{\bar{M}\bar{K}^{-1}\bar{M}^T}_{m \times m} \boldsymbol{\lambda} = \bar{M}\bar{K}^{-1}\bar{\mathbf{h}} \in \mathbb{R}^m. \quad (4.9)$$

The conditions for switching off any of the active constraints are now contained in the right hand side of equation (4.9), since

$$\dot{\mathbf{f}}|_{\dot{\mathbf{z}}_{\text{abs}}} \equiv \frac{\partial \mathbf{f}}{\partial \dot{\mathbf{z}}} \dot{\mathbf{z}}_{\text{abs}} \equiv \bar{M}\dot{\mathbf{z}}_{\text{abs}} \equiv \bar{M}\bar{K}^{-1}\bar{\mathbf{h}} \quad (4.10)$$

due to the definitions. The  $i$ th active constraint ( $1 \leq i \leq m$ ) is to be switched off when the  $i$ th component of  $\dot{\mathbf{f}}|_{\dot{\mathbf{z}}_{\text{abs}}}$  changes its sign from minus to plus.

When we insert the Lagrange multipliers calculated from (4.9) in (4.8) we obtain  $\dot{\mathbf{z}}_{\text{con}}$ , needed for propagation. Numerically, the calculation of  $\bar{K}^{-1}\bar{\mathbf{h}}$  and  $\bar{K}^{-1}\bar{M}^T$  in (4.9) requires only one factorization of the large matrix  $\bar{K}$ . After multiplying with  $\bar{M}$  from the left the small set of linear equations (4.9) for determining  $\boldsymbol{\lambda}$  is obtained. Compared to the factorization of  $\bar{K}$  the solution of the  $m \times m$  matrix equation (4.9) for the Lagrange multipliers is negligible, since the number of parameters  $n$  will in general exceed the number of constraints  $m$  by far, e.g. in our numerical calculation presented in section 4.3 for the basis of 11 GWPs there is  $2n_p = 132$  and the number  $m$  of simultaneously active constraints is not larger than two.

## 4.2. Inequality constrained TDVP applied to GWP

When GWP are used as trial function, it is convenient to formulate a set of linear equations for the coefficients  $\mathbf{v} = \mathbf{v}_r + i\mathbf{v}_i$  first and then to obtain  $\dot{\mathbf{z}}$  from (3.30a)-(3.30d) in a second step, just as was done in chapter 3. For these coefficients  $\mathbf{v}_r$  and  $\mathbf{v}_i$ ,

#### 4. Inequality constrained TDVP

---

summarized by the notation  $(\mathbf{v}_r, \mathbf{v}_i) = \bar{\mathbf{v}}$ , a similar set of linear equations is obtained. Equations (3.30a)-(3.30d) which describe the connection between the time derivatives of the parameters and the coefficients, are written in real formulation, where all complex quantities are split into their real and imaginary parts. We obtain

$$\dot{A}_r^k = -\frac{1}{2}V_{2r}^k - 2((A_r^k)^2 - (A_i^k)^2), \quad (4.11a)$$

$$\dot{A}_i^k = -\frac{1}{2}V_{2i}^k - 2A_r^k A_i^k - 2A_i^k A_r^k, \quad (4.11b)$$

$$\dot{\mathbf{p}}^k = -\mathbf{v}_{1r}^k - V_{2r}^k \mathbf{q}^k + 2A_r^k \Lambda^k \mathbf{v}_{1i}^k + 2A_r^k \Lambda^k V_{2i}^k \mathbf{q}^k, \quad (4.11c)$$

$$\dot{\mathbf{q}}^k = \Lambda^k \mathbf{v}_{1i}^k + \Lambda^k V_{2i}^k \mathbf{q}^k + \mathbf{p}^k, \quad (4.11d)$$

$$\dot{\gamma}_r^k = -v_{0r}^k - \mathbf{v}_{1r}^k \cdot \mathbf{q}^k - \frac{1}{2} \mathbf{q}^k V_{2r}^k \mathbf{q}^k + \mathbf{p}^k \Lambda^k \mathbf{v}_{1i}^k + \mathbf{p}^k \Lambda^k V_{2i}^k \mathbf{q}^k - \text{tr} A_i^k + \frac{1}{2} (\mathbf{p}^k)^2, \quad (4.11e)$$

$$\dot{\gamma}_i^k = -v_{0i}^k - \mathbf{q}^k \cdot \mathbf{v}_{1i}^k - \frac{1}{2} \mathbf{q}^k V_{2i}^k \mathbf{q}^k + \text{tr} A_r^k, \quad (4.11f)$$

with  $\Lambda^k = \frac{1}{2}(A_i^k)^{-1}$ .

Using the notation  $\bar{\mathbf{z}} = (A_r^1, A_i^1, \mathbf{p}^1, \mathbf{q}^1, \gamma_r^1, \gamma_i^1, \dots, A_r^N, A_i^N, \mathbf{p}^N, \mathbf{q}^N, \gamma_r^N, \gamma_i^N)$  the complete set of equation (4.11) for all  $k = 1, \dots, N$ , which are linear in  $(v_0^k, \mathbf{v}_1^k, V_2^k)$ , may be written in short form  $\dot{\bar{\mathbf{z}}} = \tilde{U} \bar{\mathbf{v}} + \tilde{\mathbf{d}}$ . The matrix  $\tilde{U}$  is block-diagonal with  $N$  blocks. Each block consists of those coefficients in equation (4.11) linear in  $(v_0^k, \mathbf{v}_1^k, V_2^k)$ . The constant terms are absorbed in the vector  $\tilde{\mathbf{d}}$ . The linear equality constraint (4.3) for a GWP trial function reads

$$\dot{f} = \sum_{k=1}^N \left( \frac{\partial f}{\partial A_r^k} \dot{A}_r^k + \frac{\partial f}{\partial A_i^k} \dot{A}_i^k + \frac{\partial f}{\partial \mathbf{p}^k} \cdot \dot{\mathbf{p}}^k + \frac{\partial f}{\partial \mathbf{q}^k} \cdot \dot{\mathbf{q}}^k + \frac{\partial f}{\partial \gamma_r^k} \dot{\gamma}_r^k + \frac{\partial f}{\partial \gamma_i^k} \dot{\gamma}_i^k \right) = 0 \quad (4.12)$$

where the notation

$$\frac{\partial f}{\partial A_r^k} \dot{A}_r^k = \sum_{l,j=1}^D \frac{\partial f}{\partial (A_r^k)_{lj}} (\dot{A}_r^k)_{lj} \quad (4.13)$$

is used. Expressing the time derivatives in equation (4.12) by the coefficients  $\mathbf{v}_r$  and  $\mathbf{v}_i$  using (4.11),  $m$  arbitrary constraints  $(\mathbf{f} = (f_1, \dots, f_m) \in \mathbb{R}^m)$  imply

$$\dot{\mathbf{f}} = \frac{\partial \mathbf{f}}{\partial \bar{\mathbf{z}}} \tilde{U} \bar{\mathbf{v}} + \frac{\partial \mathbf{f}}{\partial \bar{\mathbf{z}}} \tilde{\mathbf{d}} \equiv \bar{U} \bar{\mathbf{v}} + \bar{\mathbf{d}} = 0, \quad (4.14)$$

and hence a set of linear equations for  $(\mathbf{v}_r, \mathbf{v}_i)$  and the Lagrange multipliers  $\boldsymbol{\lambda} \in \mathbb{R}^m$  is obtained

$$\left( \begin{array}{c|c} \bar{K} & \bar{U}^T \\ \hline \bar{U} & 0 \end{array} \right) \begin{pmatrix} \bar{\mathbf{v}} \\ \boldsymbol{\lambda} \end{pmatrix} = \begin{pmatrix} \bar{\mathbf{r}} \\ -\bar{\mathbf{d}} \end{pmatrix}, \text{ with } \bar{K} = \begin{pmatrix} K_r & -K_i \\ K_i & K_r \end{pmatrix}, \bar{\mathbf{r}} = \begin{pmatrix} \mathbf{r}_r \\ \mathbf{r}_i \end{pmatrix}. \quad (4.15)$$



Here, the matrix  $K = K_r + iK_i$  and the vector  $\mathbf{r} = \mathbf{r}_r + i\mathbf{r}_i$  are the left and right hand side of equation (3.28), respectively.

We now have all equations needed for propagation of coupled GWPs subject to arbitrary constraints (4.1). Instead of (3.28) we solve (4.15) for  $(\mathbf{v}_r, \mathbf{v}_i)$  (when no constraints are active both sets of equations are equivalent) after each time step. These coefficients are inserted in (3.30a)-(3.30d) (or equivalently in (4.11)) to obtain the time derivatives of the Gaussian parameters, which are needed by the integration routine to integrate the next time step. The explicit constraints suitable to prevent the breakdown of the wave packet propagation are introduced in section 4.3 for the model calculations on the two-dimensional diamagnetic Kepler problem.

### 4.3. 2D diamagnetic hydrogen atom

The method of GWPs propagation developed so far is now applied to a model system. The matrix singularity problem is addressed and adequate inequality constraints are introduced. The computations are performed for a two-dimensional model potential, viz. a harmonic oscillator with an anharmonic perturbation. The Hamiltonian of the system is

$$H = -\frac{1}{2} \left( \frac{\partial^2}{\partial \mu^2} + \frac{\partial^2}{\partial \nu^2} \right) + V(\mu, \nu), \quad (4.16)$$

with the potential

$$V(\mu, \nu) = \alpha(\mu^2 + \nu^2) + \frac{1}{8}\beta^2\mu^2\nu^2(\nu^2 + \mu^2), \quad (4.17)$$

and the parameters  $\alpha = 0.5$ ,  $\beta = 0.2$ . As described in chapter 6 the Hamiltonian (4.16) effectively describes the diamagnetic hydrogen atom in a 2D rotating frame. In the rotating frame the semiparabolic coordinates  $\mu = \sqrt{r+z}$  and  $\nu = \sqrt{r-z}$  are treated like Cartesian coordinates ranging from minus to plus infinity. Here, the 2D diamagnetic hydrogen atom (4.16) serves as a test ground for investigating the propagation of coupled GWPs (3.4). Since the potential is polynomial, the integrals needed to set up the matrix equation (3.28) are moments of complex Gaussians and are computed recursively in appendix A.1. The equations of motion (3.30a)-(3.30d) as obtained from unconstrained variation become ill-behaved with increasing number of GWPs leading to tiny step sizes of the integration or in the worst case to a complete breakdown of the method. As explained above these numerical problems occur when the matrix  $K$  in the equations of motion becomes nearly singular. For the case of numerical singularity of the matrix a singular value decomposition for the solution of the linear equations has been proposed [14]. This prevents the propagation from a breakdown due to a failure of the inversion of the singular matrix, however, the equations of motion obtained from applying the singular value decomposition are still ill-behaved in the sense that the time steps of the integration stay impracticably small [12]. The reason for the ill-conditioned matrix as

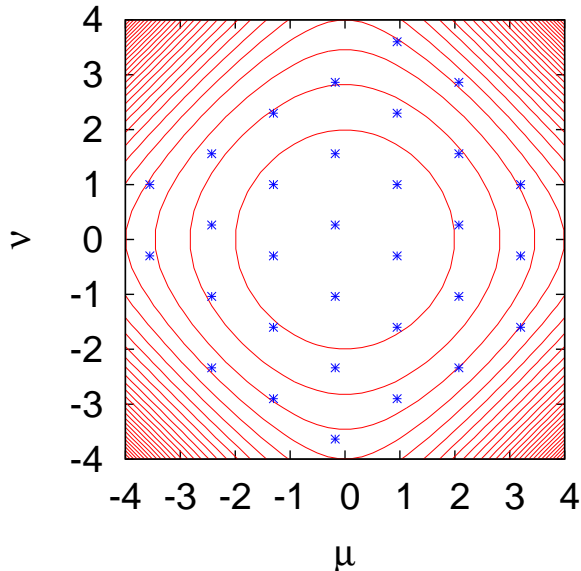


Figure 4.2.: Equipotential lines of the potential (4.17) together with the hexagonal grid, where the GWPs used for the computations in this section are initially placed.

obtained from unconstrained variation is investigated for the model system (4.16) and suitable constraints are introduced which heal the numerical problem of tiny step sizes by keeping the matrix  $K$  regular. The additional error introduced by the constraints is investigated. The numerical efficiencies of the different propagation techniques, i.e. propagation with and without constraints are compared. To demonstrate the high accuracy of the method comparisons with exact computations with the split-operator method are presented. The split-operator method is briefly explained in appendix C.

For the computations in this chapter a superposition of GWPs (3.4) is used whose centers  $\mathbf{q}^k \equiv (\mu^k, \nu^k)$ ,  $k = 1, \dots, N$  are placed on a  $2D$  equidistant grid in position space  $(\mu, \nu)$ . The equidistant hexagonal grid together with the isolines of the potential of the system are shown in figure 4.2. An equidistant hexagonal grid is chosen to distribute the GWPs in space with preferably large distance to their next neighbors. The regular hexagonal grid is not centered with respect to the potential in order to obtain no undesired, incidental symmetry in the wave functions. The GWPs are distributed around the minimum of the potential (4.17). In fig. 4.2 those grid points  $(\mu^k, \nu^k)$  are plotted with  $V(\mu^k, \nu^k) \leq 8.5$ . The computations in this section are performed for initial wave functions consisting of different numbers  $N$  of GWPs each placed

on selected grid points in figure 4.2. All GWPs are chosen to be initially real valued, i.e. their initial momenta  $\mathbf{p}^k(\tau = 0)$ ,  $k = 1, \dots, N$  are zero and their width matrices are purely imaginary. For these width matrices the particularly simple diagonal form  $A^k(\tau = 0) = \frac{i}{2}\mathbf{1}$ ,  $k = 1, \dots, N$  is chosen. Remember that for the GWP (3.1) to be normalizable the imaginary part of the complex symmetric matrices  $A^k$  must be positive definite. In absence of the anharmonic coupling in the potential (4.17), the above choice of  $A^k(t = 0)$  yields coherent states of the harmonic oscillator and the widths are constant in time. The norms of the individual GWPs are selected in the way that there is one large GWP surrounded by small “satellite” GWPs.

In order to find adequate constraints that prevent the matrix  $K$  from becoming singular, it is suggestive to investigate the evolution of the eigenvalues of the matrix during the integration together with the step size of the integration algorithm. Here an Adams integration routine is applied to a superposition of  $N = 11$  GWPs. The results are plotted in fig. 4.3. In panel (a) the step size  $\Delta\tau$  of the integration routine, necessary to match the prescribed error tolerances is shown as a function of time  $\tau$ . The step sizes vary between  $10^{-3}$  and  $10^{-2}$ , except for two short intervals where  $\Delta\tau$  suddenly becomes about three orders of magnitude smaller  $\Delta\tau \approx 5 \times 10^{-6}$ , i.e. the method gets very slow. The intervals of slow integration are  $14.6 \leq \tau \leq 16.3$  and  $40.6 \leq \tau \leq 41.9$ , where most of the computational time of the numerical integration is spent. As mentioned above, numerical problems occur when the matrix  $K$  associated with the equations of motion becomes ill-conditioned. It is therefore worthwhile to check its eigenvalues during integration. Of special interest are the least and the largest eigenvalues of this matrix, whose ratio known as the condition number characterizes the regularity of a matrix. The least and the largest eigenvalues are plotted in fig. 4.3(b) as functions of time. There is an apparent correlation between the tiny time steps around  $\tau \approx 15$  and  $\tau \approx 41$  and the very large magnitude of the largest eigenvalue  $\lambda_{\max}$  at these intervals, while the least eigenvalues stays unaffected. This means that the matrix singularities which render the method impracticably slow come from diverging eigenvalues  $\lambda_{\max}$  instead of vanishing eigenvalues  $\lambda_{\min}$ . The situation of diverging eigenvalues depicted here by one example, seems to be quite general and was encountered in different systems. For further investigations we use the Gershgorin circle theorem [46], which states that all eigenvalues of a  $n \times n$  matrix lie within  $n$  circles in the complex plane whose centers are the diagonal elements of the matrix and their radii are the sums of the modulus of the off diagonal elements along the corresponding column or row, respectively. Following this theorem, very large eigenvalues of a matrix are only possible when there are some very large matrix elements too. The matrix elements of the matrix  $K$  (3.28) are Gaussian overlap integrals of the form  $\langle g^l | \mu^m \nu^n | g^k \rangle$ . Very large matrix elements are possible when the norm  $\langle g^k | g^k \rangle$  becomes unreasonably large for some GWPs. This can occur when the determinant of the imaginary part of the complex symmetric width matrix  $A^k$  approaches zero for some GWPs which means that some GWPs become extremely broad. The other possibility is that some GWPs have very large amplitude, i.e. the imaginary part of the phase  $\gamma^k$  becomes too negative for some GWPs leading to exponential increase

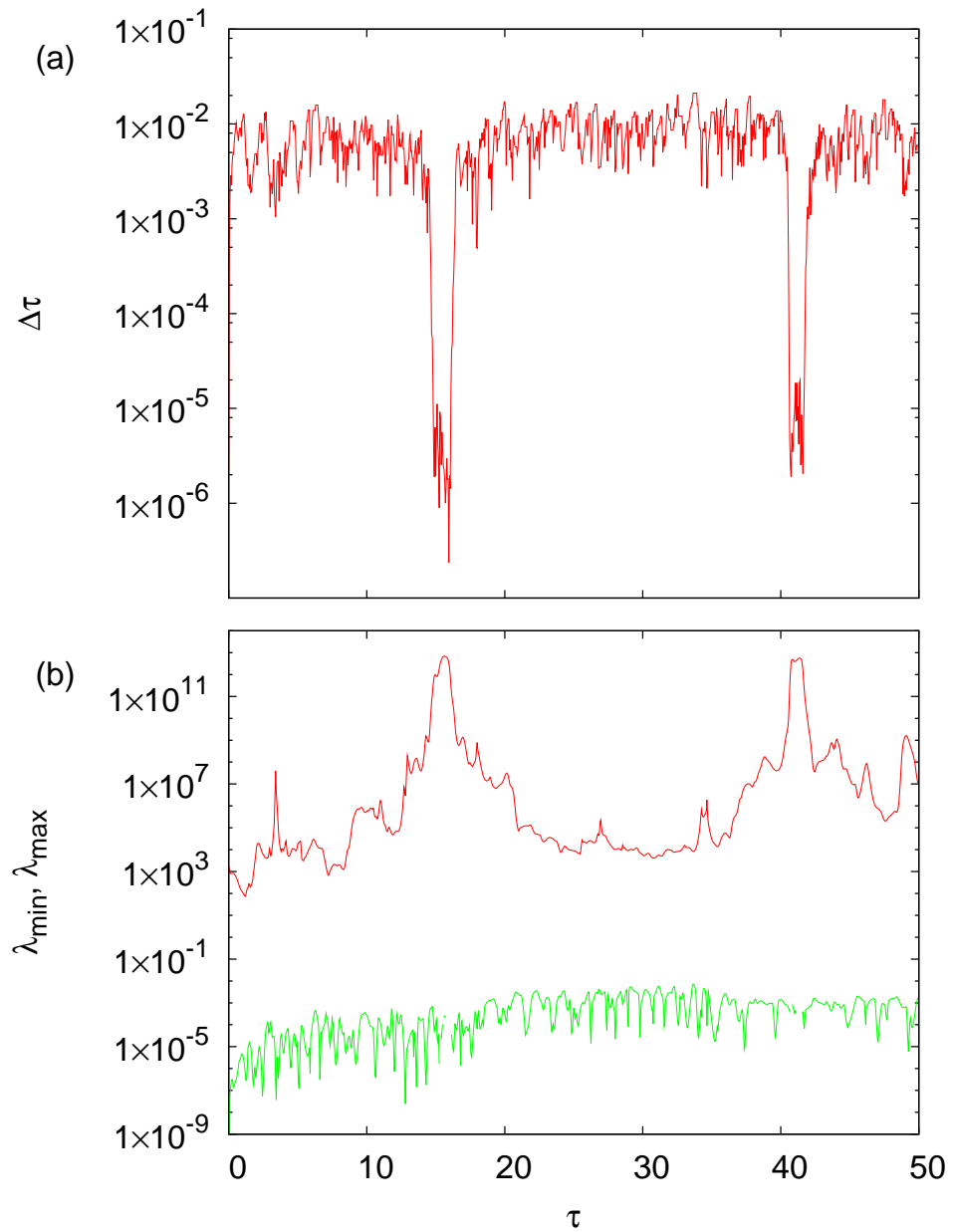


Figure 4.3.: (a) Step size required by the integration routine to match the prescribed error tolerance. (b) Least and largest eigenvalues of the matrix  $K$  associated with the equations of motion. There is an apparent correlation between the tiny required step size at  $\tau \approx 15$  and  $\tau \approx 41$  and the magnitude of the largest eigenvalue of the matrix  $K$ .

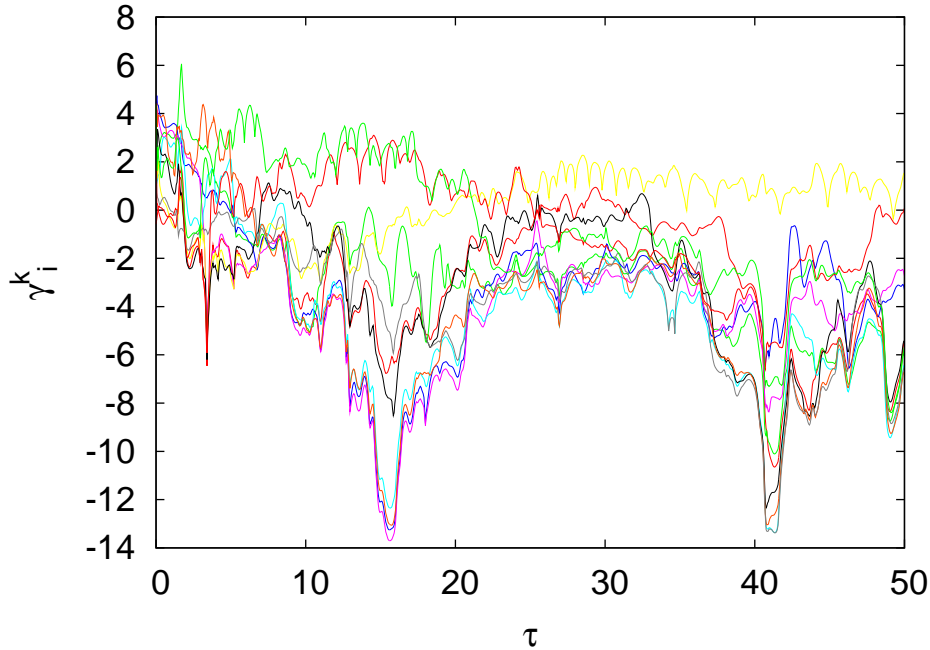


Figure 4.4.: Imaginary part of the phase factors  $\gamma^k$  for all 11 GWPs. Some  $\gamma_i^k, k = 1, \dots, 11$  are especially small around  $\tau \approx 15$  and  $\tau \approx 41$  and cause the numerical problems shown in fig. 4.3.

of the norm  $\|g^k\|^2 \propto \exp(-2\gamma_i^k)$  (for the evaluation of the integrals see appendix A.1). Inspection of the imaginary parts  $\gamma_i^k$  of all 11 GWPs in fig. 4.4 reveals that indeed very negative values of  $\gamma_i^k$  are the reason for the extremely large eigenvalues. Whenever some of the  $\gamma_i^k$  become too small, which happens here in the intervals  $14.6 \leq \tau \leq 16.3$  and  $40.6 \leq \tau \leq 41.9$ , the method of GWP propagation becomes impracticably slow or may even completely break down. Therefore reasonable constraints which prevent the matrix from becoming singular are the requirements

$$f_{\min} \equiv \gamma_{\min} \leq f^k(\tilde{\mathbf{z}}) = \text{Im } \gamma^k = \gamma_i^k, \quad k = 1, \dots, N \quad (4.18)$$

on the amplitudes of the GWP. In the computation presented in figs. 4.3 and 4.4 a value of about  $\gamma_{\min} = -9.0$  should be adequate. For those constraints which are currently active ( $\gamma_i^k = \gamma_{\min}$ ) equation (4.3) using (4.11) translates into

$$\dot{\gamma}_i^k = -v_{0i}^k - \mathbf{q}^k \cdot \mathbf{v}_{1i}^k - \frac{1}{2} \mathbf{q}^k V_{2i}^k \mathbf{q}^k + \text{tr } A_r^k = 0. \quad (4.19)$$

Therefore, the entries of  $\bar{U}$  in equations (4.14) and (4.15) are mostly zero except for the terms of equation (4.19) linear in  $v_0, \mathbf{v}_1$  or  $V_2$  and  $\bar{d} = \text{tr } A_r^k$ . This especially simple case of constraints, where Gaussian parameters are bounded directly, leads to temporary

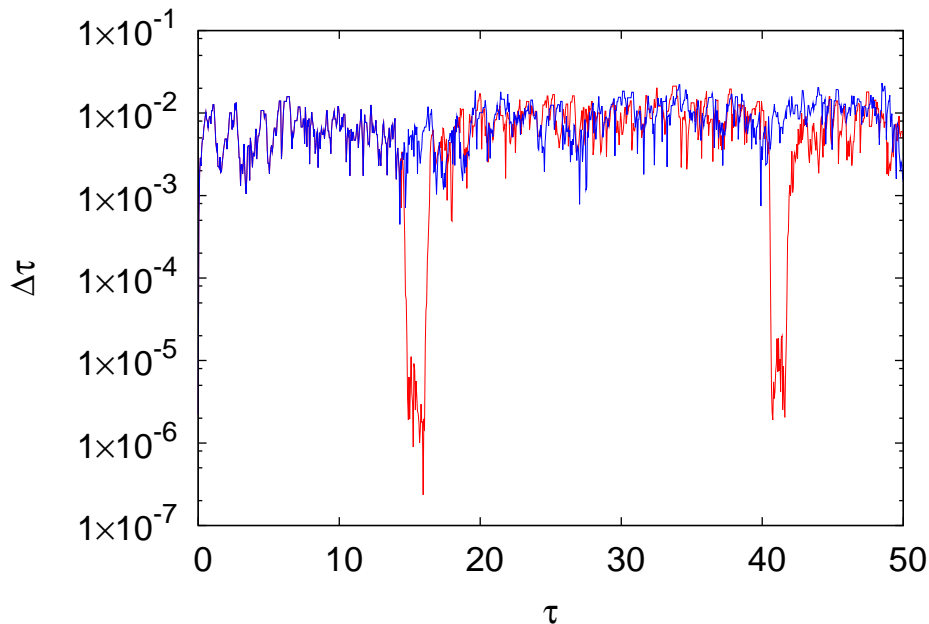


Figure 4.5.: Comparison of the step sizes applied by the integration routine to meet the error tolerance, without constraints (red line) as in fig. 4.3(a) and with constraints (4.18) with  $\gamma_{\min} = -9.0$  (blue line).

freezing these parameters  $\gamma_i^k$  when  $\gamma_i^k = \gamma_{\min}$  is reached. Instead of using Lagrange multipliers the equations of motion alternatively can be obtained by elimination of the dependent parameters. The frozen  $\gamma_i^k$  must be simply ignored in the variation. However, in that case additional calculations are necessary to find the criteria for switching off the constraints.

In cases where the restriction on the amplitudes (4.18) is not adequate, an upper bound on the maximum of the allowed overlap of neighboring GWPs or a lower bound on the least eigenvalue of the matrix  $K$  can be applied.

The gain of efficiency introduced by the constraints (4.18) with  $\gamma_{\min} = -9.0$  as compared to the unconstrained propagation is impressively visualized by plotting the associated step sizes of the same initial wave function with the same error tolerance. For comparison both time steps are plotted in figure 4.5. The red line shows again the required step size of the unconstrained propagation as shown already in fig. 4.3 (a) which become tiny in the intervals  $14.6 \leq \tau \leq 16.3$  and  $40.6 \leq \tau \leq 41.9$ . The blue line shows the required time steps with the constraints  $\gamma_{\min} = -9.0 \leq \gamma_i^k$  for  $k = 1, \dots, 11$ . For times  $\tau \lesssim 14.6$  the step sizes of both propagation methods exactly agree as is expected, since the constraints  $\gamma_i^k \geq -9.0$  become active at  $\tau = 14.6$  (see fig. 4.4) when one of the  $\gamma_i^k$  reaches  $\gamma_{\min}$  for the first time. Up to this time both computations are identical. The

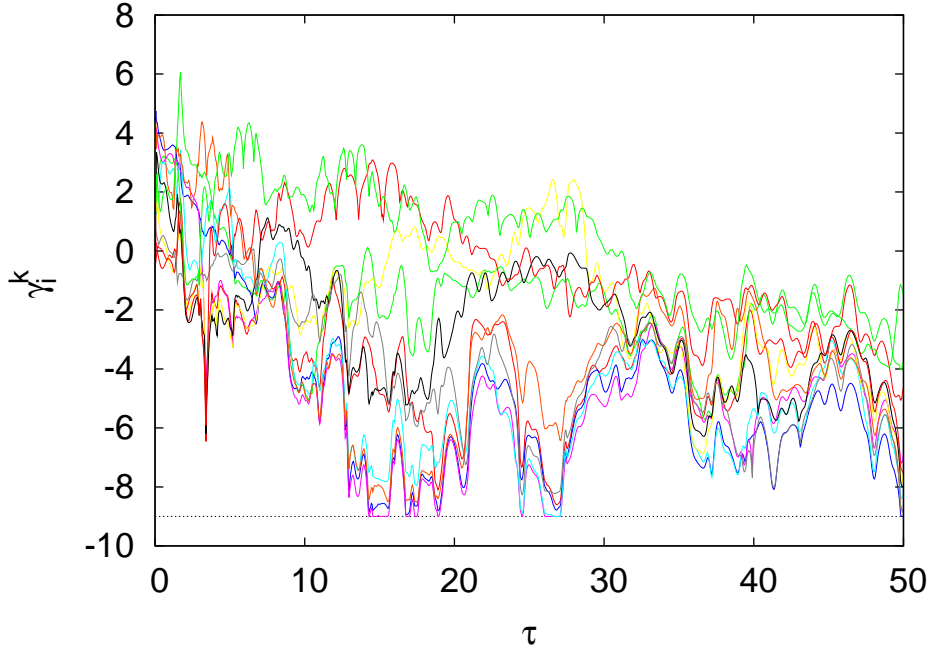


Figure 4.6.: Imaginary parts of the normalization parameters  $\gamma^k$  for  $k = 1, \dots, 11$  subject to the constraints  $\gamma_i^k \geq \gamma_{\min} = -9.0$ . Obviously the constraints become active for only short time periods while the full variational freedom of the trial function is left otherwise. For a better orientation the value of  $\gamma_{\min} = -9.0$  is marked by a dotted line.

extremely slow integration during the periods  $14.6 \leq \tau \leq 16.3$  and  $40.6 \leq \tau \leq 41.9$  is accelerated by three to four orders of magnitude. When no constraints are applied most time of the integration process is spent on such singularity points, and thus with the constraints the overall integration time is reduced by orders of magnitude, making the method applicable in the first place.

The parameters  $\gamma_i^k$  of the constrained propagation are plotted in fig. 4.6. In terms of fig. 4.1,  $\dot{\mathbf{z}}_{\text{abs}}$  is taken for integration during  $\tau \leq 14.6$ , i.e. as long as  $\gamma_i^k > -9.0$  when  $\gamma_i^k = \gamma_{\min}$  is reached,  $\dot{\mathbf{z}}_{\text{con}}$  is used for the further propagation leaving  $\gamma_i^k = \gamma_{\min}$  for the relevant  $k$  until at some later point in time  $\dot{\gamma}_i^k$  becomes positive again, e.g. at  $\tau \approx 16.3$  in fig. 4.6. In practice, a CPU time of about 20 hours needed for unconstrained propagation could be reduced to a few minutes when using constraints.

### 4.3.1. Error introduced by the constraints

The error of the TDVP has been estimated in section 2.4. We now investigate the additional error introduced by the constraints for the model Hamiltonian (4.16). The

error of the variational approximation without constraints is compared to the error of the computation with the constraints (4.18) for a chosen value of  $\gamma_{\min} = -9.0$ .

The square root of  $I$  in eq. (2.15) at its minimum is a measure of the accuracy of the variational approximation [43, 44], c.f. section 2.4. Its value is zero for the exact solution, and according to eq. (2.38) it presents an upper bound on the local error implied by the TDVP. Therefore a comparison of the square roots of the minima  $I|_{\dot{\mathbf{z}}_{\text{abs}}}$  of the unconstrained propagation and  $I|_{\dot{\mathbf{z}}_{\text{con}}}$  of the constrained propagation allows for an estimate of the loss of accuracy introduced by the constraints.

A comparison of the square roots of the minima in fig. 4.7 shows that the error bound of the constrained propagation (blue) is practicably not increased at  $\tau \approx 14.6$ , i.e. the time when the constraints are switched on, as compared to the error bound of the unconstrained propagation (red), see fig. 4.7(a). In the long run, see fig. 4.7(b), the constrained approximation may be even better than the unconstrained approximation, although a poorer approximation of the constrained wave function to the exact one would be expected.

An explanation might be that the approximate wave function determined by TDVP is not always the “best” possible approximation of the trial function to the exact wave function [43]. There might be regions on the manifold of the trial function that are closer to the exact wave function than the function determined variationally, especially when the manifold has a large curvature and long time intervals are considered. This fact, together with the insensitivity of the wave function to small variations of the parameters in some directions in case of a singular matrix, may explain the behavior of only temporary slight loss of accuracy introduced by the constraints. The insensitivity of the trial wave function to the constraints can also be deduced from investigating the auto-correlation functions  $C(t) = \langle \chi(t=0) | \chi(t) \rangle$  obtained by both methods since they almost coincide and no deviation from each other could be seen.

A hint for properly chosen constraints is to monitor the norm of the trial function during the propagation. The constraints destroy the exact conservation of the norm, but for an adequate value of  $\gamma_{\min}$  the loss of norm is only within a few percent for typical propagation times. We conclude that the use of constraints can accelerate the numerical computations by orders of magnitude without any significant loss of accuracy of the results.

### 4.3.2. Comparison with exact computations

To demonstrate the power of the constrained GWP method a superposition of 30 GWPs having all the same width and zero momenta, again distributed on the grid in fig. 4.2 is employed. This initial wave packet is propagated by three different methods. The real parts of the resulting auto-correlation functions are plotted in figure 4.8. The imaginary parts, not shown the figure, exhibit similar qualitative behavior. The result of the constrained propagation is plotted with the blue line, and the result of frozen Gaussian propagation is plotted with the green line. For reference the numerically exact propa-



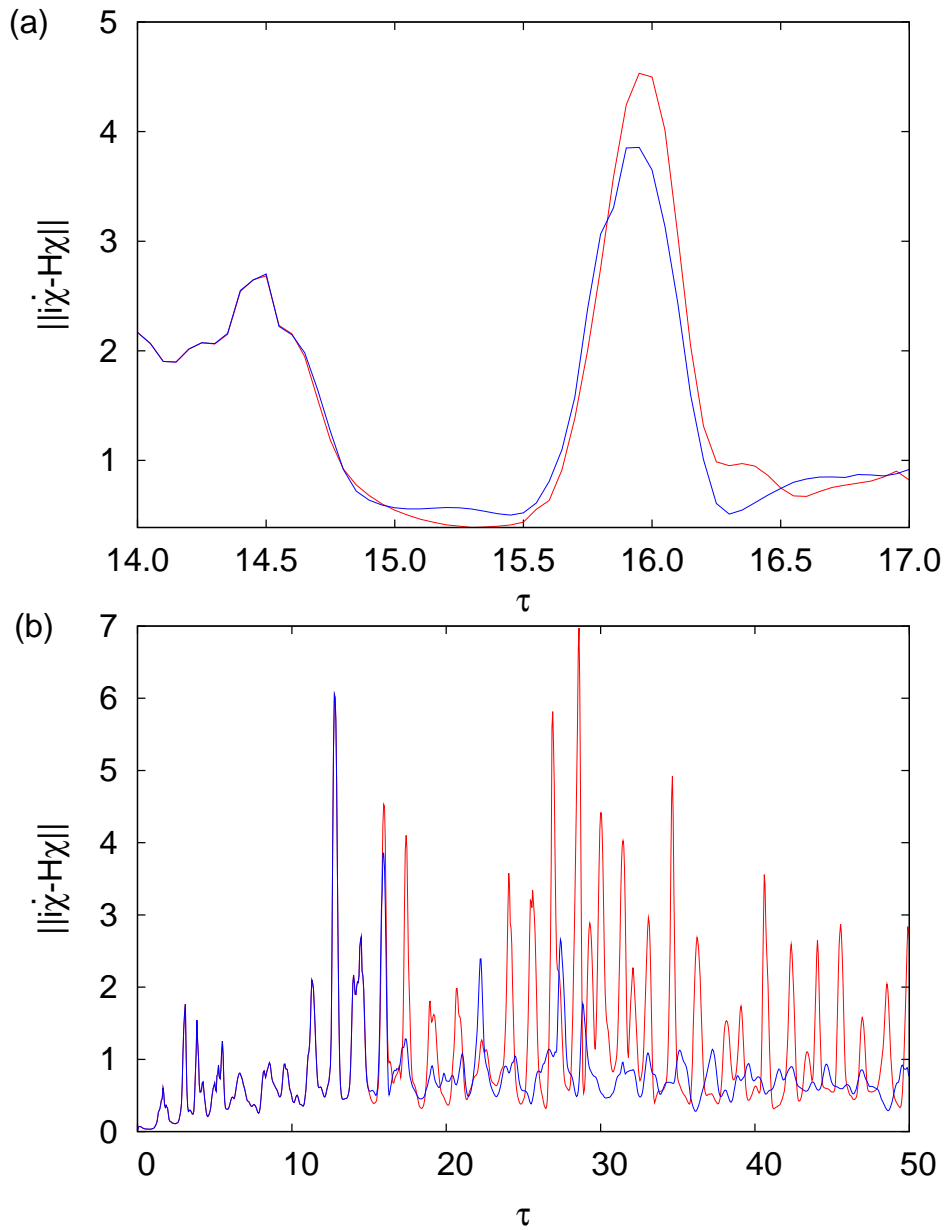


Figure 4.7.: Accuracy of the variational approximation with (blue) and without (red) use of the constraints (4.18) with  $\gamma_{\min} = -9.0$ . The local upper bound (2.38) on the variational approximations is plotted (a) in the region where the constraints become active for the first time and (b) in the long run. At  $\tau \approx 14.6$ , i.e. at the time when the constraints are switched on, nearly no increase of the error bound of the constrained propagation as compared to unconstrained propagation is visible. On the long run the error bound on the computation with constraints is even lower in the average than without constraints.

gation is performed by the split-operator method [47] (red line, for a short explanation see appendix C). The result of our constrained ( $\gamma^k \geq -6.0$ ) GWP propagation is mostly very accurate and nearly no deviation from the exact solution is visible during the whole propagation time. By contrast, the result obtained from the frozen Gaussian propagation, where the width matrices are kept fixed, turns out to be much less accurate. This becomes particularly apparent for long propagation times, where the deviation between the exact time signal and the time signals obtained from constrained “thawed” width, i.e. without keeping the width matrices fixed, propagation is still very good. This is not completely unexpected since the constrained trial function still has more free variational parameters than the frozen GWP method and therefore the constrained calculation is somewhat slower. Note that an unconstrained propagation of these 30 GWPs with “thawed” widths according to the TDVP is not possible, because of matrix singularities.

The deviation of the two GWP auto-correlation functions to the numerically exact one is revealed in fig. 4.9. Throughout the plotted time range, the constrained propagation is accurate while the frozen GWP method loses its accuracy.

With the propagated wave packet at hand it is possible to obtain the eigenvalues of the Hamiltonian (4.16) by Fourier transform or harmonic inversion (for a review of the harmonic inversion method see [48–51]) of the auto-correlation function and even to extract the eigenfunctions of the system [52, 53]. The eigenvalues  $E_i$  resulting from the harmonic inversion of the time signals presented in fig. 4.8 are plotted with blue impulses for the constrained GWP computation and are compared with the numerically exact eigenvalues (red impulses) in fig. 4.10. The amplitudes of the lines in the spectrum are determined by the magnitude of overlap between the initial trial function  $|\chi(\tau = 0)\rangle$  and the eigenstate  $|E_i\rangle$ . For a better comparison the numerically exact results are inverted. Both spectra show good agreement.

With the tool of constraining the GWPs, the equations of motion become well behaved and the basis for further computations is established. We now turn to the physical 3D hydrogen atom.

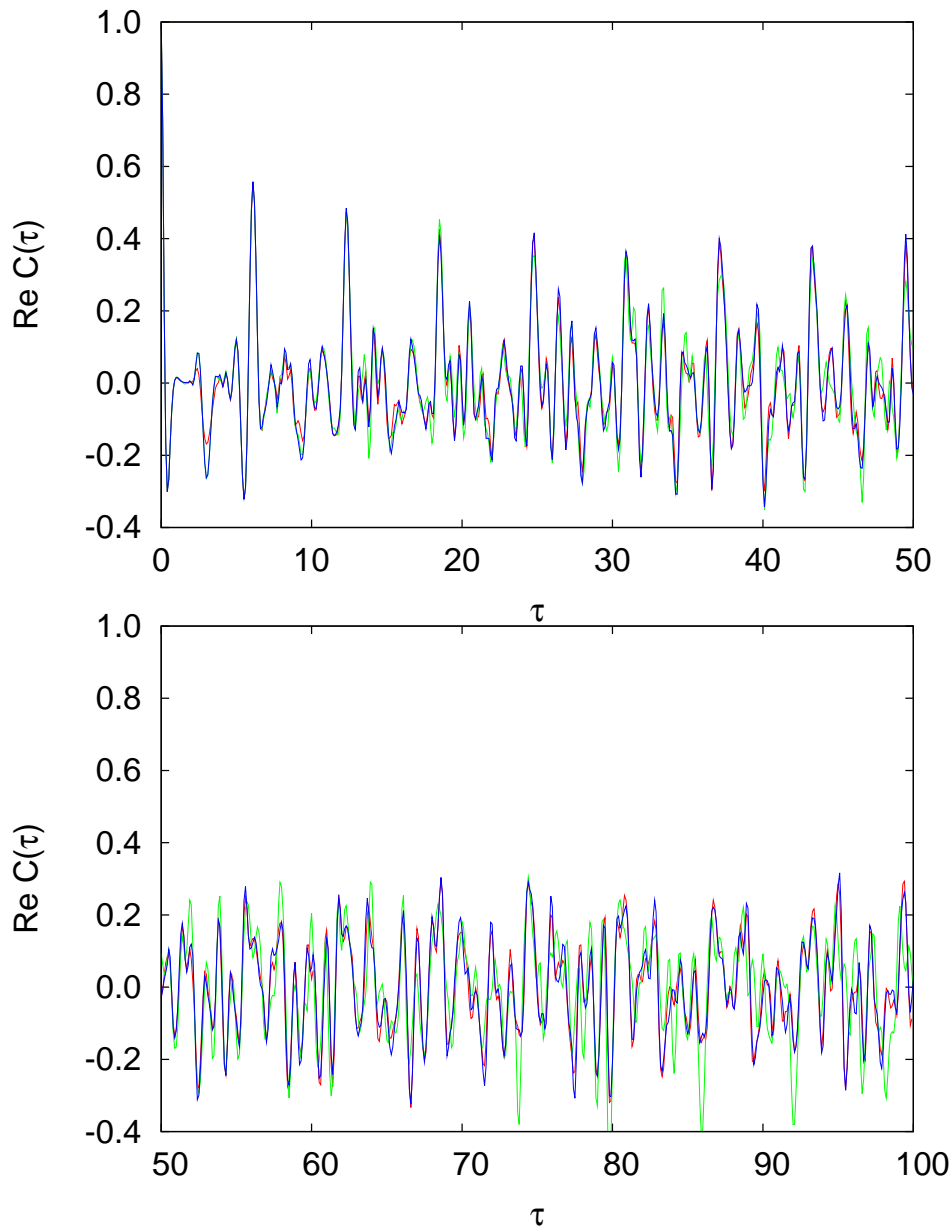


Figure 4.8.: Real part of the auto-correlation function  $C(\tau)$  for the 2D diamagnetic Kepler problem. The initial wave function is a superposition of 30 GWP positioned on the grid shown in fig. 4.2. Variational propagation with the constraints  $\gamma^k \geq -6.0$  (blue line) is compared with numerically exact calculations obtained with the split-operator method (red line) and with frozen GWP propagation, where the width of the GWPs is fixed (green line). The results of the constrained calculation and the numerically exact calculation agree very well, i.e. nearly no deviations are visible, while the frozen Gaussian computation shows larger deviations especially for long propagation times.

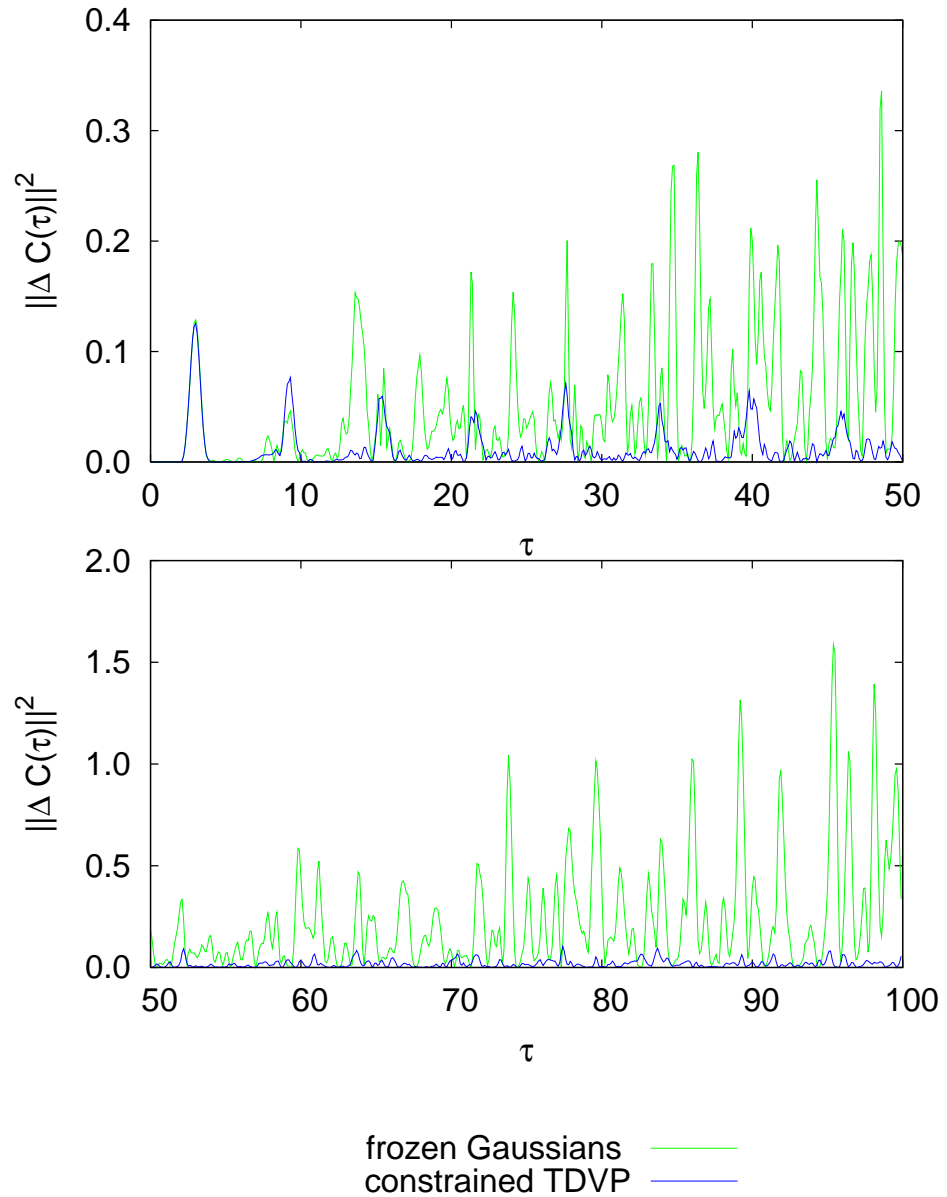


Figure 4.9.: Accuracy of the auto-correlation functions shown in fig. 4.8. The difference between the frozen Gaussian propagation and the exact computation is plotted by the green line. The difference between the constrained Gaussian propagation and the exact computation is plotted by the blue line.

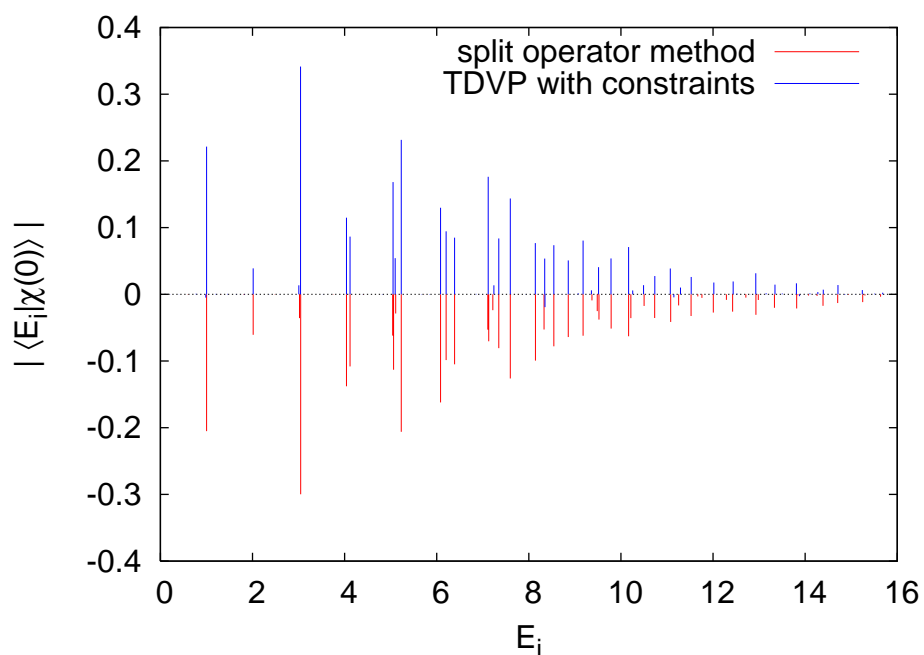


Figure 4.10.: Eigenvalues extracted from the auto-correlation function of fig. 4.8 by harmonic inversion. The amplitudes of the spectrum are given by the magnitude of the overlap of the initial wave function  $|\chi(\tau = 0)\rangle$  with the respective eigenstate  $|E_i\rangle$ . The results obtained by the constrained GWP method are plotted with blue impulses, the results of the numerically exact computation are plotted with red inverted impulses for comparison. Both spectra show good agreement.



## 5. Wave packet dynamics in the hydrogen atom

The success of applying the TDVP on a quantum system crucially depends on the choice of the trial function. GWPs are certainly well suited for smooth and nearly harmonic potentials. Therefore the Coulomb potential is not a promising candidate for successfully propagating GWPs directly. Nevertheless, the GWP method based on the local harmonic approximation has already been applied in one dimension to the singular Coulomb-potential [22–24]. A regularization [25, 26] originally introduced in the field of classical celestial mechanics, but also adapted to the hydrogen atom [54], transforms the Coulomb potential to a harmonic potential with a restriction. In the regularized hydrogen atom the application of the GWP method should therefore be able to yield exact results when the restriction can be handled. The regularization implies a fictitious time variable which has been shown to be the eccentric anomaly of the corresponding classical orbit [55]. Various approaches have been made to construct coherent states for the hydrogen atom [56–60] in the fictitious time in analogy to the coherent states found by Schrödinger [61] for the harmonic oscillator. These approaches construct the coherent states as the eigenstates of the lowering operators associated with the harmonic potential. The hydrogen atom in an external magnetic field and in crossed electric and magnetic fields has attracted much attention in recent decades [27–30]. Both systems show a transition from regularity to chaos in the underlying classical mechanics and hence the systems allow for an investigation of the impact of irregular classical dynamics on quantum spectra, i.e. the phenomenon of “quantum chaos”. The hydrogen atom with and without external fields presents a fundamental quantum system. It is desirable to extend the GWP method to be successfully applied also to the hydrogen atom with and without external fields in such a way that the hydrogen atom itself is treated exactly by the GWP method, and only the external fields need a variational approximation. In this chapter we discuss the regularization of the hydrogen atom and the exact wave propagation in the fictitious time. The TDVP is then applied to the hydrogen atom in external fields in chapter 6.

## 5.1. Regularization of the hydrogen atom

The time-independent Schrödinger equation for the hydrogen atom reads

$$H_3\psi = \left(-\frac{1}{2}\Delta_3 - \frac{1}{r}\right)\psi = E\psi, \quad (5.1)$$

with  $\Delta_3$  the Cartesian form of the Laplace operator. A regularization of the singular Coulomb potential is obtained by introducing Kustaanheimo-Stiefel (KS) coordinates  $\mathbf{u} = (u_1, u_2, u_3, u_4)$  [25, 26] which are introduced here, according to [56], differing by a factor of two as compared to the original definition

$$\begin{aligned} x_1 \equiv x &= u_1u_3 - u_2u_4, \\ x_2 \equiv y &= u_1u_4 + u_2u_3, \\ x_3 \equiv z &= \frac{1}{2}(u_1^2 + u_2^2 - u_3^2 - u_4^2). \end{aligned} \quad (5.2)$$

Introducing a fourth component  $x_4$  with the constant value zero to the physical position vector  $\mathbf{x} = (x_1, x_2, x_3, x_4)$  the transformation can be written in matrix notation

$$\mathbf{x} = L(\mathbf{u})\mathbf{u}, \quad (5.3)$$

with the matrix

$$L(\mathbf{u}) = \frac{1}{2} \begin{pmatrix} u_3 & -u_4 & u_1 & -u_2 \\ u_4 & u_3 & u_2 & u_1 \\ u_1 & u_2 & -u_3 & -u_4 \\ u_2 & -u_1 & -u_4 & u_3 \end{pmatrix}. \quad (5.4)$$

The introduction of the auxiliary degree of freedom, which makes the originally three-dimensional problem four-dimensional, implies a restriction on physically allowed wave functions  $\psi$ , i.e.

$$X\psi \equiv \left(u_2 \frac{\partial}{\partial u_1} - u_1 \frac{\partial}{\partial u_2} - u_4 \frac{\partial}{\partial u_3} + u_3 \frac{\partial}{\partial u_4}\right)\psi = 0. \quad (5.5)$$

With the definition in equation (5.2) it follows

$$2r = 2(x^2 + y^2 + z^2)^{1/2} = u_1^2 + u_2^2 + u_3^2 + u_4^2. \quad (5.6)$$

The Schrödinger equation (5.1) transformed in Kustaanheimo-Stiefel coordinates reads

$$\left(-\frac{1}{2\mathbf{u}^2}\Delta_4 - \frac{2}{\mathbf{u}^2}\right)\psi = E\psi, \quad (5.7)$$

with  $\Delta_4$  the four-dimensional Cartesian form of the Laplace operator. Multiplication with  $\mathbf{u}^2$  and reordering of the terms yields

$$H\psi = \left(-\frac{1}{2}\Delta_4 - E\mathbf{u}^2\right)\psi = 2\psi. \quad (5.8)$$



Equation (5.8) is not a standard linear eigenvalue problem. A scaling of the coordinates

$$\mathbf{u} \rightarrow \sqrt{n} \mathbf{u}, \quad H \rightarrow n H, \quad (5.9)$$

and setting

$$E = -\frac{1}{2n^2}, \quad (5.10)$$

leads to the time-independent Schrödinger equation

$$H\psi = \left( -\frac{1}{2}\Delta_4 + \frac{1}{2}\mathbf{u}^2 \right) \psi = 2n\psi, \quad (5.11)$$

which represents the Schrödinger equation of the four-dimensional harmonic oscillator with the restriction given in equation (5.5). The scaling parameter which takes only integer values  $n = 1, 2, 3, \dots$  turns out to be the principal quantum number of the hydrogen atom.

### 5.1.1. Eigenstates of the regularized hydrogen atom

The product of the four one-dimensional eigenstates of the four harmonic oscillators, i.e. the separation of eq. (5.11) in the Cartesian coordinates  $(u_1, u_2, u_3, u_4)$ , in general violates the restriction (5.5) and therefore presents unphysical solutions. The restriction in equation (5.5) rather suggests the introduction of two sets of polar coordinates, namely the semiparabolic coordinates

$$\begin{aligned} u_1 &= \mu \cos \varphi_\mu, & \text{and} & & u_3 &= \nu \cos \varphi_\nu, \\ u_2 &= \mu \sin \varphi_\mu, & & & u_4 &= \nu \sin \varphi_\nu, \end{aligned} \quad (5.12)$$

with the associated angular momenta ( $p_i = \frac{1}{i} \frac{\partial}{\partial u_i}$ )

$$\begin{aligned} L_\mu &= u_1 p_2 - u_2 p_1 = \frac{1}{i} \frac{\partial}{\partial \varphi_\mu}, \\ L_\nu &= u_3 p_4 - u_4 p_3 = \frac{1}{i} \frac{\partial}{\partial \varphi_\nu}, \end{aligned} \quad (5.13)$$

such that the restriction (5.5) can be written as

$$L_\mu = L_\nu \equiv L_z. \quad (5.14)$$

The connection between the physical Cartesian coordinates and the semiparabolic coordinates is obtained using the definitions (5.2) and (5.12)

$$\begin{aligned} x &= \mu\nu(\cos \varphi_\mu \cos \varphi_\nu - \sin \varphi_\mu \sin \varphi_\nu) = \mu\nu \cos(\varphi_\mu + \varphi_\nu) = \mu\nu \cos \varphi, \\ y &= \mu\nu(\cos \varphi_\mu \sin \varphi_\nu + \sin \varphi_\mu \cos \varphi_\nu) = \mu\nu \sin(\varphi_\mu + \varphi_\nu) = \mu\nu \sin \varphi, \\ z &= \frac{1}{2}(\mu^2 - \nu^2), \end{aligned} \quad (5.15)$$

with the physical azimuthal angle  $\varphi = \varphi_\mu + \varphi_\nu$ . In the semiparabolic coordinates the Schrödinger equation reads

$$\left[ -\frac{1}{2}\Delta_\mu - \frac{1}{2}\Delta_\nu + \frac{1}{2}(\mu^2 + \nu^2) \right] \psi = 2n \psi, \quad (5.16)$$

with

$$\Delta_\rho = \frac{1}{\rho} \frac{\partial}{\partial \rho} \rho \frac{\partial}{\partial \rho} + \frac{1}{\rho^2} \frac{\partial^2}{\partial \varphi_\rho^2}, \quad \rho = \mu, \nu. \quad (5.17)$$

The Schrödinger equation is separated in two 2D harmonic oscillators in the coordinates  $\mu, \varphi_\mu$  and  $\nu, \varphi_\nu$  respectively. The solution is the product wave function

$$\psi(\mu, \nu, \varphi) = \Phi_{N_\mu m}(\mu) \Phi_{N_\nu m}(\nu) e^{im\varphi} \quad (5.18)$$

where

$$\left[ -\frac{1}{2\rho} \frac{\partial}{\partial \rho} \rho \frac{\partial}{\partial \rho} + \frac{m^2}{2\rho^2} + \frac{1}{2}\rho^2 \right] \Phi_{N_\rho m}(\rho) = (2N_\rho + |m| + 1) \Phi_{N_\rho m}(\rho), \quad (5.19)$$

with  $\rho = \mu, \nu$  and  $N_\rho = 0, 1, 2, \dots$ . The coordinate representation of the eigenstates is

$$\Phi_{N_\rho m}(\rho) = \sqrt{\frac{N!}{\pi(N_\rho + |m|)}} \rho^{|m|} L_{N_\rho}^{|m|}(\rho^2) e^{-\frac{1}{2}\rho^2}, \quad (5.20)$$

with the associated Laguerre polynomials  $L_{N_\rho}^{|m|}$ . For the principal quantum number  $n$  introduced above we obtain the relation

$$n = N_\mu + N_\nu + |m| + 1 = 1, 2, 3, \dots, \quad (5.21)$$

and therefore via equation (5.10) the correct Rydberg spectrum.

To perform time-dependent computations it is necessary to formulate the time-dependent version of the Schrödinger equation (5.11). In analogy to the usual identification  $E \rightarrow i \frac{\partial}{\partial t}$  where  $t$  is the physical time, the “fictitious time” variable  $\tau$  is introduced, c.f. [56, 58] as the conjugate variable to the principal quantum number  $n$

$$2n \rightarrow i \frac{\partial}{\partial \tau}. \quad (5.22)$$

The regularized Schrödinger equation for the hydrogen atom in the fictitious time then reads

$$i \frac{\partial}{\partial \tau} \psi = H \psi. \quad (5.23)$$

In this chapter and in chapter 6 the fictitious time  $\tau$  will simply be denoted by the term time for brevity. The real time  $t$  will be named physical time.

In Kustaanheimo-Stiefel coordinates the restriction (5.5) on physically allowed wave functions must explicitly be accounted for when the Hamiltonian (5.11) in KS coordinates

is used. On the other hand, the KS coordinates are of Cartesian form and therefore are especially suitable for a Gaussian ansatz of the form (3.1). They are the exact solutions of the field-free hydrogen atom (5.11), provided the restriction is fulfilled. The question is about the impact of the restriction on a GWP trial function. Can the restriction be exactly fulfilled by a Gaussian in the first place, and in case, are those GWPs fulfilling the restriction reasonable trial functions in the sense that they still present a complete basis set? The advantage of the formulation of the Hamiltonian in semiparabolic coordinates (5.16) is that the restriction (5.5) is already incorporated. The semiparabolic coordinates bear the difficulty to find trial functions for the exact solution of the time-dependent Schrödinger equation, which have not the simple Gaussian form. The reason is that although the potential is harmonic, the Laplace operator is not of Cartesian form, c.f. (5.17), but rather has radial character.

We now turn to the investigation of the impact of the restriction (5.5) on a Gaussian trial function and discuss the properties of the resulting restricted GWP.

## 5.2. Restricted Gaussian wave packets in Kustaanheimo-Stiefel coordinates

The regularization of the hydrogen atom in section 5.1 has transformed the Coulomb potential to a harmonic potential in the Schrödinger equation (5.11). The aim is now to find exact wave packet propagation in the fictitious time  $\tau$  for the hydrogen atom. The choice of GWPs as trial functions is especially suitable, since they present exact solutions of harmonic oscillators, however, the restriction (5.5) on physically allowed wave functions must be fulfilled. We therefore must investigate the impact of the restriction (5.5) on a 4D Gaussian wave packet in Kustaanheimo-Stiefel coordinates. Consider the Gaussian ansatz (3.1) in KS coordinates  $\mathbf{u}$

$$g(\mathbf{y}, \mathbf{u}) = e^{i((\mathbf{u}-\mathbf{q})A(\mathbf{u}-\mathbf{q})+\boldsymbol{\pi}\cdot(\mathbf{u}-\mathbf{q})+\gamma)}, \quad (5.24)$$

where, in general,  $A$  is a complex symmetric  $4 \times 4$  matrix and the momentum  $\boldsymbol{\pi}$  and center  $\mathbf{q}$  are real, 4-dimensional vectors in the Kustaanheimo-Stiefel coordinates, representing the expectation values of the position and the momentum operator, respectively, i.e.  $\mathbf{q} = \langle g|\mathbf{u}|g \rangle$  and  $\boldsymbol{\pi} = \langle g|\frac{1}{i}\nabla_4|g \rangle$ . The phase and normalization is given by the complex scalar  $\gamma$ . Collectively the parameters are denoted by  $\mathbf{y} = (A, \boldsymbol{\pi}, \mathbf{q}, \gamma)$ . The Gaussian wave packet (5.24) in general does not obey the restriction (5.5) on physical wave functions, i.e. the use of these 4D GWPs as trial functions would lead to unphysical results. However it is shown now that the restriction can be fulfilled by a 4D GWP if the space of admissible configurations of the parameters  $\mathbf{y}$  is confined. Consider the structure matrix

$$J = \begin{pmatrix} 0 & 1 & 0 & 0 \\ -1 & 0 & 0 & 0 \\ 0 & 0 & 0 & -1 \\ 0 & 0 & 1 & 0 \end{pmatrix}, \quad (5.25)$$

which allows for the compact notation of the restriction (5.5)

$$X\psi = \mathbf{u}J^T\nabla_4\psi = 0. \quad (5.26)$$

The application of the constraint operator  $X$  on the trial function (5.24) yields

$$Xg(\mathbf{y}, \mathbf{u}) = \mathbf{u}J^T(2A(\mathbf{u} - \mathbf{q}) + \boldsymbol{\pi})g(\mathbf{y}, \mathbf{u}) \stackrel{!}{=} 0. \quad (5.27)$$

The result is a quadratic polynomial in the coordinates  $\mathbf{u}$  times the GWP itself. The restriction (5.27) should be satisfied pointwise for all  $\mathbf{u} \in \mathbb{R}^4$ . For nontrivial wave packets the polynomial in (5.27) must vanish and an algebraic equation is left,

$$2\mathbf{u}J^T A\mathbf{u} + \mathbf{u}J^T(\boldsymbol{\pi} - 2A\mathbf{q}) \stackrel{!}{=} 0. \quad (5.28)$$

This is only possible if all coefficients of the second order polynomial in (5.28) are zero. Let us first investigate the linear term whose coefficients must vanish, i.e.

$$J^T(\boldsymbol{\pi} - 2A\mathbf{q}) = 0. \quad (5.29)$$

For the wave function to be normalizable it is necessary that the imaginary part of the symmetric matrix  $A$  is non zero, especially it must be positive definite. According to their definition the expectation values  $\boldsymbol{\pi}$  and  $\mathbf{q}$  must be real and therefore (5.29) only holds if

$$\mathbf{q} = 0, \quad \text{and} \quad \boldsymbol{\pi} = 0. \quad (5.30)$$

For the restriction (5.27) to be exactly fulfilled also the bilinear form in (5.28) must be zero, i.e.

$$2\mathbf{u}J^T A\mathbf{u} = 0. \quad (5.31)$$

This is exactly the case when the matrix of the bilinear form  $J^T A$  is skew symmetric, i.e.  $J^T A = -(J^T A)^T = -AJ$ . Explicitly the matrix reads

$$J^T A = \begin{pmatrix} 0 & -1 & 0 & 0 \\ 1 & 0 & 0 & 0 \\ 0 & 0 & 0 & 1 \\ 0 & 0 & -1 & 0 \end{pmatrix} \cdot \begin{pmatrix} a_{11} & a_{12} & a_{13} & a_{14} \\ a_{12} & a_{22} & a_{23} & a_{24} \\ a_{13} & a_{23} & a_{33} & a_{34} \\ a_{14} & a_{24} & a_{34} & a_{44} \end{pmatrix} = \begin{pmatrix} -a_{12} & -a_{22} & -a_{23} & -a_{24} \\ a_{11} & a_{12} & a_{13} & a_{14} \\ a_{14} & a_{24} & a_{34} & a_{44} \\ -a_{13} & -a_{23} & -a_{33} & -a_{34} \end{pmatrix}.$$

For the matrix  $J^T A$  to be skew symmetric  $A$  must have the following symmetries. The diagonal elements of  $J^T A$  must vanish,

$$a_{12} = a_{34} = 0, \quad (5.32)$$

and from the off diagonal elements we obtain

$$a_{11} = a_{22}, \quad a_{33} = a_{44}, \quad a_{24} = -a_{13}, \quad a_{23} = a_{14}. \quad (5.33)$$

Obviously, only four parameters are left. Thus the overall number of parameters has reduced from originally  $4 \times (4 + 1)/2 + 4 + 1 = 15$  complex parameters of the general GWP in four dimensions (where the variational freedom of the two real vectors  $\mathbf{q}, \boldsymbol{\pi}$  is understood as a single complex vector, in the spirit of eq. (3.25)) to only 5 independent parameters of the GWP

$$g(\mathbf{y}, \mathbf{u}) = e^{i(\mathbf{u}A\mathbf{u}+\gamma)} \quad (5.34)$$

satisfying the restriction (5.27). With the definitions  $a_{11} = a_\mu$ ,  $a_{33} = a_\nu$ ,  $a_{13} = a_x$ ,  $a_{14} = a_y$ , in matrix notation  $A$  reads

$$A = \begin{pmatrix} a_\mu & 0 & a_x & a_y \\ 0 & a_\mu & a_y & -a_x \\ a_x & a_y & a_\nu & 0 \\ a_y & -a_x & 0 & a_\nu \end{pmatrix}. \quad (5.35)$$

The question arises whether the restricted GWPs form a complete basis set, such that any physically allowed state can be expanded in this basis. Indeed it is not obvious whether a superposition of restricted GWPs (5.34) whose centers are all located at the origin and only differ by their complex widths, is flexible enough to represent arbitrary quantum states. The usual form of the resolution of the identity [62] for a continuous basis set of normalized, unrestricted GWPs of the form (5.24) is

$$\mathbf{1} = \frac{1}{(2\pi)^4} \int d\pi^4 dq^4 |g(\mathbf{y})\rangle \langle g(\mathbf{y})|, \quad (5.36)$$

where the width of each GWP basis state is kept fixed. Anyway, this formula is not applicable to the restricted GWPs (5.34), since both parameters  $\boldsymbol{\pi}$  and  $\mathbf{q}$  do not run from minus to plus infinity but must be set to zero according to the restriction and the only freedom we have in the restricted GWP (5.34) is to vary the 5 independent parameters in the width matrix  $A$  (5.35). However, it must be kept in mind, that it is sufficient to require the restricted GWPs to be complete in the three-dimensional physical space only. It is not necessary that any (possibly unphysical) wave function in the four-dimensional KS space is expandable in the restricted GWP basis. To clarify this question it is advantageous to transform the restricted GWP in KS coordinates into Cartesian coordinates of the 3D space

$$g(\mathbf{y}, \mathbf{x}) = e^{i(\mathbf{u}A\mathbf{u}+\gamma)} \quad (5.37a)$$

$$= e^{i(a_\mu(u_1^2+u_2^2)+a_\nu(u_1^2-u_2^2)+2a_x(u_1u_3-u_2u_4)+2a_y(u_1u_4+u_2u_3)+\gamma)} \quad (5.37b)$$

$$= e^{i(a_\mu\mu^2+a_\nu\nu^2+2a_x x+2a_y y+\gamma)} \quad (5.37c)$$

$$= e^{i(a_\mu(r+z)+a_\nu(r-z)+2a_x x+2a_y y+\gamma)} \quad (5.37d)$$

$$= e^{i((a_\mu+a_\nu)r+(a_\mu-a_\nu)z+2a_x x+2a_y y+\gamma)} \quad (5.37e)$$

$$= e^{i(p_r r + \mathbf{p} \cdot \mathbf{x} + \gamma)}, \quad (5.37f)$$

with the semiparabolic coordinates  $\mu^2 = r+z$ ,  $\nu^2 = r-z$ . In (5.37f) the set of parameters  $(a_\mu, a_\nu, a_x, a_y)$  is replaced by an equivalent set of parameters, viz.

$$\begin{aligned} p_x &= 2a_x, \\ p_y &= 2a_y, \\ p_z &= a_\mu - a_\nu, \\ p_r &= a_\mu + a_\nu, \end{aligned} \tag{5.38}$$

and the three complex Gaussian parameters  $p_x, p_y, p_z$  are summarized in the complex vector  $\mathbf{p} = (p_x, p_y, p_z)$ . As a side note, it is mentioned that the matrix  $A$  can be written as a superposition of Dirac matrices  $\alpha^i$ ,  $i = x, y, z$  and  $\beta$  in standard notation [63] by  $A = p_r \mathbf{1} + p_z \beta + p_y \alpha^x + p_x \alpha^z$ . For normalization it is necessary that  $\text{Im } p_r > 0$ , yielding an exponential damping for  $r \rightarrow \infty$ . Choosing  $p_r = i\epsilon$  the restricted GWP in Cartesian coordinates (5.37f) reduces to a plane wave  $e^{i\mathbf{p}\cdot\mathbf{x}}$  if the Gaussian parameters  $p_x, p_y, p_z$  are chosen real valued in the limit  $\epsilon \rightarrow 0$ . Since plane waves  $e^{i\mathbf{p}\cdot\mathbf{x}}$  are known to form a complete basis it can be concluded that the restricted GWP (5.37f), forming a superset of plane waves, are also complete or even over-complete. However, they are not complete with respect to the expansion of unphysical functions in the four-dimensional KS space.

The GWP (5.37) has been constructed to satisfy the restriction (5.5). Furthermore the set of restricted GWPs has been argued to be complete and any physical wave function is expandable in the basis set. Their time evolution, contained in the time-dependent parameters, is an exact solution of the time-dependent Schrödinger equation (5.11), and can even be determined analytically, as shown below. These features make the restricted GWP basis particularly convenient for the propagation of states in the regularized hydrogen atom. The scope of the next section is the expansion and exact time evolution of wave functions in the basis (5.37), and in addition, in modified bases sets for certain symmetry subspaces of the hydrogen atom.

### 5.3. Analytical wave packet dynamics in the hydrogen atom

For the expansion of arbitrary states without any well defined angular momentum quantum number  $l$  or  $m$ , the basis states (5.37) are employed. Their analytic, exact dynamics followed by a description of the expansion of arbitrary wave functions in the restricted GWP basis, and example calculations are presented in subsection 5.3.1. Analogous results are shown in subsection 5.3.2 for wave packets with well defined magnetic quantum number  $m$ , and in subsection 5.3.3 for radial wave packets with well defined quantum numbers  $l, m$ .

### 5.3.1. Propagation of wave packets without well defined angular momentum

The aim is an exact time propagation of arbitrary wave functions in the H atom. The initial wave function  $\psi(0)$  is expanded as a superposition of the restricted GWPs (5.37). These basis states are then propagated analytically in time. We start with the time evolution of the basis states. For the restricted GWPs (5.37) the dynamics can be calculated analytically as will be shown now. The equations of motion for the  $4 \times 4$  width matrix  $A$  and the complex phase factor  $\gamma$  are given by (3.30). Taking into account that the linear terms in the exponent of the restricted GWP (5.37a) vanish, i.e.  $\boldsymbol{\pi} = \mathbf{q} = 0$ , the linear potential coefficients  $\mathbf{v}_1$  must also vanish due to their definition in eq. (3.9). The equations of motion (3.30) thus reduce to

$$\dot{A} = -2A^2 - \frac{1}{2}V_2, \quad (5.39a)$$

$$\dot{\gamma} = i \operatorname{tr} A - v_0. \quad (5.39b)$$

In the absence of external fields the GWP method yields exact results since the potential of the Schrödinger equation (5.11) is harmonic. The coefficients  $v_0, V_2$  of the effective potential need not be determined by solving a matrix equation as prescribed by the TDVP, but can be directly read from the potential in the Hamiltonian (5.11)  $V(\mathbf{u}) = (u_1^2 + u_2^2 + u_3^2 + u_4^2)/2$  to be

$$v_0 = 0, \quad \mathbf{v}_1 = 0, \quad V_2 = \mathbf{1}. \quad (5.40)$$

Both equations (5.39) can be solved analytically. Most easily equation (5.39a) is solved when introducing two auxiliary complex matrices  $B, C$  according to  $A = \frac{1}{2}BC^{-1}$ , c.f. eq. (3.31), with the initial condition  $B(0) = 2A(0)$ , and  $C(0) = \mathbf{1}$ . Then (5.39a) is replaced by the two equations  $\dot{C} = B$  and  $\dot{B} = -C$  or equivalently  $\ddot{B} = -B$ . Due to the diagonal form of  $V_2$ , the matrices  $B$  and  $C$  have the same structure as the width matrix  $A$  (5.35), with the solution for the matrix  $B$

$$\begin{aligned} b_\mu(\tau) &= 2a_\mu(0) \cos \tau - \sin \tau, \\ b_\nu(\tau) &= 2a_\nu(0) \cos \tau - \sin \tau, \\ b_x(\tau) &= 2a_x(0) \cos \tau, \\ b_y(\tau) &= 2a_y(0) \cos \tau, \end{aligned} \quad (5.41)$$

and for the matrix  $C$

$$\begin{aligned} c_\mu(\tau) &= \cos \tau + 2a_\mu(0) \sin \tau, \\ c_\nu(\tau) &= \cos \tau + 2a_\nu(0) \sin \tau, \\ c_x(\tau) &= 2a_x(0) \sin \tau, \\ c_y(\tau) &= 2a_y(0) \sin \tau. \end{aligned} \quad (5.42)$$

The matrix  $A$  is obtained from the above definition  $A = \frac{1}{2}BC^{-1}$  and the four elements in the form of eq. (5.38) read

$$\begin{aligned} p_r(\tau) &= \frac{p_r(0) \cos 2\tau + \frac{1}{2} ((p_r(0))^2 - (p(0))^2 - 1) \sin 2\tau}{Z(\tau)}, \\ p_x(\tau) &= \frac{p_x(0)}{Z(\tau)}, \\ p_y(\tau) &= \frac{p_y(0)}{Z(\tau)}, \\ p_z(\tau) &= \frac{p_z(0)}{Z(\tau)}, \end{aligned} \quad (5.43)$$

where  $p = |\mathbf{p}|$  and  $Z(\tau)$  abbreviates the expression

$$Z(\tau) = \cos^2 \tau + ((p_r(0))^2 - (p(0))^2) \sin^2 \tau + p_r(0) \sin 2\tau. \quad (5.44)$$

With the matrix  $A$  at hand it is possible to solve the integral (5.39b) for  $\gamma$ . The phase and normalization of the wave function  $e^{-i\gamma}$  with the initial value  $\gamma(0) = 0$  reads

$$\begin{aligned} \mathcal{N}(\tau) \equiv e^{-i\gamma(\tau)} &= \frac{1}{2} ((p_r(0))^2 - (p(0))^2 + 1) \\ &+ \frac{1}{2} [((p(0))^2 - (p_r(0))^2 + 1) \cos 2\tau + 2p_r(0) \sin 2\tau]. \end{aligned} \quad (5.45)$$

A time-independent factor is introduced for normalization of the wave packet to unity, i.e.

$$\mathcal{N}_0 = \frac{\pi}{2\sqrt{\text{Im}a_\mu(0)\text{Im}a_\nu(0) - (\text{Im}a_x(0))^2 - (\text{Im}a_y(0))^2}}. \quad (5.46)$$

The analytic time evolution of the wave function is obtained by inserting the time-dependent parameters in the wave function (5.37f) which finally reads

$$\begin{aligned} g(\tau, \mathbf{y}(0), \mathbf{x}) &= \frac{1}{\mathcal{N}(\tau)\mathcal{N}_0} \\ &\times \exp \left[ \frac{i(2(\mathbf{p}(0) \cdot \mathbf{x} + p_r(0)r \cos 2\tau) + ((p_r(0))^2 - (p(0))^2 - 1)r \sin 2\tau)}{2\mathcal{N}(\tau)} \right]. \end{aligned} \quad (5.47)$$

This is an important intermediate result. The time evolution of a restricted GWP (5.37f) is analytically computed and takes the compact form (5.47). The parameters in eqs. (5.43) and (5.45) are periodic functions of the time  $\tau$  with period  $\pi$ . The periodicity carries over to the  $\pi$ -periodic wave function (5.47). In the physical time wave packets disperse in the hydrogen atom [64]. By contrast, the wave packets in the fictitious time show an oscillating behavior with no long time dispersion in  $\tau$ .

Now that the time evolution of basis states is known we want to expand arbitrary functions in the basis states (5.37f). The time evolution of arbitrary states is then analytically given by the superposition of the time-dependent restricted GWPs  $g(\tau, \mathbf{y}(0), \mathbf{x})$



(5.47). Particularly we are interested in the expansion of states localized around a given point  $\mathbf{x}_0, \mathbf{p}_0$  in the physical position and momentum space, respectively. An arbitrary function  $\psi(\mathbf{x})$  is written as a superposition of wave packets of the form (5.37f)

$$\psi(\mathbf{x}) = \sum_{k=1}^N g(\mathbf{y}^k, \mathbf{x}) \equiv \sum_{k=1}^N e^{i(a_\mu^k \mu^2 + a_\nu^k \nu^2 + a_x^k x + a_y^k y + \gamma^k)} \equiv \sum_{k=1}^N e^{i(p_r^k r + \mathbf{p}^k \cdot \mathbf{x} + \gamma^k)}, \quad (5.48)$$

where the two sets of parameters  $\mathbf{y}^k = (a_\mu^k, a_\nu^k, a_x^k, a_y^k, \gamma^k)$  and  $\mathbf{y}^k = (p_r^k, \mathbf{p}^k, \gamma^k)$  as introduced in section 5.2 are equivalent. The index  $k$  runs over all wave packets, and  $N$  is the number of employed basis functions. In general the number  $N$  of packets required for an exact expansion is infinite. However, for numerical computations it will in general be sufficient to use a finite number of basis functions to obtain converged results.

A procedure for finding the “optimal” expansion for a given number  $N$  of basis states is to minimize the deviation

$$\Delta = \|\psi(\mathbf{x}) - \sum_{k=1}^N g(\mathbf{y}^k, \mathbf{x})\|^2 \stackrel{!}{=} \min. \quad (5.49)$$

with respect to the parameters  $\mathbf{y}^k$ ,  $k = 1, \dots, N$  [9]. This is a nontrivial task. Equation (5.49) presents a highly nonlinear minimization problem which is solved by searching for stationary points  $\frac{\partial \Delta}{\partial \mathbf{y}^k} = 0$ ,  $k = 1, \dots, N$ . In general many stationary points exist. The stationary point found by a standard minimization routine like the conjugate gradients method, depends on the initial choice of the parameters. For different starting points different stationary points may be found. Comparison yields the best approximation, i.e. hopefully the global minimum. Alternatively a method which is supposed to find the global minimum directly could be applied. These simulated annealing methods combine a random walk and a standard minimum search [65].

Here an alternative and more direct approach based on a Fourier transform is chosen. The restricted GWPs (5.37f) contain plane waves for real  $\mathbf{p}^k \in \mathbb{R}^3$  and  $p_r^k = i\epsilon$  with an infinitely small but positive  $\epsilon$ . Now, the procedure is the following. The initial state  $\psi(\mathbf{x})$  to be expanded is Fourier transformed into momentum space. The Fourier transformed state

$$\tilde{\psi}(\mathbf{p}) = (2\pi)^{-3/2} \int d^3x \psi(\mathbf{x}) e^{-i\mathbf{p} \cdot \mathbf{x}} \quad (5.50)$$

provides the weights and relative phases of the superposition of plane waves contributing to the desired state. The inverse Fourier transform recovers the original state in position space representation

$$\psi(\mathbf{x}) = (2\pi)^{-3/2} \int d^3p \tilde{\psi}(\mathbf{p}) e^{i\mathbf{p} \cdot \mathbf{x}}. \quad (5.51)$$

However, a finite number of restricted 4D GWPs is desired for the expansion and propagation. The backward Fourier integral (5.51) is therefore discretized and approximated

by a finite sum

$$\psi(\mathbf{x}) \approx (2\pi)^{-3/2} \sum_{k=1}^N (\Delta p)_k^3 \tilde{\psi}(\mathbf{p}^k) e^{i\mathbf{p}^k \cdot \mathbf{x}}. \quad (5.52)$$

Comparison of the right hand sides of eqs. (5.48) and (5.52) yields the complex Gaussian parameters  $\mathbf{p}^k$  as the (real valued) sampling points of a numerical integration in equation (5.52). The inverse Fourier transform (5.51) presents a three-dimensional integration and a Monte Carlo technique appears to be convenient. In principle other numerical integration algorithms might be possible. The comparison implies  $p_r^k = 0$  which is not allowed for normalized states. The damping parameters  $p_r^k$  which guarantee normalized basis states must be chosen with a positive imaginary part. A common damping parameter  $p_r^k = i\epsilon$ ,  $k = 1, \dots, N$  is suggested for all basis states and the value of  $\epsilon$  is small but positive and depends on the desired accuracy of the expansion. For convergence it must be chosen small enough that  $e^{ip_r r} \approx 1$  in the region where the wave function to be expanded differs significantly from zero. The complete information of the expanded state  $\psi(\mathbf{x})$  is contained in the phases  $\gamma^k$  and is obtained to be

$$(2\pi)^{-3/2} (\Delta p)_k^3 \tilde{\psi}_{\mathbf{x}_0 \mathbf{p}_0}(\mathbf{p}^k) \stackrel{!}{=} e^{i\gamma^k} \quad (5.53)$$

Note that in the limit  $\epsilon \rightarrow 0$ ,  $N \rightarrow \infty$  the expansion is exact. The presented procedure allows for an expansion of arbitrary states in the basis functions (5.37f). A localization of  $\psi(\mathbf{x})$  at  $\mathbf{x}_0$ ,  $\mathbf{p}_0$  away from the origin presents no difficulty.

A natural choice of a wave packet with localization  $\mathbf{x}_0$ ,  $\mathbf{p}_0$  in position and momentum space is a Gaussian wave packet. The Fourier transformation can be performed analytically and a Monte Carlo technique, with Gaussian, randomly distributed sampling points is especially suitable for the inverse Fourier transform. The normalized Gaussian wave packet reads

$$\psi_{\mathbf{x}_0 \mathbf{p}_0}(\mathbf{x}) = (2\pi\sigma^2)^{-3/4} e^{-\frac{1}{4\sigma^2}(\mathbf{x}-\mathbf{x}_0)^2 + i\mathbf{p}_0 \cdot (\mathbf{x}-\mathbf{x}_0)} \quad (5.54)$$

with the center  $\mathbf{x}_0$  and momentum  $\mathbf{p}_0$  (not to be mixed up with the parameters  $\mathbf{p}^k$  of the basis states (5.48)) and the width  $\sigma$  in the basis of (5.48). The Fourier transform into momentum space is performed analytically and yields

$$\tilde{\psi}_{\mathbf{x}_0 \mathbf{p}_0}(\mathbf{p}) = \left( \frac{2\sigma^2}{\pi} \right)^{3/4} e^{-\sigma^2(\mathbf{p}-\mathbf{p}_0)^2 - i\mathbf{x}_0 \cdot \mathbf{p}}. \quad (5.55)$$

For fast convergence of the inverse Fourier integral a normalized Gaussian weighting function

$$w(\mathbf{p}) = \frac{\sigma}{\sqrt{\pi}} e^{-\sigma^2(\mathbf{p}-\mathbf{p}_0)^2}, \quad (5.56)$$

for the Monte Carlo integration (5.52) is introduced. The weighting function has the same width as the wave packet in momentum space and the sampling points  $\mathbf{p}^k$  of the

numerical integration are distributed according to (5.56). We obtain

$$\psi_{\mathbf{x}_0\mathbf{p}_0}(\mathbf{x}) = (2\pi\sigma^2)^{-3/4} \frac{1}{N} \sum_{k=1}^N e^{i(\mathbf{x}-\mathbf{x}_0)\cdot\mathbf{p}^k}, \quad (5.57)$$

and

$$\gamma^k = -i \log \left[ \frac{(2\pi\sigma^2)^{-3/4}}{N} \right] - \mathbf{x}_0 \cdot \mathbf{p}^k. \quad (5.58)$$

The final result of this subsection is thus

$$\psi(\tau, \mathbf{x}) = \mathcal{N}_0 \sum_{k=1}^N g(\tau, \mathbf{y}^k(0), \mathbf{x}) e^{i\gamma^k}, \quad (5.59)$$

where  $\mathbf{y}^k(0) = (p_r^k, \mathbf{p}^k, 0)$  with the Gaussian distributed  $\mathbf{p}^k$  according to (5.56) and the  $\gamma^k$  are given by eq. (5.58). For higher accuracy of the expansion of the GWP (5.54) in the basis states (5.37f) it is possible to Fourier transform rather  $\psi_{\mathbf{x}_0, \mathbf{p}_0}(\mathbf{x})e^{\epsilon r}$  than  $\psi_{\mathbf{x}_0, \mathbf{p}_0}(\mathbf{x})$  itself. For analytical integrability the exponential  $\epsilon r$  is expanded in a Taylor series around the center  $\mathbf{x}_0$  of the GWP, i.e.  $\epsilon r = \epsilon(|\mathbf{x}_0| + \frac{\mathbf{x}_0}{|\mathbf{x}_0|} \cdot (\mathbf{x} - \mathbf{x}_0)) + O(\mathbf{x}^2)$ .

In fig. 5.1 an initially Gaussian wave packet (5.54) expanded and propagated analytically in a basis of  $N = 10000$  restricted GWP basis states is plotted. The basis states are propagated according to eq. (5.47), without the normalization factor  $\mathcal{N}_0$  but instead multiplied by a factor  $e^{i\gamma^k}$  with the initial values of  $\gamma^k$  given by eq. (5.58), which guarantees normalization of the total wave packet. The probability density in the  $z = 0$  plane is plotted at equidistant times with step size  $\Delta\tau = \pi/5$ . The initial GWP presented in fig. 5.1 for  $\tau = 0$  is centered at  $\mathbf{x}_0 = (8, 0, 0)$  with the mean momentum  $\mathbf{p}_0 = (1, 2, 0)$ . The damping factor is set to  $\epsilon = 0.01$ . Classically the electron with these initial conditions is running on the ellipse plotted by dots on the bottom of each panel in fig. 5.1. For every time step, that part of the ellipse that has been passed by the electron so far is shown by a black solid line for time resolved comparison. The position of the maximum of the probability density agrees well with the classical position of the electron on the ellipse for all times. The  $\pi$ -periodicity of the motion is reflected by the coincidence of the wave packet after one period at  $\tau = \pi$  with the initial GWP at  $\tau = 0$ .

### 5.3.2. Propagation of wave packets with conserved angular momentum component $l_z$

In this subsection basis functions based on the restricted GWP (5.37c) with a well defined angular momentum component  $l_z = m$  are presented. This case is especially important in view of chapter 6.2, where an external magnetic field applied to the H atom is considered, since the rotational symmetry is maintained. First wave packets with definite  $l_z$  are constructed and their exact, analytic dynamics in the H atom is

## 5. Wave packet dynamics in the hydrogen atom

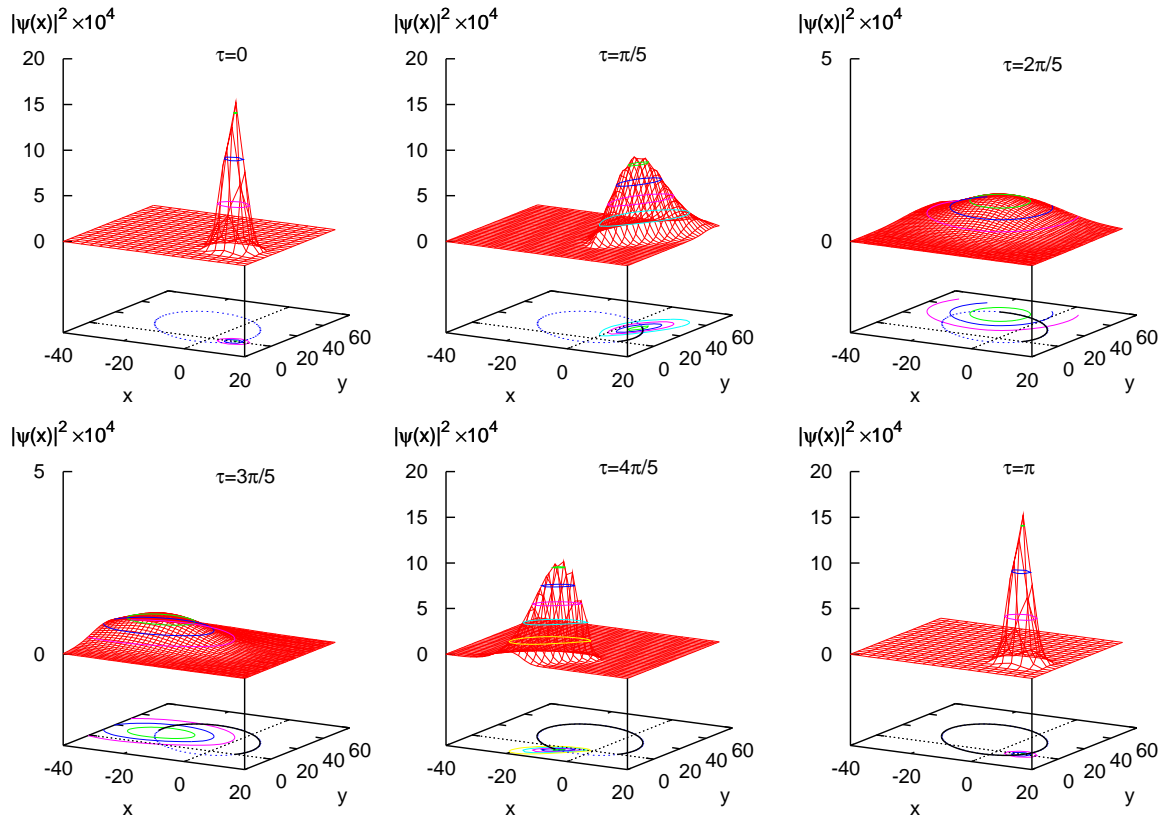


Figure 5.1.: Propagation of the initially Gaussian wave packet (5.54) located at  $\mathbf{x}_0 = (8, 0, 0)$  with the momentum  $\mathbf{p}_0 = (1, 2, 0)$  plotted in the plane  $z = 0$ . The classical Kepler ellipse with the same initial conditions is plotted by a dotted line on the bottom of each panel. For time resolved comparison, that part of the ellipse that has been traversed by the particle so far in each plot is shown by a solid black line. Although the Gaussian wave packet does not stay Gaussian during the period it follows in general the classical path and is recovered after one period  $\tau = \pi$ , indicating the periodicity of the wave packet.

discussed. Then we introduce a procedure to expand quantum states of defined  $l_z$  in the basis states.

A rotationally symmetric restricted GWP (5.37) is obtained by setting  $2a_x \equiv p_x = 2a_y \equiv p_y = 0$  in (5.37c), i.e.

$$g_0(\mathbf{y}, \mathbf{x}) = e^{i(a_\mu \mu^2 + a_\nu \nu^2 + \gamma)} = e^{i(p_r r + p_z z + \gamma)}. \quad (5.60)$$

These states are symmetric with the quantum number  $m = 0$ , but can be generalized to arbitrary  $m$  by

$$g_m(\mathbf{y}, \mathbf{x}) = (\mu\nu)^{|m|} e^{i(a_\mu \mu^2 + a_\nu \nu^2 + \gamma)} e^{im\varphi} = \rho^{|m|} e^{i(p_r r + p_z z + \gamma)} e^{im\varphi}. \quad (5.61)$$

The time-dependent parameters are  $\mathbf{y} = (a_\mu, a_\nu, \gamma)$ . The quantum number  $m$  is constant. As will be shown, the wave packet (5.61) still presents an exact solution to the regularized Schrödinger equation. The Laplace operator in semiparabolic coordinates (5.19) and the time derivative applied to the wave packet (5.61) read

$$\begin{aligned} \Delta g_m(\mathbf{y}, \mathbf{x}) &= [4i(a_\mu + a_\nu)(1 + |m|) - 4a_\mu^2 \mu^2 - 4a_\nu^2 \nu^2] g_m(\mathbf{y}, \mathbf{x}), \\ i \frac{\partial}{\partial \tau} g_m(\mathbf{y}, \mathbf{x}) &= (-\dot{a}_\mu \mu^2 - \dot{a}_\nu \nu^2 - \dot{\gamma}) g_m(\mathbf{y}, \mathbf{x}), \end{aligned} \quad (5.62)$$

and thus the Schrödinger equation (5.16) yields

$$\begin{aligned} 0 &= \frac{(-i \frac{\partial}{\partial \tau} + H) g_m(\mathbf{y}, \mathbf{x})}{g_m(\mathbf{y}, \mathbf{x})} \\ &= \dot{a}_\mu \mu^2 + \dot{a}_\nu \nu^2 + \dot{\gamma} - [2i(a_\mu + a_\nu)(1 + |m|) - 2a_\mu^2 \mu^2 - 2a_\nu^2 \nu^2] + \frac{1}{2}(\mu^2 + \nu^2). \end{aligned}$$

This equation is exactly solved if the Gaussian parameters obey the equations of motion

$$\dot{a}_\mu = -2a_\mu^2 - \frac{1}{2}V_\mu, \quad (5.63a)$$

$$\dot{a}_\nu = -2a_\nu^2 - \frac{1}{2}V_\nu, \quad (5.63b)$$

$$\dot{\gamma} = 2i(a_\mu + a_\nu)(1 + |m|) - v_0, \quad (5.63c)$$

or using the matrix notation (5.35) for  $A$  (with  $a_x = a_y = 0$ )

$$\dot{A} = -2A^2 - \frac{1}{2}V_2, \quad (5.64a)$$

$$\dot{\gamma} = i \operatorname{tr} A (1 + |m|) - v_0, \quad (5.64b)$$

with  $v_0 = 0$ ,  $V_\mu = 1$ ,  $V_\nu = 1$  and  $V_2 = \mathbf{1}$ . The equations of motion for the two remaining complex width parameters  $a_\mu$  and  $a_\nu$  stay completely unchanged as compared

to the restricted GWP in subsection 5.3.1. The only change is the additional factor of  $(1 + |m|)$  in equation (5.64b) for the phase parameter  $\gamma$ . The solution of the equations (5.64a) is

$$\begin{aligned} a_\mu(\tau) &= \frac{2(a_\mu(0) - a_\nu(0)) + 2(a_\mu(0) + a_\nu(0)) \cos(2\tau) - (1 - 4a_\mu(0)a_\nu(0)) \sin(2\tau)}{Z(\tau)}, \\ a_\nu(\tau) &= \frac{2(a_\nu(0) - a_\mu(0)) + 2(a_\mu(0) + a_\nu(0)) \cos(2\tau) - (1 - 4a_\mu(0)a_\nu(0)) \sin(2\tau)}{Z(\tau)}, \end{aligned}$$

with

$$Z(\tau) = 2 [1 + 4a_\mu(0)a_\nu(0) + (1 - 4a_\mu(0)a_\nu(0)) \cos(2\tau) + 2(a_\mu(0) + a_\nu(0)) \sin(2\tau)].$$

The solution of eq. (5.64b) is  $(1 + |m|)$  times the solution of eq. (5.39b) and the phase and normalization of the wave function  $\mathcal{N}_m(\tau) = e^{-i\gamma}$  with  $\gamma(0) = 0$  reads

$$\begin{aligned} \mathcal{N}_m(\tau) &\equiv e^{-i\gamma(\tau)} \\ &= \left\{ \frac{1 + 4a_\mu(0)a_\nu(0) + (1 + 4a_\mu(0)a_\mu(0)) \cos(2\tau) + 2(a_\mu(0) + a_\nu(0)) \sin(2\tau)}{2} \right\}^{|m|+1}. \end{aligned} \quad (5.65)$$

The norm of the wave function (5.61) at  $\tau = 0$  with  $\gamma(0) = 0$  is

$$\mathcal{N}_m(0) = \frac{\pi m!}{\left(2\sqrt{\text{Im } a_\mu(0)\text{Im } a_\nu(0)}\right)^{|m|+1}}, \quad (5.66)$$

and the time evolution of the normalized wave packet (5.61) is

$$g_m(\tau, \mathbf{y}(0), \mu, \nu) = \frac{1}{\mathcal{N}_m(\tau)\mathcal{N}_m(0)} (\mu\nu)^{|m|} e^{i(a_\mu(\tau)\mu^2 + a_\nu(\tau)\nu^2)} e^{im\varphi}. \quad (5.67)$$

The time evolution of the basis states with constant magnetic quantum number  $m$  (5.67) is the basis for the propagation of arbitrary states with  $l_z = m$ , which are expanded in the basis states (5.67) for  $\tau = 0$ .

The expansion of states with definite angular momentum  $l_z = m$  in the basis states (5.61) follows a similar procedure as demonstrated in subsection 5.3.1. Suitable coordinates are needed where the GWP part (5.60) of the basis functions (5.61) describes plane waves. This is provided by the parabolic coordinates  $\xi = r + z$ ,  $\eta = r - z$  when setting  $a_\mu = p_\xi + i\epsilon$  and  $a_\nu = p_\eta + i\epsilon$ . The basis states (5.61) eq. (5.61) in parabolic coordinates read

$$g_m(\mathbf{y}, \mathbf{x}) = (\xi\eta)^{|m|/2} e^{i(p_\xi\xi + p_\eta\eta + \gamma)} e^{-\epsilon(\xi + \eta)} e^{im\varphi}, \quad (5.68)$$

which contain plane waves in the limit  $\epsilon \rightarrow 0$ . In analogy to subsection 5.3.1 the expansion of an arbitrary state

$$\begin{aligned}
 \psi_m(\mathbf{x}) = \rho^{|m|} \psi(\rho, z) e^{im\varphi} &= \sum_{k=1}^N (\mu\nu)^{|m|} e^{i(a_\mu^k \mu^2 + a_\nu^k \nu^2 + \gamma^k)} e^{im\varphi} \\
 &= \sum_{k=1}^N \rho^{|m|} e^{i(p_r^k r + p_z^k z + \gamma^k)} e^{im\varphi} \\
 &= \sum_{k=1}^N (\xi\eta)^{|m|/2} e^{i(p_\xi^k \xi + p_\eta^k \eta + \gamma^k) - \epsilon(\xi + \eta)} e^{im\varphi} \quad (5.69)
 \end{aligned}$$

in parabolic coordinates is investigated. The common prefactor  $(\xi\eta)^{|m|/2} e^{im\varphi}$  can be separated and an expansion of the  $\psi(\rho, z) \equiv \psi(\xi, \eta)$  part remains. Due to the conditions  $\xi, \eta > 0$  resulting from the definition of the parabolic coordinates it is possible to use the Laplace transformation instead of the Fourier transformation for the expansion of  $\psi(\xi, \eta)$ . The Laplace transform in two dimensions reads

$$\tilde{\psi}(\tilde{p}_\xi, \tilde{p}_\eta) = \mathcal{L}\{\psi(\xi, \eta)\} = \int_0^\infty \int_0^\infty d\xi d\eta \psi(\xi, \eta) e^{-\tilde{p}_\xi \xi - \tilde{p}_\eta \eta}, \quad (5.70)$$

In the Laplace transformation the conjugate variable, i.e. the momenta  $\tilde{p}_\xi, \tilde{p}_\eta$ , may be complex, which allows for the incorporation of the damping factor  $\epsilon$  in the complex “momenta”  $\tilde{p}_\xi, \tilde{p}_\eta$ . This is possible because the damping factor  $e^{-\epsilon r} = e^{-\epsilon(\xi + \eta)}$  separates in the parabolic coordinates while it does not in Cartesian coordinates. It is therefore not necessary to require an infinitesimal  $\epsilon > 0$  (in contrast to subsection 5.3.1) in order to obtain an accurate expansion, but *any* positive value leads to accurate results for a sufficiently large number  $N$  of basis states. The inverse Laplace transformation is given by

$$\mathcal{L}^{-1}\{\tilde{\psi}(\tilde{p}_\xi, \tilde{p}_\eta)\} = \frac{1}{(2\pi i)^2} \int_{c-i\infty}^{c+i\infty} \int_{c-i\infty}^{c+i\infty} d\tilde{p}_\xi d\tilde{p}_\eta \tilde{\psi}(\tilde{p}_\xi, \tilde{p}_\eta) e^{\tilde{p}_\xi \xi + \tilde{p}_\eta \eta}, \quad (5.71)$$

where the integration runs parallel to the imaginary axes with an arbitrary distance  $c$ , as long as the integrals (5.71) and (5.70) exist. The path of integration, i.e. the distance  $c$  is chosen to be  $-\epsilon$  in order to reproduce the functional form of eq. (5.68) in the kernel of eq. (5.71). The complex momenta  $\tilde{p}_\xi$  and  $\tilde{p}_\eta$  on the path of integration are written in the form  $\tilde{p}_\xi = -\epsilon + ip_\xi$  and  $\tilde{p}_\eta = -\epsilon + ip_\eta$ . Then the inverse Laplace transformation reads

$$\mathcal{L}^{-1}\{\tilde{\psi}(\tilde{p}_\xi, \tilde{p}_\eta)\} = \frac{1}{(2\pi)^2} \int_{-\infty}^{+\infty} dp_\xi dp_\eta \tilde{\psi}(-\epsilon + ip_\xi, -\epsilon + ip_\eta) e^{i(p_\xi \xi + p_\eta \eta)} e^{-\epsilon(\xi + \eta)}. \quad (5.72)$$

Note that the Laplace transformation (5.70) guarantees  $\mathcal{L}^{-1}\{\tilde{\psi}(\tilde{p}_\xi, \tilde{p}_\eta)\} = 0$ , in the forbidden region  $\xi, \eta < 0$ . Formally it is allowed to include the negative regime  $\xi, \eta < 0$

and to extend the integration ranges from  $[0, \infty]$  to  $[-\infty, \infty]$ . For some wave functions this can simplify the integration. In general, integration ranges of  $[\xi_A, \infty]$  and  $[\eta_A, \infty]$  in eq. (5.70) yield  $\mathcal{L}^{-1}\{\tilde{\psi}(\tilde{p}_\xi, \tilde{p}_\eta)\} = 0$  for  $\xi < \xi_A$ ,  $\eta < \eta_A$  and the original wave function is recovered, i.e.  $\mathcal{L}^{-1}\{\tilde{\psi}(\tilde{p}_\xi, \tilde{p}_\eta)\} = \psi(\xi, \eta)$  in the region  $\xi > \xi_A$ ,  $\eta > \eta_A$ . In the discretized version eq. (5.72) reads

$$\psi(\xi, \eta) = \sum_{k=1}^N (\Delta p)_k^2 \tilde{\psi}(-\epsilon + ip_\xi^k, -\epsilon + ip_\eta^k) e^{i(p_\xi^k \xi + p_\eta^k \eta)} e^{-\epsilon(\xi + \eta)}. \quad (5.73)$$

The functional form of the part  $e^{i(p_\xi \xi + p_\eta \eta)} e^{-\epsilon(\xi + \eta)}$  in eq. (5.73) exactly matches the functional form of the basis states in eq. (5.68) after separation of the common prefactor. By comparison, the initial Gaussian parameters  $p_\xi^k, p_\eta^k$  in eq. (5.69) are identified with the momenta  $p_\xi^k$  and  $p_\eta^k$  in (5.73), which are the sampling points of the numerical integration. The complex phase parameters  $\gamma^k$  for each basis state (5.68) must be

$$\gamma^k = -i \log \left[ \frac{(\Delta p)_k^2}{(2\pi)^2} \tilde{\psi}(-\epsilon + ip_\xi^k, -\epsilon + ip_\eta^k) \right], \quad (5.74)$$

and contain the whole information about the quantum state.

As an example we investigate a Gaussian wave packet in parabolic coordinates located around  $\xi_0$  and  $\eta_0$  with the mean momenta  $p_{\xi_0}$  and  $p_{\eta_0}$ , width  $\sigma$  and amplitude  $A$

$$\psi(\xi, \eta) = A e^{-(\xi - \xi_0)^2 / (4\sigma^2) - (\eta - \eta_0)^2 / (4\sigma^2) + ip_{\xi_0}(\xi - \xi_0) + ip_{\eta_0}(\eta - \eta_0)}, \quad (5.75)$$

which is expanded and propagated in the basis states (5.68). First perform the Laplace transform (5.70) with an extension of the integration range from  $[0, \infty]$  to  $[-\infty, \infty]$ . Nevertheless the application of complex momenta is allowed since an exponential increase of the integrand due to the factor  $e^{-\epsilon(\xi + \eta)}$  for  $\xi, \eta \rightarrow -\infty$  is intercepted by the strong Gaussian decay of  $\psi(\xi, \eta)$  and the integral converges. The transformation yields

$$\psi(\tilde{p}_\xi, \tilde{p}_\eta) = 4\pi\sigma^2 A e^{-\sigma^2[(p_{\xi_0} - p_\xi)^2 + (p_{\eta_0} - p_\eta)^2] + 2i\sigma^2\epsilon((p_{\xi_0} - p_\xi) + (p_{\eta_0} - p_\eta)) + 2\sigma^2\epsilon^2 + \epsilon(\xi_0 + \eta_0) - i(p_\xi \xi_0 + p_\eta \eta_0)}, \quad (5.76)$$

with  $\tilde{p}_\xi = -\epsilon + ip_\xi$  and  $\tilde{p}_\eta = -\epsilon + ip_\eta$ . The numerical integration of the inverse transformation is again performed by a Monte Carlo technique. The sampling points  $p_\xi^k, p_\eta^k$  are randomly distributed around  $p_{\xi_0}, p_{\eta_0}$  according to the weighting function  $w(p) = (\sigma/\sqrt{\pi}) e^{-\sigma^2(p - p_0)^2}$ . The initial values of the phase factors  $\gamma^k$  read

$$\begin{aligned} \gamma^k = & -i \left[ \log \left( \frac{A}{N} \right) + (2\sigma^2\epsilon^2 + \epsilon(\xi_0 + \eta_0)) \right] \\ & + 2\sigma^2\epsilon((p_{\xi_0} - p_\xi) + (p_{\eta_0} - p_\eta)) - (p_\xi \xi_0 + p_\eta \eta_0). \end{aligned} \quad (5.77)$$

Thus the time evolution of the wave packet (5.75) reads

$$\psi(\tau, \xi, \eta) = \mathcal{N}_m(0) \sum_{k=1}^N g_m(\tau, \mathbf{y}^k(0), \xi, \eta) e^{i\gamma^k}, \quad (5.78)$$



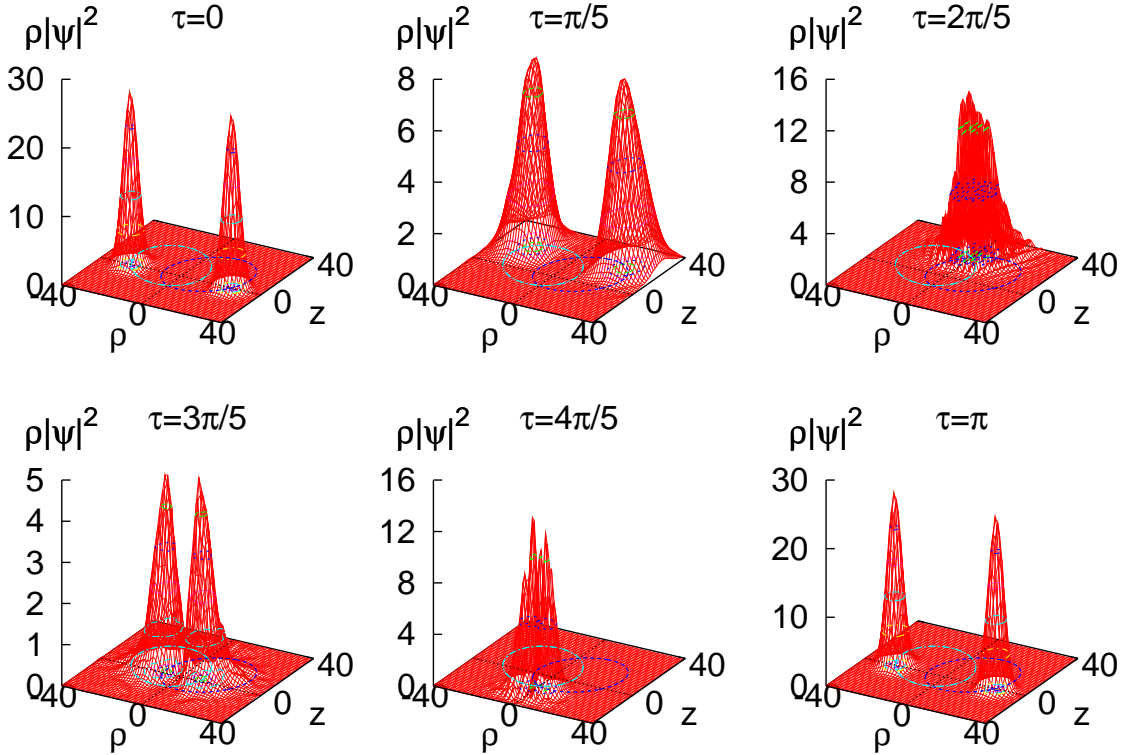


Figure 5.2.: Propagation of a GWP (5.75) with magnetic quantum number  $m = 0$ . The part on the negative  $\rho$ -axis is obtained by reflecting the positive part at the  $z$ -axis. The figure shows the associated probability density for a fixed angle  $\varphi$  around the  $z$ -axis. The wave packet runs along the classical Kepler ellipse with the corresponding initial values. For details see text.

with  $\mathbf{y}^k(0) = (p_\xi^k, p_\eta^k, 0)$  and the time evolution of the basis states (5.67) in parabolic coordinates.

In fig. 5.2 the expansion of a GWP (5.75) is shown with the center  $\xi_0 = \eta_0 = 25.0$  and the momenta  $p_{\xi_0} = 0.535$  and  $p_{\eta_0} = -0.117$  or in terms of cylindrical coordinates  $\rho_0 = 25.0, z_0 = 0.0$  and  $p_{\rho_0} = 0.419, p_{z_0} = 0.652$  and the width  $\sigma = 4.472$ . Note that a Gaussian shape of a wave packet in parabolic coordinates is nearly Gaussian also in cylindrical coordinates (see e.g. the wave packet at  $\tau = 0$  in fig. 5.2). The presented wave function has zero angular momentum component  $l_z = 0$ . The originally positive radial coordinate  $\rho$  is extended to take on negative values and the symmetry  $\psi(-\rho) = \psi(\rho)$  is used. The  $(\rho, z)$ - plane presents the probability density  $\rho|\psi(\rho, z)|^2$  along a plane of constant azimuthal angle  $\varphi = \text{const}$ . The complete probability density is obtained by rotation about the  $z$ -axis due to the rotational symmetry. The Kepler ellipses plotted on the bottom in each panel of fig. 5.2 show the corresponding classical motion of the

particle with the initial conditions given above. The second ellipse again is obtained by reflection symmetry as the intersection of the torus, which is obtained from rotating the ellipse around the  $z$ -axis, with the intersecting plane  $\varphi = \text{const}$ . At times  $\tau \approx 2\pi/5$  and  $\tau \approx 4\pi/5$  the high probability density close to the  $z$ -axis leads to interference patterns. After one period  $\tau = \pi$  the initial wave function  $\tau = 0$  is recovered.  $N = 5000$  modified basis states (5.68) with  $\epsilon = 0.05$  are employed. Results for the case  $m \neq 0$  are not presented since they show similar qualitative behavior.

### 5.3.3. Wave packet propagation with conserved angular momentum

$$l^2, l_z$$

The procedure of the two previous subsections is applied to quantum states with a conserved angular momentum  $l^2, l_z$ . First an extension of the basis states (5.37f) to basis states with well defined angular momentum quantum numbers  $l, m$  is presented and they are shown to be exact solutions of the time-dependent Schrödinger equation of the regularized H atom. Then the procedure of expanding states with definite  $l, m$  in the constructed basis states together with an example are presented. For radial symmetry the complex width matrix  $A$  (5.35) of the restricted GWP must be a multiple of the identity matrix  $A = a\mathbf{1}$ , i.e.  $a_x = a_y = 0$ ,  $a_\mu = a_\nu = a$ . The restricted GWP reduces to

$$g(r) = e^{i(2ar+\gamma)}. \quad (5.79)$$

This is a suitable basis state with vanishing angular momentum. The correct extension to arbitrary angular momentum is given by

$$g_{lm}(r, \theta, \varphi) = r^l e^{i(2ar+\gamma)} Y_{lm}(\theta, \varphi), \quad (5.80)$$

where  $Y_{lm}(\theta, \varphi)$  denotes the spherical harmonics. Insertion of the ansatz (5.80) into the time-dependent version of the Schrödinger equation (5.11) in spherical coordinates

$$\left( -\frac{\partial^2}{\partial r^2} r + \frac{l^2}{r} + r \right) g_{lm}(r, \theta, \varphi) = i\dot{g}_{lm}(r, \theta, \varphi) \quad (5.81)$$

yields

$$[-4i(l+1)a + \dot{\gamma} + r(1 + (2a)^2 + 2\dot{a})] g_{lm}(r, \theta, \varphi) = 0. \quad (5.82)$$

The basis states (5.80) present an exact solution of the Schrödinger equations provided the time-dependent parameters obey the equations of motion

$$\dot{a} = -2a^2 - \frac{1}{2}, \quad (5.83a)$$

$$\dot{\gamma} = 4ia(l+1), \quad (5.83b)$$

with the analytic solution

$$a(\tau) = \frac{4a(0) \cos(2\tau) - (1 - 4(a(0))^2) \sin(2\tau)}{2[1 + 4(a(0))^2 + (1 - 4(a(0))^2) \cos(2\tau) + 4a(0) \sin(2\tau)]} \quad (5.84)$$

and

$$\gamma(\tau) = i \log \left[ (1 + 4(a(0))^2 + (1 - 4(a(0))^2) \cos(2\tau) + 4a(0) \sin(2\tau)) / 2 \right]. \quad (5.85)$$

Now we come to the expansion of states with definite quantum numbers  $l, m$  in the basis (5.80) and make the ansatz

$$\psi_{lm}(r, \theta, \varphi) = r^l \psi(r) Y_{lm}(\theta, \varphi) = \sum_{k=1}^N g_{lm}(r, \theta, \varphi) = \sum_{k=1}^N r^k e^{i(2a^k r + \gamma^k)} Y_{lm}(\theta, \varphi). \quad (5.86)$$

The common factor  $r^l Y_{lm}(\theta, \varphi)$  is separated and the problem is reduced to expand the radial part  $\psi(r)$  only. The proceeding is the same as in subsection 5.3.2, i.e. a superposition of plane waves is constructed using discrete Laplace transformation. Having computed the wave function  $\tilde{\psi}(\tilde{p}_r)$  in the complex momentum space by

$$\tilde{\psi}(\tilde{p}_r) = \int_b^\infty dr \psi(r) e^{-\tilde{p}_r r} \quad (5.87)$$

the original wave function in position space representation  $\psi(r)$  is recovered by the inverse Laplace transformation

$$\psi(r) = \frac{1}{2\pi i} \int_{c-i\infty}^{c+i\infty} d\tilde{p}_r \tilde{\psi}(\tilde{p}_r) e^{\tilde{p}_r r}, \quad (5.88)$$

in the region  $r > b$ . For  $r < b$  it yields  $\psi(r) = 0$ . An extension of the integration range to negative values and also  $b \rightarrow -\infty$  is possible as long as the integrals exist. The existence of the integrals depends on the decay of the wave function  $\psi(r)$  for  $r \rightarrow \pm\infty$ . The choice  $b = -\infty$  simplifies the integration for some wave functions. Choosing the path of integration  $c = -\epsilon$  gives the desired functional dependence on  $r$ . The complex momentum  $\tilde{p}_r = -\epsilon + ip_r$  along the path is inserted in the inverse Laplace transform (5.88) and yields

$$\psi(r) = \frac{1}{2\pi} \int_{-\infty}^{+\infty} dp_r \tilde{\psi}(-\epsilon + ip_r) e^{ip_r r - \epsilon r} \quad (5.89a)$$

$$\approx \frac{1}{2\pi} \sum_{k=1}^N \Delta p_r^k \tilde{\psi}(-\epsilon + ip_r^k) e^{ip_r^k r - \epsilon r}. \quad (5.89b)$$

The second line is the discrete form of the integral, and is identified with the part  $\sum_{k=1}^N e^{i(2a^k r + \gamma^k)}$  in eq. (5.86). Comparison demands to set  $2ia^k = -\epsilon + ip_r^k$  and for the phase parameters  $\gamma^k$  we obtain

$$\gamma^k = -i \log \left[ \frac{\tilde{\psi}(-\epsilon + ip_r^k) \Delta p_r^k}{2\pi} \right]. \quad (5.90)$$

In the following explicit computations are performed for the radial Gaussian function

$$\psi(r) = Ae^{-(r-r_0)^2/(4\sigma^2)+ip_{r_0}(r-r_0)}, \quad (5.91)$$

with the Laplace transformed function ( $b = -\infty$ ) in momentum space

$$\tilde{\psi}(-\epsilon + ip_r) = A4\pi\sigma^2 e^{-\sigma^2(p_{r_0}-p_r)^2+2i\sigma^2\epsilon(p_{r_0}-p_r)+\sigma^2\epsilon^2+\epsilon r_0-ip_r r_0}, \quad (5.92)$$

where again the integral (5.89a) is numerically integrated using Monte Carlo technique with the sampling points  $p_r^k$  being Gaussian distributed random numbers according to the distribution  $w(p) = \sigma/\sqrt{\pi}e^{-\sigma^2(p_{r_0}-p_r)^2}$ . The phases  $\gamma^k$  are identified to be

$$\gamma^k = -i \left[ \log \left( \frac{A}{N} \right) + \sigma^2\epsilon^2 + \epsilon r_0 \right] + 2\sigma^2\epsilon(p_r^k - p_{r_0}) - p_r^k r_0. \quad (5.93)$$

The results of the propagation of the wave function  $\psi_{lm}(r, \theta, \varphi) = r^l \psi(r) Y_{lm}(\theta, \varphi)$  with  $\psi(r)$  of eq. (5.91) and the initial values  $r_0 = 10$ ,  $p_{r_0} = -0.5$  and the width  $\sigma = 3$  is presented in fig. 5.3 for different times  $0 \leq \tau \leq \pi$ . The imaginary parts of  $2a^k$  are set to  $\epsilon = 0.2$  and the number of basis states (5.80) is  $N = 10000$ . In panel (a) the angular momentum is set to  $m = l = 0$  and in panel (b) the components of the angular momentum are  $l = 5$  and  $m = 0$ . Due to the negative initial value of the radial momentum  $p_{r_0}$  the wave is initially running towards the nucleus located at the origin. The wave function with zero angular momentum (a) comes close to the origin  $r = 0$ . Similar to the radial symmetric case in subsection 5.3.2 there appears to occur some interference pattern due to the overlapping parts of the incoming wave function at the inner turning point for  $\tau = 2\pi/5$ . In the nonvanishing angular momentum case (fig. 5.3(b)) the barrier of rotational energy prevents the wave function from reaching the nucleus. Instead there is a turning point whose distance from the nucleus increases with increasing angular momentum. Again an interference pattern is observed ( $\tau = 2\pi/5$ ) at the inner turning point. In both panels the maximum of the probability density overshoots the position of the initial maximum  $r_0 = 10$  at  $\tau = 4\pi/5$  due to the initial kinetic energy and returns to the initial wave packet after the period  $\tau = \pi$ , indicating the periodicity of the wave function.

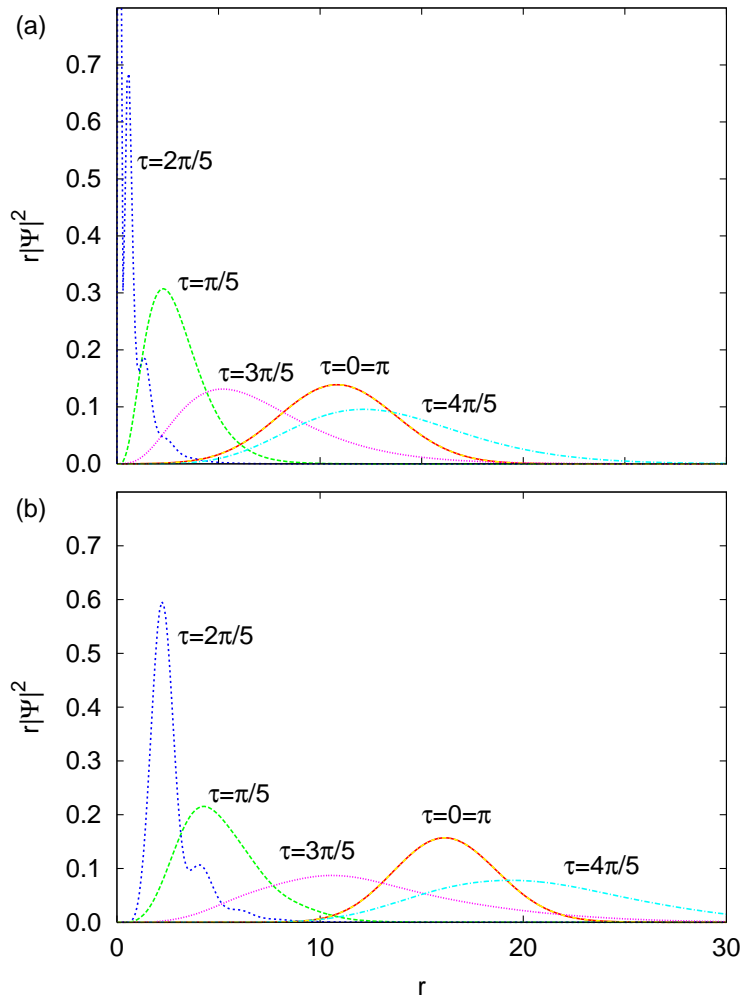


Figure 5.3.: Propagation of the wave function (5.86) with  $\psi(r)$  given by the Gaussian (5.91) with  $r_0 = 10.0$ ,  $p_{r_0} = -0.5$  and  $\sigma = 3.0$  for angular momentum quantum numbers (a)  $l = 0$ ,  $m = 0$ , and (b)  $l = 5$ ,  $m = 0$ . An interference pattern is observed at the turning points at approximately  $\tau = 2\pi/5$  in both panels. The initial wave function is expanded in  $N = 10000$  basis states (5.80) with  $\epsilon = 0.2$ .



## 6. Wave packet dynamics in the hydrogen atom in external fields

The wave packets constructed in chapter 5 are exact solutions of the field-free hydrogen atom. This is no longer true when external fields are applied. The approximate evolution of the wave packets is determined by the TDVP. A sufficiently large number of wave packets is required for accurate results. In the presence of a single external homogeneous field the rotational symmetry of the H atom is preserved and the corresponding component of the angular momentum, say  $l_z$ , is conserved. It is in this case especially advantageous to employ the wave packets introduced and discussed in subsection 5.3.2 and to perform computations in the subspaces of the different magnetic quantum numbers  $m$  separately. When two crossed external fields are applied, the cylindrical symmetry is broken and computations are performed in the basis of the restricted GWPs discussed in subsection 5.3.1. First the Kustaanheimo-Stiefel regularization is applied to the hydrogen atom in homogeneous external electric and magnetic fields, in analogy to section 6.1. Then the wave packet dynamics for the hydrogen atom in a magnetic field and in crossed electric and magnetic fields is investigated in sections 6.2 and 6.3, respectively.

### 6.1. Regularized hydrogen atom in external fields

When external fields are applied the Kustaanheimo-Stiefel regularization of the hydrogen atom is introduced in the same manner as in section 5.1. In this thesis perpendicular electric and magnetic fields are considered. The electric field of strength  $F$  is assumed to lie along the  $x$  axis and the magnetic field  $B$  is assumed to lie along the  $z$  axis. The Schrödinger equation in Cartesian coordinates reads

$$H_3\psi = \left( -\frac{1}{2}\Delta_3 - \frac{1}{r} + \frac{1}{2}Bl_z + \frac{1}{8}B^2(x^2 + y^2) + Fx \right) \psi = E\psi. \quad (6.1)$$

In a first step the regularization procedure described in section 5.1 yields the Hamiltonian in KS coordinates

$$\begin{aligned}
 H_4\psi = & \left[ -\frac{1}{2\mathbf{u}^2}\Delta_4 - \frac{2}{\mathbf{u}^2} + \frac{1}{4}B((u_1p_2 - u_2p_1) + (u_3p_4 - u_4p_3)) \right. \\
 & + \frac{1}{8}B^2(u_1^2 + u_2^2)(u_3^2 + u_4^2) \\
 & \left. + F(u_1u_3 - u_2u_4) \right] \psi = E\psi.
 \end{aligned} \tag{6.2}$$

Multiplication of the Schrödinger equation by a factor of  $\mathbf{u}^2$  and the introduction of the scaled coordinates

$$\mathbf{u} \rightarrow \sqrt{n_{\text{eff}}}\mathbf{u}, \quad H = n_{\text{eff}}H_4, \tag{6.3}$$

yields the regularized Schrödinger equation for the hydrogen atom in external crossed fields

$$\begin{aligned}
 H\psi = & \left[ \frac{1}{2}(p_1^2 + p_2^2 + p_3^2 + p_4^2) + (\alpha + \zeta(u_1u_3 - u_2u_4))(u_1^2 + u_2^2 + u_3^2 + u_4^2) \right. \\
 & + \frac{1}{2}\beta((u_1p_2 - u_2p_1)(u_3^2 + u_4^2) + (u_3p_4 - u_4p_3)(u_1^2 + u_2^2)) \\
 & \left. + \frac{1}{8}\beta^2((u_1^2 + u_2^2)^2(u_3^2 + u_4^2) + (u_1^2 + u_2^2)(u_3^2 + u_4^2)^2) \right] \psi \\
 = & 2n_{\text{eff}}\psi,
 \end{aligned} \tag{6.4}$$

with an effective real valued quantum number  $n_{\text{eff}}$ . The eigenvalues of the scaled Hamiltonian  $H$  in (6.4) for fixed values of  $\alpha, \zeta, \beta$  are the discrete effective quantum numbers  $n_{\text{eff}i}$ ,  $i = 1, 2, 3, \dots$ , i.e.  $H\psi_i = 2n_{\text{eff}i}\psi_i$ . The corresponding eigenenergies and the related field strengths can be obtained by using the definitions

$$\alpha \equiv -E_in_{\text{eff}i}^2, \quad \zeta \equiv F_in_{\text{eff}i}^3, \quad \beta \equiv B_in_{\text{eff}i}^2, \tag{6.5}$$

with  $i = 1, 2, 3, \dots$ , implied by the scaling (6.3). For fixed values of  $\alpha, \beta, \zeta$  scaled spectra of the Hamiltonian are obtained, i.e. different field strengths  $B_i$  and  $F_i$  belong to each energy eigenvalue  $E_i$  of the hydrogen atom. The transition to the time-dependent formulation is in analogy to eq. (5.22) done by the introduction of a fictitious time parameter  $\tau$  and the assignment  $2n_{\text{eff}} \rightarrow i\frac{\partial}{\partial\tau}$ .

Particularly for the computations including only the external magnetic field, oriented along the  $z$  direction, the representation of the regularized Hamiltonian (6.4) in semi-parabolic coordinates is advantageous

$$H = -\frac{1}{2}\left(\frac{\partial^2}{\partial\mu^2} + \frac{1}{\mu}\frac{\partial}{\partial\mu} + \frac{\partial^2}{\partial\nu^2} + \frac{1}{\nu}\frac{\partial}{\partial\nu} - l_z^2\left(\frac{1}{\mu^2} + \frac{1}{\nu^2}\right)\right) \tag{6.6}$$

$$+ \left(\alpha + \zeta\mu\nu\cos(\varphi) + \frac{\beta}{2}l_z + \frac{\beta^2}{8}\mu^2\nu^2\right)(\mu^2 + \nu^2). \tag{6.7}$$



In the absence of the electric field  $\zeta = 0$  the magnetic quantum number  $m$  is conserved. Omitting the paramagnetic contribution the substitution  $\psi \rightarrow \psi/\sqrt{\mu\nu}$  yields

$$H = -\frac{1}{2} \left( \frac{\partial^2}{\partial \mu^2} + \frac{\partial^2}{\partial \nu^2} \right) + \frac{m^2 - \frac{1}{4}}{2} \left( \frac{1}{\mu^2} + \frac{1}{\nu^2} \right) + \alpha (\mu^2 + \nu^2) + \frac{1}{8} \beta^2 (\mu^2 \nu^2 (\mu^2 + \nu^2)). \quad (6.8)$$

For the unphysical choice  $|m| = 1/2$  the Hamiltonian describes the 2D H atom used in section 4.3 as a model system when the semiparabolic coordinates are extended to negative values and can be interpreted as Cartesian coordinates. We now apply the TDVP to the physical 3D H atom in external fields.

## 6.2. Variational GWP dynamics in the diamagnetic hydrogen atom

The rotational symmetry of the H atom in a homogeneous external magnetic field yields conservation of the  $l_z$  component of the angular momentum. The basis states (5.61) with definite  $m$  account for the cylindrical symmetry of the system. In this chapter the time evolution of wave functions  $\psi_m(\mathbf{x})$  with magnetic quantum number  $m$  expanded in the wave packets (5.61) according to eq. (5.69) is investigated. In contrast to the dynamics of the basis states (5.61) in the hydrogen atom without external fields discussed in subsection 5.3.2, the basis states are no longer exact solutions of the Schrödinger equation when external fields are applied. The reason is that external fields introduce terms of order higher than harmonic into the Hamiltonian (6.4). The evolution of the basis states is obtained by the TDVP. The Hamiltonian determines the evolution of the system when setting the electric field strength  $\zeta = 0$ . The paramagnetic term  $\beta l_z = \beta m$  is not accounted for in this section since it only presents a constant energy shift due to the conservation of  $l_z$  that will be not considered here. The trial function is a superposition of  $N$  wave packets according to eq. (5.69). It turns out that a sensible choice of the initial superposition is crucial for the numerical propagation of the wave function. For an unreasonable choice the numerical problems discussed in chapter 4 occur for few basis states already and bad unconverged results are obtained. A good choice of the initial wave function has proven to be the expansion of the Gaussian wave packet in parabolic coordinates (5.75) discussed in subsection 5.3.2 for the field-free H atom. The variational equations of motion are set up by evaluating eq. (2.22). The evaluation of the ket-vector requires the knowledge of the action of the time derivative and the Laplace operator on

the trial function (5.62) and we obtain

$$\begin{aligned}
 \left( i \frac{\partial}{\partial \tau} - T \right) g_m(\mathbf{y}^k, \mathbf{x}) &= [-\dot{\gamma}^k + 2i(a_\mu^k + a_\nu^k)(1 + |m|) + \\
 &\quad (-\dot{a}_\mu^k - 2(a_\mu^k)^2)\mu^2 + (-\dot{a}_\nu^k - 2(a_\nu^k)^2)\nu^2] g_m(\mathbf{y}^k, \mathbf{x}) \\
 &\equiv \left[ v_0^k + \frac{1}{2}(V_\mu^k \mu^2 + V_\nu^k \nu^2) \right] g_m(\mathbf{y}^k, \mathbf{x}), \tag{6.9}
 \end{aligned}$$

for  $k = 1, \dots, N$ . The last row of eq. (6.9) defines the coefficients  $V_\mu, V_\nu, v_0$  as functions of the parameters  $a_\mu, a_\nu, \gamma$  and their time derivatives  $\dot{a}_\mu, \dot{a}_\nu, \dot{\gamma}$ . Solving for the time derivatives yields the equations of motion

$$\dot{a}_\mu^k = -2(a_\mu^k)^2 - \frac{1}{2}V_\mu^k, \tag{6.10a}$$

$$\dot{a}_\nu^k = -2(a_\nu^k)^2 - \frac{1}{2}V_\nu^k, \tag{6.10b}$$

$$\dot{\gamma}^k = 2i(a_\mu^k + a_\nu^k)(1 + |m|) - v_0^k, \tag{6.10c}$$

with  $k = 1, \dots, N$ . Formally eqs. (6.10) are exactly the same as in eqs. (5.63). However, in the presence of anharmonic potentials the coefficients  $V_\mu^k, V_\nu^k$  and  $v_0^k$  are not simply given as the coefficients of the harmonic potential, c.f.  $V_\mu^k = 1, V_\nu^k = 1$  and  $v_0^k = 0$  as in eq. (5.63), but become time-dependent and must be determined from a system of linear equations, in analogy to eq. (3.28).

The starting point for setting up the equations of motion, i.e. to determine the coefficients  $V_\mu^k, V_\nu^k, v_0^k, k = 1, \dots, N$  is eq. (2.22). The ingredients of the ket-vector have been discussed above, the bra-vector of eq. (2.22) requires the knowledge of the derivatives of the trial function (5.61) with respect to the variational parameters  $\mathbf{y}^k = (a_\mu^k, a_\nu^k, \gamma^k), k = 1, \dots, N$  which read

$$\frac{\partial g_m(\mathbf{y}^k, \mathbf{x})}{\partial \gamma^k} = i g_m(\mathbf{y}^k, \mathbf{x}), \quad \frac{\partial g_m(\mathbf{y}^k, \mathbf{x})}{\partial a_\mu^k} = i \mu^2 g_m(\mathbf{y}^k, \mathbf{x}), \quad \frac{\partial g_m(\mathbf{y}^k, \mathbf{x})}{\partial a_\nu^k} = i \nu^2 g_m(\mathbf{y}^k, \mathbf{x}).$$

They lead to the resulting matrix equation

$$\begin{aligned}
 \sum_{k=1}^N \left( \langle g_m^l | g_m^k \rangle v_0^k + \frac{1}{2} \langle g_m^l | \mu^2 | g_m^k \rangle V_\mu^k + \frac{1}{2} \langle g_m^l | \nu^2 | g_m^k \rangle V_\nu^k \right) &= \sum_{k=1}^N \langle g_m^l | V(\mu, \nu) | g_m^k \rangle \\
 \sum_{k=1}^N \left( \langle g_m^l | \mu^2 | g_m^k \rangle v_0^k + \frac{1}{2} \langle g_m^l | \mu^4 | g_m^k \rangle V_\mu^k + \frac{1}{2} \langle g_m^l | \mu^2 \nu^2 | g_m^k \rangle V_\nu^k \right) &= \sum_{k=1}^N \langle g_m^l | \mu^2 V(\mu, \nu) | g_m^k \rangle \\
 \sum_{k=1}^N \left( \langle g_m^l | \nu^2 | g_m^k \rangle v_0^k + \frac{1}{2} \langle g_m^l | \mu^2 \nu^2 | g_m^k \rangle V_\mu^k + \frac{1}{2} \langle g_m^l | \nu^4 | g_m^k \rangle V_\nu^k \right) &= \sum_{k=1}^N \langle g_m^l | \nu^2 V(\mu, \nu) | g_m^k \rangle, \tag{6.11}
 \end{aligned}$$

where the index  $l = 1, \dots, N$  runs over all basis states and the notation  $g_m^k \equiv g_m(\mathbf{y}^k, \mathbf{x})$  is used. The explicit computation of the integrals is presented in appendix A.2. In analogy to eq. (3.28) the potential  $V(\mu, \nu)$  of the Hamiltonian (6.4) with  $\zeta = 0$  and neglecting the paramagnetic term, enters the right hand side of the matrix equation (6.11).

For better numerical performance we introduce the auxiliary complex quantities  $b_\mu^k, b_\nu^k, c_\mu^k, c_\nu^k$ ,  $k = 1, \dots, N$ , i.e. the diagonal elements of the matrices  $B^k, C^k$  according to  $a^k = \frac{1}{2}b^k(c^k)^{-1}$ , in analogy to eq. (3.31) and to integrate their equations of motion

$$\dot{c}_\mu^k = b_\mu^k, \quad \dot{b}_\mu^k = -V_\mu^k c_\mu^k, \quad \text{and} \quad \dot{c}_\nu^k = b_\nu^k, \quad \dot{b}_\nu^k = -V_\nu^k c_\nu^k, \quad (6.12)$$

rather than integrating eqs. (6.10a) and (6.10b) directly. Thus the number of parameters per basis state that must be integrated increases from 3 to 5.

In the following a numerical example is presented. The initial wave function is most conveniently chosen to be a GWP in parabolic coordinates given by (5.75) with center  $(\xi_0, \eta_0)$  and mean momentum  $(p_{\xi_0}, p_{\eta_0})$ . The GWP is expanded in the basis states (5.61) according to the procedure described in detail subsection 5.3.2, including the Monte Carlo technique with importance sampling for the computation of the inverse Laplace transformation. The procedure yields the initial values of the variational parameters  $a_\mu^k, a_\nu^k, \gamma^k$ ,  $k = 1, \dots, N$ .

For the excitation of eigenstates at a certain, desired effective quantum number  $n_{\text{eff}}$  the following selection of the initial values of the GWP, i.e. the center  $(\xi_0, \eta_0)$  and mean momentum  $(p_{\xi_0}, p_{\eta_0})$  has proven to be useful. Starting from the unscaled field-free classical energy equation of the hydrogen atom

$$\frac{p_0^2}{2} - \frac{1}{r_0} = -\frac{1}{2n_{\text{eff}}^2} \quad (6.13)$$

and considering the motion in a plane spanned by the cylindric coordinates  $\rho, z$  the scaled mean momenta  $p_{z_0}$  and  $p_{\rho_0}$  of the GWP for  $z_0 = 0$  read

$$p_{\rho_0} = \sqrt{\frac{2n_{\text{eff}}}{\rho_0} - 1} \cos \alpha, \quad (6.14a)$$

$$p_{z_0} = \sqrt{\frac{2n_{\text{eff}}}{\rho_0} - 1} \sin \alpha, \quad (6.14b)$$

which depend on the three input parameters  $n_{\text{eff}}, \rho_0 \equiv r_0$  and the angle  $\alpha$  which determines the splitting of the momentum  $p_0$  on the perpendicular directions  $\rho$  and  $z$ , and  $\rho_0$  must lie in the range  $0 < \rho_0 \leq 2n_{\text{eff}}$ . The width of the GWP (5.75) is set to  $\sigma = \sqrt{n_{\text{eff}}}$ . The transformation of the momenta into parabolic coordinates  $\xi = r + z$  and  $\eta = r - z$  with  $r_0 = \sqrt{\rho_0^2 + z_0^2}$  is

$$p_{\xi_0} = \frac{\rho_0 p_{\rho_0} + z_0 p_{z_0} + r_0 p_{z_0}}{2\xi_0}, \quad (6.15a)$$

$$p_{\eta_0} = \frac{\rho_0 p_{\rho_0} + z_0 p_{z_0} - r_0 p_{z_0}}{2\eta_0}. \quad (6.15b)$$

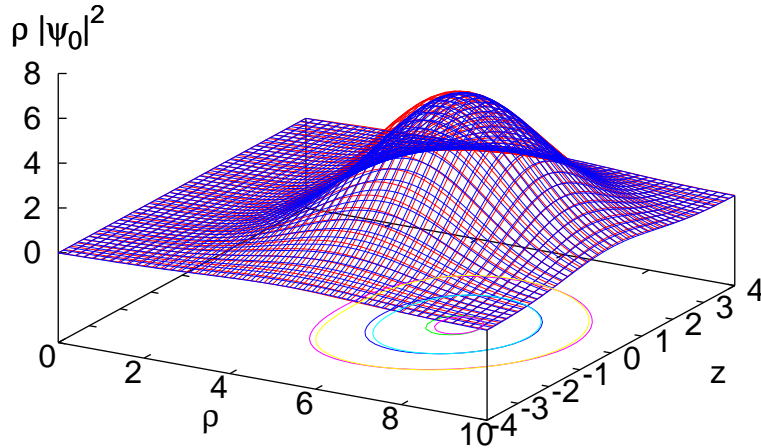


Figure 6.1.: Gaussian wave function (5.75) with  $n_{\text{eff}} = 6.0$ ,  $\rho_0 = 6.0$ ,  $\alpha = 1.0$  (blue lines) and its expansion in the basis states (5.61) with  $N = 70$  and  $\epsilon = 0.1$  (red lines) according to the Monte Carlo technique developed in subsection 5.3.2. Only minor deviations are visible and the overall agreement is very good.

In the field-free hydrogen atom thousands of basis functions could be used for the expansion (5.69) because the propagation was performed analytically for every basis state. In contrast to the analytic propagation in the field-free H atom where the motion of each basis state is exact and independent of the other basis states, a coupling of all basis states implied by the variational procedure must be taken care of when external fields are present. The coupling of the basis states is contained in the coefficients  $V_\mu^k, V_\nu^k, v_0^k$ ,  $k = 1, \dots, N$  obtained as the solution of the matrix equation (6.11) and the equations of motion must be solved numerically. When setting  $\beta = n^2 B = 0$  in the potential  $V(\mu, \nu)$  entering the right hand side of eq. (6.11) a decoupling of the basis states is retained. Each basis state has three variational parameters  $a_\mu^k, a_\nu^k, \gamma^k$ , such that  $N$  basis states require the solution of a  $3N \times 3N$  matrix equation after every integration step and the usual numerical problems discussed in detail in section 4.3 occur with increasing number of basis states. It turns out that constraints on the imaginary parts of the phase parameters  $\gamma_i^k$  of the form (4.18) introduced in section 4.3 are in this system also suitable to prevent the matrix from becoming singular. However, it is not realistic to propagate several thousands of basis states numerically with the full coupling. Reasonable results are obtained by far fewer basis states than used in the expansion and propagation of the GWP (5.75) in the field-free H atom as described in subsection 5.3.2. Reasonable numbers of basis states are in the range of  $N=10-100$ . A numerical example is presented for the magnetic quantum number  $m = 0$  with the center of the initial packet (5.75) lying in the plane  $z_0 = 0$  with the distance  $\rho_0 = 6.0$  to the nucleus, the effective quantum

number  $n_{\text{eff}} = 6.0$ , and  $\alpha = 1.0$ .  $N = 70$  basis states are used for the expansion and propagation. The damping factor  $\epsilon$  introduced in subsection 5.3.2 is set to  $\epsilon = 0.1$

The accuracy of the expansion of the GWP (5.75) in only  $N = 70$  basis states is surprisingly good as depicted in fig. 6.1. The original wave function (5.75) is drawn with blue lines, the red lines present its expansion according to eq. (5.69). Only minor deviations are visible. The time evolution of the wave function is shown in fig. 6.2. The probability density for six different times  $\tau = 0.4, 0.8, 1.2, 3.0, 5.0, 7.0$  is shown in a plane of constant azimuthal angle  $\varphi = \text{const}$ . The part  $\rho < 0$  is obtained by reflection of the positive  $\rho > 0$  part. The influence of the magnetic field  $\beta = n^2 B = 0.2$  is becoming quickly visible since the packet leaves the Kepler ellipse, i.e. the trajectory of a classical particle with the same initial values in absence of the magnetic field. The parameter of the harmonic part of the potential in the Hamiltonian (6.7) is set to  $\alpha = 0.5$ . Even for short times  $\tau \lesssim 3$  the wave function does not any more obey the field-free motion, for only a bit longer propagation time the state becomes even completely delocalized. The  $\pi$  periodicity of the evolution of the wave function that is present in the field-free H atom, is destroyed now.

The auto-correlation function of the propagation can be used to extract spectral information by Fourier transform or by harmonic inversion of the time signal.

To reduce the density of states the auto-correlation function is reduced to the subspaces of even and odd parity by taking the symmetrized states  $\psi_0^s(\rho, z) = \psi_0(\rho, z) + \psi_0(\rho, -z)$  and the anti-symmetrized states  $\psi_0^a(\rho, z) = \psi_0(\rho, z) - \psi_0(\rho, -z)$ . The auto-correlation function  $C^P(\tau) = \langle \psi_0^P(0) | \psi_0^P(\tau) \rangle$ ,  $P = s, a$  is shown in fig. 6.3(a) for symmetrized states and in 6.3(b) for the anti-symmetric states. The spectral results for the diamagnetic H atom, obtained from the time signals are plotted in fig. 6.4. A harmonic inversion has been employed. The amplitudes of the peaks are determined by the magnitude of the overlap between the eigenstates, denoted by  $|n_{\text{eff}}\rangle$  and in fig. 6.4(a) with the symmetric initial state  $\psi_0^s(\tau = 0)$  and in fig. 6.4(b) with the anti-symmetric state  $\psi_0^a(\tau = 0)$ , respectively. The amplitudes are plotted by red impulses. The numerically exact eigenvalues of the diamagnetic hydrogen atom are plotted with blue impulses for comparison. The agreement of the positions is excellent. The highest amplitudes are located in the region  $n_{\text{eff}} \approx 6$  according to the choice of the input parameters of the initial GWP in eq. (6.14).

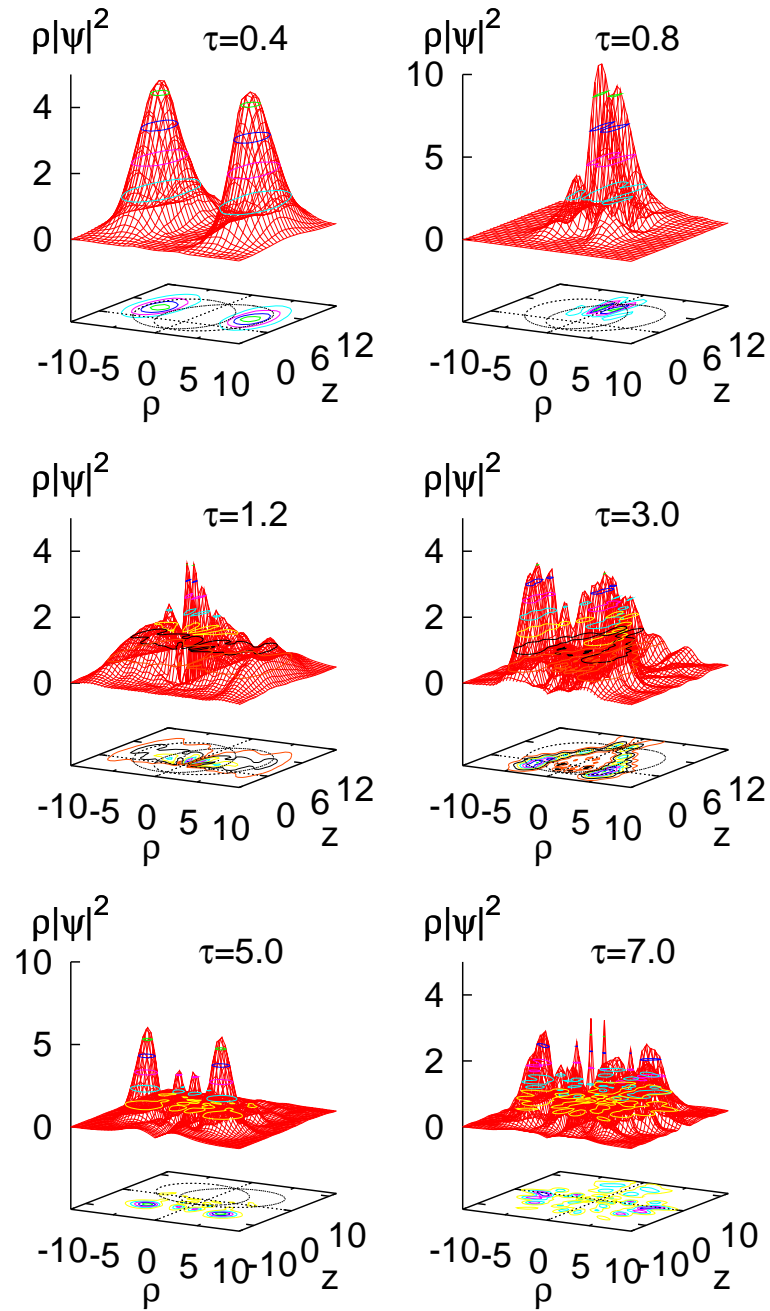


Figure 6.2.: Time evolution of the state (5.75) with  $n_{\text{eff}} = 6.0$ ,  $\rho_0 = 6.0$ ,  $\alpha = 1.0$  presented in fig. 6.1. The wave function is plotted for the times  $\tau = 0.4, 0.8, 1.2, 3.0, 5.0, 7.0$ . Even for very short propagation times  $\tau \approx 0.4$  the wave packet leaves the classical field-free orbit due to the influence of the magnetic field. Quickly a complete delocalization of the quantum state sets in.

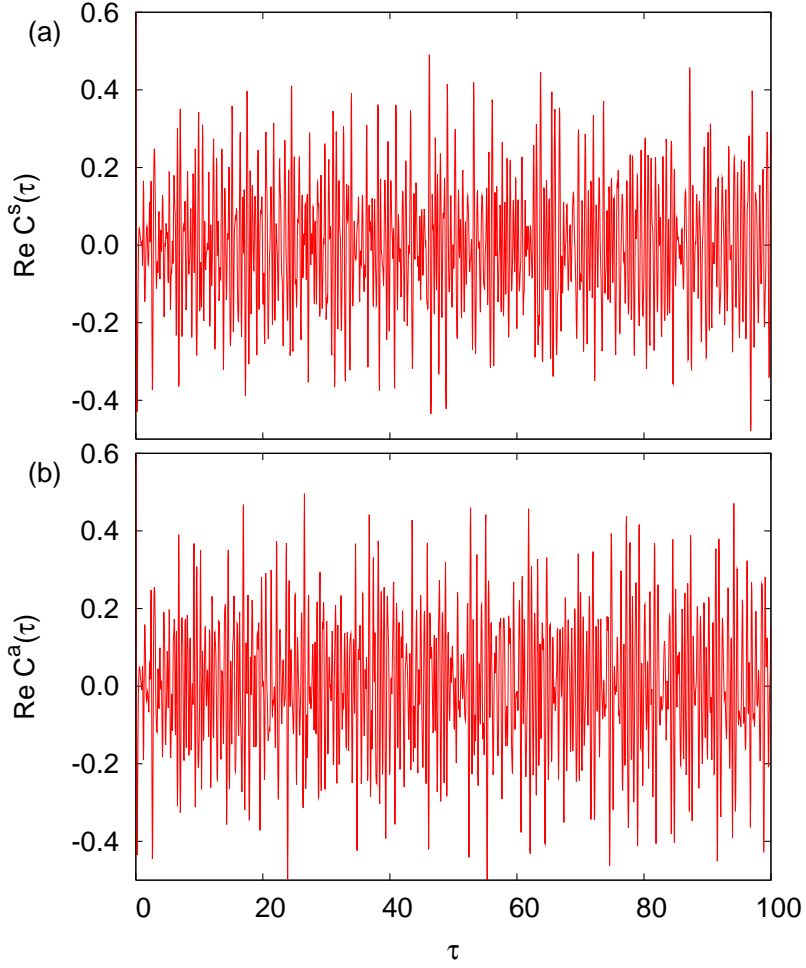


Figure 6.3.: Real part of the auto-correlation function  $C^P(\tau) = \langle \psi_0^P(0) | \psi_0^P(\tau) \rangle$  for the GWP (5.75) with  $n_{\text{eff}} = 6.0$ ,  $\rho_0 = 6.0$ ,  $\alpha = 1.0$ . (a) Signal of the states with even parity,  $P = s$  and (b) odd parity,  $P = a$ .

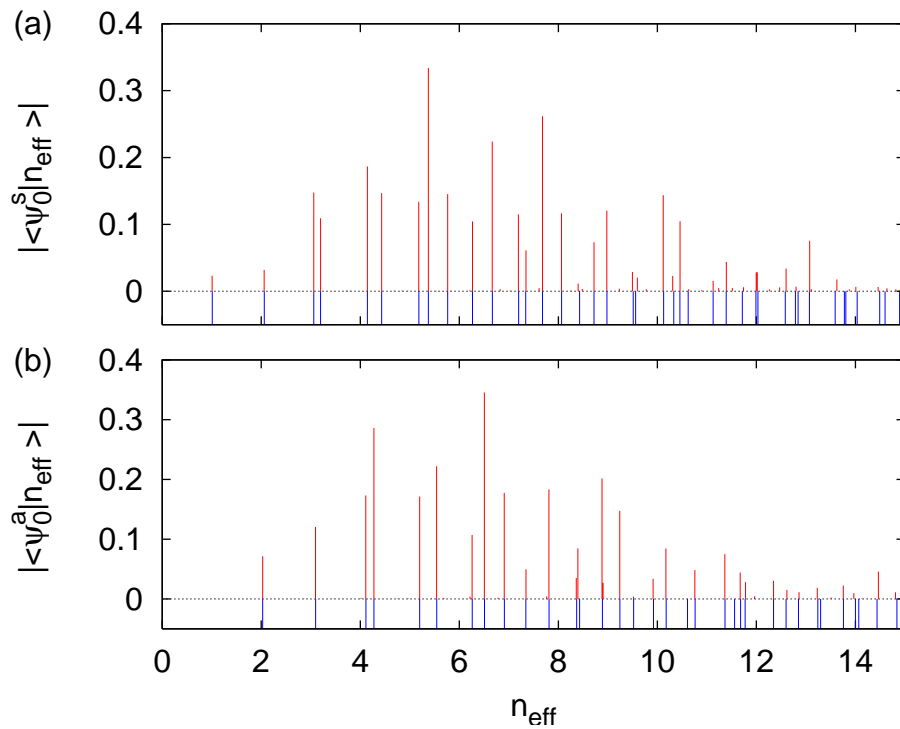


Figure 6.4.: Spectrum extracted from the auto-correlation function  $C^P(\tau) = \langle \psi_0^P(\tau = 0) | \psi_0^P(\tau) \rangle$  computed from the evolution of the wave function (5.75) plotted in fig. 6.1 ( $\tau = 0$ ) and fig. 6.2 ( $\tau \geq 0$ ). Eigenvalues of the states of (a) even parity and (b) odd parity (red lines). The amplitudes are given by the magnitude of overlap between the initial wave function with the respective eigenstate. For comparison of the positions of the eigenvalues the numerically exact values obtained from a diagonalization are plotted with blue lines. The related eigenenergies and the magnetic field strength follow simply from eq. (6.5).



### 6.3. Variational GWP dynamics in the hydrogen atom in crossed fields

The rotational symmetry that is preserved in the presence of a single external field as discussed in the previous section 6.2 is broken when a second external field with a different orientation is applied. None of the three degrees of freedom can be separated. The paramagnetic term that contributed only a constant energy shift in the diamagnetic hydrogen atom must now be taken into account since  $l_z$  is not conserved and the full Hamiltonian (6.4) determines the evolution. Still, the restriction (5.5) implied by the regularization must be fulfilled by physically reasonable wave functions. Thus, the restricted 4D Gaussian wave packets in KS coordinates (5.34) with the  $4 \times 4$  width matrix  $A$  in equation (5.35) which are exact solutions of the field-free hydrogen atom are considered here as the trial functions. For sufficiently large variational freedom it is necessary to take a superposition of restricted GWP of the form (5.48). In the numerical examples below, a 3D Gaussian wave packet (5.54) is expanded and propagated in the restricted GWPs. The time evolution of the restricted GWPs is determined by the TDVP and is integrated numerically in contrast to the field-free H atom discussed in subsection 5.3.1. Formally the equations of motion for the variational parameters keep their form (5.39) for each restricted GWP in the superposition. Due to the potential terms of third or higher order introduced by the external fields (6.4) the coefficients  $v_0^k, V_2^k$  that are simply obtained by comparison with the harmonic underlying potential ( $v_0^k = 0, V_2^k = \mathbf{1}$ ) in subsection 5.3.1 are time-dependent now and are obtained as described by the TDVP. The motion of the linear combination of the restricted GWPs is coupled through the coefficients  $v_0^k, V_2^k$ . Since the symmetry of the matrices  $A^k$  (5.35) is also present in the matrix  $(A^k)^2$ , the symmetry carries over to the  $4 \times 4$  complex symmetric matrices  $V_2^k$  due to their definition (3.8). Therefore, they have only four independent coefficients  $V_\mu^k, V_\nu^k, V_x^k, V_y^k$ , in the notation of eq. (5.35). The set of linear equations, c.f. (3.28) for the computation of the coefficients  $v_0, V_2$  requires the derivatives of the restricted GWPs with respect to their variational parameters  $A^k, \gamma^k$ . The derivatives of the GWPs with respect to their parameters (c.f. (3.11)) now read

$$\begin{aligned}
 \frac{\partial g(\mathbf{y}^k, \mathbf{x})}{\partial \gamma^k} &= ig(\mathbf{y}^k, \mathbf{x}), \\
 \frac{\partial g(\mathbf{y}^k, \mathbf{x})}{\partial a_\mu^k} &= i(u_1^2 + u_2^2)g(\mathbf{y}^k, \mathbf{x}), \\
 \frac{\partial g(\mathbf{y}^k, \mathbf{x})}{\partial a_\nu^k} &= i(u_3^2 + u_4^2)g(\mathbf{y}^k, \mathbf{x}), \\
 \frac{\partial g(\mathbf{y}^k, \mathbf{x})}{\partial a_x^k} &= i2(u_1u_3 - u_2u_4)g(\mathbf{y}^k, \mathbf{x}), \\
 \frac{\partial g(\mathbf{y}^k, \mathbf{x})}{\partial a_y^k} &= i2(u_1u_4 - u_2u_3)g(\mathbf{y}^k, \mathbf{x}).
 \end{aligned} \tag{6.16}$$

The resulting set of linear equations reads

$$\begin{aligned}
 \sum_{k=1}^N \left( I_{11}^{lk} v_0^k + I_{12}^{lk} \frac{1}{2} V_\mu^k + I_{13}^{lk} \frac{1}{2} V_\nu^k + I_{14}^{lk} V_x^k + I_{15}^{lk} V_y^k \right) &= \sum_{k=1}^N I_{v1}^{lk} \\
 \sum_{k=1}^N \left( I_{12}^{lk} v_0^k + I_{22}^{lk} \frac{1}{2} V_\mu^k + I_{23}^{lk} \frac{1}{2} V_\nu^k + I_{24}^{lk} V_x^k + I_{25}^{lk} V_y^k \right) &= \sum_{k=1}^N I_{v2}^{lk} \\
 \sum_{k=1}^N \left( I_{13}^{lk} v_0^k + I_{23}^{lk} \frac{1}{2} V_\mu^k + I_{33}^{lk} \frac{1}{2} V_\nu^k + I_{34}^{lk} V_x^k + I_{35}^{lk} V_y^k \right) &= \sum_{k=1}^N I_{v3}^{lk} \\
 \sum_{k=1}^N \left( I_{14}^{lk} v_0^k + I_{24}^{lk} \frac{1}{2} V_\mu^k + I_{34}^{lk} \frac{1}{2} V_\nu^k + I_{44}^{lk} V_x^k + I_{45}^{lk} V_y^k \right) &= \sum_{k=1}^N I_{v4}^{lk} \\
 \sum_{k=1}^N \left( I_{15}^{lk} v_0^k + I_{25}^{lk} \frac{1}{2} V_\mu^k + I_{35}^{lk} \frac{1}{2} V_\nu^k + I_{45}^{lk} V_x^k + I_{55}^{lk} V_y^k \right) &= \sum_{k=1}^N I_{v5}^{lk}, \quad (6.17)
 \end{aligned}$$

with  $l = 1, \dots, N$ . The integrals are listed in appendix A.3. The matrix  $K$  associated with the set of linear equations (6.17) is Hermitean as shown in eq. (2.11) and the integrals have the properties  $I_{ij}^{lk} = (I_{ij}^{kl})^*$  and  $I_{ij}^{lk} = I_{ji}^{lk}$ . The potential enters the right hand side. As mentioned, the equations of motion have the familiar form (5.39), i.e.

$$\dot{A}^k = -2(A^k)^2 - \frac{1}{2}V_2^k \quad (6.18a)$$

$$\dot{\gamma}^k = -v_0^k + i \text{tr} A^k, \quad (6.18b)$$

with  $k = 1, \dots, N$ . As usual it is recommended to make the substitution  $A^k = \frac{1}{2}B^k(C^k)^{-1}$ , c.f. eq. (3.31) and to integrate the eq. (3.32) rather than integrating eq. (6.18a) directly. As mentioned in chapter 3 these matrices  $B^k, C^k$  are no more complex symmetric. In the  $4D$  KS coordinates the introduction of the  $B^k, C^k$  matrices would lead to an increase of the number of parameters that have to be integrated from four complex parameters in the width matrix  $A^k$  per GWP to a number of 32 complex parameters per GWP in the two matrices  $B^k, C^k$ . However, the special symmetry of the matrices  $A^k$  (5.35) can be exploited to halve the number of parameters from 32 to 16 in the matrices  $B^k, C^k$ . A further reduction of the parameters from 16 to 12 is possible but it turns out that the resulting equations of motion are numerically unstable. Details concerning the reduction from 32 to 16 parameters are explained in appendix B.

In order to leave the Cartesian form of the Laplace operator in KS coordinates unchanged, the paramagnetic term is incorporated in the potential of the Hamiltonian (6.4) and enters the matrix equation (6.17) on the right hand side vector.

Two numerical examples are presented for the propagation of the GWP (5.54) with the same width  $\sigma = 3.5$ , the same initial position  $\mathbf{x}_0 = (6, 0, 0)$  and the two different initial mean momenta  $\mathbf{p}_0 = (0, \pm 1/\sqrt{2}, 1/\sqrt{2})$ , i.e. two initial GWPs are propagated, one

with the positive  $p_{y_0}$  component and one with the negative. The GWPs start running in opposite directions around the  $z$ -axis. The parameters of the Hamiltonian (6.4) are  $\alpha = 0.5$ ,  $\beta = 0.05$ ,  $\zeta = 0.01$ . The damping constant of the restricted GWPs is set to  $\epsilon = 0.15$ .  $N = 41$  and  $N = 31$  basis states are employed, respectively. For a better numerical performance constraints on the imaginary parts of the phase parameters  $\gamma^k$  of the form (4.18) introduced in section 4.3 with  $\gamma_{\min} = -4.0$  are applied. To reduce the number of frequencies in the time signal the states of odd and even parity are investigated separately. This is achieved by the projection of the propagates wave packet into the subspaces  $\psi_{\mathbf{x}_0\mathbf{p}_0}^s(x, y, z) = \psi_{\mathbf{x}_0\mathbf{p}_0}(x, y, z) + \psi_{\mathbf{x}_0\mathbf{p}_0}(x, y, -z)$  and  $\psi_{\mathbf{x}_0\mathbf{p}_0}^a(x, y, z) = \psi_{\mathbf{x}_0\mathbf{p}_0}(x, y, z) - \psi_{\mathbf{x}_0\mathbf{p}_0}(x, y, -z)$ . The spectra obtained from Fourier transforming the auto-correlation functions  $C^P(\tau) = \langle \psi_{\mathbf{x}_0\mathbf{p}_0}^P(0) | \psi_{\mathbf{x}_0\mathbf{p}_0}^P(\tau) \rangle$ ,  $P = s, a$  associated with the two propagated wave functions are shown in fig. 6.5. The green line is the result of the propagation with the positive mean momentum component  $p_{y_0} = 1/\sqrt{2}$ , the red line follows from the propagation of the GWP (5.54) with  $p_{y_0} = -1/\sqrt{2}$ . Fig. 6.5(a) shows the results for the symmetrized states with even parity and fig. 6.5(b) presents the results for the states with odd parity. The eigenvalues obtained from numerically exact computations are shown by the blue impulses. Comparison shows good agreement between the exact results and the results obtained by the wave packet propagation. In the perturbative regime of the chosen field strengths the paramagnetic term is dominant as compared to the diamagnetic contribution. The direction of the initial mean momentum of the two examples, i.e. clockwise or anticlockwise around the  $z$ -axis, determines the sign of the angular momentum quantum number  $m$ , such that the lower and the higher levels in the spectrum of fig. 6.5 within one multiplet are excited.

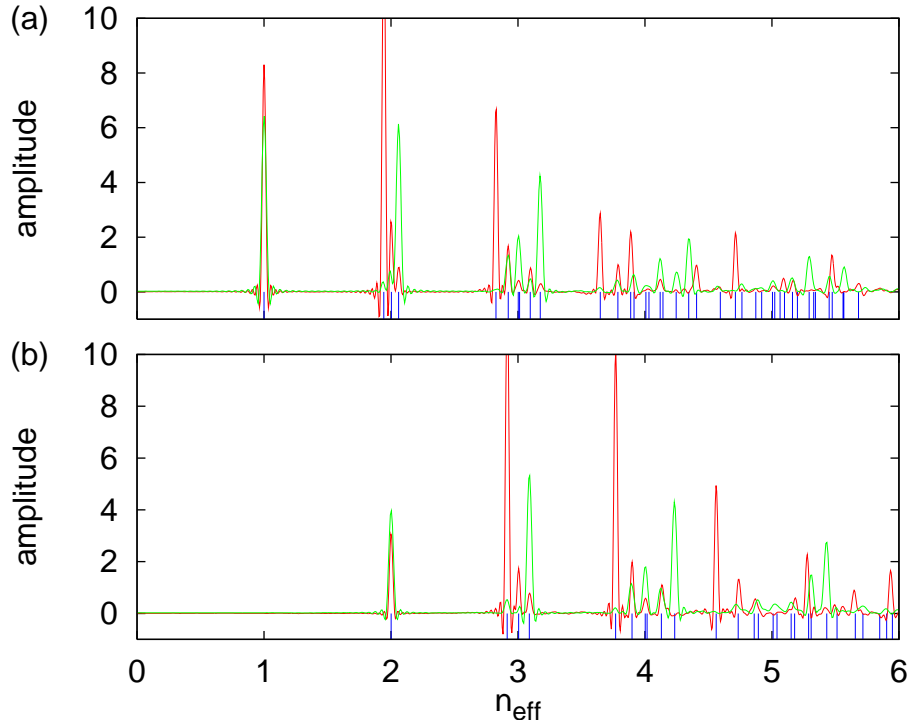


Figure 6.5.: Spectra obtained from the propagation of two different GWP's of the form (5.54) with  $\mathbf{x}_0 = (6, 0, 0)$ ,  $\mathbf{p}_0 = (0, \pm 1/\sqrt{2}, 1/\sqrt{2})$ , and  $\sigma = 3.5$ . The green line is the result of the propagation of the GWP with the positive  $y$ -component of the mean momentum  $p_{y_0} = 1/\sqrt{2}$  the red line is the result of  $p_{y_0} = -1/\sqrt{2}$ . (a) Projection to states with even parity and (b) states with odd parity. The eigenvalues are extracted from the auto-correlation function by Fourier transformation. The positions of the eigenvalues of the effective quantum number  $n_{\text{eff}}$  agree very good with numerically exact computations (blue impulses). The parameters of the Hamiltonian (6.4) are  $\alpha = 0.5$ ,  $\beta = 0.05$ ,  $\zeta = 0.01$ . The related eigenenergies and the field strengths follow simply from eq. (6.5).

## 7. Wave packet dynamics of Bose-Einstein condensates with attractive $1/r$ interaction

In this chapter and in chapter 8 the method of GWP propagation is applied to cold quantum gases described by the nonlinear Gross-Pitaevskii (GP) equation. Gaussian type trial functions have been used for time-dependent [33], and especially for time-independent variational computations [31, 32] on Bose-Einstein condensates. The nonlinearity of the Gross-Pitaevskii equation offers a variety of different qualitative dynamical behavior, which is not known from the linear Schrödinger equation, like bifurcations and collapsing wave functions. Additionally to the standard short-range contact interaction term contained in the GP equation long-range particle interactions may occur in cold quantum gases. Of particular interest are the properties of degenerate quantum gases in which the relative strengths of long- and short-range interactions can be continuously adjusted by tuning the contact interaction via a Feshbach resonance [34, 35].

The method of GWP propagation according to the TDVP is applied to two different kinds of long-range interactions. The isotropic, attractive  $1/r$  long-range interaction in a Bose-Einstein condensate (BEC) [31] is treated in this chapter. In chapter 8 the dynamics of a BEC with the anisotropic magnetic dipole-dipole interaction [66–70] is investigated.

Bose-Einstein condensation of neutral atoms with electromagnetically induced attractive  $1/r$  interaction has been proposed by O’Dell et al. [71]. “Monopolar” quantum gases could be realized by a combination of 6 appropriately arranged “triads” of intense off-resonant laser beams. In that arrangement, the  $1/r^3$  interactions of the retarded dipole-dipole interaction of neutral atoms in the presence of intense electromagnetic radiation are averaged out in the near-zone limit, while the weaker  $1/r$  interaction is retained. An outstanding feature of this type of long-range interaction is that for attractive contact interaction stable Bose-Einstein condensates are predicted that are *self-bound* (without an additional trap). Collapse of the self-bound condensates sets in below some critical value of the scattering length.

It was recently shown [32] that these critical values in fact correspond to bifurcation points where two solutions of the Gross-Pitaevskii disappear: one is the true ground state, and the other a collectively excited state. It was also demonstrated [72] that at the bifurcation the two stationary solutions exhibit the typical structure known from stud-

ies of *exceptional points* [73–77] in open quantum systems described by non-Hermitian Hamiltonians. At the exceptional points both the energies *and* the corresponding wave functions are identical, a situation which is forbidden for bound states of the linear Schrödinger equation (which must be orthogonal) but is possible here because of the nonlinearity of the Gross-Pitaevskii equation.

Using a complex continuation of the Gross-Pitaevskii equation the existence of complex eigenstates at (real) negative scattering lengths below the bifurcation point has also been revealed [72]. The physical interpretation of these states is the collapse (or explosion) of the condensate with a decay rate given by the imaginary part of the complex eigenvalues of the chemical potential.

It is the purpose of this chapter to analyze self-bound spherically symmetric Bose-Einstein condensates with attractive  $1/r$  interaction in the vicinity of the bifurcation points from the point of view of nonlinear dynamics, and to investigate the time evolution of arbitrary condensate wave functions. We do this by solving the time-dependent Gross-Pitaevskii equation both by means of a variational approach with time-dependent Gaussian wave packets and by exact numerical computations using the split-operator method. We will show that of the two stationary solutions created in a tangent bifurcation one is dynamically stable and the other unstable, corresponding to elliptic and hyperbolic fixed points, respectively. The stable state is surrounded by solutions periodically oscillating in time, whereas wave functions in the unstable region undergo a collapse within finite time. Below the tangent bifurcation no stationary solutions exist, i.e., the condensate is always unstable and collapsing.

The special appeal of investigations of the properties of spherically symmetric self-trapped Bose-Einstein condensates with attractive  $1/r$  interaction lies in the fact that the extremization of the variational mean-field energy can be carried out fully analytically. The reason is that in absence of a trap the extremization conditions for the mean-field energy become quadratic equations, while with a trap potential the equations become at least polynomials of order 5, caused by the combination of the trap and contact interaction terms, regardless of whether or not a long-range interaction is present, and of its type. Therefore generic properties of Bose-Einstein condensates can be elucidated in a very simple and transparent way, and later be checked in numerical calculations and in more complex systems such as dipolar Bose-Einstein condensates in chapter 8.

The evolution of a wave function is determined by the time-dependent extended Gross-Pitaevskii equation for self-trapped Bose-Einstein condensates with attractive  $1/r$  interaction without external trap potential, which reads

$$i\frac{d}{dt}\psi(\mathbf{r},t) = \left( -\Delta + 8\pi Na|\psi(\mathbf{r},t)|^2 - 2N \int d^3\mathbf{r}' \frac{|\psi(\mathbf{r}',t)|^2}{|\mathbf{r}-\mathbf{r}'|} \right) \psi(\mathbf{r},t), \quad (7.1)$$

where the natural “atomic” units introduced in Ref. [32] were used. Lengths are measured in units of a “Bohr radius”  $a_u = \hbar^2/(mu)$ , energies in units of a “Rydberg energy”  $E_u = \hbar^2/(2ma_u^2)$ , and times in units of  $t_u = \hbar/E_u$ , where  $u$  determines the strength of

the atom-atom interaction [31], and  $m$  is the mass of one boson. The number of bosons is  $N$  and  $a$  is the scattering length.

## 7.1. TDVP for BECs with attractive $1/r$ interaction

The TDVP is applied to solving the time-dependent Gross-Pitaevskii equation 7.1. Exploiting the scaling properties presented in ref. [32] and introducing the scaled variables

$$(\tilde{\mathbf{r}}, \tilde{a}, \tilde{t}, \tilde{\psi}) = (Nr, N^2a, N^2t, N^{-3/2}\psi), \quad (7.2)$$

the system is transformed to

$$i\frac{d}{d\tilde{t}}\tilde{\psi}(\tilde{\mathbf{r}}, \tilde{t}) = \tilde{H}\tilde{\psi}(\tilde{\mathbf{r}}, \tilde{t}) = \left[-\Delta_{\tilde{\mathbf{r}}} + \tilde{V}_c + \tilde{V}_u\right]\tilde{\psi}(\tilde{\mathbf{r}}, \tilde{t}), \quad (7.3)$$

where the potentials

$$\tilde{V}_c = 8\pi\tilde{a}|\tilde{\psi}(\tilde{\mathbf{r}}, \tilde{t})|^2, \quad (7.4a)$$

$$\tilde{V}_u = -2 \int d^3\tilde{\mathbf{r}}' \frac{|\tilde{\psi}(\tilde{\mathbf{r}}', \tilde{t})|^2}{|\tilde{\mathbf{r}} - \tilde{\mathbf{r}}'|} \quad (7.4b)$$

depend on the coordinates and the wave function, i.e.,  $\tilde{H}$  is a *nonlinear* operator. The scaling reveals that the system has only one external parameter, viz.  $\tilde{a} = N^2a/a_u$  [32]. If not stated otherwise, we use the scaled variables throughout the rest of this chapter and omit the tilde in what follows.

In time-independent calculations for condensates with  $1/r$  interaction Gaussian wave functions have been used as an ansatz for the two stationary solutions created in the tangent bifurcation [31, 32]. To apply the TDVP to the Gross-Pitaevskii equation (7.3) we choose as a test function a radially symmetric Gaussian wave packet

$$\psi(r, t) = e^{i(Ar^2 + \gamma)} = e^{-(A_i r^2 + \gamma_i) + i(A_r r^2 + \gamma_r)} \quad (7.5)$$

with the time-dependent variational parameters

$$\mathbf{z}(t) = \{A(t), \gamma(t)\} = \{A_r(t) + iA_i(t), \gamma_r(t) + i\gamma_i(t)\}. \quad (7.6)$$

A similar time-dependent Gaussian trial function has been applied in studies of the dynamics of the Gross-Pitaevskii equation in an external trap without  $1/r$  interaction [33]. In contrast to the previous chapters a single GWP is employed here as the trial function and proves to be sufficient to obtain qualitatively correct results. In the context of Cartesian coordinates the complex width matrix  $\bar{A}$  of the GWP is a multiple of the identity matrix  $\bar{A} = A\mathbf{1}_3$ , such that the trace of the matrix  $\bar{A}$  is  $3A$ . The equations of motion read

$$\dot{A} = -4A^2 - \frac{1}{2}V_2, \quad (7.7a)$$

$$\dot{\gamma} = 6iA - v_0. \quad (7.7b)$$

Note that eqs. (7.7) slightly differ from eqs. (6.18) because the ‘‘Rydberg’’ like energy unit introduced above removes the factor  $1/2$  in the kinetic energy operator in the GP equation (7.1). According to the TDVP, the coefficients  $v_0$  and  $V_2$  are obtained as the solution of a matrix equation, c.f. (3.28). To set up the linear equations the derivatives of the trial function (7.5) with respect to  $\gamma$  and  $A$  are required in analogy to eq. (3.11). They read

$$\frac{\partial\psi(r,t)}{\partial\gamma} = i\psi(r,t), \quad \frac{\partial\psi(r,t)}{\partial A} = ir^2\psi(r,t), \quad (7.8)$$

and thus  $v_0$  and  $V_2$  are the solution of the two linear equations

$$\langle\psi|\psi\rangle v_0 + \frac{1}{2}\langle\psi|r^2|\psi\rangle V_2 = \langle\psi|V_c + V_u|\psi\rangle, \quad (7.9a)$$

$$\langle\psi|r^2|\psi\rangle v_0 + \frac{1}{2}\langle\psi|r^4|\psi\rangle V_2 = \langle\psi|r^2(V_c + V_u)|\psi\rangle. \quad (7.9b)$$

The integrals are calculated in appendix A.4. Inserting  $v_0$  and  $V_2$  in (7.7a) and (7.7b) yields the differential equations

$$\dot{A} = -4A^2 + \pi 2\sqrt{2}e^{-2\gamma_i} \left( aA_i - \frac{1}{6} \right), \quad (7.10a)$$

$$\dot{\gamma} = 6iA + \frac{\pi e^{-2\gamma_i}}{2\sqrt{2}A_i} (5 - 14aA_i). \quad (7.10b)$$

The imaginary part of eq. (7.10b) can be integrated analytically,

$$\gamma_i(t) = -\frac{3}{4} \ln \frac{2A_i(t)}{\pi}, \quad (7.11)$$

and guarantees the normalization condition  $\|\psi\|^2 = 1$ . The final form of the equations of motion in real number representation is given by

$$\dot{A}_r = -4(A_r^2 - A_i^2) + \frac{8}{\sqrt{\pi}} A_i^{3/2} \left( aA_i - \frac{1}{6} \right), \quad (7.12a)$$

$$\dot{A}_i = -8A_r A_i, \quad (7.12b)$$

$$\dot{\gamma}_r = -6A_i + \frac{1}{\sqrt{\pi}} \sqrt{A_i} (5 - 14aA_i), \quad (7.12c)$$

which are solved under the initial conditions  $A_r(0) = \gamma_r(0) = 0$ ,  $A_i(0) > 0$  for an initially real valued Gaussian wave packet.

## 7.2. Linear stability of the bifurcating states

In this section we study the stability of the two stationary eigenstates that are born in the tangent bifurcations. The analysis is adopted from Refs. [78, 79], where variational



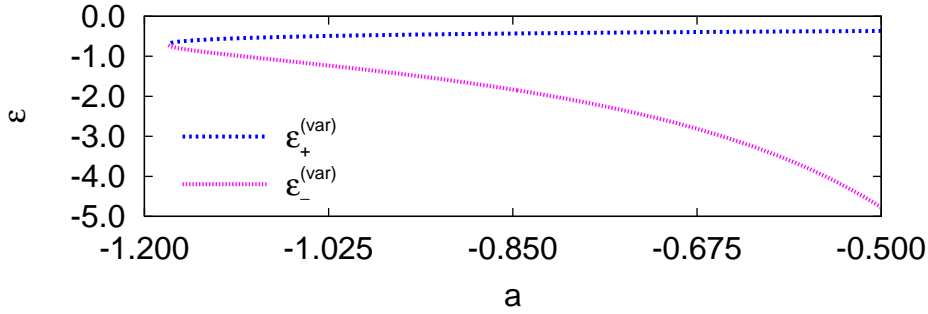


Figure 7.1.: Chemical potentials of the ground state ( $\varepsilon_+$ ) and the nodeless excited state ( $\varepsilon_-$ ) in the variational calculation. They emerge in a tangent bifurcation at a critical value of the scaled scattering length  $a_{\text{cr}} = -3\pi/8 = -1.1780$  [32, 72, 79].

and numerical results are presented. Here we focus on the variational results of the stability analysis.

In the time-dependent variational approach, the two stationary states of the Gross-Pitaevskii equation (7.3) appear as the time-independent solutions (fixed points) of the equations of motion (7.12). Requiring  $\dot{A}_i = 0$  and  $\dot{A}_r = 0$  immediately leads to

$$\hat{A}_r = 0, \quad (7.13a)$$

$$\hat{A}_i = \frac{1}{6a} + \frac{\pi}{8a^2} \left( 1 \pm \sqrt{1 + \frac{8a}{3\pi}} \right). \quad (7.13b)$$

The vanishing of the real part of  $\hat{A}$  implies that the state indeed is a stationary Gaussian. The scaled chemical potentials  $\varepsilon$  are given by the negative time derivative  $-\dot{\gamma}_r$  of the phase of the wave function in eq. (7.12c)

$$\varepsilon_{\pm}^{(\text{var})} = -\dot{\gamma}_r = -\frac{4}{9\pi} \frac{5 \pm 4\sqrt{1 + \frac{8a}{3\pi}}}{\left(1 \pm \sqrt{1 + \frac{8a}{3\pi}}\right)^2}. \quad (7.14)$$

The chemical potentials of the two solutions (7.14) are drawn in fig. 7.1. The tangent bifurcation behavior of the chemical potential at the critical scattering length  $a_{\text{cr}} = -3\pi/8 = -1.1780$  is clearly visible. The branch with the lower chemical potential in fig. 7.1 turns out to have higher mean-field energy than the other branch [32]. Therefore the plus sign refers to the ground state, and the minus sign to the collectively excited state. The results obtained here via the fixed points of the time-dependent equations of motion for the variational parameters fully agree with the results derived in Refs. [31, 32] applying a time-*independent* variational approach to extremize the mean-field energy,

and which were used to compare with numerically exact solutions of the stationary extended Gross-Pitaevskii equation in Refs. [32, 72].

The linearization of the equations of motion (7.12) around the stationary solutions  $\hat{A}_r, \hat{A}_i$  are given by

$$\delta\dot{A}_{r\pm} = \pm \frac{4}{9\pi} \frac{\sqrt{1 + \frac{8a}{3\pi}}}{\left(\sqrt{1 + \frac{8a}{3\pi}} \pm 1\right)^2} \delta A_{i\pm}, \quad (7.15a)$$

$$\delta\dot{A}_{i\pm} = -\frac{16}{9\pi} \frac{1}{\left(\sqrt{1 + \frac{8a}{3\pi}} \pm 1\right)^2} \delta A_{r\pm}. \quad (7.15b)$$

The eigenmodes with the eigenvalues  $\lambda$  of eqs. (7.15) are calculated with the usual ansatz  $\delta A_{r,i}(t) = \delta A_{r,i}^{(0)} e^{\lambda t}$ . For the stationary ground state we find the two eigenvalues

$$\lambda_+ = \pm \frac{8i}{9\pi} \frac{\sqrt[4]{1 + \frac{8a}{3\pi}}}{\left(\sqrt{1 + \frac{8a}{3\pi}} + 1\right)^2}, \quad (7.16)$$

which are always imaginary for  $a > -3\pi/8$  (i.e., above the bifurcation point). They describe an *elliptic fixed point*, which is stable. The two eigenvalues of the excited stationary state,

$$\lambda_- = \pm \frac{8}{9\pi} \frac{\sqrt[4]{1 + \frac{8a}{3\pi}}}{\left(\sqrt{1 + \frac{8a}{3\pi}} - 1\right)^2}, \quad (7.17)$$

are always real for negative scattering lengths  $a > -3\pi/8$ , and one eigenvalue is positive. Hence, the eigenstate is unstable and belongs to a *hyperbolic fixed point*.

## 7.3. Dynamics of the condensate

In this section we investigate the time evolution of the BEC. We do this first by the variational approach and then by exact numerical calculations. The variational calculations will reveal the different types of dynamics in the vicinity of the elliptic and the hyperbolic fixed points, viz. oscillatory or collapsing solutions. Furthermore, the collapse of the condensate for  $a < a_{\text{cr}}$  can be followed as a function of time. The numerically exact approach will confirm these findings and, in addition, exhibit a larger variety of qualitatively different dynamical behavior of the condensate.

### 7.3.1. Variational approach

We solve the two ordinary differential equations (7.12a) and (7.12b) for various scaled scattering lengths  $a$  above and below the critical value  $a_{\text{cr}} = -3\pi/8 = -1.1780$ . Phase

portraits of the dynamics can be obtained by plotting the imaginary part as a function of the real part of the time-dependent trajectories  $A(t) = A_r(t) + iA_i(t)$ . The phase portraits of trajectories with different initial conditions are shown in fig. 7.2 for three values of the scaled scattering length, one above the bifurcation point ( $a = -1$ , fig. 7.2(a)), one near the bifurcation point ( $a = -1.18$ , fig. 7.2(b)), and one below the bifurcation point ( $a = -1.3$ , fig. 7.2(c)). For  $a > a_{\text{cr}}$  the elliptic and the hyperbolic fixed points are clearly recognizable in fig. 7.2(a), they correspond to the stationary eigenstates. The two fixed points coalesce at the critical scattering length  $a_{\text{cr}}$  (see fig. 7.2(b)), and disappear for  $a < a_{\text{cr}}$  (fig. 7.2(c)) implying that stationary eigenstates no longer exist.

For the physical interpretation of the phase portraits it is useful to note that the width  $\sqrt{\langle r^2 \rangle(t)}$  of the condensate is related to  $A_i(t)$  via

$$\langle r^2 \rangle(t) = \frac{\langle \psi | r^2 | \psi \rangle}{\langle \psi | \psi \rangle} = \frac{3}{4A_i(t)}. \quad (7.18)$$

Thus, in the stable region surrounding the elliptic fixed point the width of the condensate oscillates periodically. This is illustrated in fig. 7.3 for a condensate with scattering length  $a = -1$  and initial condition  $A_i(0) = 0.3$ .

In the unstable regions  $A_i(t)$  increases to infinity, which means the collapse of the condensate. In fig. 7.4(a) the width  $\sqrt{\langle r^2 \rangle}$  is shown for a condensate with scaled scattering length  $a = -1$  and initial condition close to the hyperbolic fixed point, given by eqs. (7.13a) and (7.13b) at  $A_r = 0$ ,  $A_i = 0.3787$ . The width first stays approximately constant, as is to be expected in the vicinity of the unstable stationary state, however, as soon as the decrease of the width becomes noticeable, the complete collapse to zero width occurs within finite time. This behavior demonstrates the existence of a collapse induced by the attractive atom-atom interactions. In a realistic experimental situation further mechanisms, which go beyond the scope of this thesis, have to be taken into account. In particular, the contraction of the wave function amplifies density-dependent inelastic collisions which result in a loss of particles [34, 80] and change the time evolution. Note that the calculations presented here assume a constant scaled scattering length (cf. eq. (7.2)). Of course, for initial conditions close to the hyperbolic fixed point the evolution of the collapse depends sensitively on the initial deviation from the fixed point, i.e., the closer the initial conditions approach the hyperbolic fixed point the longer it takes before the collapse sets in.

At scattering lengths  $a < a_{\text{cr}}$  the square root in eq. (7.13b) becomes imaginary which means that no fixed points and thus no stationary states can exist. The condensate collapses for all initial conditions  $A(0)$  of the wave function. This is illustrated for  $a = -1.3$  in fig. 7.4(b) with the initial condition of the “least” unstable non-stationary state,  $A_i(0) = \frac{1}{6a} + \frac{\pi}{8a^2} = 0.10416$  (cf. eq. (7.13b)). Contrary to the situation shown in fig. 7.4(a) the decrease of the condensate width starts immediately without any plateau. Ignoring a loss of particles we find that the width vanishes after the finite time  $T_c = 9.2522$ .

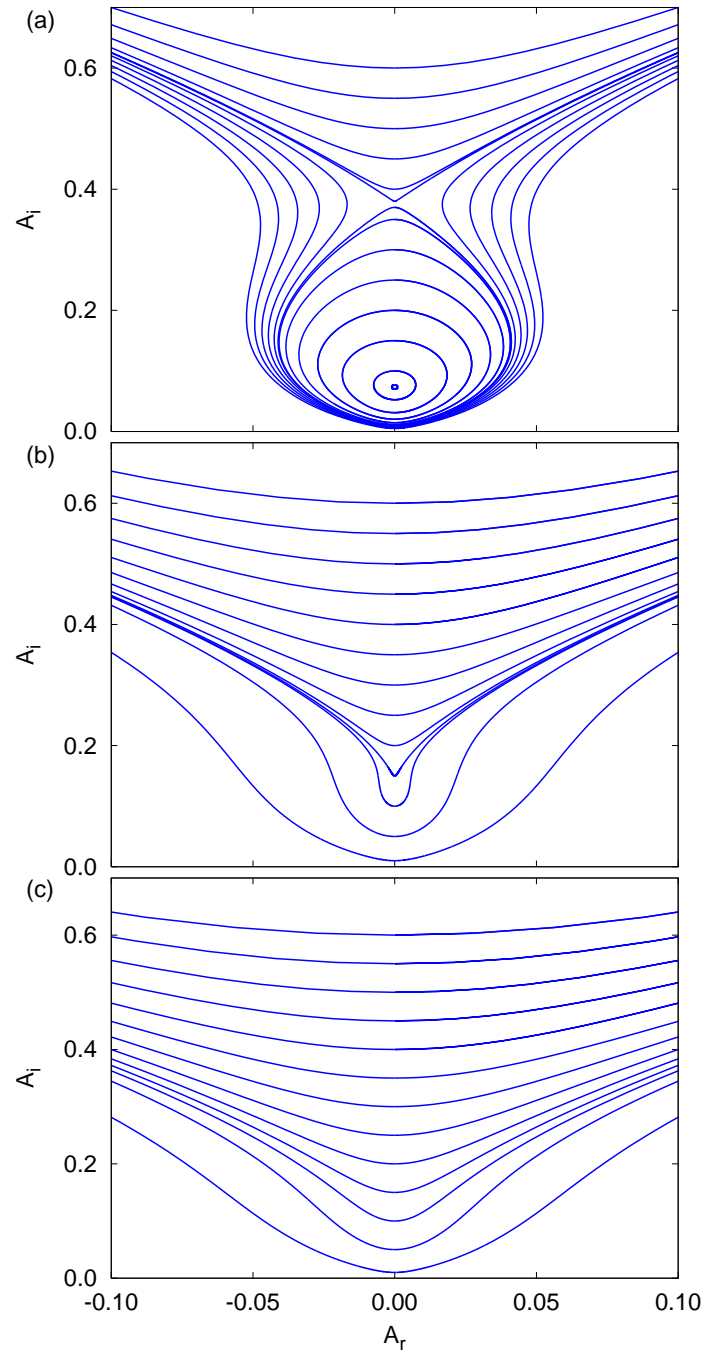


Figure 7.2.: Phase portraits of the dynamics obtained from time-dependent trajectories of the complex function  $A(t)$ . (a) For  $a = -1$  the two stationary solutions appear as fixed points. (b) They coalesce for  $a = -1.18$ . (c) For  $a = -1.3$ , below the bifurcation point, there are no stationary solutions.

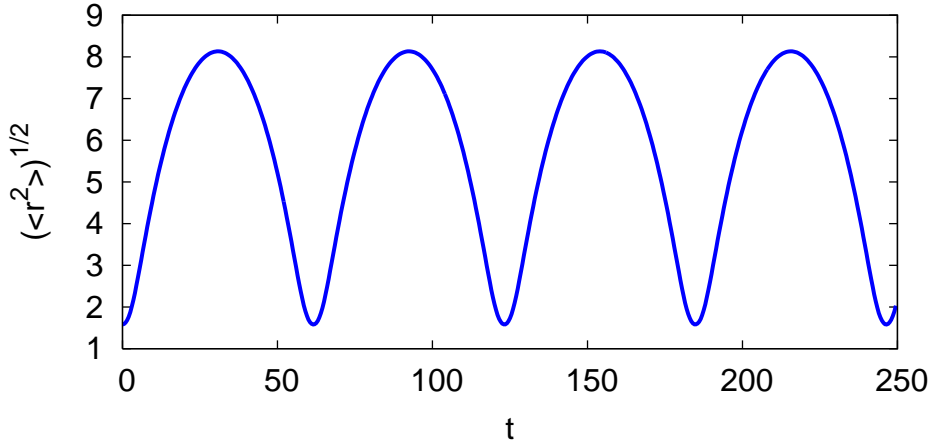


Figure 7.3.: Periodically oscillating condensate for the scattering length  $a = -1$  and the initial condition  $A_i(0) = 0.3$ .

The variational approach with complex parameters  $A(t)$  and  $\gamma(t)$  in eq. (7.5) ensures that the mean-field energy

$$E = \frac{3(A_i^2 + A_r^2)}{A_i} + \frac{2\sqrt{A_i}(2aA_i - 1)}{\sqrt{\pi}} \quad (7.19)$$

is conserved. Thus, the phase portraits in fig. 7.2 can be calculated alternatively as equipotential lines  $E = \text{const}$  instead of integrating the equations of motion (7.12).

In fact, the equations of motion obtained from the time-dependent variational principle can be brought into Hamiltonian form if the variational parameters  $A_r, A_i$  are replaced with two other dynamical quantities, of which one is assigned to be the momentum and the other the coordinate variable. Such adequate canonical variables are [37]

$$q = \frac{1}{2} \sqrt{\frac{3}{A_i}} = \sqrt{\langle r^2 \rangle}, \quad (7.20a)$$

$$p = A_r \sqrt{\frac{3}{A_i}}, \quad (7.20b)$$

and in this set the mean-field energy reads

$$E = H(q, p) = T + V = p^2 + \frac{9}{4q^2} + \frac{3\sqrt{3}a}{2\sqrt{\pi}q^3} - \frac{\sqrt{3}}{\sqrt{\pi}q} \quad (7.21)$$

with the decomposition into a “kinetic” part  $T$  depending on the “momentum”  $p$  and a “potential” part  $V$  depending only on the “coordinate”  $q$ . Note that  $q$  has the physical meaning of the square root of the radius of the condensate, according to equation (7.18).

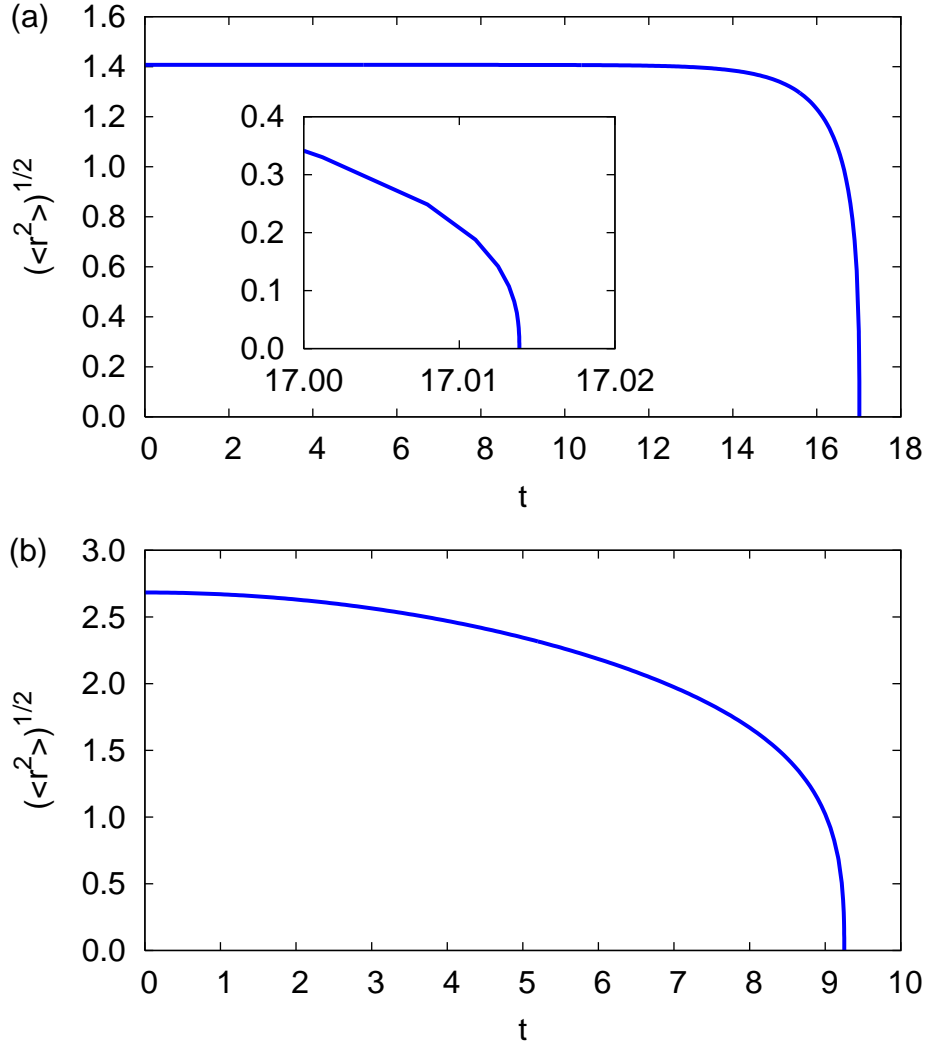


Figure 7.4.: Collapse of the unstable eigenstate. (a) Scaled scattering length  $a = -1$  and initial condition close to the hyperbolic fixed point at  $A_r = 0$ ,  $A_i = 0.3787$ . The collapse after finite time is clearly visible in the inset, but depends sensitively on the initial conditions (see text). (b) Collapse of the non-stationary state at  $a = -1.3$  with initial condition  $A_i(0) = \frac{1}{6a} + \frac{\pi}{8a^2} = 0.10416$ .

If the mean-field energy (7.21) is identified with a Hamiltonian, it describes the one-dimensional motion of a particle in the potential  $V(q)$  obeying Hamilton's equations:

$$\dot{q} = \frac{\partial H}{\partial p} = 2p, \quad (7.22a)$$

$$\dot{p} = -\frac{\partial H}{\partial q} = \frac{9}{2q^3} + \sqrt{\frac{3}{\pi}} \frac{9a}{2q^4} - \sqrt{\frac{3}{\pi}} \frac{1}{q^2}. \quad (7.22b)$$

Of course the backward substitution  $A_r = \frac{p}{2q}$ ,  $A_i = \frac{3}{4q^2}$  together with (7.22a) and (7.22b) yields the same equations of motion for  $A_r$  and  $A_i$  as obtained from the TDVP. Conversely, if the trial wave function (7.5) had been parametrized by  $q$ ,  $p$ ,  $\gamma$ , the TDVP would have yielded their equations of motion (7.22a) and (7.22b).

The ‘‘potential’’ part  $V(q)$  of the mean-field energy (7.21) is plotted in fig. 7.5 as a function of the ‘‘position’’ variable  $q$  for different scattering lengths below, at, and above the critical scattering length  $a_{cr}$ . It agrees with the mean-field energy plotted in Ref. [31], calculated using a real-valued spherically symmetric (stationary) Gaussian trial wave function. In our approach the ‘‘kinetic’’ term  $p^2$  in eq. (7.21) appears additionally in the mean-field energy because of the complex ansatz (7.5). In other words, the full mean-field energy of Ref. [31] corresponds to our potential part  $V$ , in which the condensate moves like a classical particle.

Above  $a_{cr}$  the potential possesses two stationary points, a stable one at the minimum and an unstable one at the maximum. At  $a_{cr}$  the bifurcation takes place, i.e., the two extrema coincide and there is only a saddle point of the potential. For  $a < a_{cr}$  the potential has no stationary points. For  $a > a_{cr}$  the motion of the condensate is stable as long as the mean-field energy lies below the maximum of the peak of the potential and if it is located close to the local minimum on the right-hand side of the unstable fixed point. The one-dimensional motion is periodic between two turning points. If the energy is increased above the energy of the unstable fixed point, only one turning point remains, and the condensate collapses when  $q$  approaches zero.

The phase space portrait of the dynamics in  $(p, q)$ -variables is presented in fig. 7.6 for the scattering length  $a = -0.8$ . The equipotential lines which asymptotically approach the  $q = 0$  axis represent the collapse of the condensate.

### 7.3.2. Exact time-dependent calculations with the split-operator method

To verify the validity of the variational approach we now compare the results obtained variationally with exact time-dependent calculations using the split-operator method. The split-operator method (c.f. appendix C and ref. [47]) assumes the decomposition of the Hamiltonian  $H = T + V$ , and makes use of the short-time approximation for the

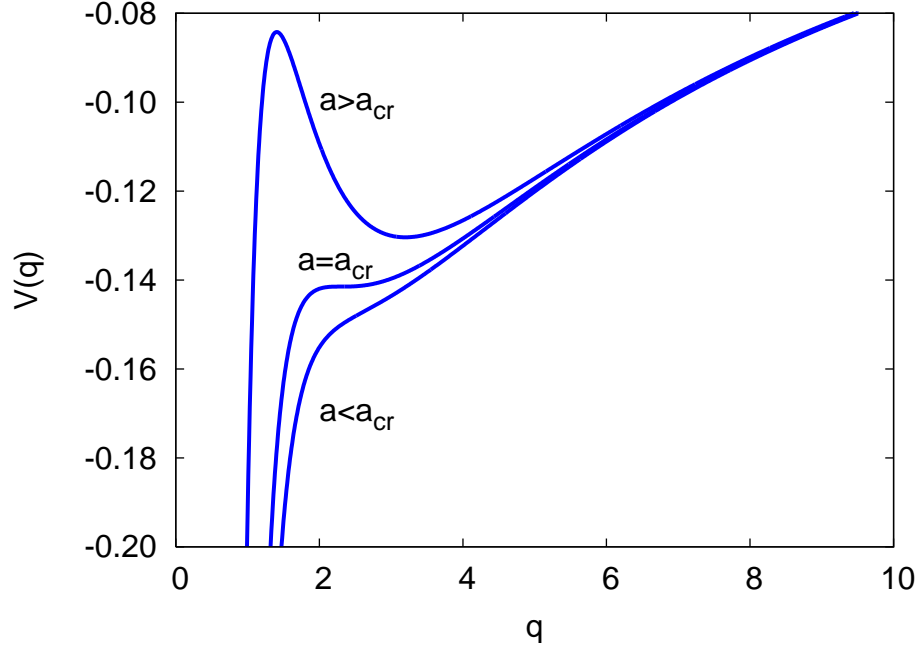


Figure 7.5.: “Potential” part of the mean-field energy for different scattering lengths. This potential part of the mean field energy (7.21) agrees with the complete mean-field energy for *stationary states* of Ref. [31] (see text). The motion of the Gaussian wave function is interpreted as the one-dimensional motion of a classical particle in the potential  $V(q)$ .

time evolution operator

$$e^{-i\tau(T+V)} = e^{-i(\tau/2)T} e^{-i\tau V} e^{-i(\tau/2)T} + O(\tau^3). \quad (7.23)$$

The kinetic part of the evolution operator is applied to the wave function in momentum space, the potential part is applied to the wave function in position space representation. The method is numerically especially efficient when a fast Fourier transform is used for the transition from momentum to position space representation and backwards. For the nonlinear Gross-Pitaevskii equation (7.3) the potential part of the time evolution operator needs some further investigation in comparison with the linear Schrödinger equation. Although the scattering term  $V_c$  belongs to the nonlinear part of the Gross-Pitaevskii equation, it can be treated like a conventional potential of a linear Schrödinger equation and presents no additional difficulty. The  $1/r$  interaction potential  $V_u$  however requires the additional solution of the integral (7.4b) after every time step of integration. This integral is computed using the convolution theorem, i.e.,

$$\mathcal{F}\{V_u(r, t)\} = \mathcal{F}\left\{\frac{1}{r}\right\} \mathcal{F}\{|\psi(r, t)|^2\}, \quad (7.24)$$



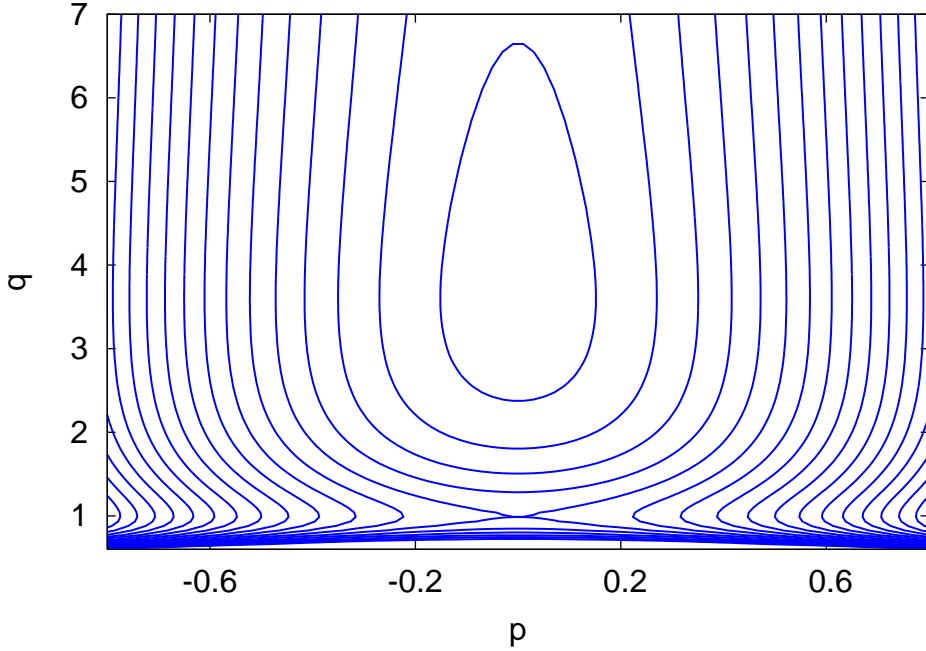


Figure 7.6.: Phase portrait of the mean-field energy formulated in the canonical variables  $q$  and  $p$  given by eqs. (7.20) for scaled scattering length  $a = -0.8$ .

where the Fourier transform of  $1/r$  is performed analytically

$$\mathcal{F}\left\{\frac{1}{r}\right\} = \frac{4\pi}{p^2}. \quad (7.25)$$

Altogether two additional fast Fourier transforms are necessary per time step and we obtain for the  $1/r$  interaction term

$$V_u(r, t) = -\frac{16}{r} \int_0^\infty dp \frac{\sin pr}{p^2} \int_0^\infty dr' r' |\psi(r', t)|^2 \sin pr'. \quad (7.26)$$

The fast Fourier transforms are performed on equidistant grids with 1024 or 2048 points. The numerical convergence is checked by monitoring that the wave function vanishes at the  $r_{\max}$ ,  $p_{\max}$  borders of the grids, both in position and in momentum space. Due to the widening of the wave function in some computations the necessary size of the grid depends on the desired propagation time. A criterion of convergence for the time step of the split-operator method is that the mean-field energy is a constant of motion. In particular for the computations in which the wave function is very close to the hyperbolic fixed point the time step must be chosen small for convergence. Specifically, for the computations in the vicinity of the hyperbolic fixed point we use  $\Delta t = 0.0001$  whereas for computations far away from the unstable stationary state a time step of  $\Delta t = 0.01$  is sufficient.

In the following, the dynamics of the condensate is investigated for regions initially close to the two stationary states. In particular, we present the evolution of those initial states which are obtained by deforming the stable and the unstable stationary state by

$$\psi \rightarrow \psi \cdot f, \quad r \rightarrow r/f^{2/3} \quad (7.27)$$

with a stretching factor  $f$ , i.e., for  $f = 1$  the stable and the unstable stationary state, respectively, are obtained. This choice of perturbation leaves the norm of the wave function unchanged.

We start with the investigation of the dynamics of wave functions close to the unstable stationary state. In fig. 7.7(a) the square root of the width (7.18) of the condensate is plotted as a function of time. The evolution presented in fig. 7.7(a) is computed at the scaled negative scattering length  $a = -0.85$  with a deformation factor  $f = 1.001$ . The wave function itself is plotted in fig. 7.7(b) as a function of the radial coordinate  $r$  at different times. The initial wave function is given by the solid red line. The condensate stays nearly stationary at the beginning for times up to  $t \approx 4$ , i.e., the dashed green line in fig. 7.7(b) representing the wave function at  $t = 4$  nearly coincides with the initial state, and the width (fig. 7.7(a)) has only slightly decreased from  $\sqrt{\langle r^2 \rangle} = 1.48$  at  $t = 0$  to  $\sqrt{\langle r^2 \rangle} = 1.44$  at  $t = 4.0$ . With increasing time and the farther away the wave function has moved from the stationary state, the shrinking of the width of the wave function is accelerated. As already predicted by the variational computation this leads to a collapse of the condensate at finite time. Both figs. 7.7(a) and 7.7(b) show that the width of the condensate tends to zero in position space when the collapse time  $T_c$  is approached. Conversely, in momentum space the wave function becomes arbitrarily wide close to  $T_c$ . Thus, the size of the grid in momentum space is the numerically limiting factor for the propagation with the split-operator method. Choosing a large grid in momentum space allows for integrating arbitrarily close to  $T_c$ .

According to the variational results there exist periodic solutions in the vicinity of the unstable stationary state, and, indeed, similar behavior is found in the numerically exact computations. In fig. 7.8(a) the width of a quasi-periodically oscillating condensate at  $a = -1.0$  is shown. The associated wave function is plotted in fig. 7.8(b) for different times. It can be seen that at the times where the root-mean-square extension of the condensate goes through a maximum, or minimum, there is also a good agreement of the respective wave functions. This shows that the wave functions indeed oscillate quasi-periodically. The calculation is started with the wave function of the unstable stationary state ( $f = 1$ ). Because of numerical deviations, the solution begins to oscillate for times larger than  $t \approx 25$ . In contrast to the variational result, the oscillation of the condensate is not strictly periodic here.

The dynamics of the condensate presented so far does not qualitatively differ from what is predicted by the variational calculation. In fig. 7.9(a), however, the situation is encountered where the width increases monotonically with time. Here we have chosen a deformation of  $f = 0.99$  at the scaled scattering length  $a = -0.85$ . For short times

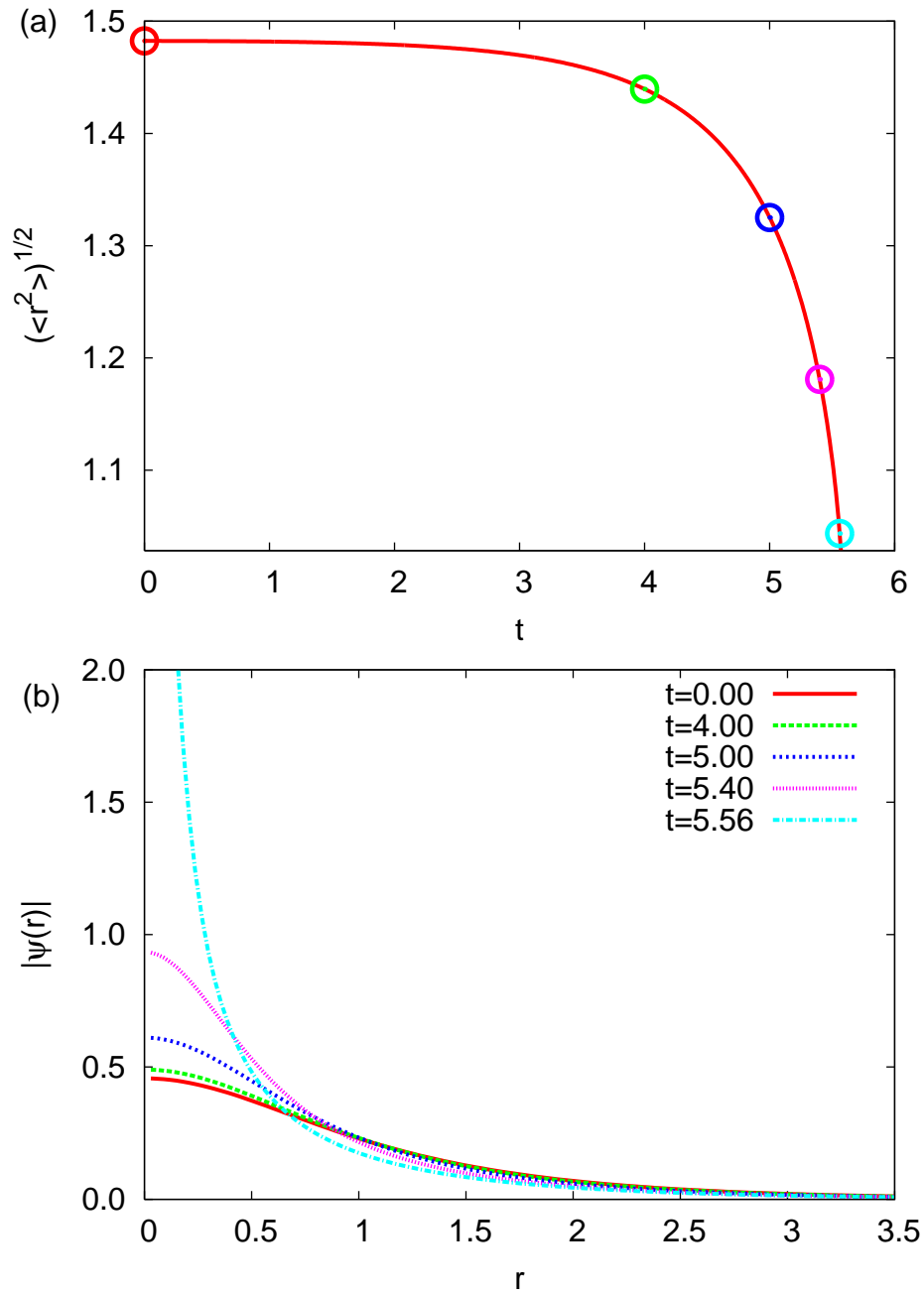


Figure 7.7.: (a) Width of a slightly perturbed stationary state ( $a = -0.85$ ,  $f = 1.001$ ) as a function of time. (b) Wave functions of the state for selected times marked by circles in (a). The collapse of the condensate is obvious from both plots.

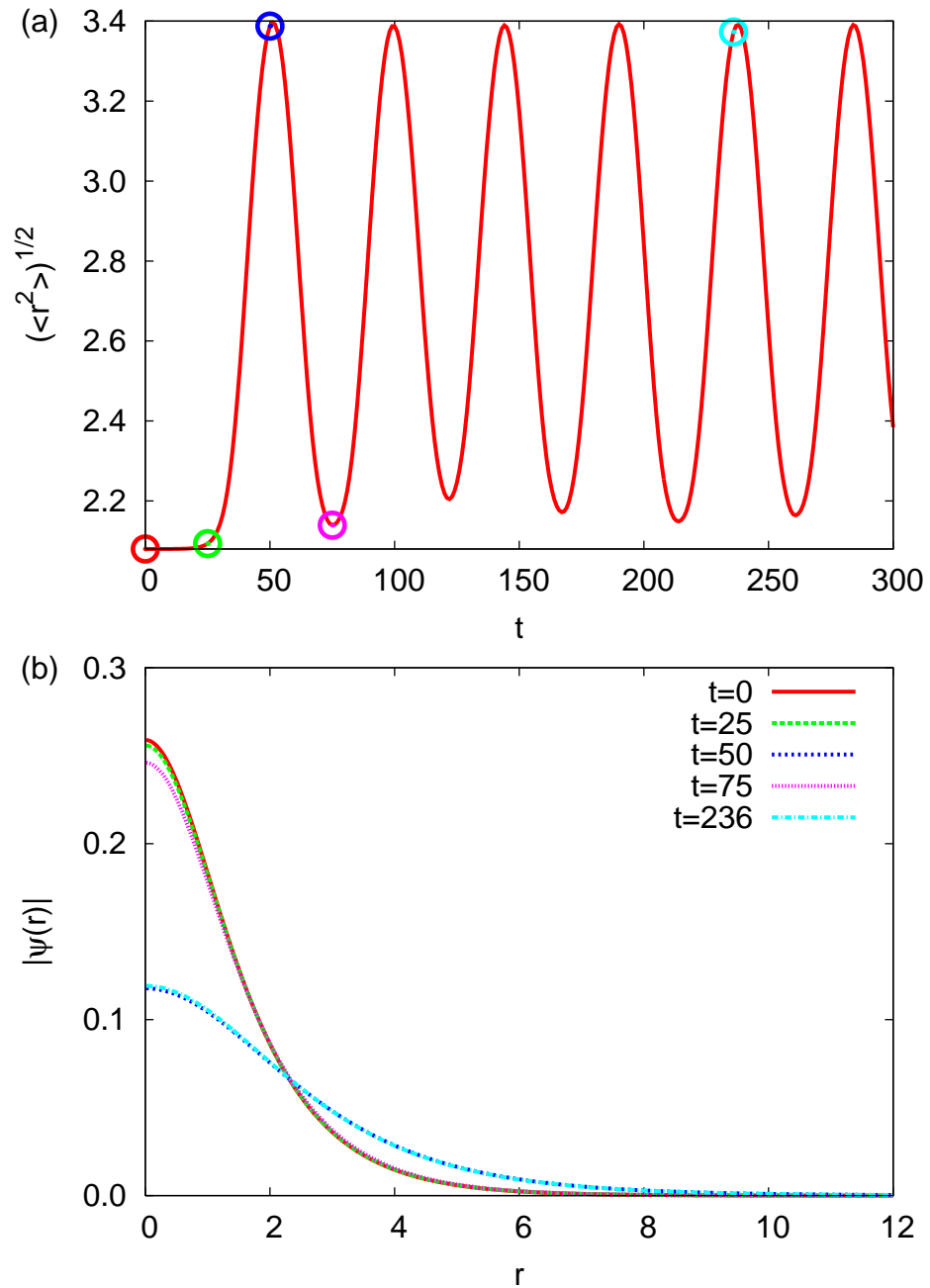


Figure 7.8.: Evolution of the unstable “stationary” state ( $f = 1$ ) at  $a = -1.0$ . (a) Due to numerical deviations an oscillation of the width starts for times larger than  $t \approx 25$ . (b) Corresponding wave functions for the times marked in (a).

there is again a plateau where the width is nearly constant as in fig. 7.8(a). The plateau is shorter than that in fig. 7.8(a) because the initial wave function of fig. 7.9(b) differs more from the stationary state than the initial state associated with fig. 7.8(a). For times  $t \gtrsim 65$ , however, the width increases linearly with time. Obviously, fig. 7.9(b) shows a broadening of the wave function for times up to  $t \approx 20$ . For longer times the main peak of the wave function located at the origin does not broaden monotonically with time as might be concluded from fig. 7.9(a). Indeed, the wave functions at  $t = 240$  and  $t = 400$  seem to be even sharper than the wave function at  $t = 20$  in fig. 7.9(b). This apparent contradiction is resolved, if the wave functions are plotted on a broader range in position space and on a logarithmic scale, which is presented in fig. 7.10. Here it is clearly visible that the wave functions have more than one peak and their width *does* increase for larger times. However, the amplitude of the run-away parts is very small compared to the first maximum at the origin. For obtaining the accurate propagation it is therefore necessary to choose a large grid in position space to make the wave function vanish on the border, in particular for long propagation times. The usual method to prevent the wave function from running to the border of the grid and being reflected there, namely to introduce an absorbing complex potential, is not applicable for the nonlinear Gross-Pitaevskii system, in which an absorption of the wave function alters the potential.

In the vicinity of the stable stationary state the condensate exhibits an oscillatory behavior shown in fig. 7.11(a). The parameter values for this computation are a stretching of  $f = 1.01$  of the stable stationary state at  $a = -0.85$ . The amplitude of the oscillation is very small compared to the oscillation in fig. 7.8(b) and ranges from about  $\sqrt{\langle r^2 \rangle} = 3.336$  to  $\sqrt{\langle r^2 \rangle} = 3.385$ . This observation is in correspondence with the variational result in fig. 7.2(a) where small deviations from the stable fixed point lead to small oscillations around the fixed point along the equipotential lines whereas small deviations from the unstable fixed point may lead to oscillations with a large amplitude. However, with increasing distance from the stable fixed point the dynamics is no longer oscillatory, but, as can be seen in fig. 7.11(b), there is also a gradual broadening of the condensate, which becomes more pronounced for larger deviations of the initial wave function from the stable stationary state as is shown in fig. 7.11(b), in which the time evolution of the width for  $f = 1.25$  is plotted. The scattering length is set to  $a = -0.85$  again. Here, the oscillatory motion at the beginning changes to a mainly expanding motion with minor modulations.

In general the exact computations qualitatively verify the variational results. In anisotropic condensates the variational approach will lead to autonomous Hamiltonian dynamics with more than one degree of freedom. Therefore in addition to the signatures discussed in this paper signatures of chaos can appear. The hope is that the variational predictions are as good as for the BEC with  $1/r$  interaction.

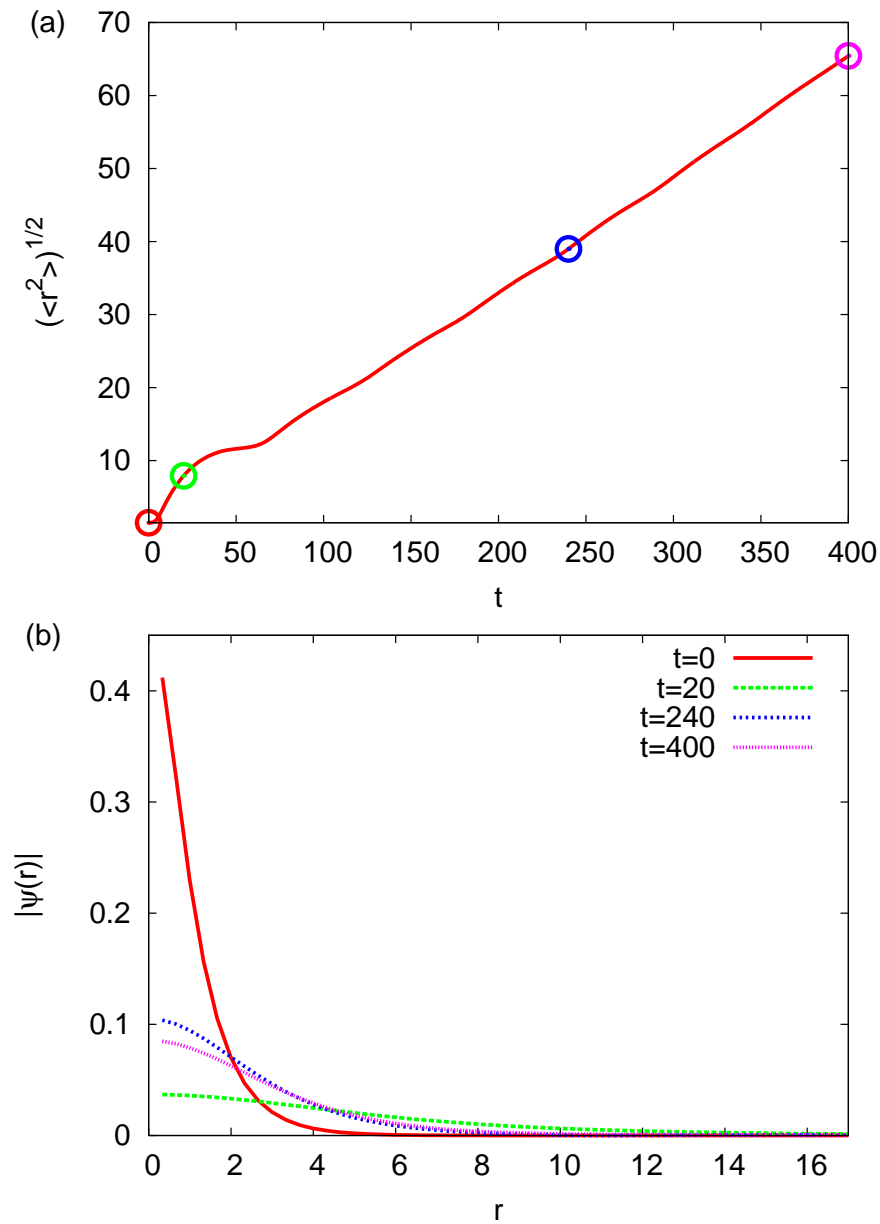


Figure 7.9.: (a) The width of the condensate, initially in the vicinity of the unstable fixed point with  $f = 0.99$  and  $a = -0.85$  increases linearly with time for  $t \gtrsim 65$ . (b) Wave functions of the same state for different times marked by circles in (a). The wave functions at  $t = 240$  and  $t = 400$  seem to be sharper than the wave function at  $t = 20$ . Note that a larger step size on the grid in position space than in figs. 7.7 and 7.8 was used. Therefore there is a visible distance between  $r = 0$  and the first point on the grid.

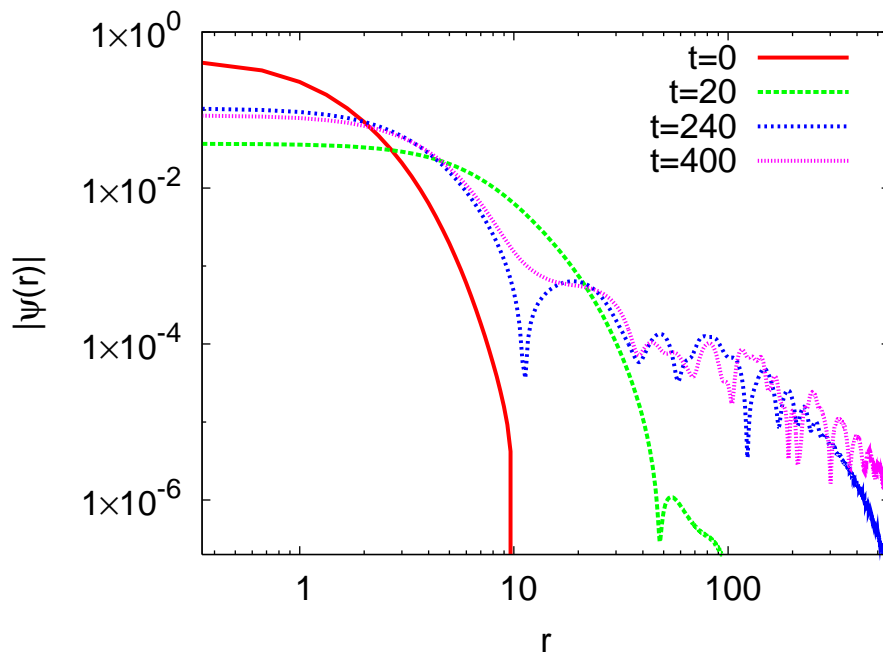


Figure 7.10.: Double logarithmic plot of the wave functions presented in fig. 7.9(b). The long-range tail occurring with increasing propagation times and leading to a monotonically increasing width in fig. 7.9(a) becomes visible.

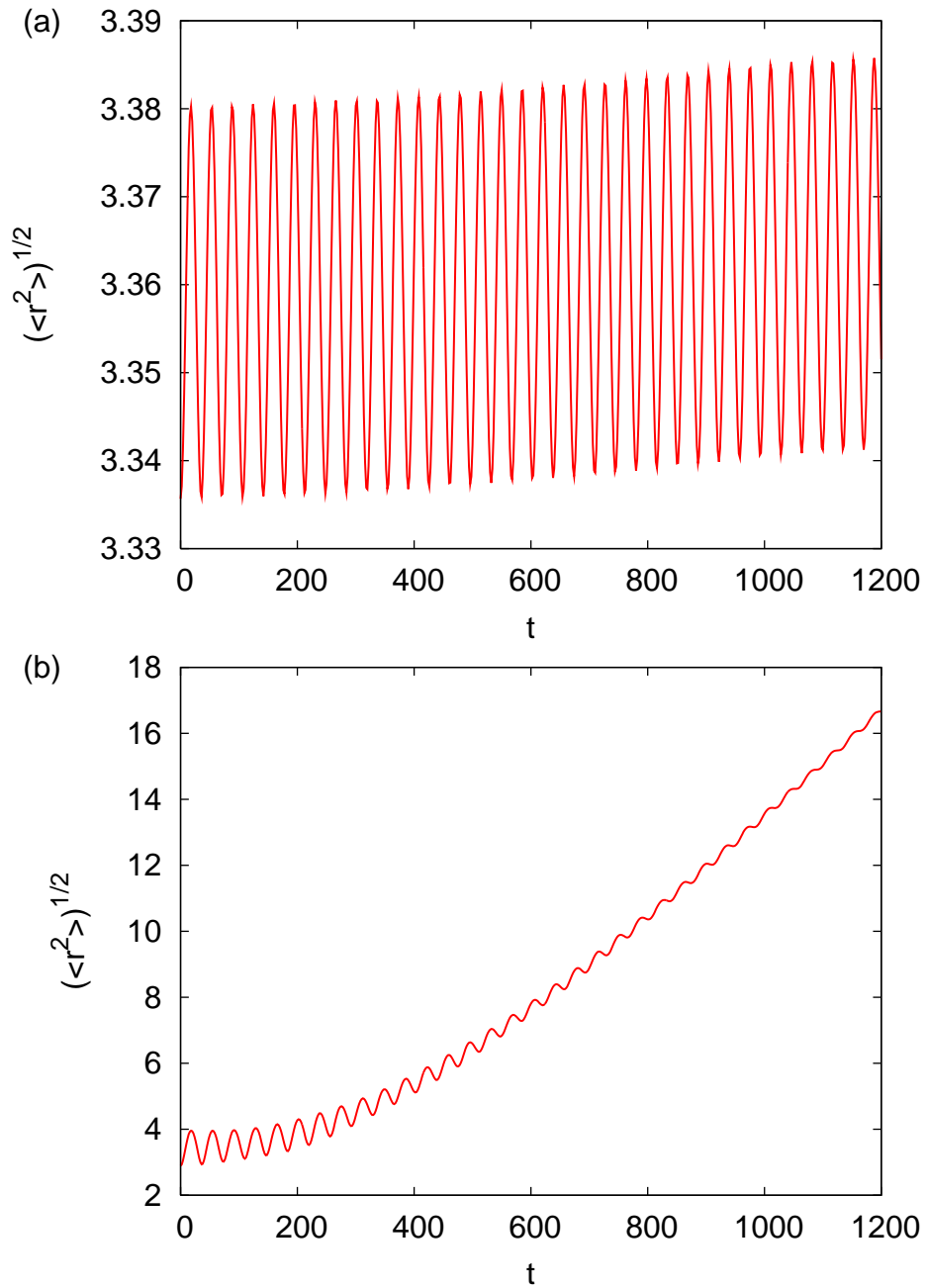


Figure 7.11.: (a) Quasi periodically oscillating condensate at a scaled scattering length of  $a = -0.85$  and  $f = 1.01$ . (b) An initially quasi periodically oscillating condensate at  $a = -0.85$ ,  $f = 1.25$  turns into expanding dynamics after long time.



## 8. Dynamics of Bose-Einstein condensates with dipolar interaction

The Bose-Einstein condensation with dipole-dipole interaction has attracted much attention in recent years [66–70], and the achievement of Bose-Einstein condensation in a gas of chromium atoms [36], with a large dipole moment, has opened the way to promising experiments on dipolar quantum gases [81, 82]. For example, the experimental observation of the dipolar collapse of a quantum gas has recently been reported by Koch et al. [35], which sets in when the scattering length of the contact interaction is reduced below some critical value. At the critical scattering length two stationary states of the Gross-Pitaevskii equation collide and vanish in a tangent bifurcation when the scattering length is reduced. One stationary state is the ground state, the other stationary state is a nodeless, unstable, excited state. In this chapter the dynamics of Bose-Einstein condensates with inter-atomic magnetic dipole-dipole interaction is investigated by means of the time-dependent variational principle applied on a Gaussian trial function. The ratio of the strengths of the two interactions can be varied by changing the scattering length of the contact interaction. In experiments this is realized by using a Feshbach resonance [34]. In chapter 7 the analogy of the TDVP equations of motion for the Gaussian wave packet to classical Hamiltonian equations of motion for a classical particle has been shown [37]. Due to the spherical symmetry of the self-trapped  $1/r$  interacting BEC the resulting conservative problem is effectively one-dimensional and the motion of the quasi-particle representing the Gaussian wave packet is regular. The anisotropy of the magnetic dipole-dipole interaction breaks the spherical symmetry. For ordered dipoles the three-dimensional system effectively reduces to a two-dimensional system with cylindrical symmetry. This symmetry is accounted for in the ansatz of the Gaussian trial function. Effectively, this yields a system of four coupled real valued equations of motion in accordance to the four-dimensional phase space of a classical system with two degrees of freedom. Although the system is conservative, for two degrees of freedom the dynamics can be chaotic. For a system with two degrees of freedom the regularity of the dynamics is most conveniently investigated by employing Poincaré surfaces of section. Associated with the regularity of the dynamics of the BEC the question for bifurcations of periodic orbits arises, i.e. where an infinitesimal change of an external parameter, leads to different modes of periodical oscillations of the BEC. This point is currently under investigation [83].

The dynamics of the system is described by the Gross Pitaevskii equation

$$\begin{aligned}
 i\hbar \frac{d}{dt} \psi(\mathbf{r}, t) &= H\psi(\mathbf{r}, t) \\
 &= \left[ -\frac{\hbar^2}{2m} \Delta_{\mathbf{r}} + V_{\text{t}}(\mathbf{r}) + N \left( \frac{4\pi a \hbar^2}{m} |\psi(\mathbf{r}, t)|^2 \right. \right. \\
 &\quad \left. \left. + \frac{\mu_0 \mu^2}{4\pi} \int d^3 r' \frac{1 - 3 \cos^2 \theta'}{|\mathbf{r} - \mathbf{r}'|^3} |\psi(\mathbf{r}', t)|^2 \right) \right] \psi(\mathbf{r}, t), \quad (8.1)
 \end{aligned}$$

with the harmonic, rotationally symmetric trap potential  $V_{\text{t}} = \frac{m}{2}(\omega_{\rho}^2 \rho^2 + \omega_z^2 z^2)$ . The scattering length is denoted by  $a$ ,  $\mu$  is the magnetic moment of the Bosons,  $\mu_0$  is the permeability of the vacuum and  $N$  is the number of bosons of mass  $m$ . Exploiting the scaling properties [84, 85]

$$(\tilde{\mathbf{r}}, \tilde{\gamma}, \tilde{t}, \tilde{\psi}, \tilde{E}) = (N^{-1} \mathbf{r}, N^2 \gamma, N^{-2} t, N^{3/2} \psi, NE)$$

leads to the scaled Gross Pitaevskii equation for dipolar gases

$$i \frac{d}{d\tilde{t}} \tilde{\psi}(\tilde{\mathbf{r}}, \tilde{t}) = \tilde{H} \tilde{\psi}(\tilde{\mathbf{r}}, \tilde{t}) = \left[ -\Delta_{\tilde{\mathbf{r}}} + \tilde{V}_{\text{t}} + \tilde{V}_{\text{c}} + \tilde{V}_{\text{d}} \right] \tilde{\psi}(\tilde{\mathbf{r}}, \tilde{t})$$

in ‘‘atomic’’ units, where lengths are measured in units of the dipole length  $a_{\text{d}} = \mu_0 \mu^2 m / (2\pi \hbar^2)$ , energies are measured in units of  $E_{\text{d}} = \hbar^2 / (2ma_{\text{d}}^2)$ , and the time in units of  $t_{\text{d}} = \hbar / E_{\text{d}}$ . Explicitly the scaled potentials read

$$\begin{aligned}
 \tilde{V}_{\text{t}} &= \tilde{\gamma}_z^2 \tilde{z}^2 + \tilde{\gamma}_{\rho}^2 \tilde{\rho}^2, \\
 \tilde{V}_{\text{c}} &= 8\pi a |\tilde{\psi}(\tilde{\mathbf{r}}, \tilde{t})|^2, \\
 \tilde{V}_{\text{d}} &= \int d^3 \tilde{\mathbf{r}}' \frac{|\tilde{\psi}(\tilde{\mathbf{r}}', \tilde{t})|^2 (1 - 3 \cos^2 \theta')}{|\tilde{\mathbf{r}} - \tilde{\mathbf{r}}'|^3}.
 \end{aligned}$$

The dipolar interaction is given by  $\tilde{V}_{\text{d}}$ , a rotationally symmetric potential, with the assumption that all dipoles are oriented along the  $z$ -axis.  $\theta'$  is the angle between  $\tilde{\mathbf{r}} - \tilde{\mathbf{r}}'$  and the  $z$ -axis, i.e. the axis of the orientation of the dipoles. In contrast to the self-trapping of the gravity like interacting BEC an external trapping potential  $\tilde{V}_{\text{t}}$  is needed in this case to stabilize the gas. According to the rotational symmetry induced by the dipole interaction a trapping potential that matches the symmetry is assumed.

In the following, all computations are performed in scaled quantities. Therefore the tilde is omitted. The short-range contact interaction may be attractive for  $a < 0$  or repulsive for  $a > 0$ . The ratio of the trap strengths in the two directions, i.e. along the symmetry axis  $z$  and along the perpendicular direction  $\rho$ , is denoted by  $\lambda = \gamma_z / \gamma_{\rho}$ . A value of  $\lambda > 1$  describes a pancake like BEC while  $\lambda < 1$  presents a cigar like BEC. In case of  $\lambda > 1$  the dipoles are mainly ordered side by side leading to a net repulsive force such that the BEC is even stable at negative scattering lengths. If the scattering

length is decreased there is always a critical length when the BEC collapses independent on the trap geometry. In the cigar like BEC the dipoles are mainly ordered in a row resulting in a net attractive force yielding a collapse of the BEC at negative scattering lengths. The stability of dipolar BEC for different trap geometries has been investigated experimentally [35] and theoretically [85].

## 8.1. TDVP for the dipolar BEC

In this chapter the dynamics of the dipolar BEC is investigated by applying the TDVP on a GWP trial function of the form

$$\psi(\mathbf{z}, \mathbf{x}) = e^{i(A_\rho \rho^2 + A_z z^2 + \gamma)}, \quad (8.3)$$

with the complex, time-dependent variational parameters  $\mathbf{z} = (A_\rho, A_z, \gamma)$  where  $A_\rho$  and  $A_z$  are the width parameters and  $\gamma$  is the phase and normalization parameter. The symmetry of the GWP is chosen according to the symmetry of the system. The GWP (8.3) employed here is obtained from eq. (3.1) by setting  $\mathbf{p} = 0$  and  $\mathbf{q} = 0$ . The index  $k$  is not needed in this chapter since only a single GWP trial function is employed. To use the equations of motion resulting from the TDVP derived in chapter 3 the GWP (8.3) is interpreted in Cartesian coordinates with the associated diagonal width matrix  $A = (A_\rho, A_\rho, A_z)$  such that  $\mathbf{x}A\mathbf{x} = A_\rho \rho^2 + A_z z^2$ , and  $i \operatorname{tr} A = i(2A_\rho + A_z)$ . The application of the Laplace operator in Cartesian coordinates yields eq. (3.5) when setting all terms containing any  $\mathbf{p}$  or  $\mathbf{q}$  to zero and bearing in mind that the kinetic operator of the GP equation does not contain the common factor of  $1/2$ , due to the introduced Rydberg like “atomic” energy unit. Similarly the equation for the time derivative of the GWP eq. (3.6) can be used while again setting all terms containing  $\mathbf{p}$ ,  $\mathbf{q}$  and their time derivatives equal to zero. The equations of motion hence read

$$\dot{A}_\rho = -4A_\rho^2 - \frac{1}{2}V_\rho, \quad (8.4a)$$

$$\dot{A}_z = -4A_z^2 - \frac{1}{2}V_z, \quad (8.4b)$$

$$\dot{\gamma} = 2i(2A_\rho + A_z) - v_0, \quad (8.4c)$$

or in real number representation

$$\dot{A}_\rho^r = -4((A_\rho^r)^2 - (A_\rho^i)^2) - \frac{1}{2}V_\rho, \quad (8.5a)$$

$$\dot{A}_\rho^i = -8A_\rho^r A_\rho^i, \quad (8.5b)$$

$$\dot{A}_z^r = -4((A_z^r)^2 - (A_z^i)^2) - \frac{1}{2}V_z, \quad (8.5c)$$

$$\dot{A}_z^i = -8A_z^r A_z^i, \quad (8.5d)$$

$$\dot{\gamma}^r = -4A_\rho^i - 2A_z^i - v_0, \quad (8.5e)$$

$$\dot{\gamma}^i = 4A_\rho^r + 2A_z^r, \quad (8.5f)$$

using the splitting  $A_\rho = A_\rho^r + iA_\rho^i$  and  $A_z = A_z^r + iA_z^i$  and  $\gamma = \gamma^r + i\gamma^i$ . The equations derived in chapter 3 may be used while taking into account the symmetry of the matrix  $A$ . Due to the reduced variational freedom eq. (3.11) becomes

$$\begin{aligned} \frac{\partial\psi(\mathbf{z}, \mathbf{x})}{\partial\gamma} &= i\psi(\mathbf{z}, \mathbf{x}), \\ \frac{\partial\psi(\mathbf{z}, \mathbf{x})}{\partial A_\rho} &= i\rho^2\psi(\mathbf{z}, \mathbf{x}), \\ \frac{\partial\psi(\mathbf{z}, \mathbf{x})}{\partial A_z} &= iz^2\psi(\mathbf{z}, \mathbf{x}). \end{aligned} \quad (8.6)$$

Therefore the matrix equation (3.28) reduces to a  $3 \times 3$  matrix equation for the real parameters  $V_2$ , a diagonal matrix with the elements  $(V_\rho, V_\rho, V_z)$ , and  $v_0$ . The linear equations read

$$\begin{pmatrix} I_{00} & I_{20} & I_{02} \\ I_{20} & I_{40} & I_{22} \\ I_{02} & I_{22} & I_{04} \end{pmatrix} \begin{pmatrix} v_0 \\ \frac{1}{2}V_\rho \\ \frac{1}{2}V_z \end{pmatrix} = \begin{pmatrix} I_{V_{00}} \\ I_{V_{20}} \\ I_{V_{02}} \end{pmatrix}. \quad (8.7)$$

The integrals

$$I_{2n2m} = \langle \psi | \rho^{2n} z^{2m} | \psi \rangle \quad (8.8)$$

and

$$I_{V_{2n2m}} = \langle \psi | \rho^{2n} z^{2m} V(x, y, z) | \psi \rangle$$

are computed and listed in appendix A.5.

The solution of the GP equation is now recast as an ordinary initial value problem (8.5), solved with the initial values  $A_\rho^i > 0, A_z^i > 0$ . We choose real valued initial wave functions, i.e.  $A_\rho^r = 0, A_z^r = 0$ .

The equation of motion (8.5f) for  $\gamma^i$  can be solved analytically and gives

$$\gamma^i = \frac{1}{2} \ln \frac{\pi^{3/2}}{2\sqrt{2}A_\rho^i \sqrt{A_z^i}},$$

by solving eqs. (8.5b) and (8.5d) for  $A_\rho^r$  and  $A_z^r$  respectively and inserting the result in (8.5f) together with the initial condition  $|\psi(t=0)|^2 = 1$ . The equation of motion (8.5e) for the real part of  $\gamma$  is in contrast to the equations of motion for the width parameters  $A_\rho$  and  $A_z$  not a differential equation but a simple integral. Therefore the dynamics of the BEC is described essentially by the four remaining coupled ODEs (8.5a)-(8.5d) for  $\dot{A}_\rho^r, \dot{A}_\rho^i, \dot{A}_z^r, \dot{A}_z^i$ .

## 8.2. Poincaré surfaces of section

The regularity of the dynamics of a Hamiltonian system is studied by the investigation of the phase space. Consider a conservative system with two degrees of freedom. The associated phase space is four-dimensional. Taking the energy conservation into account, the motion takes place on a three-dimensional hyperplane. Defining an intersecting 2D plane, called Poincaré surface of section, by requiring e.g. a momentum component to vanish, i.e.  $p = 0$ , allows for an investigation of the dynamics in the three-dimensional hyperplane. Each time the Poincaré surface of section is crossed by the trajectory the values of the variables are recorded. If there is another integral of motion the dynamics is regular. Then the motion in phase space takes place on  $2D$  tori whose intersections with the Poincaré surface of section appear as regular one-dimensional structures. If there is no further constant of motion the dynamics is chaotic and the motion fills the whole three-dimensional hyperspace. The crossing points of the chaotic trajectory through the surface of section then fill a two dimensional area. It has been mentioned in chapter 2 that the TDVP leads to a generalized Poissonian dynamics [38] and the variational BEC evolution described by the four eqs. (8.5a)-(8.5d) can be interpreted as the equations of motion in a generalized four-dimensional phase space. Taking the conservation of the mean-field energy into account there are three remaining independent parameters. The dynamics is best investigated by Poincaré surfaces of section, which are introduced here by the intersection condition  $A_z^r = 0$ . Two independent parameters (e.g.  $A_\rho^i, A_\rho^r$ ) can conveniently be plotted, and visualize in an appealing way the dynamical behavior of the dipolar system. The scaled mean-field energy  $\langle \psi | H | \psi \rangle$  reads

$$\begin{aligned}
\langle H \rangle &= \langle E_{\text{kin}} \rangle + \langle V_t \rangle + \langle V_c \rangle + \langle V_d \rangle \\
&= 2 \left( A_\rho^i + \frac{(A_\rho^r)^2}{A_\rho^i} \right) + A_z^i + \frac{(A_z^r)^2}{A_z^i} + \frac{\gamma_\rho^2}{2A_\rho^i} + \frac{\gamma_z^2}{4A_z^i} + \frac{4a\sqrt{A_z^i}A_\rho^i}{\sqrt{\pi}} \\
&\quad + \frac{2\sqrt{A_z^i}(A_\rho^i)^2}{3(A_z^i - A_\rho^i)\sqrt{\pi}} \left( -\frac{3 \tan^{-1} \left( \sqrt{\frac{A_z^i}{A_\rho^i}} - 1 \right) A_z^i}{A_\rho^i \sqrt{\frac{A_z^i}{A_\rho^i} - 1}} + \frac{2A_z^i}{A_\rho^i} + 1 \right). \quad (8.9)
\end{aligned}$$

The mean-field energy is a smooth function of the parameters and is plotted in fig. 8.1 for a better understanding of what follows. The mean-field energy is plotted as a function of the two imaginary parts of the width parameters  $A_\rho^i, A_z^i$ , the real parts  $A_\rho^r, A_z^r$  are set

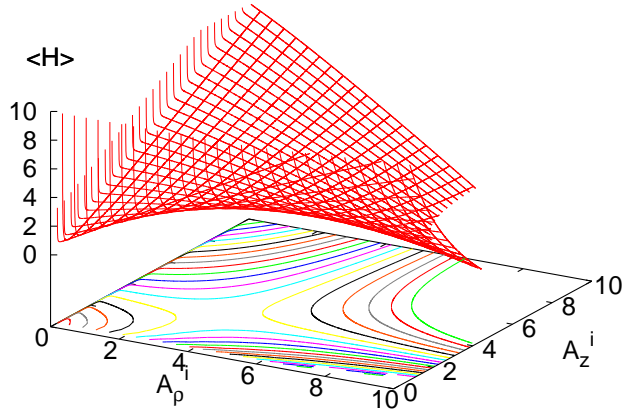


Figure 8.1.: Sketch of the mean-field functional as a function of the width parameters  $A_\rho^i, A_z^i$  for fixed external parameters. The real parts  $A_\rho^r, A_z^r$  are set equal to zero. The stable stationary state (ground state) of the GP equation is located at the minimum of the potential close to the origin. The unstable stationary state is located at the saddle point. For  $A_\rho^i, A_z^i \rightarrow \infty$ , i.e. vanishing width of the BEC at the collapse, the mean-field energy goes to  $-\infty$ .

to zero. The local minimum is located close to the origin and describes the ground state of the GP equation. In contrast to this stable state there is also an unstable one situated at the saddle point of the mean-field energy which separates the stable region around the local minimum where the condensate is stable, from the collapsing region where the extension of the BEC is shrinking to zero, i.e.  $A_\rho^i, A_z^i \rightarrow \infty$ . As long as the energy of the gas is below the saddle point energy the BEC is not collapsing, above the saddle point energy the saddle point can be crossed by the trajectories of the parameters such that a collapse may be expected. It will be shown that surprisingly this is not necessarily the case, but some stable, non collapsing regions persist even far above the saddle point energy!

Poincaré surfaces of section are presented for increasing mean-field energies, beginning slightly above the energy of the stable stationary point  $E_{\text{gr}} = 4.24 \times 10^5$ . The access of the region  $\langle H \rangle < E_{\text{gr}}$  is kinematically not allowed. The external parameters for the following Poincaré surfaces of section are a scattering length of  $a = 0.1$ , and the trap potential is set to  $\sqrt[3]{\gamma_z \gamma_\rho^2} = 3.4 \times 10^4$ ,  $\gamma_z / \gamma_\rho = 6$ . Due to the pancake like form of the BEC imposed by the trap geometry, the dipole interaction is repulsive and the Bose-Einstein gas stays stable even for slightly negative scattering lengths, i.e. the critical scattering length is  $a_{\text{cr}} = -0.02$ . For the dynamical investigation, quite a larger value of the scattering length is chosen  $a > a_{\text{cr}}$ . This allows to access the bound dynamics of the condensate which does not exist for  $a \leq a_{\text{cr}}$ .

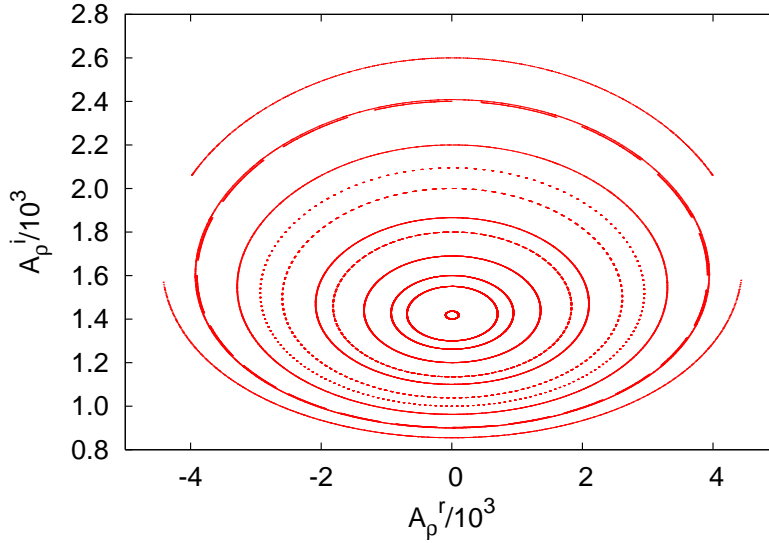


Figure 8.2.: Poincaré surface of section at the energy  $\langle H \rangle = 4.50 \times 10^5$ , a scattering length  $a = 0.1$  and the trap geometry  $\sqrt[3]{\gamma_z \gamma_\rho^2} = 3.4 \times 10^4$ ,  $\gamma_z / \gamma_\rho = 6$ . Regular dynamics is exhibited and a central periodic orbit corresponding to a periodically oscillating BEC is surrounded by quasi periodic orbits, seen as concentric “ellipses” surrounding the periodic orbit.

The lowest energy selected for a Poincaré surface of section is  $\langle H \rangle = 4.50 \times 10^5$  presented in fig. 8.2. Obviously the dynamics is regular. There is a periodic orbit representing a BEC whose width in  $\rho$  and  $z$  direction is oscillating periodically in such a way that the norm stays unaltered with time, i.e. the BEC is pulsating in the two perpendicular directions. The periodic orbit is surrounded by ellipses where quasi periodically oscillating BECs exist. If the energy is decreased further the size of the kinematically accessible region plotted in fig 8.2 would further shrink and finally reduce to a single point, the ground state, when the ground state energy  $E_{\text{gr}}$  is reached. The regular behavior of the system is maintained when the energy is increased to  $\langle H \rangle = 6.00 \times 10^5$ , see fig 8.3, which is still below the saddle point energy  $E_{\text{ex}} = 6.24 \times 10^5$ . However new islands have been created in a bifurcation which surround the central periodic orbit. In the centers of the islands there is a new stable periodic orbit representing a new mode of periodically oscillating BEC while in between the islands there is an unstable non-collapsing, periodically oscillating BEC. Note that here the term stable or unstable describes the character of the respective orbit in the sense of Lyapunov. It does not mean the stability of the BEC concerning a collapse. In an experiment different modes of pulsating BECs at the same energy should be observed corresponding to the central periodic orbit and the central orbit of the surrounding island chain, respectively.

When the saddle point is energetically approached the procedure is repeated and new

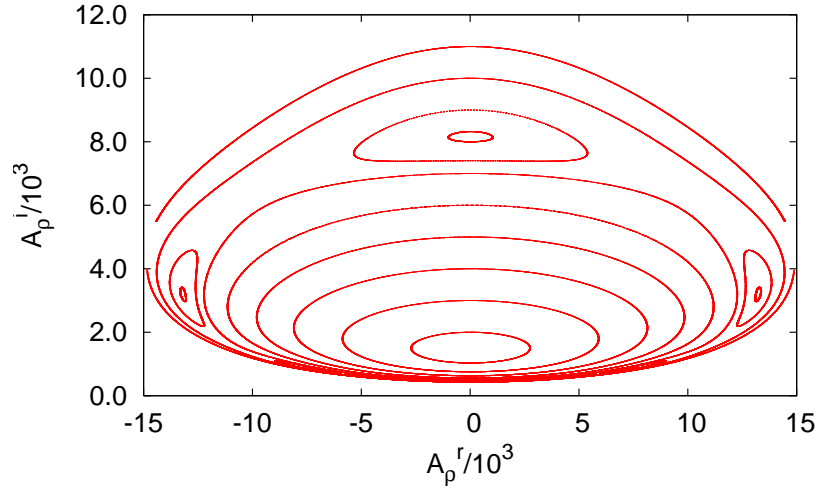


Figure 8.3.: Poincaré surface of section at the energy  $\langle H \rangle = 6.00 \times 10^5$ , a scattering length  $a = 0.1$  and the trap geometry  $\sqrt[3]{\gamma_z \gamma_\rho^2} = 3.4 \times 10^4$ ,  $\gamma_z/\gamma_\rho = 6$ . Regular dynamics is exhibited and the central periodic orbit is surrounded by other stable and unstable periodic orbits forming the island chain.

islands with new periodic orbits appear, see fig 8.4 (a). The energy is close to the saddle point energy  $\langle H \rangle \lesssim E_{\text{ex}}$  and in the region of  $A_p^i \approx 18000$  and  $A_p^r \approx 0$  there occurs chaotic behavior of the condensate as is best seen in fig. 8.4(b), which shows a magnification of the chaotic region of fig. 8.4(a). The chaotic region is located below the saddle point at  $A_p^i = 20408.3$ . However in between the chaotic region and the saddle point again there is a small stable island. The chaotic region represents an irregularly fluctuating, nevertheless non decaying (since  $\langle H \rangle \lesssim E_{\text{ex}}$ ) BEC. It is astonishing that above the saddle point energy, as depicted in fig. 8.5 at the energy  $\langle H \rangle = 9.00 \times 10^5$ , the collapse sets in for only a certain region, while some other region stays stable and does not collapse, i.e. it forms islands of stability. The ergodic motion surrounding the stability islands of course leads to the collapse of the condensate, however the chaotic character could still be visualized in the Poincaré surface of section since the orbit still traverses the intersecting plane  $A_z^r = 0$  many times before the trajectory crosses the saddle point and drives the condensate into collapse. With increasing energy the collapse sets in quicker and the Poincaré surface of section is hardly ever crossed before the collapse sets in, such that nearly no structures are visible outside the stability island in fig. 8.6. One single island survived in fig. 8.6, the others have vanished.

Of course, the size of the island of stability shrinks with increasing energy, but nevertheless it persists to energies even at approximately ten times the saddle point energy, see fig. 8.6.



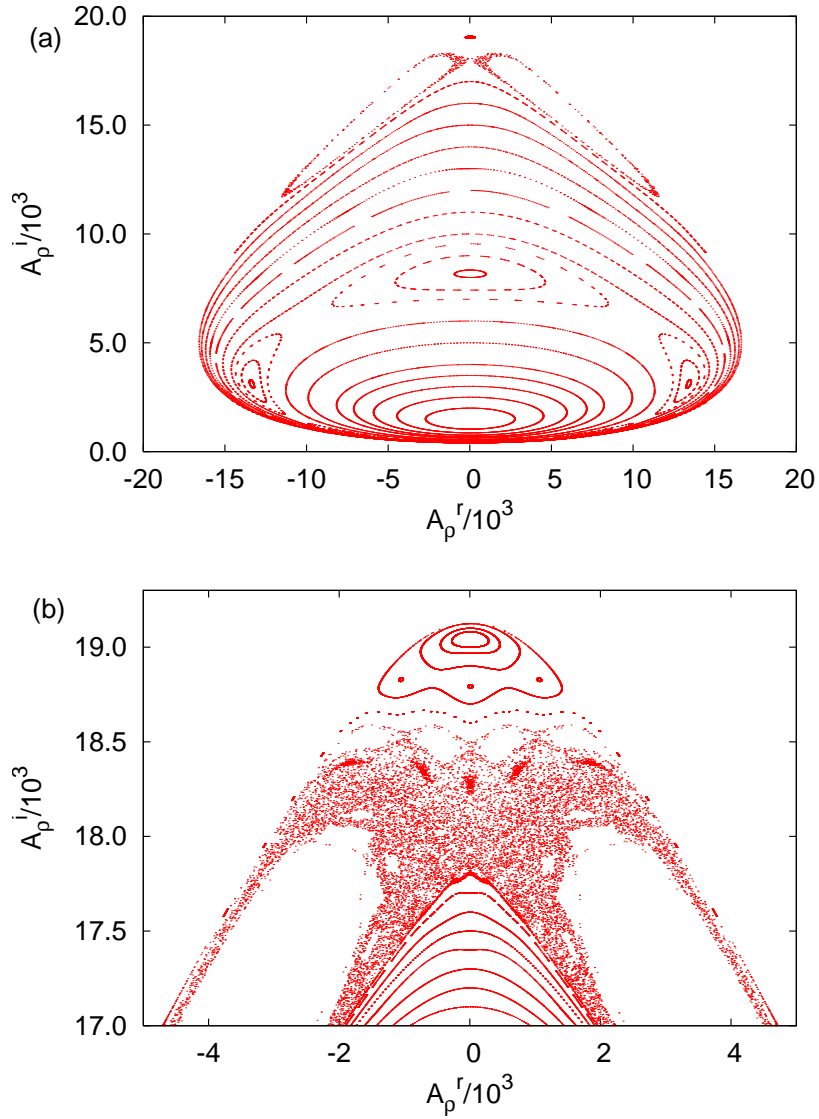


Figure 8.4.: Poincaré surface of section at approximately the saddle point energy  $\langle H \rangle \lesssim E_{\text{ex}}$ . In panel (a) the complete kinematically accessible region is plotted, in panel (b) a magnification of the chaotic region in the upper part of panel (a) is visible.

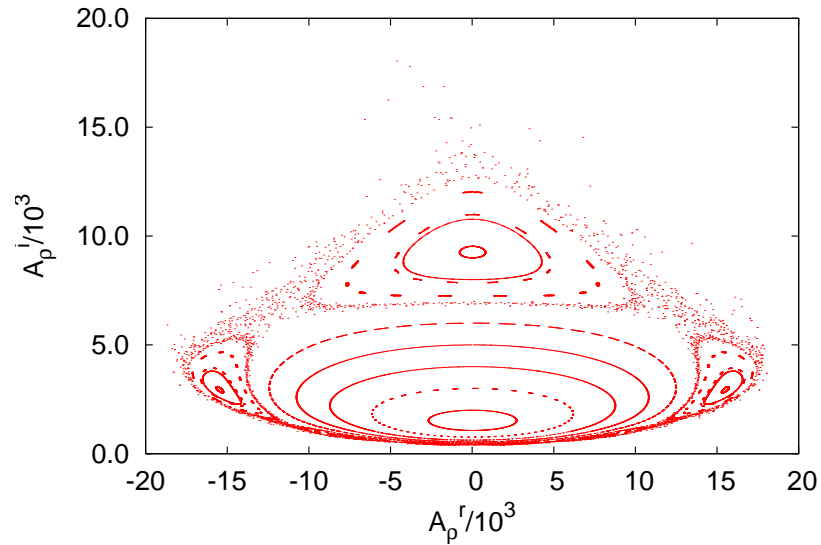


Figure 8.5.: Poincaré surface of section above the saddle point energy at  $\langle H \rangle = 9.00 \times 10^5$ . There are still some islands of stability surrounded by ergodic, collapsing regions.

A question concerning the experimental preparation of a BEC in a stable mode above the saddle point energy is, whether the required energy for excitation lies within the temperatures which allow for condensation. For an investigation of this point the energy gap between the ground state and the excited state is supposed to be the minimal energy necessary for preparation in a “meta” stable state. The example is performed for  $^{52}\text{Cr}$  where the units are  $a_d = 91a_0$ ,  $E_d = 1.7 \times 10^{-8}\text{eV}$ . The difference of the scaled energies between the saddle point and the ground state is  $E_{\text{ex}} - E_{\text{gr}} = \frac{1}{N}(6.24 \times 10^5 - 4.24 \times 10^5)1.7 \times 10^{-8}\text{eV} = N \times 8.62 \times 10^{-5} \frac{\text{eV}}{\text{K}} \Delta T$  which yields  $\Delta T = \frac{39.4\text{K}}{N^2}$ . If a particle number of  $N = 20000$  is assumed it follows that the excitation of the gas into “meta” stable state could in the worst case lead to a thermal energy corresponding to a temperature of  $\sim 10^{-7}\text{K}$ . This temperature might be somewhat high, but in this case the scattering length should be reduced in order to approach the critical scattering length. Then the two solutions of the GP equation approach each other and the associated energy gap reduces.

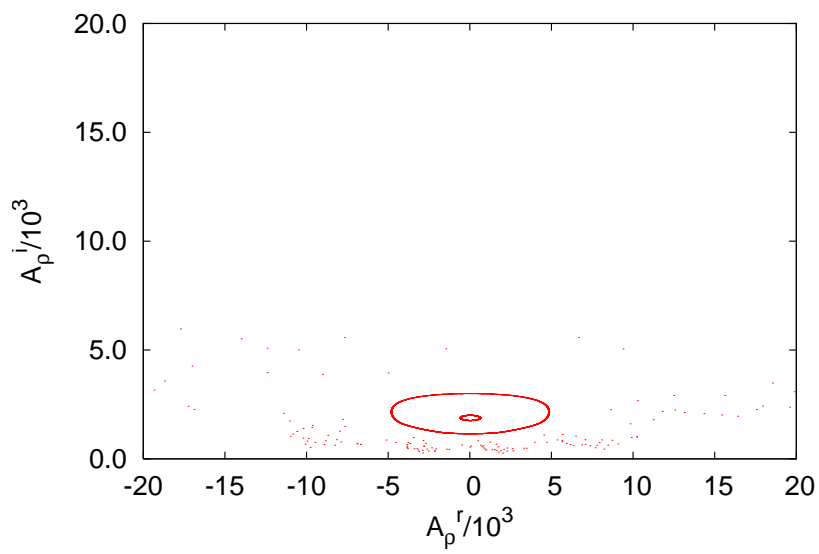


Figure 8.6.: Poincaré surface of section high above the saddle point energy at  $\langle H \rangle = 6.00 \times 10^6$ . One stable island has survived. Nearly no structures are visible outside the island due to the quickly incipient collapse.



## 9. Conclusion

The method of wave packet propagation has been introduced thirty years ago but suffers from fundamental problems. The matrix-singularity problem makes the step sizes of the numerical integration extremely small and the method impracticable. Furthermore, for the Gaussian wave packets the potential should not deviate too much from a harmonic potential, i.e. the method is inapplicable for atomic systems close to the Coulomb singularity. These problems have been addressed and solved in this thesis.

The basis for the successful application of the GWP method to arbitrary quantum systems are numerically well behaved equations of motion of the Gaussian parameters. However, there is a discrepancy between the number of GWPs that are necessary for accurate results and the number of Gaussian wave packets that can be propagated without numerical difficulties, a problem concerning the evolution of non-orthogonal basis functions according to the time-dependent variational principle. A solution to this outstanding problem based on the introduction of constraints on the motion of the parameters is developed and applied to the propagation of the GWPs. Suitable constraints for the quantum systems considered in this thesis are formulated and employed. The additional error introduced to the variational approach by the constraints is found to be negligible.

The regularized hydrogen atom is a promising candidate for the exact propagation of Gaussian wave packets, provided the restriction is fulfilled. A GWP is shown to satisfy the restriction, implied by the Kustaanheimo-Stiefel transformation, if the Gaussian parameters have certain restrictions.

These restricted GWPs are shown to form a complete set of basis functions with respect to physical wave functions, such that an expansion of arbitrary quantum states is possible. In the field-free hydrogen atom the propagation of the restricted GWPs is done analytically. Based on the restricted GWP, a modification of the wave packets to states with conserved magnetic quantum number, and to states with conserved angular momentum is presented. When external magnetic and crossed magnetic and electric fields are applied, the restricted GWPs are no exact solutions of the Schrödinger equation any more and the evolution is determined by the constrained time-dependent variational principle. The accuracy of the method is checked by comparison of the results with numerically exact computations and is proven to be high.

Furthermore, the GWP method is employed to investigate cold gases with long-range interaction. For the  $1/r$  interacting BEC the results are compared with numerically exact computations performed by the split-operator method. The qualitative agreement of the results of both approaches is mainly good, however the numerically exact approach shows a larger variety of qualitative different behaviors that is not all reproduced by the

GWP method. In particular there is the expanding dynamics of the BEC in the self-trapped gravity-like BEC, which is not reproduced by the Gaussian trial function. By the introduction of a convenient parametrization of the GWP classically looking equations of motion of a conservative one-dimensional Hamiltonian system are obtained.

For the dipolar BEC with rotational symmetry the GWP ansatz leads to a generalized conservative Hamiltonian dynamics with two degrees of freedom. The dynamics exhibits regular and chaotic behavior of the condensate, as revealed by the Poincaré surfaces of section. At energies somewhat above the stationary ground state the dynamics is regular and exhibits periodic and quasi periodic oscillations of the BEC. With increasing mean-field energy the dynamics becomes complex and slightly below the saddle point chaos sets in. Regular and chaotic regions coexist. The regular, non-collapsing regions of the oscillating BEC persist to energies high above the saddle point.

# Zusammenfassung

Der Aufwand für die numerisch exakte Lösung der zeitabhängigen Schrödingergleichung nimmt exponentiell mit der Zahl der Freiheitsgrade des Systems zu, und Näherungslösungen werden benötigt. Dazu zählen semiklassische Methoden [1, 2] sowie verschiedene Methoden, die auf dem zeitabhängigen Variationsverfahren beruhen, wie zum Beispiel die zeitabhängige Multikonfigurations-Hartree-Methode [3] oder die Methode der Gaußwellenpaketdynamik [4–9]. Die Methode der Gaußwellenpakete besteht darin, daß per Konstruktion ein Gaußwellenpaket mit der Zeit Gaußförmig bleibt und die Zeitabhängigkeit in den Parametern des Pakets, d.h. Breite, Schwerpunkt, mittlerer Impuls und Phase, steckt. Die Lösung der Schrödingergleichung ist damit auf die Lösung eines gewöhnlichen Anfangswertproblems reduziert. Für ein einzelnes Gaußpaket ist diese Näherung im Allgemeinen nur für kurze Zeiten erfüllt. Das Verfahren wird erheblich verbessert, wenn eine Superposition von Gaußpaketen verwendet wird und die Aufstellung der Bewegungsgleichungen für die Parameter über das zeitabhängige Variationsprinzip geschieht. Die Bewegungsgleichungen, die sich aus dem Variationsprinzip ergeben, erfordern nach jedem Integrationsschritt die Lösung eines linearen Gleichungssystems. Dies bewirkt eine Kopplung zwischen den Gaußpaketen. Diese Kopplung entfällt für harmonische Potentiale, wo jede Gaußfunktion eine exakte Lösung der Schrödingergleichung darstellt. Mit zunehmender Zahl von Wellenpaketen kommt es häufiger vor, daß die Matrix des linearen Gleichungssystem von Zeit zu Zeit während der Integration schlecht konditioniert wird. Dies führt zu erheblichen numerischen Problemen, die sich in einer extrem kleinen Schrittweite der Integrationsroutine äußern und zu einem Zusammenbruch der Methode führen können. Die Zahl der für eine akkurate Propagation erforderlichen Wellenpakete übersteigt dabei im Allgemeinen die Zahl der Wellenpakete, die numerisch problemlos propagiert werden können [6]. Verschiedene Vorschläge zur Lösung des Problems wurden gemacht [6, 7, 9, 14–17], jedoch steht eine zufriedenstellende Lösung des Problems noch aus. Sie ist ein zentraler Gegenstand dieser Arbeit.

Ein weiteres Ziel dieser Arbeit ist es, die Methode der Gaußwellenpropagation auf das Wasserstoffatom ohne und mit äußeren elektrischen und magnetischen Felder anzuwenden. Dies soll in der Weise geschehen, daß der Coulomb-Anteil exakt durch die Wellenpakete gelöst wird und Näherungen nur für die äußeren Felder eingeführt werden. Dazu bietet sich die Regularisierung der Schrödingergleichung des Wasserstoffatoms mit und ohne äußeren Feldern durch die Einführung der Kustaanheimo-Stiefel-Koordinaten [25, 26] und einer fiktiven Zeit an. Dies transformiert das Coulomb-Potential auf ein harmonisches isotropes Potential, anharmonische Störungen stammen von den äußeren Feldern. Gaußpakete in den Kustaanheimo-Stiefel-Koordinaten stellen exakte Lösun-

gen des regularisierten Wasserstoffatomproblems dar, wenn sie die Zwangsbedingung, die die Regularisierung impliziert, erfüllen.

Ein weiteres Feld, in dem Gaußwellenpakete Anwendung finden, sind Bose-Einstein Kondensate. Die Lösung der zeitabhängigen Gross-Pitaevskii-Gleichung, die die Dynamik der Kondensate beschreibt, wird durch die Einführung des zeitabhängigen Variationsprinzips und der Gaußwellenfunktion wesentlich vereinfacht.

Die Arbeit ist wie folgt aufgebaut. In **Kapitel 2** werden zwei Varianten zeitabhängiger Variationsprinzipien vorgestellt. **Abschnitt 2.1** behandelt das Variationsprinzip der kleinsten Wirkung. In Analogie zur klassischen Mechanik wird in diesem Zusammenhang eine *Quanten-Lagrangefunktion* definiert. Auf dieser Lagrangefunktion wird eine Wirkung definiert als Zeitintegral dieser Lagrangefunktion. Das Variationsprinzip schreibt nun in Analogie zum Hamiltonschen Prinzip in der klassischen Mechanik vor, daß die Parameter der Testwellenfunktion auf Bahnen laufen, entlang welcher die Variation der Wirkung verschwindet. Diese Bahnen ergeben sich als Lösungen der Bewegungsgleichungen, gegeben durch die zugehörigen Euler-Lagrange-Gleichungen [20, 37, 41]. Aufgrund dieser Analogie zur klassischen Mechanik lassen sich für die Testwellenfunktion die Bewegungsgleichungen als verallgemeinerte Poissonklammer schreiben. Bei geeigneter Wahl der Parametrisierung können die Bewegungsgleichungen auch in kanonischer Form dargestellt werden, in der der Erwartungswert des Hamiltonoperators als Hamiltonfunktion und die Parameter als Koordinaten und als die dazugehörigen kanonischen Impulse interpretiert werden. Am Beispiel eines Gaußwellenpaketes wird dies in Referenz [37] vorgeführt. In **Abschnitt 2.2** wird das Variationsverfahren nach McLachlan [42], welches in der Literatur auch als *minimum error method* [9] bekannt ist, vorgestellt. Es fordert eine Zeitentwicklung der Wellenfunktion in der Weise, daß der Fehler in der Schrödingergleichung, d.h. die Norm der Differenz zwischen linker und rechter Seite der Schrödingergleichung, bei eingesetzter Testwellenfunktion minimal wird. Für parametrisierte Testfunktionen führt diese Forderung zu einer quadratischen Minimierungsaufgabe, die sich in ein lineares Gleichungssystem umschreiben läßt. Die resultierenden Bewegungsgleichungen, die aus dem Prinzip der kleinsten Wirkung und dem McLachlan-Prinzip hervorgehen, werden verglichen und die notwendige Bedingung für Übereinstimmung, genannt das “Komplementaritätsprinzip” [37], wird vorgestellt. **Abschnitt 2.3** stellt vor, unter welchen Bedingungen Erwartungswerte quantenmechanischer Erhaltungsgrößen auch bei Propagation der Wellenfunktion  $\chi$  über das zeitabhängige Variationsprinzip nach McLachlan erhalten sind. Es wird gezeigt, daß der Erwartungswert eines Operators  $A$ , der mit dem Hamiltonoperator vertauscht  $[A, H] = 0$ , dann erhalten ist, wenn der Operator  $A$  angewendet auf die Testwellenfunktion  $\chi$  im Raum der zulässigen Variationen der Testwellenfunktion liegt, d.h.  $A\chi \in \delta\chi$ . Die besonders wichtigen Spezialfälle der Energieerhaltung und der Erhaltung der Norm werden gesondert in **Unterabschnitt 2.3.1** behandelt. Es wird gezeigt, daß das Variationsprinzip nach McLachlan die Norm erhält, wenn die Testwellenfunktion selbst im Raum der zulässigen Variationen der Wellenfunktion liegt, d.h. wenn  $\chi \in \delta\chi$ . Das Variationsprinzip der kleinsten Wirkung erhält dagegen der Erwartungswert des Hamilton-



---

operators. In **Abschnitt 2.4** wird eine Fehlerabschätzung für die Variationsverfahren angegeben. In **Kapitel 3** wird das zeitabhängige Variationsverfahren auf eine Superposition von Gaußwellenpaketen angewendet, und die daraus resultierenden Bewegungsgleichungen für die Gaußparameter werden hergeleitet. Die numerische Lösung der Differentialgleichungen erfordert die Lösung eines linearen Gleichungssystems nach jedem Integrationsschritt. Bekanntermaßen treten während der Propagation mit zunehmender Anzahl von Gaußwellenpaketen numerische Singularitäten der Matrix auf. Leider ist im Allgemeinen die Zahl der benötigten Wellenpakete, die für eine akkurate Propagation notwendig sind, höher als die Zahl der Pakete, die numerisch noch unproblematisch propagiert werden können [6]. An diesen Singularitäten bricht die Methode der Gaußwellenpropagation in der Regel zusammen. Dieser Zusammenbruch kann an der Unlösbarkeit des singulären Gleichungssystems liegen, oder an der extrem kleinen adaptiven Schrittweite der Integrationsroutine, die eine weitere Integration unmöglich macht. Verschiedene Lösungsmöglichkeiten werden in der Literatur diskutiert. Eine ist die Lösung des singulären Gleichungssystems mittels Singulärwertzerlegung [14]. Ein anderer Vorschlag beruht auf der Reduktion der Zahl der Gaußwellenpakete an den Singularitäten. Beide Vorschläge haben entscheidende Nachteile. Die Singulärwertzerlegung führt nicht zu einer Verbesserung des numerischen Verhaltens der Differentialgleichungen, d.h. das Verfahren bleibt extrem langsam oder sogar „stecken“ [12]. Die Verringerung der Zahl der Gaußwellenpakete hat den Nachteil, daß es nicht immer möglich ist, die ursprüngliche Wellenfunktion durch den reduzierten Satz von Wellenpaketen hinreichend genau darzustellen. Die Lösung des Problems der Matrixsingularitäten wird in **Kapitel 4** vorgestellt. Die Idee ist, geeignete Nebenbedingungen, denen die Gauß Pakete während der Propagation unterworfen werden, anzuwenden [13]. Insbesondere geht es hier um nichtholonome Nebenbedingungen in Form von Ungleichungen, die Methode läßt sich aber auch unmittelbar auf holonome Nebenbedingungen in Form von Gleichungen anwenden. Zunächst wird das zeitabhängige Variationsprinzip mit Nebenbedingungen für beliebige parametrisierte Testwellenfunktionen in **Abschnitt 4.1** durchgeführt. Die Nebenbedingungen müssen so gewählt werden, daß die Matrix, deren Elemente aus den Überlappintegralen der nach ihren Parametern abgeleiteten Testwellenfunktion, besteht, nicht singulär wird. Solche Nebenbedingungen lassen sich im Allgemeinen als nicht-lineare Ungleichungen für die Parameter der Testwellenfunktion formulieren. Es wird gezeigt, daß die Ungleichungen, die die Parameter erfüllen müssen, unter Berücksichtigung einer Fallunterscheidung zwischen aktiven und inaktiven Nebenbedingungen zu *linearen* Ungleichungen, die die *Zeitableitungen* der Parameter erfüllen müssen, umformuliert werden können. Weiterhin wird gezeigt, daß diese nichtholonomen Nebenbedingungen für die Zeitableitungen der Parameter auf *holonome* Nebenbedingungen reduziert werden können. Dieses Minimierungsproblem läßt sich dann wie gewöhnlich mit Hilfe von Lagrange-Multiplikatoren lösen, und es ergeben sich die Bewegungsgleichungen bei aktiven Nebenbedingungen. Die Struktur dieser Bewegungsgleichungen, im Vergleich zu den Bewegungsgleichungen ohne Nebenbedingungen, bleibt hiervon unberührt, d.h. es handelt sich weiterhin um implizite Differentialgleichungen erster Ordnung, und es muss

nach jedem Integrationsschritt ein lineares Gleichungssystem gelöst werden. Das zeitabhängige Variationsverfahren mit Nebenbedingungen führt nun dazu, daß sich gemäß der Fallunterscheidung bei inaktiven Nebenbedingungen die Parameter frei nach den Bewegungsgleichungen, wie sie aus dem Variationsverfahren ohne Nebenbedingungen ergeben, zeitentwickeln können, solange die Nebenbedingungen nicht verletzt werden. Sobald die freie Zeitentwicklung der Parameter dazu führen würde, daß die Nebenbedingungen verletzt würden, werden die Nebenbedingungen aktiv, und die modifizierten Bewegungsgleichungen, wie sie mit Hilfe der Lagrange-Multiplikatoren berechnet wurden, bestimmen die weitere Propagation. Sobald die Zeitentwicklung unter Berücksichtigung der Nebenbedingungen zu Parameterwerten führt, für die eine weitere Propagation mittels der freien Bewegungsgleichungen möglich ist ohne die Nebenbedingung zu verletzen, werden die Nebenbedingungen wieder inaktiv und die Testwellenfunktion erhält ihre freie Beweglichkeit zurück. Die Kriterien, wann die Nebenbedingungen abzuschalten sind, werden angegeben. In **Abschnitt 4.2** wird dieses Verfahren auf eine Superposition von Gaußwellenpaketen angewendet, und die sich ergebenden Bewegungsgleichungen werden explizit hergeleitet. In **Abschnitt 4.3** wird die Methode am Beispiel des diamagnetischen, zweidimensionalen Wasserstoffatoms numerisch untersucht. Die Gründe für Matrixsingularitäten werden anhand eines numerischen Beispiels mit 11 gekoppelten Wellenpaketen gefunden und entsprechend geeignete Nebenbedingungen formuliert. Es zeigt sich, daß die numerischen Singularitäten durch divergierende große Eigenwerte verursacht werden, während die kleinsten Eigenwerte der Matrix deutlich von Null verschieden bleiben. Diese „riesigen“ Eigenwerte resultieren aus einigen überlappenden extrem großen Gauß-Paketen, die sich in der Weise überlagern, daß die Norm der gesamten Superposition von Gaußwellenpaketen konstant bleibt. Die riesigen Normen einzelner Wellenpakete stammen von extremen Werten der entsprechenden komplexen Phasenparameter  $\gamma$ , die die Amplituden der Gauß-Pakete darstellen. Die Nebenbedingungen werden daher so gewählt, daß die Amplituden der einzelnen Wellenpakete auf einen gewissen sinnvollen Bereich beschränkt werden. Anhand von Schaubildern wird gezeigt, daß in Intervallen in denen die Matrix schlecht konditioniert ist, die adaptive Schrittweite der Integrationsroutine bei Anwendung der Nebenbedingungen um drei bis vier Größenordnungen größer ist als die der freien Propagation ohne Nebenbedingungen.

Da die meiste Rechenzeit für die Integration der Intervalle mit schlecht konditionierter Matrix aufgewendet wird, führt das in diesem Kapitel eingeführte Verfahren der zeitabhängigen Variationsrechnung mit Nebenbedingungen insgesamt zu einer Beschleunigung der Methode um einige Größenordnungen, bzw. die Methode wird überhaupt erst allgemein anwendbar. Die Nebenbedingungen stellen einen Eingriff dar, der den Fehler der Variationsrechnung gegenüber der exakten quantenmechanischen Rechnung vergrößern könnte. Unter Verwendung der Fehlerabschätzung aus Abschnitt 2.4 wird in **Unterabschnitt 4.3.1** an dem numerischen Beispiel gezeigt, daß bei sinnvoll gewählten Nebenbedingungen die Fehlerschranke für die Propagation der Wellenpakete mit Nebenbedingungen gegenüber der Propagation ohne Nebenbedingungen während der Dauer der aktiven Nebenbedingungen praktisch nicht zunimmt und langfristig sogar zu einer Verringerung

---

der oberen Fehlerschranke führen kann. Die Leistungsfähigkeit der Methode wird am Beispiel des diamagnetischen Wasserstoffatoms demonstriert. Die aus der Propagation folgende Autokorrelationsfunktion  $C(\tau) = \langle \chi(0) | \chi(t) \rangle$  wird berechnet. Dazu werden 30 Gaußwellenpakete unter Berücksichtigung der Nebenbedingungen propagiert. Das Resultat wird mit numerisch exakten Rechnungen der Split-Operator-Methode verglichen. Über den gesamten gezeigten Bereich ist nur eine geringe Abweichung zwischen den Autokorrelationsfunktionen festzustellen. Im Vergleich dazu werden dieselben 30 Gaußpakete mit fester Breite propagiert. Das Ergebnis ist deutlich schlechter und zeigt insbesondere für längere Zeiten deutliche Fehler. Die hohe Genauigkeit kann auch am Vergleich der Spektren, die aus den Autokorrelationsfunktionen durch harmonische Inversion [48–50] berechnet wurden, abgelesen werden.

Der Erfolg des zeitabhängigen Variationsprinzips hängt entscheidend von der Wahl der Testwellenfunktion ab. So stellen Gaußpakete für das Wasserstoffatom keine exakte Lösung dar. Ihre unmittelbare Anwendung auf das eindimensionale H-Atom liefert gute [22–24] jedoch keinesfalls exakte Ergebnisse. Die Kustaanheimo-Stiefel-Regularisierung [25, 26] transformiert die Schrödingergleichung des Wasserstoffatoms auf die eines vierdimensionalen isotropen harmonischen Oszillators mit einer Zwangsbedingung. Die Propagation Gaußscher Wellenpakete erscheint besonders im regularisierten H-Atom sinnvoll und ist hier exakt, wenn die Pakete die Zwangsbedingung erfüllen. **Kapitel 5** behandelt die exakte Anwendung der Gaußwellen Propagation auf das regularisierte H-Atom. In **Abschnitt 5.1** wird die Regularisierung der singulären Schrödingergleichung des Wasserstoffatoms dargestellt. Sie beruht im Wesentlichen auf der Einführung der vierdimensionalen Kustaanheimo-Stiefel-Koordinaten [25, 26]. Die Erweiterung des dreidimensionalen physikalischen Raumes auf vier Dimensionen erfordert eine weitere Erhaltungsgröße. Diese äußert sich als Zwangsbedingung für physikalisch sinnvolle Wellenfunktionen. Eine Skalierung der Koordinaten mit der Quadratwurzel der Hauptquantenzahl ergibt die Schrödingergleichung als gewöhnliches Eigenwertproblem mit der doppelten Hauptquantenzahl des Wasserstoffatoms als Eigenwert. In **Abschnitt 5.1.1** werden die Eigenzustände des regularisierten H-Atoms angegeben. Die Produktzustände der vier eindimensionalen harmonischen Oszillatoren erfüllen im Allgemeinen nicht die Zwangsbedingungen. Deswegen werden semiparabolische Koordinaten eingeführt, in denen die Schrödingergleichung *und* die Zwangsbedingung separieren. Die Eigenzustände ergeben sich dann als die Produktzustände zweier zweidimensionaler harmonischer Oszillatoren, deren Drehimpuls gemäß der Zwangsbedingung jeweils gleich ist. Für die Zeitentwicklung von Wellenfunktionen wird eine fiktive Zeit [56–60] eingeführt, als zur Hauptquantenzahl konjugierte Variable, und man erhält die zeitabhängige Schrödingergleichung. Die Wirkung der Zwangsbedingungen auf die vierdimensionalen Gaußwellenfunktionen wird in **Abschnitt 5.2** untersucht. Die Zwangsbedingungen an die Gaußwellenfunktion ergeben Zwangsbedingungen für die Gaußparameter. Es wird gezeigt, daß die vierdimensionalen Gaußpakete einerseits im Ursprung lokalisiert sein müssen, außerdem muß die komplex symmetrische  $4 \times 4$  Matrix, die die Breite des Wellenpaketes bestimmt und im Allgemeinen Fall  $4 \times (4+1)/2 = 10$  unabhängige Parameter hat, eine spezielle Symmetrie

mit nur vier unabhängigen Parametern aufweisen, damit die Zwangsbedingung erfüllt ist. Außerdem wird begründet, daß diese, die Zwangsbedingung erfüllenden Gaußpakete, im folgenden Basiszustände genannt, eine vollständige Basis bilden. Entscheidend ist, daß nicht jede Wellenfunktion in den vierdimensionalen Kustaanheim-Stiefel-Koordinaten darstellbar sein muss, sondern daß es genügt, wenn jede Wellenfunktion des dreidimensionalen physikalischen Raumes in dieser Basis darstellbar ist. Es wird gezeigt, daß diese vierdimensionalen Gaußpakete ausgedrückt in den kartesischen physikalischen Koordinaten als Spezialfall ebene Wellen im Limes enthalten. **Abschnitt 5.3** behandelt die Entwicklung beliebiger (lokalisierter) Wellenfunktionen nach den Basiszuständen, und deren exakte Bewegungsgleichungen, wie sie sich aus der regularisierten Schrödingergleichung ergeben, werden analytisch gelöst. Der Abschnitt ist in drei Unterabschnitte aufgeteilt. Im ersten Unterabschnitt wird der Fall ohne scharfen Drehimpuls mit den obigen Basiszuständen untersucht. In den beiden folgenden Unterabschnitten werden die Zustände mit scharfer magnetischer Quantenzahl  $m$  und mit scharfem Drehimpuls  $l, m$  gesondert behandelt. Die analytische exakte Propagation der Basiszustände gemäß der zeitabhängigen regularisierten Schrödingergleichung wird in **Unterabschnitt 5.3.1** behandelt. Die exakten Bewegungsgleichungen für die Gaußparameter werden aufgestellt und analytisch gelöst. Wie oben erwähnt sind die Basiszustände um den Ursprung lokalisiert. Für die exakte Propagation von beliebigen, insbesondere um einen vom Ursprung verschiedenen Bereich lokalisierten Wellenfunktionen, ist eine Entwicklung dieser Wellenfunktionen nach den Basiszuständen erforderlich. Eine Strategie für diese Entwicklung basierend auf der Fourierdarstellung der gewünschten Wellenfunktion wird vorgestellt. Dazu werden die Basiszustände als ebene Wellen im dreidimensionalen physikalischen Raum aufgefasst, nach denen wie gewohnt entwickelt werden kann, d.h. die zu entwickelnde Wellenfunktion im Impulsraum gibt die benötigten Amplituden und Phasen der ebenen Wellen an. Rechnungen für die Entwicklung eines dreidimensionalen Gaußpaketes lokalisiert um  $\mathbf{x}_0, \mathbf{p}_0$  nach den Basiszuständen und dessen exakte Zeitentwicklung in fiktiver Zeit werden vorgestellt. Im Gegensatz zur Propagation in physikalischer Zeit tritt hier keine Langzeitdispersion auf, vielmehr sind sämtliche Wellenfunktionen  $\pi$ -periodisch in der fiktiven Zeit. Die Auswertung des bei dem Verfahren auftretenden dreidimensionalen inversen Fourierintegrals geschieht vorzugsweise mittels Monte-Carlo-Integration. Dabei wird in einem Beispiel nach 10000 Basiszuständen entwickelt. In **Unterabschnitt 5.3.2** wird die Prozedur aus Unterabschnitt 5.3.1 für Wellenfunktionen mit magnetischer Quantenzahl  $m$  wiederholt. Zunächst werden modifizierte Basiszustände mit scharfer magnetischer Quantenzahl  $m$  angegeben. Ihre exakten Bewegungsgleichungen folgen durch Einsetzen der modifizierten Basiszustände in die regularisierte Schrödingergleichung. Sie werden analytisch gelöst. Die Entwicklung einer beliebiger Wellenfunktionen mit magnetischer Quantenzahl  $m$  nach diesen modifizierten Basiszuständen erfolgt in Analogie zu Unterabschnitt 5.3.1, d.h. man macht sich nach der Abseparation des gemeinsamen winkelabhängigen Anteils  $e^{im\varphi}$  und des gemeinsamen Vorfaktors  $\rho^{|m|}$  mit  $\rho = \sqrt{x^2 + y^2}$  die Darstellung der modifizierten Basiszustände als "komplexe" ebene Wellen mit komplexen "Impulsen" in parabolischen

---

Koordinaten zunutze. Die Entwicklung eines Gaußwellenpaketes in parabolischen Koordinaten mit  $m = 0$  nach den modifizierten Basiszuständen und seine exakte analytische Entwicklung in der fiktiven Zeit wird vorgeführt. In **Unterabschnitt 5.3.3** werden nun modifizierte Basiszustände mit scharfen Drehimpulsquantenzahlen  $l, m$  eingeführt. Nach diesen können in analoger Weise zu den vorigen Unterabschnitten beliebige Wellenfunktionen mit den Quantenzahlen  $l, m$  entwickelt und anschließend analytisch propagiert werden. Als Beispiel wird ein radiales Gaußpaket mit den Quantenzahlen  $(l, m) = (0, 0)$  bzw.  $(l, m) = (5, 0)$  nach den modifizierten Basiszuständen mit den jeweiligen Drehimpulsquantenzahlen entwickelt und analytisch propagiert.

In **Kapitel 6** wird das Wasserstoffatom in äußeren homogenen Feldern behandelt. Dazu werden die in Kapitel 5 entwickelten Basiszustände genommen, und nach den Methoden aus den Kapiteln 2 bis 4 propagiert. Die entwickelten Basiszustände und die modifizierten Basiszustände mit scharfer magnetischer Quantenzahl  $m$ , die für das feldfreie Wasserstoffatom exakte Lösungen darstellen, sind bei Anwesenheit äußerer Felder keine exakten Lösungen mehr und werden nach dem zeitabhängigen Variationsprinzip propagiert. Zunächst wird die Regularisierung wie in Abschnitt 5.1 basierend auf der Einführung der Kustaanheimo-Stiefel-Koordinaten auf die Schrödingergleichung des H-Atoms in äußeren Feldern in **Abschnitt 6.1** erweitert. Insbesondere gehen wir von senkrecht gekreuzten elektrischen und magnetischen Feldern aus. Die Regularisierung erfolgt in analoger Weise zu Abschnitt 5.1, das Coulomb-Potential führt auf ein harmonisches Potential, die äußeren Felder ergeben anharmonische Störungen höherer Ordnung. Die Skalierung erfolgt nun bezüglich einer effektiven Hauptquantenzahl, die reelle Werte annehmen kann. Die fiktive Zeit, in der die Propagation erfolgt, wird als die zu der effektiven Hauptquantenzahl konjugierte Variable eingeführt. In **Abschnitt 6.2** wird das diamagnetische H-Atom behandelt. Hier wird das Wasserstoffatom in nur einem äußeren Feld, dem Magnetfeld, untersucht. Das System ist rotationssymmetrisch und daher ist die Komponente des Drehimpulses  $l_z = m$  entlang des Magnetfeldes erhalten. Daher bieten sich die modifizierten Basiszustände aus Unterabschnitt 5.3.2 mit scharfer magnetischer Quantenzahl  $m$  für die Entwicklung und Propagation einer Anfangswellenfunktion mit gegebener magnetischer Quantenzahl an. Es zeigt sich, daß die Wahl eines in parabolischen Koordinaten Gaußförmigen Wellenpaketes, d.h. eines Gaußförmigen Ringes um die  $z$ -Achse, mit der gewünschten magnetischen Quantenzahl  $m$  wie in Unterabschnitt 5.3.2, als Startwellenfunktion gut geeignet ist. Diese Startwellenfunktion wird nach den modifizierten Basiszuständen entwickelt, welche dann nach dem zeitabhängigen Variationsprinzip in der fiktiven Zeit propagiert werden. Die anharmonischen Potentialanteile, die durch das magnetische äußere Feld hervorgerufen werden, führen zu einer Kopplung der superponierten Basiszustände. Die numerische Lösung der Bewegungsgleichungen der Parameter der modifizierten Basiszustände erfordert nach jedem Integrationsschritt die Lösung eines linearen Gleichungssystems, dessen Dimension der Zahl der Parameter entspricht. Die Kopplung zwischen den modifizierten Basiszuständen ergibt sich aus den nichtdiagonalen Elementen der Matrix des Gleichungssystems, die den Überlapp verschiedener, nach ihren Parametern abgeleiteter modifizierter Basiszustände

enthalten. Es treten die in Kapitel 3 beschriebenen numerischen Probleme bei der Lösung der Differentialgleichungen auf, d.h. die Matrix wird mit zunehmender Zahl von Basiszuständen an gewissen Zeitpunkten schlecht konditioniert und die Integration wird extrem langsam und kann sogar zum Stillstand kommen. Abhilfe schafft auch hier die Einführung von Nebenbedingungen gemäß Kapitel 4, Abschnitt 4.3. Sie erhöhen drastisch die Zahl der modifizierten Basiszustände, die noch ohne numerische Schwierigkeiten propagiert werden können. Natürlich können hier nicht einige Tausende Basiszustände wie im analytisch behandelbaren, feldfreien Fall propagiert werden, möglich sind bis zu etwa Hundert. Die Propagation des Gaußwellenpaketes in parabolischen Koordinaten mit  $m = 0$ , welches nach 70 modifizierten Basiszuständen entwickelt ist, wird gezeigt. Die Autokorrelationsfunktion wird berechnet, und daraus werden durch harmonische Inversion die Eigenwerte bestimmt. Der Vergleich der Eigenwerte mit numerisch exakten zeitunabhängigen Rechnungen zeigt sehr gute Übereinstimmung. **Abschnitt 6.3** widmet sich dem Wasserstoffatom in gekreuzten äußeren elektrischen und magnetischen Feldern. Es wird angenommen daß die beiden Felder senkrecht aufeinander stehen. Die Rotationssymmetrie ist gebrochen, und Ausgangspunkt für die Rechnungen sind die Basiszustände, die in Abschnitt 5.2 hergeleitet wurden, d.h. die vierdimensionalen zentrierten Gaußpakete in Kustaanheimo-Stiefel-Koordinaten, die die Nebenbedingung erfüllen. Bei Anwesenheit der äußeren Felder sind diese Basiszustände nicht mehr exakte Lösungen der Schrödingergleichung, d.h. um eine gute Näherung zu bekommen muss eine Superposition der Basiszustände benutzt werden, um die variationelle Freiheit zu erhöhen. Die Superposition gemäß Unterabschnitt 5.3.1, die ein Gaußpaket in dreidimensionalen physikalischen kartesischen Koordinaten mit beliebiger vorgegebener Lokalisierung im Phasenraum darstellt, hat sich als Startwellenfunktion als gut geeignet erwiesen. Die Propagation erfolgt über das zeitabhängige Variationsprinzip, und die Bewegungsgleichungen, die in Kapitel 3 hergeleitet wurden, können weitestgehend übernommen werden. Es muss lediglich beachtet werden, daß die vierdimensionalen Gaußpakete im Ursprung zentriert sind, und es muss der besonderen Symmetrie der Breitenmatrix Rechnung getragen werden. Die numerischen Schwierigkeiten bei der Integration können durch die Einführung der Nebenbedingungen aus Abschnitt 4.3 verringert werden. Zwei Startwellenfunktionen mit verschiedenen Startwerten werden propagiert. Das Spektrum ergibt sich durch Fouriertransformation der Autokorrelationsfunktion. Die Peaks werden mit numerisch exakten Werten verglichen und zeigen gute Übereinstimmung.

**Kapitel 7** und **Kapitel 8** wenden sich der Anwendung der Gaußwellenpaketmethode auf Bose-Einstein-Kondensate zu. Die Beschreibung der Dynamik erfolgt über die zeitabhängige Gross-Pitaevskii-Gleichung. Die Nichtlinearität der Gross-Pitaevskii-Gleichung führt im Gegensatz zu den bisher behandelten Systemen zu qualitativ verschiedenem Verhalten der Lösungen, z.B. zu kollabierenden Wellenfunktionen. In ihrer üblichen Form beschreibt die Gross-Pitaevskii-Gleichung die Wechselwirkung der Bosonen untereinander über das kurzreichweitige Kontaktpotential. Die Stärke des Kontaktpotentials kann durch Variation der Streulänge verändert werden. Für hinreichend negative

---

Streulängen, d.h. für Streulängen unterhalb eines kritischen Wertes, besitzt die Gross-Pitevskii-Gleichung keine stationären Lösungen. Bei der kritischen Streulänge tritt eine Tangentenbifurkation auf, in der der stabile Grundzustand und ein instabiler angeregter Zustand entstehen. Mit wachsender Streulänge entfernen sich die Energien der beiden Zustände voneinander [32].

In **Kapitel 7** wird ein Bose-Einstein-Kondensat untersucht, dessen Teilchen untereinander zusätzlich eine langreichweitige, isotrope, attraktive  $1/r$ -Wechselwirkung erfahren. Diese wird durch die Bestrahlung des Kondensates mit 18 nichtresonanten Lasern in einer bestimmten Anordnung erreicht [31]. Experimentell schwierig zu realisieren, allerdings mit der interessanten Eigenschaft, daß keine äußere Falle benötigt wird: Durch die attraktive  $1/r$ -Wechselwirkung der Teilchen untereinander fängt sich das Kondensat selbst ein. Durch Ausnutzung einer Skalierungseigenschaft bezüglich der Teilchenzahl hängt die Dynamik des Kondensates nur noch von einem äußeren Parameter, der skalierten Streulänge, ab. In **Abschnitt 7.1** wird das zeitabhängige Variationsprinzip in gewohnter Weise angewendet, die Nichtlinearität bereitet keine Schwierigkeiten. Entsprechend der Symmetrie des Systems wird eine zentrierte, sphärisch symmetrische Gaußwellenfunktion verwendet. Effektiv verbleibt ein komplexer Parameter, der die Breite des Paketes bestimmt, zur Beschreibung der Dynamik. Die Suche nach den stationären Lösungen der Bewegungsgleichungen ergibt die reellen stationären Zustände der Gross-Pitaevkii Gleichung. Sie stimmen mit denjenigen überein, die aus der zeitunabhängigen Variation des Mean-Field-Funktional mit Gaußschen Ansatz gefunden wurden [32]. Wie oben erwähnt ergeben sich in Abhängigkeit von der Streulänge keine stationären Zustände (für hinreichend negative Streulängen), ein angeregter Zustand und der Grundzustand bei mittleren, negativen Streulängen, und ein Grundzustand für positive Streulängen. Die Stabilität dieser stationären Zustände wird in **Abschnitt 7.2** dargestellt. Es wird gezeigt, daß der Grundzustand stabil, der angeregte Zustand instabil ist [78, 79].

In **Abschnitt 7.3** wird die Dynamik des Bose-Einstein-Kondensates mit  $1/r$ -Wechselwirkung untersucht, zunächst mit dem Variationsansatz in **Unterabschnitt 7.3.1**. Phasenportraits des komplexen Breitenparameters werden für verschiedene Streulängen gezeigt. Dazu wird der komplexe Breitenparameter in seinen Real- und Imaginärteil aufgespalten und der Imaginärteil über den Realteil aufgetragen. In den Phasenportraits erkennt man den Bereich stabiler Oszillationen und den Bereich, in dem die Wellenfunktion kollabiert. Wie in Kapitel 2 erwähnt besitzen die Bewegungsgleichungen aus dem zeitabhängigen Variationsprinzip eine verallgemeinerte Poissonsche Struktur und durch Einführung einer geeigneten Parametrisierung der Testwellenfunktion nehmen die Bewegungsgleichungen die kanonische Form an. Die Mean-Field-Energie als Funktion der Variationsparameter nimmt die Funktion der klassischen Hamiltonfunktion an, und die Variationsparameter können als kanonisch konjugierte Koordinaten und Impulse interpretiert werden [37]. Die Dynamik des Kondensates mit sphärischer Symmetrie läßt sich somit als Bewegung eines klassischen Teilchens im eindimensionalen Potential interpretieren. Die obigen Rechnungen werden qualitativ in **Unterabschnitt 7.3.2** durch

numerisch exakte Rechnungen bestätigt. Die numerisch exakten Rechnungen werden auf einem Gitter mit Hilfe der Split-Operator-Methode durchgeführt. Hierzu wird insbesondere die lokale Umgebung der beiden stationären Zustände untersucht. Wie erwartet findet man in der lokalen Umgebung des Grundzustandes stabile quasiperiodische Schwingungen des Kondensates, während man in der lokalen Umgebung des instabilen, angeregten Zustandes beides findet: Kollabierende und oszillierende Wellenfunktionen. Ein Phänomen das vom Gaußschen Ansatz nicht erfasst werden kann, sich aber in den numerisch exakten Rechnungen zeigt, betrifft das Langzeitverhalten des Kondensates. Insbesondere in der Umgebung des Grundzustandes wandelt sich die zunächst oszillierende Bewegung des Bose-Einstein-Kondensates mit zunehmender Propagationsdauer in eine expandierende Bewegung mit leichten Modulationen. Je weiter man sich vom Grundzustand entfernt desto schneller setzt dieser Effekt ein.

**Kapitel 8** behandelt die Dynamik des Bose-Einstein-Kondensates mit langreichweitiger, anisotroper magnetischer Dipol-Dipol-Wechselwirkung [35]. Dies kann experimentell durch Kondensation von  $^{52}\text{Cr}$  realisiert werden [86]. Bei ausgerichteten Dipolen ist das System rotationssymmetrisch um die Achse der Ausrichtung der Dipole, bei entsprechender Wahl der Symmetrie des Fallenpotentials. Die relativen Stärken der langreichweitigen Dipol-Dipol-Wechselwirkung und der kurzreichweitigen Kontaktwechselwirkung können durch Änderung der Streulänge über eine Feshbach-Resonanz [34] verändert werden. Die Brechung der sphärischen Symmetrie durch die dipolare Wechselwirkung erfordert ihre Berücksichtigung in der Gaußförmigen Testwellenfunktion. Somit stehen zur Beschreibung des zentrierten zylindersymmetrischen Gaußwellenpaketes effektiv zwei komplexe Parameter zur Verfügung. Einer stellt die komplexe Breite entlang der Zylinderachse dar, der andere die komplexe Breite senkrecht dazu. Aus Kapitel 2 und 7 ist bekannt, daß die Real- und Imaginärteile komplexer Parameter als verallgemeinerte Koordinaten und Impulse interpretiert werden können. Das System entspricht damit einem klassischen System mit zwei Freiheitsgraden. Hier wird in erster Linie die Dynamik auf ihre Regularität hin untersucht. In **Abschnitt 8.1** werden die Bewegungsgleichungen für das Gaußpaket gemäß dem zeitabhängigen Variationsprinzip kurz hergeleitet. Effektiv ergeben sich vier gekoppelte Differentialgleichungen für die Real- und Imaginärteile der beiden Breitenparameter. Die Regularität von konservativen Systemen mit zwei Freiheitsgraden wird am Besten mittels Poincaréschnitten untersucht. In **Abschnitt 8.2** wird die Dynamik mittels Poincaréschnitten für verschiedene Mean-Field-Energien untersucht. Für das Verständnis nützlich ist die Vorstellung (in Analogie zu Abschnitt 7.3.1) des Bose-Einstein-Kondensates als "Teilchen", das sich im zweidimensionalen Potential bewegt. Für hinreichend negative Streulängen hat das Potential kein Minimum und alle Lösungen kollabieren. Bei höheren Streulängen werden in einer Tangentenbifurkation ein Minimum und ein Sattelpunkt gebildet. Sie stellen den Grundzustand, bzw. den instabilen angeregten Eigenzustand der Gross-Pitaevskii-Gleichung dar. Ein Kondensat, das sich lokal in der Nähe des Minimums bewegt, kann nur dann kollabieren, wenn seine Mean-Field-Energie über der des Sattelpunktes liegt, da dieser auf dem Weg zum Kollaps überquert werden muss. Vorgestellt werden Poincaréschnitte von



---

Mean-Field-Energien knapp über der des Grundzustands bis zu Energien weit über der des Sattelpunktes, bei welchen man einen sofortigen Kollaps erwarten würde. Bei Energien knapp über der Minimumsenergie erhält man regelmäßige elliptische Strukturen im Poincaréschnitt. Insbesondere findet man eine kurze periodische Bahn, die aus dem stationären Zustand hervorgeht. Die Bahn ist von quasiperiodischen und langen periodischen Bahnen umgeben. Diese Bahnen entsprechen periodisch bzw. quasiperiodisch oszillierenden Kondensaten. Erhöht man die Energie, entstehen noch weit unterhalb der Sattelpunktenergie in Bifurkationen weitere periodische Bahnen. Kurz unterhalb der Sattelpunktenergie treten chaotische Bereiche auf, die unregelmäßig fluktuierenden Kondensaten entsprechen, auf. Es existieren jedoch weiterhin stabile periodisch und quasiperiodisch oszillierende Bereiche. Diese Koexistenz von regulären und chaotischen Bereichen bleibt auch oberhalb des Sattelpunkts bestehen, allerdings verkleinern sich mit steigender Mean-Field-Energie des Kondensates allmählich die stabilen Bereiche zugunsten der instabilen, kollabierenden Bereiche. Bemerkenswerterweise finden sich noch stabile Bereiche sogar bis zur zehnfachen Sattelpunktenergie.



# A. Gaussian type integrals

## A.1. Gaussian type moments in two dimensions

In this appendix the calculation of two-dimensional integrals of the form

$$I(n, l) = \int dx dy x^n y^l \exp[A_1 x^2 + A_2 y^2 + A_3 xy + b_1 x + b_2 y + c], \quad n, l \in \mathbb{N} \quad (\text{A.1})$$

is presented. Integrals of the form  $\langle g^l | x^m y^n | g^k \rangle$  as they appear in eq. (3.28) can be easily brought into the form (A.1). The integration can be performed by using integration by parts, i.e. the integral in equation (A.1) can be written in the form

$$\begin{aligned} & \int dx dy x^{n-1} y^l \left( \frac{d}{dx} \exp[\dots] - (A_3 y + b_1) \exp[\dots] \right) \frac{1}{2A_1} \\ &= -\frac{n-1}{2A_1} \int dx dy x^{n-2} y^l \exp[\dots] - \frac{A_3}{2A_1} \int dx dy x^{n-1} y^{l+1} \exp[\dots] \\ & \quad - \frac{b_1}{2A_1} \int dx dy x^{n-1} y^l \exp[\dots]. \end{aligned}$$

The undesirable increase of the exponent from  $y^l$  to  $y^{l+1}$  in the second term can again be met by partial integration, this time on the variable  $y$ . We have

$$\begin{aligned} \int dx dy x^{n-1} y^{l+1} \exp[\dots] &= \int dx dy x^{n-1} y^l \left( \frac{d}{dy} \exp[\dots] - (A_3 x + b_2) \exp[\dots] \right) \frac{1}{2A_2} \\ & \quad - \frac{l}{2A_2} \int dx dy x^{n-1} y^{l-1} \exp[\dots] - \frac{A_3}{2A_2} \int dx dy x^n y^l \exp[\dots] \\ & \quad - \frac{b_2}{2A_2} \int dx dy x^{n-1} y^l \exp[\dots]. \end{aligned}$$

Altogether we obtain

$$\begin{aligned} I(n, l) &= -\frac{n-1}{2A_1} \int dx dy x^{n-2} y^l \exp[\dots] \\ &+ \left( \frac{A_3 b_2}{4A_1 A_2} - \frac{b_1}{2A_1} \right) \int dx dy x^{n-1} y^l \exp[\dots] + \frac{A_3 l}{4A_1 A_2} \int dx dy x^{n-1} y^{l-1} \exp[\dots] \\ & \quad + \frac{A_3^2}{4A_1 A_2} I(n, l). \end{aligned}$$

## A. Gaussian type integrals

---

Dividing both sides by  $4A_1A_2$  we obtain a recursive expression for the integral in equation (A.1)

$$\begin{aligned}
 (4A_1A_2 - A_3^2) I(n, l) &= -2(n-1)A_2 \int dx dy x^{n-2} y^l \exp[\dots] \\
 &+ (A_3b_2 - 2A_2b_1) \int dx dy x^{n-1} y^l \exp[\dots] \\
 &+ A_3l \int dx dy x^{n-1} y^{l-1} \exp[\dots], \tag{A.2}
 \end{aligned}$$

or by using the abbreviation for the integrals introduced in (A.1)

$$(4A_1A_2 - A_3^2) I(n, l) = -2(n-1)A_2 I(n-2, l) \tag{A.3}$$

$$+ (A_3b_2 - 2A_2b_1) I(n-1, l) \tag{A.4}$$

$$+ A_3l I(n-1, l-1). \tag{A.5}$$

The integral  $I(0, 0)$  is known to be

$$I(0, 0) = \frac{\pi}{\sqrt{A_1A_2 - A_3^2/4}} \exp \left[ \frac{-A_2b_1^2 - A_1b_2^2 + A_3b_1b_2}{4A_1A_2 - A_3^2} + c \right]. \tag{A.6}$$

## A.2. Integrals for the diamagnetic hydrogen atom

The integrals in the matrix on the left hand side of eq. (6.11) read

$$\langle g_m^l | g_m^k \rangle = \frac{(m!)^2 \pi^2}{(-a_\mu a_\nu)^{m+1}} c, \tag{A.7}$$

$$\langle g_m^l | \mu^2 | g_m^k \rangle = -i \frac{(m!)^2 \pi^2}{(-a_\mu a_\nu)^{m+2}} a_\nu (1+m) c, \tag{A.8}$$

$$\langle g_m^l | \nu^2 | g_m^k \rangle = -i \frac{(m!)^2 \pi^2}{(-a_\mu a_\nu)^{m+2}} a_\mu (1+m) c, \tag{A.9}$$

$$\langle g_m^l | \mu^4 | g_m^k \rangle = \frac{(m!)^2 \pi^2}{(-a_\mu a_\nu)^m} \frac{(1+m)(2+m)}{a_\mu^3 a_\nu} c, \tag{A.10}$$

$$\langle g_m^l | \mu^2 \nu^2 | g_m^k \rangle = \frac{(m!)^2 \pi^2}{(-a_\mu a_\nu)^m} \frac{(1+m)^2}{a_\mu^2 a_\nu^2} c, \tag{A.11}$$

$$\langle g_m^l | \nu^4 | g_m^k \rangle = \frac{(m!)^2 \pi^2}{(-a_\mu a_\nu)^m} \frac{(1+m)(2+m)}{a_\mu a_\nu^3} c, \tag{A.12}$$

with the notation  $a_\mu = a_\mu^k - (a_\mu^l)^*$ ,  $a_\nu = a_\nu^k - (a_\nu^l)^*$  and  $c = e^{i(\gamma^k - \gamma^l)^*}$ . The integrals on the right hand side vector of eq. (6.11) read

$$\begin{aligned} \langle g_m^l | V(\mu, \nu) | g_m^k \rangle &= i \frac{(m!)^2 \pi^2}{(-a_\mu a_\nu)^m} \\ &\times \frac{(a_\mu + a_\nu)(1+m)((2+3m+m^2)\beta^2 + 8a_\mu a_\nu \alpha)c}{8a_\mu^3 a_\nu^3}, \end{aligned} \quad (\text{A.13})$$

$$\begin{aligned} \langle g_m^l | \mu^2 V(\mu, \nu) | g_m^k \rangle &= \frac{(m!)^2 \pi^2}{(-a_\mu a_\nu)^m} \\ &\times \left[ \frac{(1+m)(-(1+m)(2+m)(a_\mu(2+m) + a_\nu(3+m))\beta^2)c}{8a_\mu^4 a_\nu^3} \right. \\ &\quad \left. + \frac{(1+m)(-8a_\mu a_\nu(a_\mu + 2a_\nu + (a_\mu + a_\nu)m)\alpha)c}{8a_\mu^4 a_\nu^3} \right], \end{aligned} \quad (\text{A.14})$$

$$\begin{aligned} \langle g_m^l | \nu^2 V(\mu, \nu) | g_m^k \rangle &= \frac{(m!)^2 \pi^2}{(-a_\mu a_\nu)^m} \\ &\times \left[ \frac{(1+m)(-(1+m)(2+m)(a_\nu(2+m) + a_\mu(3+m))\beta^2)c}{8a_\mu^3 a_\nu^4} \right. \\ &\quad \left. + \frac{(1+m)(-8a_\mu a_\nu(2a_\mu + a_\nu + (a_\mu + a_\nu)m)\alpha)c}{8a_\mu^3 a_\nu^4} \right]. \end{aligned} \quad (\text{A.15})$$

### A.3. Integrals for the hydrogen atom in crossed electric and magnetic fields

Using the notation  $a_\mu = a_\mu^k - (a_\mu^l)^*$ ,  $a_\nu = a_\nu^k - (a_\nu^l)^*$ ,  $c = e^{i(\gamma^k - (\gamma^l)^*)}$  and  $h = 1/(a_x^2 + a_y^2 - a_\mu a_\nu)^2$  the elements of the matrix on the left hand side in eq. (6.17) read

$$\begin{aligned}
I_{11}^{lk} &= \langle g^l | g^k \rangle &= c/(a_x^2 + a_y^2 - a_\mu a_\nu), \\
I_{12}^{lk} &= \langle g^l | (u_1^2 + u_2^2) | g^k \rangle &= -ica_\nu h, \\
I_{13}^{lk} &= \langle g^l | (u_3^2 + u_4^2) | g^k \rangle &= -ica_\mu h, \\
I_{14}^{lk} &= \langle g^l | (u_1 u_3 - u_2 u_4) | g^k \rangle &= 2ica_x h, \\
I_{15}^{lk} &= \langle g^l | (u_1 u_4 + u_2 u_3) | g^k \rangle &= 2ica_y h, \\
I_{22}^{lk} &= \langle g^l | (u_3^2 + u_4^2)^2 | g^k \rangle &= -2a_\nu^2 I_{11}^{lk} h, \\
I_{23}^{lk} &= \langle g^l | (u_1^2 + u_2^2)(u_3^2 + u_4^2) | g^k \rangle &= -(a_\mu a_\nu + a_x^2 + a_y^2) I_{11}^{lk} h, \\
I_{24}^{lk} &= \langle g^l | (u_1^2 + u_2^2)(u_1 u_3 - u_2 u_4) | g^k \rangle &= 4a_\nu a_x I_{11}^{lk} h, \\
I_{25}^{lk} &= \langle g^l | (u_1^2 + u_2^2)(u_1 u_4 + u_2 u_3) | g^k \rangle &= 4a_\nu a_y I_{11}^{lk} h, \\
I_{33}^{lk} &= \langle g^l | (u_3^2 + u_4^2)^2 | g^k \rangle &= -2a_\mu^2 I_{11}^{lk} h, \\
I_{34}^{lk} &= \langle g^l | (u_3^2 + u_4^2)(u_1 u_3 - u_2 u_4) | g^k \rangle &= 4a_\mu a_x I_{11}^{lk} h, \\
I_{35}^{lk} &= \langle g^l | (u_3^2 + u_4^2)(u_1 u_4 + u_2 u_3) | g^k \rangle &= 4a_\mu a_y I_{11}^{lk} h, \\
I_{44}^{lk} &= \langle g^l | (u_1 u_3 - u_2 u_4)^2 | g^k \rangle &= 2(a_x^2 - 3a_y^2 - a_\mu a_\nu) I_{11}^{lk} h, \\
I_{45}^{lk} &= \langle g^l | (u_1 u_3 - u_2 u_4)(u_1 u_4 + u_2 u_3) | g^k \rangle &= -8a_x a_y I_{11}^{lk} h, \\
I_{55}^{lk} &= \langle g^l | (u_1 u_4 + u_2 u_3)^2 | g^k \rangle &= 2(a_x^2 - 3a_y^2 - a_\mu a_\nu) I_{11}^{lk} h.
\end{aligned} \tag{A.16}$$

The right hand side vector in eq. (6.17) is split into its diamagnetic and Coulomb terms whose components read

$$\begin{aligned}
I_{v1a} &= \frac{i(a_\mu + a_\nu)((a_\mu a_\nu + 2(a_x^2 + a_y^2))\beta^2 + 4(a_x^2 + a_y^2 - a_\mu a_\nu)^2 \alpha)}{4(a_x^2 + a_y^2 - a_\mu a_\nu)^4} C, \\
I_{v2a} &= \frac{[2a_\mu^2 a_\nu^2 + (a_x^2 + a_y^2)(9a_\nu^2 + 2(a_x^2 + a_y^2)) + a_\mu a_\nu(3a_\nu^2 + 8(a_x^2 + a_y^2))]\beta^2}{4(a_x^2 + a_y^2 - a_\mu a_\nu)^5} C \\
&\quad + \frac{4(a_x^2 + a_y^2 - a_\mu a_\nu)^2 (a_\nu(a_\mu + 2a_\nu) + a_x^2 + a_y^2) \alpha}{4(a_x^2 + a_y^2 - a_\mu a_\nu)^5} C, \\
I_{v3a} &= \frac{[3a_\mu^3 a_\nu + 8a_\mu a_\nu(a_x^2 + a_y^2) + 2(a_x^2 + a_y^2)^2 + a_\mu^2(2a_\nu^2 + 9(a_x^2 + a_y^2))]\beta^2}{4(a_x^2 + a_y^2 - a_\mu a_\nu)^5} C \\
&\quad + \frac{4(a_x^2 + a_y^2 - a_\mu a_\nu)^2 (a_\mu(2a_\mu + a_\nu) + a_x^2 + a_y^2) \alpha}{4(a_x^2 + a_y^2 - a_\mu a_\nu)^5} C, \\
I_{v4a} &= \frac{-(a_\mu + a_\nu)a_x(3(a_\mu a_\nu + a_x^2 + a_y^2)\beta^2 + 4(a_x^2 + a_y^2 - a_\mu a_\nu)^2 \alpha)}{(a_x^2 + a_y^2 - a_\mu a_\nu)^5} C, \\
I_{v5a} &= \frac{-(a_\mu + a_\nu)a_y(3(a_\mu a_\nu + a_x^2 + a_y^2)\beta^2 + 4(a_x^2 + a_y^2 - a_\mu a_\nu)^2 \alpha)}{(a_x^2 + a_y^2 - a_\mu a_\nu)^5} C,
\end{aligned} \tag{A.17}$$

and the terms of the electric field and the paramagnetic contribution are obtained to be

$$\begin{aligned}
 I_{v1b} &= \frac{(2(a_\mu + a_\nu)(a_y^k a_x \beta - a_x^k a_y \beta + a_x \zeta))}{(-a_\mu a_\nu + a_x^2 + a_y^2)^3} C, \\
 I_{v2b} &= \frac{(-2i(2a_\mu a_\nu + 3a_x^2 + a_x^2 + a_y^2)(a_y^k a_x \beta - a_x^k a_y \beta + a_x \zeta))}{(-a_\mu a_\nu + a_x^2 + a_y^2)^4} C, \\
 I_{v3b} &= \frac{(-2i(3a_\mu^2 + 2a_\mu a_\nu + a_x^2 + a_y^2)(a_y^k a_x \beta - a_x^k a_y \beta + a_x \zeta))}{(-a_\mu a_\nu + a_x^2 + a_y^2)^4} C, \\
 I_{v4b} &= \frac{(2i(a_\mu + a_\nu)(-6a_x^k a_x a_y \beta + a_y^k (a_\mu a_\nu + 5a_x^2 - a_y^2)\beta + (a_\mu a_\nu + 5a_x^2 - a_y^2)\zeta))}{(-a_\mu a_\nu + a_x^2 + a_y^2)^4} C, \\
 I_{v5b} &= \frac{(-2i(a_\mu + a_\nu)(a_x^k (a_\mu a_\nu - a_x^2 + 5a_y^2)\beta - 6a_x a_y (a_y^k \beta + \zeta)))}{(-a_\mu a_\nu + a_x^2 + a_y^2)^4} C.
 \end{aligned} \tag{A.18}$$

The right hand side vector in eq. (6.17) is the sum of two corresponding terms in eqs. (A.17) and (A.18), i.e.

$$I_{v1}^{lk} = I_{v1a}^{lk} + I_{v1b}^{lk}, \tag{A.19}$$

$$I_{v2}^{lk} = I_{v2a}^{lk} + I_{v2b}^{lk}, \tag{A.20}$$

$$I_{v3}^{lk} = I_{v3a}^{lk} + I_{v3b}^{lk}, \tag{A.21}$$

$$I_{v4}^{lk} = I_{v4a}^{lk} + I_{v4b}^{lk}, \tag{A.22}$$

$$I_{v5}^{lk} = I_{v5a}^{lk} + I_{v5b}^{lk}. \tag{A.23}$$

## A.4. Integrals for Bose-Einstein condensates with $1/r$ interaction

The integrals for the set of linear equations (7.9) are most simply calculated by the following strategy. First compute  $\langle \psi | \psi \rangle$ ,  $\langle \psi | V_c | \psi \rangle$  and  $\langle \psi | V_u | \psi \rangle$ . The integrals  $\langle \psi | r^{2n} | \psi \rangle$ ,  $n = 1, 2$  are obtained by differentiation of  $\langle \psi | \psi \rangle$ , i.e.

$$\langle \psi | r^{2n} | \psi \rangle = -\frac{\partial^n}{\partial (2A_i)^n} \langle \psi | \psi \rangle. \tag{A.24}$$

And similar for the integrals containing the potentials

$$\langle \psi | r^{2n} V | \psi \rangle = -\frac{\partial^n}{\partial (4A_i)^n} \langle \psi | V | \psi \rangle. \tag{A.25}$$

The different factor of two result from the nonlinear potentials  $V_u$  and  $V_c$ , which are quadratic in  $\psi$ . Altogether we obtain

$$\langle \psi | \psi \rangle = \frac{\pi^{3/2}}{2\sqrt{2}} e^{-2\gamma_i} A_i^{-3/2}, \quad (\text{A.26a})$$

$$\langle \psi | r^2 | \psi \rangle = \frac{3\pi^{3/2}}{8\sqrt{2}} e^{-2\gamma_i} A_i^{-5/2}, \quad (\text{A.26b})$$

$$\langle \psi | r^4 | \psi \rangle = \frac{15\pi^{3/2}}{32\sqrt{2}} e^{-2\gamma_i} A_i^{-7/2}, \quad (\text{A.26c})$$

$$\langle \psi | V_c | \psi \rangle = \frac{\pi^{5/2}}{2} a e^{-4\gamma_i} A_i^{-3/2}, \quad (\text{A.26d})$$

$$\langle \psi | V_u | \psi \rangle = -\frac{\pi^{5/2}}{4} e^{-4\gamma_i} A_i^{-5/2}, \quad (\text{A.26e})$$

$$\langle \psi | r^2 V_c | \psi \rangle = \frac{3\pi^{5/2}}{16} a e^{-4\gamma_i} A_i^{-5/2}, \quad (\text{A.26f})$$

$$\langle \psi | r^2 V_u | \psi \rangle = -\frac{5\pi^{5/2}}{32} e^{-4\gamma_i} A_i^{-7/2}. \quad (\text{A.26g})$$

## A.5. Integrals for Bose-Einstein condensates with dipolar interaction

Now the integrals related to dipolar BEC are given. All integrals in eq. (8.7) are obtained from the the integrals  $I_{00}$  and  $I_{V00}$  by differentiation with respect to the imaginary parts  $A_\rho^i$  and  $A_z^i$  of the complex width parameters  $A_\rho = A_\rho^r + iA_\rho^i$  and  $A_z = A_z^r + iA_z^i$  and  $\gamma = \gamma^r + i\gamma^i$ . The overlap integral is

$$I_{00} = \langle \chi | \chi \rangle = \frac{\pi^{3/2}}{2\sqrt{2} A_\rho^i A_z^{i1/2}} \exp[-2\gamma^i],$$

and higher moments are computed by

$$\begin{aligned} I_{2n2m} &= \langle \psi | \rho^{2n} z^{2m} | \psi \rangle = \int dx^3 \rho^{2n+1} z^{2m} e^{-2A_\rho^i \rho^2 - 2A_z^i z^2 - 2\gamma^i} \\ &= \frac{1}{(-2)^{n+m}} \frac{\partial^n}{(\partial A_\rho^i)^n} \frac{\partial^m}{(\partial A_z^i)^m} I_{00}. \end{aligned} \quad (\text{A.27})$$



The integrals of the matrix on the left hand side of eq. (8.7) read

$$I_{00} = \frac{k}{A_\rho^i \sqrt{A_z^i}}, \quad (\text{A.28a})$$

$$I_{20} = \frac{k}{2(A_\rho^i)^2 \sqrt{A_z^i}}, \quad (\text{A.28b})$$

$$I_{02} = \frac{k}{4A_\rho^i A_z^i \sqrt{A_z^i}}, \quad (\text{A.28c})$$

$$I_{22} = \frac{k}{8(A_\rho^i)^2 A_z^i \sqrt{A_z^i}}, \quad (\text{A.28d})$$

$$I_{40} = \frac{k}{2(A_\rho^i)^3 \sqrt{A_z^i}}, \quad (\text{A.28e})$$

$$I_{04} = \frac{3k}{16A_\rho^i (A_z^i)^2 \sqrt{A_z^i}}, \quad (\text{A.28f})$$

with  $k = (\pi)^{3/2} e^{-2\gamma^i} / (2\sqrt{2})$ . The entries on the right hand side are a bit lengthy. For a better lucidity the potential contributions are split into the trapping part  $V_t$ , the scattering part  $V_c$  and the dipolar part  $V_d$ . The trap contributions read

$$I_{V_{t00}} = \gamma_\rho^2 I_{20} + \gamma_z^2 I_{02}, \quad (\text{A.29a})$$

$$I_{V_{t20}} = \gamma_\rho^2 I_{40} + \gamma_z^2 I_{22}, \quad (\text{A.29b})$$

$$I_{V_{t02}} = \gamma_\rho^2 I_{22} + \gamma_z^2 I_{04}. \quad (\text{A.29c})$$

The nonlinear scattering term gives

$$I_{V_{c00}} = \frac{2\sqrt{2}\pi k a e^{-2\gamma^i}}{A_\rho^i \sqrt{A_z^i}}, \quad (\text{A.30a})$$

$$I_{V_{c20}} = \frac{\pi k a e^{-2\gamma^i}}{\sqrt{2}(A_\rho^i)^2 \sqrt{A_z^i}}, \quad (\text{A.30b})$$

$$I_{V_{c02}} = \frac{\pi k a e^{-2\gamma^i}}{2\sqrt{2}A_\rho^i A_z^i \sqrt{A_z^i}}, \quad (\text{A.30c})$$

which could be obtained by

$$I_{V_{c2n2m}} = \left(-\frac{1}{4}\right)^{n+m} \frac{\partial^n}{(\partial A_\rho^i)^n} \frac{\partial^m}{(\partial A_z^i)^m} I_{V_{c00}}. \quad (\text{A.31})$$

## A. Gaussian type integrals

---

The dipolar terms are

$$I_{V_{d00}} = \frac{e^{-4\gamma^i \pi^{5/2}} \left( 1 + 2 \frac{A_z^i}{A_\rho^i} - \frac{3A_z^i \arctan \left[ \sqrt{\frac{A_z^i}{A_\rho^i} - 1} \right]}{A_\rho^i \sqrt{\frac{A_z^i}{A_\rho^i} - 1}} \right)}{6\sqrt{A_z^i} (-A_z^i - A_\rho^i)}, \quad (\text{A.32a})$$

$$I_{V_{d20}} = -\frac{e^{-4\gamma^i \pi^{5/2}} \left( (A_\rho^i - A_z^i)(2(A_\rho^i)^2 + 11A_\rho^i A_z^i - 4(A_z^i)^2) \right)}{48(A_\rho^i)^2 (A_\rho^i - A_z^i)^3 \sqrt{A_z^i}} \\ + \frac{e^{-4\gamma^i \pi^{5/2}} \left( +3A_\rho^i (4A_\rho^i - A_z^i) A_z^i \sqrt{\frac{A_z^i}{A_\rho^i} - 1} \arctan \left[ \sqrt{\frac{A_z^i}{A_\rho^i} - 1} \right] \right)}{48(A_\rho^i)^2 (A_\rho^i - A_z^i)^3 \sqrt{A_z^i}}, \quad (\text{A.32b})$$

$$I_{V_{d02}} = -\frac{e^{-4\gamma^i \pi^{5/2}} \left( (A_\rho^i)^3 - 9(A_\rho^i)^2 A_z^i + 6A_\rho^i (A_z^i)^2 + 2(A_z^i)^3 \right)}{48A_\rho^i (A_\rho^i - A_z^i)^3 A_z^i \sqrt{A_z^i}} \\ + \frac{e^{-4\gamma^i \pi^{5/2}} \left( -3A_\rho^i A_z^i (A_\rho^i + 2A_z^i) \sqrt{\frac{A_z^i}{A_\rho^i} - 1} \arctan \left[ \sqrt{\frac{A_z^i}{A_\rho^i} - 1} \right] \right)}{48A_\rho^i (A_\rho^i - A_z^i)^3 A_z^i \sqrt{A_z^i}}, \quad (\text{A.32c})$$

obtained by (A.31). When the evolution of  $A_z^i(t)$  crosses  $A_\rho^i(t)$  at some time, the dipolar potential parts (A.32) must locally be expanded in Taylor series at  $\kappa = \frac{A_z^i}{A_\rho^i} = 1$  to roughly the third or fourth order. This is necessary, because for  $\kappa = 1$  terms like “ $\frac{0}{0}$ ” occur in the dipolar interaction, which present a removable discontinuity. However, for numerical reasons the exact expressions (A.32) must be replaced by their Taylor expansions in a region  $1 - \epsilon < \left| \frac{A_z^i}{A_\rho^i} \right| < 1 + \epsilon$ .

## B. Reduction of the number of parameters in the matrices $B, C$

The number of independent parameters of the  $4 \times 4$  matrices  $B^k, C^k$  can be reduced from 32 to 16 per GWP, provided the matrices  $A^k$  are of the form (5.35). This technique allows for a reduction of the overall number of differential equations, which have to be solved, from 33 to 17 per GWP. If  $B^k$  and  $C^k$  would have the form of  $A^k$  initially, given by eq. (5.35), their symmetry would be destroyed during the evolution since the product  $V_2^k C^k$ , which determines the evolution of the matrix  $B^k$ , does not preserve the symmetry (5.35), even if  $V_2^k$  and  $C^k$  do. That is, a symmetry for  $B^k, C^k$  is searched such that it is preserved by the product  $V_2^k C^k$  occurring in eq. (3.32), where the matrices  $V_2^k$  have the symmetry of  $A^k$  in eq. (5.35). Such a symmetry is provided by the form

$$B = \begin{pmatrix} b_{11} & b_{12} & b_{13} & b_{14} \\ -b_{12} & b_{11} & b_{14} & -b_{13} \\ b_{31} & b_{32} & b_{33} & b_{34} \\ b_{32} & -b_{31} & -b_{34} & b_{33} \end{pmatrix}, \quad C = \begin{pmatrix} c_{11} & c_{12} & c_{13} & c_{14} \\ -c_{12} & c_{11} & c_{14} & -c_{13} \\ c_{31} & c_{32} & c_{33} & c_{34} \\ c_{32} & -c_{31} & -c_{34} & c_{33} \end{pmatrix}, \quad (\text{B.1})$$

as may easily be shown by explicit multiplication. The superscript  $k$  running over all GWPs has been omitted here. The number of independent parameters per matrix thus has reduced from 16 to 8.

The computation of the matrix  $A$  according to the definition  $A = \frac{1}{2}BC^{-1}$  requires the inversion of the matrix  $C$ . This could be accomplished numerically, however the special symmetry of the matrix  $C$  allows for a compact analytical inversion. To this end it is convenient to introduce an auxiliary  $4 \times 4$  matrix  $D$  whose elements are rearranged elements of the matrix  $C$  and reads

$$D = \begin{pmatrix} c_{33} & -c_{34} & -c_{13} & -c_{14} \\ c_{34} & c_{33} & -c_{14} & c_{13} \\ -c_{31} & -c_{32} & c_{11} & -c_{12} \\ -c_{32} & c_{31} & c_{12} & c_{11} \end{pmatrix}. \quad (\text{B.2})$$

The product  $C_1 = CD$  gives

$$C_1 = \begin{pmatrix} h & k & 0 & 0 \\ -k & h & 0 & 0 \\ 0 & 0 & h & -k \\ 0 & 0 & k & h \end{pmatrix}, \quad (\text{B.3})$$

*B. Reduction of the number of parameters in the matrices  $B, C$*

---

with  $h = -c_{13}c_{31} - c_{14}c_{32} + c_{11}c_{33} + c_{12}c_{34}$  and  $k = c_{14}c_{31} - c_{13}c_{32} + c_{12}c_{33} - c_{11}c_{34}$ . Due to the definition  $C_1 = CD$  the inverse of  $C$  may easily be computed by  $C^{-1} = DC_1^{-1}$  when the inverse of  $C_1$  is known. Due to the simple structure of  $C_1$  its inverse is simply

$$C_1^{-1} = \frac{1}{h^2 + k^2} \begin{pmatrix} h & -k & 0 & 0 \\ k & h & 0 & 0 \\ 0 & 0 & h & k \\ 0 & 0 & -k & h \end{pmatrix}, \quad (\text{B.4})$$

and then  $A = \frac{1}{2}BC^{-1} = \frac{1}{2}BDC_1^{-1}$ . The four independent parameters read

$$a_\mu = \frac{(b_{11}c_{33} - b_{14}c_{32} + b_{12}c_{34} - b_{13}c_{31})h}{2(h^2 + k^2)} + \frac{(b_{14}c_{31} + b_{12}c_{33} - b_{11}c_{34} - b_{13}c_{32})k}{2(h^2 + k^2)}, \quad (\text{B.5})$$

$$a_\nu = \frac{(b_{33}c_{11} + b_{34}c_{12} - b_{31}c_{13} - b_{32}c_{14})h}{2(h^2 + k^2)} + \frac{(b_{33}c_{12} - b_{34}c_{11} - b_{32}c_{13} + b_{31}c_{14})k}{2(h^2 + k^2)}, \quad (\text{B.6})$$

$$a_x = \frac{(b_{13}c_{11} + b_{14}c_{12} - b_{11}c_{13} - b_{12}c_{14})h}{2(h^2 + k^2)} + \frac{(b_{13}c_{12} - b_{14}c_{11} - b_{12}c_{13} + b_{11}c_{14})k}{2(h^2 + k^2)}, \quad (\text{B.7})$$

$$a_y = \frac{(b_{14}c_{11} - b_{13}c_{12} + b_{12}c_{13} - b_{11}c_{14})h}{2(h^2 + k^2)} + \frac{(b_{13}c_{11} + b_{14}c_{12} - b_{11}c_{13} - b_{12}c_{14})k}{2(h^2 + k^2)}. \quad (\text{B.8})$$

The parameters  $a_\mu, a_\nu, a_x, a_y$  are needed to build up the integrals in eq. (6.17) listed in appendix A.3, and must be computed after every time step of integration.

## C. Split-operator method

The split-operator method (SPO) [47] provides a powerful method for numerically exact quantum dynamics. Consider the following splitting of the time evolution operator where we assume that the Hamiltonian can be written as a sum of a kinetic and a potential part  $H = T + V$

$$e^{-i\tau H} = e^{-i\frac{\tau}{2}T} e^{-i\tau V} e^{-i\frac{\tau}{2}T} + \mathcal{O}(\tau^3). \quad (\text{C.1})$$

The splitting is exact up to second order in  $\tau$ . The Integration starts with the kinetic part of the operator in equation (C.1) which is applied to the momentum space representation of the wave function  $\tilde{\psi}(p)$  where the action of the momentum operator is simply multiplicative and the integration over the (half-)time step can be done analytically and yields

$$\tilde{\psi}(p, t + \tau/2) = e^{-i\frac{p^2}{2m}\frac{\tau}{2}} \tilde{\psi}(p, t). \quad (\text{C.2})$$

Then a full time step is taken with the potential part, which gives a phase shift of the wave function in configuration space representation  $\psi(x)$ .

$$\psi(x, t + \tau) = e^{-iV(x)\tau} \psi(x, t). \quad (\text{C.3})$$

The transformation between configuration and momentum space is done most efficiently by fast Fourier transform. The last part of the integration step is to take again a half time step of the kinetic part in momentum space. In practice multiple integration steps are applied in succession. Two successive half time steps in momentum space are combined in a single full time step.

The Fourier transform is approximated by a sum over discrete values given on an equidistant grid in configuration as well as in momentum space. In one dimension the discrete Fourier transform is written as

$$\tilde{\Psi}(p_k, t) = \sum_{l=-n/2+1}^{n/2} \Psi(x_l, t) e^{-i2\pi p_k x_l} \Delta x = \sum_{l=-n/2+1}^{n/2} \Psi(x_l, t) e^{-i2\pi k l/n} \Delta x \quad (\text{C.4})$$

where  $p_k = k\Delta p$ ,  $x_l = l\Delta x$  and  $k, l \in [-n/2 + 1, n/2]$ . The step length in momentum space is chosen to be  $\Delta p = 1/n\Delta x$ . The grid sizes and the number of points must be large enough so that the wave functions vanish on the boundaries in either spaces. A check for a converged step size  $\tau$  is to observe the expectation value of the Hamiltonian, which should be constant for a time-independent Hamiltonian. Note, that the conservation of the norm of the wave function presents no criterion, since the algorithm is unitary and the norm is exactly conserved.



# Bibliography

- [1] M. F. Herman and E. Kluk, *A semiclassical justification for the use of non-spreading wavepackets in dynamics calculations*, Chem. Phys. **91**, 27 (1984).
- [2] E. Kluk, M. F. Herman, and H. L. Davis, *Comparison of the propagation of semiclassical frozen Gaussian wave functions with quantum propagation for a highly excited anharmonic oscillator*, J. Chem. Phys. **84**, 326 (1986).
- [3] M. H. Beck, A. Jäckle, G. A. Worth, and H.-D. Meyer, *The multiconfigurational time-dependent Hartree (MCTDH) method: A highly efficient algorithm for propagating wavepackets*, Pys. Rep. **324**, 1 (2000).
- [4] V. Buch, *Exploration of multidimensional variational Gaussian wave packets as a simulation tool*, J. Chem. Phys. **117**, 4738 (2002).
- [5] R. D. Coalson and M. Karplus, *Multidimensional variational Gaussian wave packet dynamics with application to photodissociation spectroscopy*, J. Chem. Phys. **93**, 3919 (1990).
- [6] F. Hansen, N. E. Henriksen, and G. D. Billing, *The time propagation of the stationary states of a Morse oscillator by the Gaussian wave packet method*, J. Chem. Phys. **90**, 3060 (1989).
- [7] R. Heather and H. Metiu, *A numerical study of the multiple Gaussian representation of time dependent wave functions of a Morse oscillator*, J. Chem. Phys. **84**, 3250 (1986).
- [8] E. J. Heller, *Time dependent variational approach to semiclassical dynamics*, J. Chem. Phys. **64**, 63 (1976).
- [9] S.-I. Sawada, R. Heather, B. Jackson, and H. Metiu, *A strategy for time dependent quantum mechanical calculations using a Gaussian wave packet representation of the wave function*, J. Chem. Phys. **83**, 3009 (1985).
- [10] E. J. Heller, *Time-dependent approach to semiclassical dynamics*, J. Chem. Phys. **62**, 1544 (1975).
- [11] E. J. Heller, *Frozen Gaussians: A very simple semiclassical approximation*, J. Chem. Phys. **75**, 2923 (1981).

- [12] T. Fabčić, J. Main, and G. Wunner, *Gaussian wave packet dynamics in the diamagnetic H-atom*, Nonlinear Phenomena in Complex Systems **10**, 86 (2007).
- [13] T. Fabčić, J. Main, and G. Wunner, *Time propagation of constrained coupled Gaussian wave packets*, J. Chem. Phys. **128**, 044116 (2008).
- [14] K. G. Kay, *The matrix singularity problem in the time-dependent variational method*, Chem. Phys. **137**, 165 (1989).
- [15] R. T. Skodje and D. G. Truhlar, *Localized Gaussian wave packet methods for inelastic collisions involving anharmonic oscillators*, J. Chem. Phys. **80**, 3123 (1984).
- [16] I. Horenko, M. Weiser, B. Schmidt, and C. Schütte, *Fully adaptive propagation of the quantum-classical Liouville equation*, J. Chem. Phys. **120**, 8913 (2004).
- [17] J. Zoppe, M. L. Parkinson, and M. Messina, *A variational solution of the time-dependent Schrödinger equation by a restricted superposition of frozen Gaussian wavepackets*, Chem. Phys. Lett. **407**, 308 (2005).
- [18] N. E. Henriksen and E. J. Heller, *Quantum dynamics for vibrational and rotational degrees of freedom using Gaussian wave packets: Application to the three-dimensional photodissociation dynamics of ICN*, J. Chem. Phys. **91**, 4700 (1989).
- [19] B. Jackson and H. Metiu, *A multiple Gaussian wave packet theory of H<sub>2</sub> diffraction and rotational excitation by collision with solid surfaces*, J. Chem. Phys. **85**, 4129 (1986).
- [20] H. Feldmeier, *Fermionic molecular dynamics*, Nucl. Phys. **A515**, 147 (1990).
- [21] H. Feldmeier and J. Schnack, *Molecular dynamics for Fermions*, Rev. Mod. Phys. **72**, 655 (2000).
- [22] I. M. S. Barnes, *Semiclassical wavepacket propagation in a hydrogen atom*, Chaos, Solitons & Fractals **6**, 531 (1995).
- [23] I. M. S. Barnes, M. Nauenberg, M. Nockleby, and S. Tomsovic, *Classical orbits and semiclassical wavepacket propagation in the Coulomb Potential*, J. Phys. A **71**, 1961 (1993).
- [24] I. M. S. Barnes, M. Nauenberg, M. Nockleby, and S. Tomsovic, *Semiclassical theory of quantum propagation: The Coulomb Potential*, Phys. Rev. Lett. **71**, 1961 (1993).
- [25] P. Kustaanheimo and E. Stiefel, *Perturbation theory of Kepler motion based on spinor regularization*, Journal für die reine und angewandte Mathematik **218**, 204 (1965).



- 
- [26] E. Stiefel and G. Scheifele, *Linear and Regular Celestial Mechanics* (Springer, 1971).
- [27] T. Bartsch, J. Main, and G. Wunner, *Semiclassical quantization of the hydrogen atom in crossed electric and magnetic fields*, Phys. Rev. A **67**, 063411 (2003).
- [28] J. Main, G. Wiebusch, A. Holle, and K. H. Welge, *New Quasi-Landau Structure of Highly Excited Atoms: The Hydrogen Atom*, Phys. Rev. Lett. **57**, 2789 (1986).
- [29] J. Main and G. Wunner, *Ericson fluctuations in the chaotic ionization of the hydrogen atom in crossed magnetic and electric fields*, Phys. Rev. Lett. **69**, 586 (1992).
- [30] J. Main and G. Wunner, *Rydberg atoms in external fields as an example of open quantum systems with classical chaos*, J. Phys. B **27**, 2835 (1994).
- [31] D. O'Dell, S. Giovanazzi, G. Kurizki, and V. M. Akulin, *Bose-Einstein Condensates with  $1/r$  Interatomic Attraction: Electromagnetically Induced "Gravity"*, Phys. Rev. Lett. **84**, 5687 (2000).
- [32] I. Papadopoulos, P. Wagner, G. Wunner, and J. Main, *Bose-Einstein condensates with attractive  $1/r$  interaction: The case of self-trapping*, Phys. Rev. A **76**, 053604 (2007).
- [33] V. M. Pérez-García, H. Michinel, J. Cirac, M. Lewenstein, and P. Zoller, *Dynamics of Bose-Einstein condensates: Variational solutions of the Gross-Pitaevskii equations*, Phys. Rev. A **56**, 1424 (1997).
- [34] E. A. Donley, N. R. Claussen, S. L. Cornish, J. L. Roberts, E. A. Cornell, and C. E. Wieman, *Dynamics of collapsing and exploding Bose Einstein-condensates*, Nature **412**, 295 (2001).
- [35] T. Koch, T. Lahaye, J. Metz, B. Fröhlich, A. Griesmaier, and T. Pfau, *Stabilization of a purely dipolar quantum gas against collapse*, Nature physics **4**, 218 (2008).
- [36] A. Griesmaier, J. Werner, S. Hensler, J. Stuhler, and T. Pfau, *Bose-Einstein Condensation of Chromium*, Phys. Rev. Lett. **94**, 160401 (2005).
- [37] J. Broeckhove, L. Lathouwers, and P. V. Leuven, *Time-dependent variational principles and conservation laws in wavepacket dynamics*, J. Phys. A **22**, 4395 (1989).
- [38] E. Faou and C. Lubich, *A Poisson integrator for Gaussian wavepacket dynamics*, Computing and Visualization in Science **9**, 45 (2006).
- [39] P. A. M. Dirac, *Note on exchange phenomena in the Thomas atom*, Proc. Cam. Phil. Soc. **26**, 376 (1930).
- [40] J. Frenkel, *Wave mechanics, advanced general theory* (Clarendon Press, Oxford, 1934).

- [41] P. Kramer and M. Saraceno, *Geometry of the time-dependent variational principle in quantum mechanics* (Berlin: Springer, Lecture notes in physics, 1981).
- [42] A. D. McLachlan, *A variational solution of the time-dependent Schrodinger equation*, Mol. Phys. **8**, 39 (1964).
- [43] C. Lubich, *On variational approximations in quantum molecular dynamics*, Math. Comp. **74**, 765 (2005).
- [44] A. Raab, *On the Dirac-Frenkel/McLachlan variational principle*, Chem. Phys. Lett. **319**, 674 (2000).
- [45] E. J. Heller, *Classical S-matrix limit of wave packet dynamics*, J. Chem. Phys. **65**, 4979 (1976).
- [46] S. Gershgorin, *Über die Abgrenzung der Eigenwerte einer Matrix*, Izv. Akad. Nauk. USSR Otd. Fiz.-Mat. Nauk **7**, 749 (1931).
- [47] M. D. Feit, J. A. Fleck, Jr., and A. Steiger, *Solution of the Schrödinger equation by a spectral method*, J. Comp. Phys. **47**, 412 (1982).
- [48] Dž. Belkić, P. A. Dando, J. Main, and H. S. Taylor, *Three novel high-resolution nonlinear methods for fast signal processing*, J. Chem. Phys. **113**, 6542 (2000).
- [49] J. Main, *Use of harmonic inversion techniques in semiclassical quantization and analysis of quantum spectra*, Phys. Rep. **316**, 233 (1999).
- [50] J. Main, P. A. Dando, D. Belkic, and H. S. Taylor, *Decimation and harmonic inversion of periodic orbit signals*, J. Phys. A **33**, 1247 (2000).
- [51] V. A. Mandelshtam and H. S. Taylor, *Harmonic inversion of time signals and its applications*, J. Chem. Phys **107**, 6756 (1997).
- [52] J. R. Reimers and E. J. Heller, *The exact eigenfunctions and eigenvalues of a two-dimensional rigid rotor obtained using Gaussian wave packet dynamics*, J. Chem. Phys. **83**, 511 (1985).
- [53] J. R. Reimers and E. J. Heller, *The exact eigenfunctions and eigenvalues of a particle in a box obtained using Gaussian wavepacket dynamics*, J. Phys. A **19**, 2559 (1986).
- [54] M. Boiteux, *The three dimensional hydrogen atom as a restricted four-dimensional harmonic oscillator*, Physica **65**, 381 (1972).
- [55] B. R. Johnson, *Time variables in propagators and coherent states for the Kepler-Coulomb problem*, Phys. Rev. A **35**, 1412 (1987).

- 
- [56] C. C. Gerry, *Coherent states and the Kepler-Coulomb problem*, Physical Review A **33**, 6 (1986).
- [57] S. A. Pol'shin, *Coherent states for the hydrogen atom: discrete and continuous spectra*, J. Phys. A **34**, 11083 (2001).
- [58] T. Toyoda and S. Wakayama, *Coherent states for the Kepler motion*, Physical Review A **59**, 1021 (1999).
- [59] N. Unal, *Parametric time-coherent states for the hydrogen atom*, Physical Review A **63**, 052105 (2001).
- [60] B.-W. Xu and G.-H. Ding, *Nonspreading coherent states for the hydrogen atom*, Physical Review A **62**, 022106 (2000).
- [61] E. Schrödinger, *Der stetige Übergang von der Mikro- zur Makromechanik*, Die Naturwissenschaften **14**, 664 (1926).
- [62] D. Huber and E. J. Heller, *Hybrid mechanics: A combination of classical and quantum mechanics*, J. Chem. Phys. **89**, 4752 (1988).
- [63] F. Schwabl, *Quantenmechanik für Fortgeschrittene* (Springer, Berlin, 2000).
- [64] D. Bhaumik, B. Dutta-Roy, and G. Ghosh, *Classical limit of the hydrogen atom*, J. Phys. A **19**, 1355 (1986).
- [65] W. H. Press, S. A. Teukolsky, W. T. Vetterling, and B. P. Flannery, *Numerical Recipes* (University Press, Cambridge, 1992).
- [66] M. Baranov, L. Dobrek, K. Góral, L. Santos, and M. Lewenstein, *Ultracold dipolar gases - a challenge for experiments and theory*, Phys. Scr. **T102**, 74 (2002).
- [67] S. Giovanazzi, A. Görlitz, and T. Pfau, *Tuning the dipolar interaction in quantum gases*, J. Opt. B. **5**, S208 (2003).
- [68] K. Góral and L. Santos, *Ground state and elementary excitations of single and binary Bose-Einstein condensates of trapped dipolar gases*, Phys. Rev. A **66**, 023613 (2002).
- [69] K. Góral, L. Santos, and M. Lewenstein, *Quantum phases of dipolar bosons in optical lattices*, Phys. Rev. Lett. **88**, 170406 (2002).
- [70] L. Santos, G. V. Shlyapnikov, P. Zoller, and M. Lewenstein, *Bose-Einstein condensation in trapped dipolar gases*, Phys. Rev. Lett. **85**, 1791 (2000).

- [71] D. O'Dell, S. Giovanazzi, G. Kurizki, and V. M. Akulin, *Bose-Einstein condensates with  $1/r$  interatomic attraction: Electromagnetically induced "Gravity"*, Phys. Rev. Lett. **84**, 5687 (2000).
- [72] H. Cartarius, J. Main, and G. Wunner, *Discovery of exceptional points in the Bose-Einstein condensation of gases with attractive  $1/r$ -interaction*, Phys. Rev. A **77**, 013618 (2008).
- [73] H. Cartarius, J. Main, and G. Wunner, *Exceptional points in atomic systems*, Phys. Rev. Lett. **99**, 173003 (2007).
- [74] U. Günther, I. Rotter, and B. F. Samsonov, *Projective Hilbert space structures at exceptional points*, J. Phys. A **40**, 8815 (2007).
- [75] W. D. Heiss, *Phase of wave functions and level repulsion*, Eur. Phys. J. D **7**, 1 (1999).
- [76] W. D. Heiss, *Exceptional points of non-Hermitian operators*, J. Phys. A **37**, 2455 (2004).
- [77] T. Kato, *Perturbation theory for linear operators* (Springer, Berlin, 1966).
- [78] H. Cartarius, Dissertation, Universität Stuttgart (in preparation).
- [79] H. Cartarius, T. Fabčić, J. Main, and G. Wunner, *Dynamics and stability of Bose-Einstein condensates with attractive  $1/r$  interaction* (2008), Phys. Rev. A **78**, 013615 (2008).
- [80] Y. Kagan, A. E. Muryshev, and G. V. Shlyapnikov, *Collapse and Bose-Einstein Condensation in a Trapped Bose Gas with Negative Scattering Length*, Phys. Rev. Lett. **81**, 933 (1998).
- [81] T. Lahaye, T. Koch, B. Fröhlich, M. Fattori, J. Metz, A. Griesmaier, S. Giovanazzi, and T. Pfau, *Strong dipolar effects in a quantum ferrofluid*, Nature **448**, 672 (2007).
- [82] J. Stuhler, A. Griesmaier, T. Koch, M. Fattori, T. Pfau, S. Giovanazzi, P. Pedri, and L. Santos, *Observation of dipole-dipole interaction in a degenerate quantum gas*, Phys. Rev. Lett. **95**, 150406 (2005).
- [83] T. Schwidder, Diplomarbeit, Universität Stuttgart (in preparation).
- [84] P. Wagner, *Bose-Einstein condensates with electromagnetically induced  $1/r$ -potential*, Diplomarbeit, Universität Stuttgart (2007).
- [85] P. Köberle, H. Cartarius, T. Fabčić, J. Main, and G. Wunner, *Bifurcations, order, and chaos in the Bose-Einstein condensation of dipolar gases* (2008), preprint arXiv:0802.4055.

- [86] A. Griesmayer, J. Werner, S. Hensler, J. Stuhler, and T. Pfau, *Bose-Einstein condensation of chromium*, Phys. Rev. Lett. **94**, 160401 (2005).

*Bibliography*

---

# Danksagung

Viele haben in der einen oder anderen Weise zum Gelingen dieser Arbeit beigetragen. Bei den folgenden Personen möchte ich mich an dieser Stelle bedanken:

- Prof. Dr. J. Main für die hervorragende und freundliche Betreuung.
- Prof. Dr. G. Wunner für die Anstellung am 1. Institut für Theoretische Physik.
- Prof. Dr. H. P. Büchler für die Übernahme des Mitberichtes.
- Bei den Systemadministratoren für das gut funktionierende Rechnersystem.
- Bei Holger Cartarius, Jan Gehrke, Torsten Schwidder, Peter Diemand und Patrick Köberle für das gute Arbeitsklima und die angenehme Atmosphäre.





### **Lebenslauf**

Name Tomaz Fabčič  
geboren am 7. September 1975  
in Stuttgart  
Familienstand verheiratet mit Sandra Weipert,  
Kinder: Luka, Tim, Hanna

### **Schulen**

1982 – 1986 Steinenbergschule  
1986 – 1995 Württemberg-Gymnasium  
Juli 1995 Abitur

### **Studium**

1995 – 2002 Studium der Physik an der Universität Stuttgart  
September 2002 Physik Diplom  
Thema der Diplomarbeit: *„Das Wasserstoffatom im Magnetfeld:  
Berechnung des Wiederkehrsignals unter Berücksichtigung  
gleichmäßiger semiklassischer Näherungen“*



### **Ehrenwörtliche Erklärung**

Ich erkläre, daß ich diese Dissertation, abgesehen von den ausdrücklich bezeichneten Hilfsmitteln, selbständig verfaßt habe.

Stuttgart, 4. Juni 2008

*Tomaž Fabčič*